A locally conservative Galerkin approach for subject-specific biofluid dynamics.

Bevan, Rhodri L.T

Swansea University
Prifysgol Abertawe

Civil & Computational Engineering Centre
Swansea University

A locally conservative Galerkin approach for subject-specific biofluid dynamics

Rhodri L. T. Bevan

Civil and Computational Engineering Centre, School of Engineering, Swansea University, Swansea, Singleton Park, Swansea, SA2 8PP.

Thesis submitted to Swansea University in candidature for the degree of Doctor of Philosophy

September 2010

Summary

In this thesis, a parallel solver was developed for the modelling of blood flow through a number of patient-specific geometries. A locally conservative Galerkin (LCG) spatial discretisation was applied along with an artificial compressibility and characteristic based split (CBS) scheme to solve the 3D incompressible Navier-Stokes equations. The Spalart-Allmaras one equation turbulence model was also optionally employed. The solver was constructed using FORTRAN and the Message Passing Interface (MPI). Parallel testing demonstrated linear or better than linear speedup on hybrid patient-specific meshes. These meshes were unstructured with structured boundary layers. From the parallel testing it is clear that the significance of inter-processor communication is negligible in a three dimensional case.

Preliminary tests on a short patient-specific carotid geometry demonstrated the need for ten or more boundary layer meshes in order to sufficiently resolve the peak wall shear stress (WSS) along with the peak time-averaged WSS. A time sensitivity study was also undertaken along with the assessment of the order of the real time step term. Three backward difference formulae (BDF) were tested and no significant difference between them was detected. Significant speedup was possible as the order of time discretisation increased however, making the choice of BDF important in producing a timely solution.

Followed by the preliminary investigation, four more carotid geometries were investigated in detail. A total of six haemodynamic wall parameters have been brought together to analyse the regions of possible atherogenesis within each carotid. The investigations revealed that geometry plays an overriding influence on the wall parameter distribution. Each carotid artery displayed high time-averaged WSS at the apex, although the value increased significantly with a proximal stenosis. Two out of four meshes contained a region of low time-averaged WSS distal to the flow divider and within the largest connecting artery (internal or external carotid artery), indicating a potential region of atherosclerosis plaque formation. The remaining two meshes already had a stenosis in the corresponding region. This is in excellent agreement with other established works.

From the investigations, it is apparent that a classification system of stenosis severity may be possible with potential application as a clinical diagnosis aid. Finally, the flow within a thoracic aortic aneurysm was investigated in order to assess the influence of a proximal folded neck. The folded neck had a significant effect on the wall shear stress, increasing by up to 250% over an artificially smoothed neck. High wall shear stresses may be linked to aneurysm rupture. Being proximal to the aneurysm, this indicated that local geometry should be taken into account when assessing the rupture potential of an aneurysm.

Declaration and Statements

DECLARATION

This work has not previously been accepted in substance for any degree and is not being concurrently submitted in candidature for any degree.

Signed ..... (candidate)

Date ..... 20/4/2011 .....

STATEMENT 1

This thesis is the result of my own investigations, except where otherwise stated. Where correction services have been used, the extent and nature of the correction is clearly marked in a footnote(s).

Other sources are acknowledged by footnotes giving explicit references. A bibliography is appended.

Signed ..... (candidate)

Date ..... 20/4/2011 .....

STATEMENT 2

I hereby give consent for my thesis, if accepted, to be available for photocopying and for inter-library loan, and for the title and summary to be made available to outside organisations.

Signed ..... (candidate)

Date ..... 20/4/2011 .....

Table of Contents

List of Figures

List of Tables

Acknowledgements

I would like to thank my supervisors, Professor P. Nithiarasu and Dr R. van Loon for their guidance and patience. I would also like to thank Dr I. Sazonov for his help in mesh generation and Dr J. Jones for his mesh partitioning program. Others that provided assistance were Professor M. Vazquez during my stay in Barcelona and Dr H. Luckraz from the Royal Wolverhampton Hospital. Finally, I would like to thank my friends and family for their support and understanding throughout the duration of the work, as well as pretending enthusiasm when listening to any story of a computational programming triumph!

I would like to express my gratitude for the financial aid provided by the Engineering and Physical Sciences Research Council (EPSRC) without which this research would not have been possible. I would also like to thank the Barcelona Supercomputing Center for a thoroughly productive time spent as a research visitor. This was made possible by the funding provided through the EU HPC-EUROPA2 program. I would also like to express my thanks to the School of Engineering for the computational facilities provided.

Chapter 1

Introduction

1.1 General Background and Importance of Topic

Cardiovascular disease (CVD) is the principle cause of death in the United States, Europe and regions of Asia [3]. Indeed, in the United States, CVD claims as many lives as cancer, accidents, diabetes mellitus and chronic lower respiratory disease together, which in numerical terms is 2400 Americans each day [4]. Within this thesis, two locations within the human cardiovascular system are examined, the carotid artery and the aorta. Numerical modelling of the blood flow in the carotid artery bifurcation is of interest with regard to the genesis and diagnosis of atherosclerotic plaque. Atherosclerosis is a disease characterised by increases in the arterial wall thickness due to an accumulation of lipids and fibrous elements [3]. Within the past century, the view on the pathophysiology of atherosclerosis has altered drastically. Inflammation is now regarded as having a role in atherosclerosis [3,5–7]. Due to the disease, the arterial wall will experience cellular and molecular responses [8]. The work of Ridker *et al* [9] measured plasma C-reactive protein (which is a marker for systemic inflammation) using 1086 subjects from the Physicians' Health Study. They concluded that higher concentrations of the protein were found in those that suffered a myocardial infarction or ischemic stroke.

It is apparent from clinical observations that atherosclerotic disease typically occurs at locations of complex haemodynamics such as arterial bifurcations, or regions of high curvature. An example of atherosclerotic plaque in a carotid endarterectomy specimen is given in Figure 1.1 [10] at the bifurcation. The two carotid arteries supply the head and neck with oxygenated blood, and severe narrowing (stenosis) of these arteries may lead to a stroke. In the UK, potentially 10,000 people are waiting in any given year

Figure 1.1: Atherosclerotic plaque within the carotid artery

for an operation to remove this narrowing [11]. During this waiting period, around 20% will suffer a stroke. When the extent of the stenosis is unclear, the patient is referred for a second scan and the wait for the operation is significantly increased. One of the aims of the research outlined in this thesis is to determine the suitability of a classification system that reduces or avoids the need for a second scan for a majority of patients, thus saving lives. The classification system would be based on previously analysed patient-specific arterial geometries.

As opposed to plaque formation leading to a stenosis of the artery, the aorta is of interest with regards to aneurysm formation and rupture. An aneurysm or bulge is a localised weakening and dilation of the vessel wall. Aortic aneurysms cause about 2% of deaths in men in England and Wales ($\approx$ 6,000 per year) due to the rupture of the aneurysm [12]. This number is currently on the increase [13].

In the study of cardiovascular disease, there have been a number of approaches employed. Clinical studies such as the Physicians' Health Study have been undertaken to provide epidemiological information as to disease progression. Atherosclerosis has since been linked to many risk factors such as smoking, diabetes and gender [14]. As well as human studies, animal studies have also been undertaken (both *in vivo* and *in vitro* in order to enhance understanding of disease mechanics [15, 16]. The computational modelling of the cardiovascular network is a vibrant field utilising a number of approaches, from simulation of the cardiac network [2], arterial structure analysis [17] to modelling of the blood flow. It is the approach of blood flow simulation that this thesis employs.

There are three objectives within this thesis, firstly the development of a fast and robust parallel solver capable of providing a timely solution is sought. This solver is analysed

to examine performance and accuracy through comparison with established methods and benchmark data. Secondly, through the use of sensitivity studies, the appropriate meshes are determined for resolved wall shear stress calculations. The third and final objective of the work involves applying the solver in the study of high resolution patient-specific meshes of both healthy and diseased arteries with the eventual aim of producing a clinical tool to refine patient diagnosis.

1.2 Current Research

Low or oscillatory shear stresses are associated with atherogenesis [18–25]. High oscillation in shear stress or disturbed flow conditions have been shown to induce inflammatory pro-atherogenesis effects such as monocyte adhesion [26–28]. Work by Cheng *et al* [29] investigated the influence of both low and oscillatory shear stress on atherosclerotic plaque formation within mouse carotid arteries. They concluded that while both low and oscillating shear stresses induce atherosclerotic lesions to develop (as opposed to high shear stress) the composition of the plaque was dependent on whether low shear stress was encountered individually or in combination with oscillatory shear. Under low shear stress conditions, the lesions were larger, contained less smooth muscle cells and collagen but more lipids than the low and oscillatory shear combination. Differences in composition ranged from 25% to 100% difference in these components. From the obtained results they concluded that low shear stress lesions were larger and more prone to a vulnerable plaque phenotype whereas high oscillatory shear contributed to the development of stable lesions. Vulnerable plaque is prone to inducing sudden onset of life threatening conditions such as stroke or myocardial infarction.

On the other hand, high shear stress has been shown to induce mechanical and/or chemical mechanisms that work in concert to provide athero-protective effects [30, 31]. Traub *et al* [32] determined that steady laminar shear promotes the release of secreted factors that inhibit coagulation and smooth muscle cell production while also suppressing leukocyte adhesion and transmission. Turbulent or oscillatory shear stresses increase endothelial cell turnover while sustained laminar shear stresses are required for optimum repair of the endothelial cells. In [33] narrow intimal wounds in rabbit carotids were incised and monitored for 24 hours in both artificially reduced arterial flow and normal conditions. After the 24 hours closure had occurred in the steady flow case while the wound was still open in the low flow case. In addition, orientation of the endothelial cells, along with close contact was also different between the two cases.

The definition of low shear stress is dependent upon the work consulted. In [29] this is defined as less than 15 dyne/cm^2 and above this value athero-protective influences are induced. From [34] low shear stress is defined as less than 5 dyne/cm^2 and athero-protective when the shear stress exceeds 25 dyne/cm^2. The work of Sharefkin *et al* [35] demonstrated that a steady wall shear stress of 25 dyne/cm^2 decreased Endothelin-1, a smooth muscle cell mitogen, by between 60-70% within 24 hours. With smooth muscle cells proliferating at regions of atherosclerotic plaque formation this is an indicator of one of the athero-protective actions of high shear stress.

An increased carotid artery intima-media thickness (IMT) is an indicator of atherogenesis [36]. The work of Vermeersch *et al* [37] quantified the relationship between the IMT and derived haemodynamic parameters for the common carotid artery (CCA) and internal carotid artery (ICA). The mentioned work clearly demonstrates that calculation of the WSS and OSI on patient-specific carotid geometries is important. Pedersen *et al* [38] also examined the relationship between the IMT and derived haemodynamic wall parameters in the case of the human abdominal aorta, finding good agreement with that of Vermeersch *et al* [37] for the parameter relationships.

In order to understand carotid artery haemodynamics, many patient-specific geometries need to be studied. Among other steps, such as using invasive X-ray contrast angiography or non-invasive magnetic resonance imaging (MRI) to track progression of early atherosclerosis, computational studies could play a major role in obtaining an understanding. The following paragraph provides a brief literature survey on flow through carotid bifurcations.

A limited number of studies are available on flow through carotid bifurcations. Glor *et al* [19] examined wall shear stress (WSS), the oscillating shear index (OSI), and the wall shear stress angle deviation (WSSAD) along with time-averaged spatial (WSSG) and temporal (WSSTG) gradients on eight bifurcations to determine reproducibility between patient scans within a prescribed time period. The derived wall parameters are outlined in Section 2.10. Two scans of the carotid artery, taken between two and four weeks apart, were examined for each patient. The OSI and WSSAD results were reproduced accurately between the scans. However, reproducibility of time-averaged WSS, WSSG and WSSTG was low and the authors claim that this is due to the fact that these values dependent on mesh construction near the apex. Lee *et al* [39] examined the effect of geometry, utilising fifty carotid bifurcations and a generalised flow profile, on WSS and OSI distribution and determined that certain geometrical features were robust indicators of exposure to disturbed flow. The work of Kaazempur-Mofrad *et al* [21] examined time-averaged WSS, OSI and maximum WSSTG in four individuals with varying degrees

of carotid stenosis. WSS, OSI and maximum WSSTG were correlated against four variables, namely number of smooth muscle cells, macrophages, interstitial collagen and lipids. It is apparent from this study that, high values of WSS are indicative of large number of smooth muscle cells and collagen, and low values of these variables were indicative of low WSS, i.e., a positive correlation between these variables and WSS. It was also demonstrated by Kaazempur-Mofrad *et al* [21] that high WSS indicates low quantities of macrophages/lipids and vice versa. Hyun *et al* [40] examined several design options for surgical reconstruction of diseased carotid bifurcations using OSI and wall shear stress angle gradient (WSSAG) to deduce the merits of each design option. Younis *et al* [41] examined the distribution of time-averaged WSS, OSI and maximum WSSTG on the carotid bifurcations of three healthy patients using the rigid wall assumption. The work also examined the influence of moving vessel walls using fluid-structure interaction modelling for one of the individuals. Comparison between the FSI results and the rigid wall assumption revealed low WSS distribution was similar but high WSS at the apex varied modestly (up to 25%). OSI revealed a greater influence on the rigid wall assumption with more wide-spread variations. The impact of the rigid wall assumption in diseased arteries is believed to be minimal [21]. Due to relatively smaller size of the carotid arteries, the rigid wall assumption is reasonable for assessing the distribution of WSS and related quantities.

In blood flow applications, using appropriate domain discretisation is important in accurately predicting the flow quantities. The meshes used in the literature for carotid bifurcation flow problems varied dramatically between studies. Glor *et al* [19] conducted a mesh sensitivity analysis on four meshes before employing a structured multiblock mesh with 41,600 trilinear hexahedral elements. It is unclear whether boundary refinement is implemented in this study, although previous work by this group recognised its importance [42]. Based upon an undocumented grid sensitivity analysis Younis *et al* [41] employed unstructured meshes with the number of elements ranging from 116,000 to 124,000 linear tetrahedrals to model the fluid domain for three patients. From their grid sensitivity analysis, the element edge size required was obtained to be 0.4mm, which is identical to the work of Kaazempur-Mofrad *et al* [21]. Grid independence was determined using a constant flow rate at the CCA inlet in the work of Nguyen *et al* [25], giving a mesh of 331,000 tetrahedral cells. Only one of these studies may have employed boundary layer meshes.

Examining the literature shows that none of the studies bring all the six wall parameters (WSS, OSI, WSSG, WSSTG, WSSAD, WSSAG) together to analyse the relationship between them and to make a thorough assessment of atherogenesis. It is also surprising that the number of degrees of freedom employed in these studies is relatively small.

It is known that capturing and converging WSS requires good boundary layer meshes. However, only one of the studies reported in the area of flow through carotid artery has used any kind of boundary mesh refinement.

The low and oscillating wall shear stress hypothesis does not explain the continued growth of plaque, once sufficiently accumulated to alter the preceding shear stress distribution, under elevated wall shear stress conditions [15]. The mentioned work suggests the hypothesis that plaque progression depends on both low and oscillating shear stress due to the fluid and structural stresses within the arterial wall. Therefore, in order to assess plaque progression into a local occlusion and rupture, fluid-structure interaction along with turbulence modeling [42–46] may be required.

The work of Holme *et al* [47, 48] investigated the influences of high wall shear stresses on platelet activation and platelet micro-particle formation in human blood. They determined that high shear stress (>315 dyne/cm^2) did activate platelets and micro-particle formation as well as enhancing platelet thrombus formation. Mailhac *et al* [49] also concluded that fibrin(ogen) and platelet deposition is maximal at the apex of a stenosis and coincident to high shear stress on a damaged arterial wall. In the work of Groen *et al* [50], a case study of a carotid artery is outlined where plaque rupture occurs at the location of high shear stress. This indicates that shear stress has a role throughout the developmental cycle of a stenosis from beginning to end, although the stenosis growth progression is not yet fully understood.

A related problem (of wall shear stress modelling) that is also investigated within this thesis is that of an aortic aneurysm. An aortic aneurysm is currently classified on two factors, it's location within the aorta and its size [51]. If the aneurysm is close to the aortic root it is classified as a thoracic aortic aneurysm (TAA). Abdominal aortic aneurysms (AAA) are normally located above the bifurcation of the aorta but below the renal arteries. As the aneurysm bulge increases in size it is more likely to rupture with fatal consequences, making size an important factor. In cases that require medical intervention, they can be classed as elective or emergency surgeries. Elective repair is undertaken when the patient is still asymptomatic and the aneurysm has not ruptured. Emergency surgery is undertaken after the aneurysm has ruptured. Elective surgical repair for a thoracic aortic aneurysm (TAA) is based upon the location and diameter of the aneurysm. This threshold diameter is commonly regarded as 5.5cm for an ascending TAA and 6.5cm for descending TAA [52, 53]. However, when patients have a tissue disorder such as Marfan's syndrome (defective connective protein fibrillin-1) or Ehlers-Danlos Syndrome (defective collagen synthesis, which in turn influences elasticity of tissues) smaller intervention diameters are usually applied [54]. Beyond

these intervention thresholds, the rupture risk increases significantly. The problem with using these criteria is that many aneurysms below these thresholds also rupture, and conversely aneurysms above this threshold do not. Therefore a more accurate assessment of parameters that govern intervention requirements would be valuable. The aneurysm properties are normally (in the UK) determined via magnetic resonance imaging (MRI) or computer tomography (CT) scans. Growth predictions for the aneurysm are based upon previous scans, clinical data and the clinician's experience.

The computational flow modelling studies of TAAs are also limited, and due to geometrical differences the studies of AAAs are not representative. One of the studies [55] reported a preliminary analysis of an idealised aortic arch structure. In the work they demonstrated the complexity of the fluid flow was heavily influenced by distortion of the pipe centreline, as well as the choice of steady or unsteady inlet conditions. Wall shear stresses were also investigated. Another study was published only recently [56], in which patient-specific MRI data of a TAA was compared with laminar and turbulent computational flow simulations. The turbulent flow model was found to be in closer agreement with the MRI data than the laminar model. A large recirculation zone was predicted within the aneurysm, leading to low time-averaged wall shear stress along the anterior wall of the aneurysm. This region also experienced high oscillatory shear, which together with the low shear stress may be linked to enlargement of the aneurysm. High shear stresses along with high turbulent intensity values were predicted on the posterior wall of the TAA distal to the aneurysm neck. This may potentially be linked to plaque rupture. It is clear that further investigation is necessary on the development and rupture risk of TAAs.

With the medical side of the research outlined, a method for producing a timely solution is now examined. The locally conservative Galerkin (LCG) method is employed within this work with further future developments in mind. Local conservation is regarded as a highly valued property of both finite volume methods and discontinuous Galerkin finite element methods (DGM). While the conservation of the Galerkin finite element method has been investigated by many [57–62] and has been shown to be implicitly locally conservative [61] it has only recently been implemented in its explicit form [63–66]. Explicit use of the element-wise conservation properties provides the advantage of control over individual elements and their boundaries. Control over individual elements, for example, allows local problems to be solved and therefore it can be a useful technique for multiscale or multi-resolution mechanics calculations which are very important for the development of biofluid dynamics (example: thrombus formation). The LCG method employed here is both locally and globally conservative and maintains many of the advantages discontinuous Galerkin (DG) methods [67] offer such as local hp-refinement

and weak enforceability of the Dirichlet boundary conditions, but at a lower cost. This is due to DG methods solving for additional flux variables and their increased memory requirements caused by storing multiple nodal solutions at each time step. In LCG, multiple solutions at a node are averaged to produce a continuous solution for every time step, reducing the memory requirements. Only a small post-processing calculation is used to determine the interface fluxes in LCG. In order to obtain a post processed flux it is necessary that an iterative technique is employed, such as a time-stepping scheme. The corrected LCG scheme will give a solution equal to or in some cases better solution than standard Galerkin method due to unconditional local and global conservation properties.

The Characteristic-Based-Split (CBS) scheme [68, 69] uses the characteristic Galerkin method, for convection-diffusion problems, for the investigation of the Navier-Stokes equations and fluid structure interactions. The CBS algorithm can be applied to solve almost all physical problems involving fluids. The CBS scheme, although originally introduced in explicit form, it has since been adapted to be semi-implicit incompressible and compressible flow [70–73]. In [74] [75] Codina *et al* established that the stabilisation mechanism of the CBS scheme is similar to the one employed by the Galerkin Least Squares (GLS) method [76] , providing the GLS stabilisation parameter is identified with the CBS time step. The artificial compressibility technique has been incorporated into the CBS family since 2003 [77–80]. For a recent review of the abilities of the CBS scheme, the reader is referred to the work of Nithiarasu *et al.* [81].

While in general the blood flow within arteries such as the carotid is modelled as laminar, at regions of severe stenosis flow may be turbulent [24]. Turbulent flow is also expected within the aorta [56]. The field of modelling turbulence is large, although may be generalised into three distinct types. Both direct numerical simulation (DNS) and large eddy simulation (LES) are expensive due to excessive computational cost. In this thesis, a one equation Reynolds averaged Navier-Stokes (RANS) model is employed. RANS models work by determining time-averaged velocities rather than the fluctuating instantaneous velocities. The Spalart-Allmaras (SA) one equation turbulence model was developed for aerodynamic flows [82] and showed good agreement with experimental data [83]. It has since been applied to patient-specific modelling [84]. The SA model has also been implemented within a hybrid LES/RANS technique called detached eddy simulation (DES) [85].

1.3 Thesis Outline

A brief summary of the thesis structure is presented in this section. Chapter two introduces the Navier-Stokes equations before outlining the steps necessary for construction of the artificial compressibility form of the characteristic based split scheme. The Spalart-Allmaras turbulence model is also detailed. The initial and boundary conditions employed within the thesis are also outlined in this chapter. In Chapter three, the structure of the computational program and it's parallel implementation is outlined. Speed testing is performed to determine the suitability of the method. The fourth chapter applies the computational program to a series of test cases prior to its application in chapter six to patient-specific modeling. The meshing techniques used and the input file generation are briefly outlined in Chapter five. Chapter six is concerned with preliminary sensitivity testing. The seventh chapter investigates the flow conditions within three high resolution patient-specific meshes and the resultant induced wall shear stress along with associated haemodynamic wall parameters. Chapter eight investigates the influence of flow within a stenosed bifurcation on the derived haemodynamic wall parameters. In Chapter nine, the flow within a patient-specific aorta with a folded neck is examined and the neck's influence on the wall shear stress is discussed. After which, the conclusions, appendices and bibliography are presented.

Chapter 2

Governing Equations and Solution Procedure

2.1 Introduction

This chapter can be regarded as having three distinct components. The first part provides an introduction to the governing equations utilised within this thesis, along with a derivation of their non-dimensional form. The second section begins with the introduction to the stabilisation methodology behind the proposed solution procedure, before outlining the finite element procedure itself. The final part of this chapter examines the boundary conditions that can be applied to the numerical problems and the post processing calculations that can be undertaken when modelling blood flow.

2.2 The Navier-Stokes Equations

The unsteady Navier-Stokes equations can be written in conservation form, ignoring body forces, as

Conservation of mass equation

$$\frac{\partial \rho}{\partial t} + \frac{\partial U_i}{\partial x_i} = 0 \tag{2.1}$$

Conservation of momentum equation

$$\frac{\partial U_i}{\partial t} + \frac{\partial}{\partial x_j}(u_j U_i) = -\frac{\partial p}{\partial x_i} + \frac{\partial \tau_{ij}}{\partial x_j} \tag{2.2}$$

where i represents Einstein notation, $U_i = \rho u_i$, u_i is the velocity, ρ is the density and p is the pressure. The deviatoric stress components τ_{ij} are related to velocity by

$$\tau_{ij} = \mu \left(\frac{\partial u_i}{\partial x_j} + \frac{\partial u_j}{\partial u_i} - \frac{2}{3}\frac{\partial u_k}{\partial x_k}\delta_{ij} \right) \tag{2.3}$$

where μ is the dynamic viscosity and δ_{ij} is the Kronecker delta. The transient density term in Eq.(2.1), for incompressible flows, can be replaced by

$$\frac{\partial \rho}{\partial t} = \frac{1}{c^2}\frac{\partial p}{\partial t} \approx \frac{1}{\beta^2}\frac{\partial p}{\partial t} \tag{2.4}$$

where c is the speed of sound and β is the artificial wave speed. The problem is completed by specifying appropriate initial condition for u_i and p together with boundary conditions. Before the Navier-Stokes equations are utilised within the characteristic based split (CBS) scheme, the variables are non-dimensionalised using the procedure outlined in the following section.

2.2.1 Non-Dimensional Form

The use of non-dimensional equations allows the unknowns to be represented as a ratio to a set of reference values. The non-dimensional variant of the unknown is denoted by an asterisk. An example relationship is denoted by

$$u_i^* = \frac{u_i}{u_\infty} \tag{2.5}$$

where u_∞ denotes the free stream value of velocity. The following equations relate the remaining non-dimensional variants to their respective variable

$$x_i^* = \frac{x_i}{L}; \quad \rho^* = \frac{\rho}{\rho_\infty}; \quad p^* = \frac{p}{u_\infty^2 \rho_\infty}; \quad t^* = \frac{t u_\infty}{L}; \quad \beta^* = \frac{\beta}{u_\infty}; \quad \mu^* = \frac{\mu}{\mu_\infty}; \tag{2.6}$$

where L is the reference length, ρ_∞ the reference free stream density and μ_∞ the reference free stream dynamic viscosity. From these relationships it is possible to construct the non-dimensional form of the artificially compressible Navier-Stokes equations as

Conservation of mass equation

$$\frac{1}{\beta^{*2}}\frac{\partial p^*}{\partial t^*} + \frac{\partial U_i^*}{\partial x_i^*} = 0 \tag{2.7}$$

Conservation of momentum equation

$$\frac{\partial U_i^*}{\partial t^*} + \frac{\partial}{\partial x_j^*}(u_j^* U_i^*) = -\frac{\partial p^*}{\partial x_i^*} + \frac{1}{Re}\frac{\partial \tau_{ij}^*}{\partial x_j^*} \tag{2.8}$$

where $U_i^* = \rho^* u_i^*$ and Re is the Reynolds number which is defined as

$$Re = \frac{\rho_\infty u_\infty L}{\mu_\infty} \tag{2.9}$$

and the deviatoric stress components by

$$\tau_{ij}^* = \mu^* \left(\frac{\partial u_i^*}{\partial x_j^*} + \frac{\partial u_j^*}{\partial u_i^*} - \frac{2}{3}\frac{\partial u_k^*}{\partial x_k^*}\delta_{ij} \right) \tag{2.10}$$

The superscript asterisk * denotes a non-dimensional quantity although in the remainder of this thesis, while the non-dimensional form is employed, the asterisks have been dropped.

2.3 Reynolds Averaged Navier-Stokes Equations

For problems that involve turbulence, the Reynolds averaged Navier-Stokes (RANS) equations are employed. These can be derived from the Navier-Stokes equations using Reynolds decomposition. This decomposition involves representing an instantaneous variable (for a fixed location) as a function of time, with two components as shown in Figure 2.1. Each instantaneous value of the variable r may be represented by the

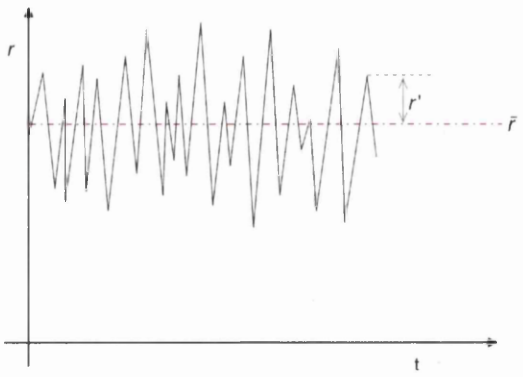

Figure 2.1: Reynolds decomposition of the variable r

time-averaged mean value $\bar{r}$ and the random component r' as expressed in Equation 2.11.

$$r = \bar{r} + r' \tag{2.11}$$

The time-averaged value of a velocity variable can be expressed as

$$\bar{u_i} = \frac{1}{T}\int_0^T u_i dt \tag{2.12}$$

where T is a time interval. Its derivative can be given as

$$\overline{\frac{\partial u_i}{\partial x_j}} = \frac{\partial}{\partial x_j}\left(\frac{1}{T}\int_0^T u_i dt\right) = \frac{\partial \bar{u}_i}{\partial x_j} \tag{2.13}$$

however the derivative of the random fluctuation component is

$$\overline{\frac{\partial u'_i}{\partial x_j}} = \frac{\partial}{\partial x_j}\left(\frac{1}{T}\int_0^T u'_i dt\right) = \frac{\partial \bar{u}'_i}{\partial x_j} = 0 \tag{2.14}$$

Using these relationships and noting that the average of the fluctuating component r' is zero it is possible to rewrite the Navier-Stokes equations in their Reynolds averaged Navier-Stokes form. Beginning from

$$\frac{1}{\beta^2}\overline{\frac{\partial p}{\partial t}} + \overline{\frac{\partial U_i}{\partial x_i}} = 0 \tag{2.15}$$

and introducing the relationship from Equation 2.11 gives

$$\frac{1}{\beta^2}\frac{\partial\left(\overline{p}+p'\right)}{\partial t}+\frac{\partial\left(\overline{U_i}+U_i'\right)}{\partial x_i}=0 \tag{2.16}$$

which is simplified to the final form of the mean continuity equation

$$\frac{1}{\beta^2}\frac{\partial\overline{p}}{\partial t}+\frac{\partial\overline{U}_i}{\partial x_i}=0 \tag{2.17}$$

where $\overline{U}_i=\rho\overline{u}_i$. The mean momentum equation is expressed as

$$\frac{\partial}{\partial t}\left(\overline{\overline{U}_i+U_i'}\right)+\frac{\partial}{\partial x_j}\left[\overline{(\overline{u}_j+u_j')(\overline{U}_i+U_i')}\right]=-\frac{\partial}{\partial x_i}\left(\overline{\overline{p}+p'}\right)+\frac{1}{\mathrm{Re}}\frac{\partial\overline{\tau_{ij}}}{\partial x_j} \tag{2.18}$$

where

$$\overline{\tau}_{ij}=\left(\frac{\partial\overline{u}_i}{\partial x_j}+\frac{\partial\overline{u}_j}{\partial x_i}-\frac{2}{3}\delta_{ij}\frac{\partial\overline{u}_k}{\partial x_k}\right) \tag{2.19}$$

Equation 2.18 simplifies to the final form of the mean momentum equation

$$\frac{\partial\overline{U}_i}{\partial t}+\frac{\partial\overline{u}_j\overline{U}_i}{\partial x_j}=-\frac{\partial\overline{p}}{\partial x_i}+\frac{1}{\mathrm{Re}}\frac{\partial\overline{\tau_{ij}}}{\partial x_j}-\frac{\partial}{\partial x_j}\left(\overline{u_j'U_i'}\right) \tag{2.20}$$

where $\left(\overline{u_j'U_i'}\right)$ is the Reynolds Stress. Further information is provided in Section 2.6.5.

2.4 Characteristic Galerkin Method

Before the Characteristic Based Split algorithm used in this work is outlined in detail, a brief background on characteristic based methods is presented in this section. Characteristic based methods are widely employed in the study of fluid dynamics and are based on the wave nature of the Navier-Stokes equations. In order to demonstrate the explicit characteristic-Galerkin method, a simple 1D transport equation is examined.

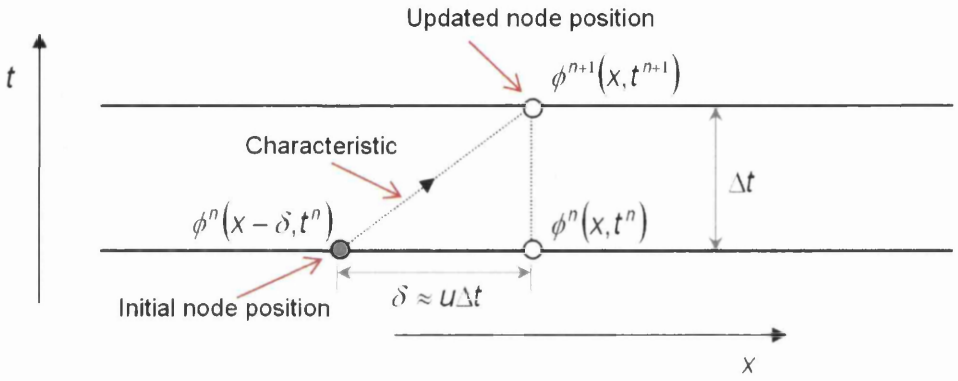

Figure 2.2: An explicit characteristic-Galerkin procedure for ϕ

$$\frac{\partial \phi}{\partial t} = u\frac{\partial \phi}{\partial x} - \frac{\partial}{\partial x}\left(k\frac{\partial \phi}{\partial x}\right) = 0 \tag{2.21}$$

where ϕ is the unknown variable, u the velocity and k is the diffusion coefficient. If the fluid is moving with a velocity u along the characteristic then this equation can be rewritten along the characteristic (from Figure 2.2) as

$$\frac{\partial}{\partial t}\phi\left(\hat{x}\left(t\right),t\right)\Big|_{t=t^{n+1}} = \left[\frac{\partial}{\partial t}\phi\left(\hat{x}\left(t\right),t\right) + \frac{\partial}{\partial x}\phi\left(\hat{x}\left(t\right),t\right)\frac{\partial x}{\partial t}\right]\Big|_{\hat{x}=x-\delta} \tag{2.22}$$

where $\partial x/\partial t = u$. Thus in the moving coordinate system $\hat{x}$, the convective term vanishes. This has the benefit of reducing the equation to a purely diffusive problem which removes any spatial oscillations due to convective instability.

Equation 2.22 can be discretised in time as

$$\frac{\phi^{n+1}\big|_x - \phi^{n}\big|_{x-\delta}}{\Delta t} = \theta\frac{\partial}{\partial x}\left(k\frac{\partial \phi}{\partial x}\right)^{n+1} + (1-\theta)\frac{\partial}{\partial x}\left(k\frac{\partial \phi}{\partial x}\right)^{n}\Big|_{x-\delta} \tag{2.23}$$

where $\theta \in [0,1]$. θ is zero for explicit forms and one for the fully implicit form. The Crank-Nicholson scheme uses $\theta = 0.5$. Taking $\theta = 0.5$, the equation becomes

$$\frac{\phi^{n+1}\big|_x - \phi^{n}\big|_{x-\delta}}{\Delta t} = \frac{1}{2}\frac{\partial}{\partial x}\left(k\frac{\partial \phi}{\partial x}\right)^{n+1} + \frac{1}{2}\frac{\partial}{\partial x}\left(k\frac{\partial \phi}{\partial x}\right)^{n}\Big|_{x-\delta} \tag{2.24}$$

From Figure 2.2

$$\delta = \check{u}\Delta t \tag{2.25}$$

is the distance travelled by a reference particle in the x direction and $\check{u}$ represents the average value of u along the characteristic. This average velocity $\check{u}$ can be approximated by [68]

$$\check{u} = \frac{1}{2}\left(u^{n+1} + u^n|_{x-\delta}\right) \tag{2.26}$$

Using the backward Taylor expansion on the $|_{x-\delta}$ terms of Equations 2.24 and 2.26 and ignoring third and higher order terms gives

$$\phi^n|_{x-\delta} \approx \phi^n|_x - \delta \left.\frac{\partial \phi^n}{\partial x}\right|_x + \left.\frac{\delta^2}{2}\frac{\partial^2 \phi^n}{\partial x^2}\right|_x + \dots \tag{2.27}$$

$$\left.\frac{1}{2}\frac{\partial}{\partial x}\left(k\frac{\partial \phi}{\partial x}\right)^n\right|_{x-\delta} = \left.\frac{1}{2}\frac{\partial}{\partial x}\left(k\frac{\partial \phi}{\partial x}\right)^n\right|_x - \left.\frac{\delta}{2}\frac{\partial}{\partial x}\left[\frac{\partial}{\partial x}\left(k\frac{\partial \phi}{\partial x}\right)^n\right]\right|_x + \dots \tag{2.28}$$

$$u^n|_{x-\delta} \approx u^n|_x - \Delta t u^n \left.\frac{\partial u^n}{\partial x}\right|_x + \dots \tag{2.29}$$

Substituting Equations 2.25 to 2.29 into Equation 2.24 gives

$$\begin{aligned}\frac{\phi^{n+1} - \phi^n}{\Delta t} &= -u^{n+1/2}\frac{\partial \phi^n}{\partial x} + \frac{\partial}{\partial x}\left(k\frac{\partial \phi}{\partial x}\right)^{n+1/2} \\ &\quad + \frac{\Delta t}{2}u^{n+1/2}\frac{\partial}{\partial x}\left[u^{n+1/2}\frac{\partial \phi^n}{\partial x} - \frac{\partial}{\partial x}\left(k\frac{\partial \phi}{\partial x}\right)^n\right]\end{aligned} \tag{2.30}$$

where

$$u^{n+1/2} = \frac{1}{2}\left(u^{n+1} + u^n\right) \tag{2.31}$$

and

$$\frac{\partial}{\partial x}\left(k\frac{\partial \phi}{\partial x}\right)^{n+1/2} = \frac{1}{2}\frac{\partial}{\partial x}\left(k\frac{\partial \phi}{\partial x}\right)^{n+1} + \frac{1}{2}\frac{\partial}{\partial x}\left(k\frac{\partial \phi}{\partial x}\right)^n \tag{2.32}$$

In order to get the fully explicit version of the scheme the $n + 1/2$ terms may be approximated by their respective terms at time level n. In multiple dimensional form the equation becomes

$$\begin{aligned}\frac{\phi^{n+1} - \phi^n}{\Delta t} &= -u_i^n \frac{\partial \phi^n}{\partial x_i} + \frac{\partial}{\partial x_j}\left(\frac{\partial k_j \phi}{\partial x_j}\right)^n \\ &\quad + \frac{\Delta t}{2} u_k \frac{\partial}{\partial x_k}\left[u_i^n \frac{\partial \phi^n}{\partial x_i} - \frac{\partial}{\partial x_j}\left(\frac{\partial k_j \phi}{\partial x_j}\right)^n\right] \qquad i,j,k = 1,..,d_n\end{aligned} \tag{2.33}$$

where d_n is the number of dimensions to the problem and i, j, k denote Einstein notation.

The characteristic-Galerkin scheme has the advantage of introducing a term (the third RHS term in Equation 2.33) which acts as additional diffusion, and thus stabilises the solution while also increasing the order of accuracy in time.

2.5 The locally conservative Galerkin method

This section provides background on the spatial discretisation to be employed within the characteristic based split scheme. This method was first developed by Nithiarasu in 2004 [63] and applied to pure diffusion problems. Since then it has been utilised first in the study of convection-diffusion type problems [65] before application to the Navier-Stokes equations [66, 86, 87].

In the locally conservative Galerkin method, the variable and its fluxes are explicitly conserved over each individual element. In order to demonstrate the method, we return to the simple transport equation. Starting from the semi-discrete characteristic-Galerkin stabilised form given in Equation 2.33, and ignoring third order and higher terms, the weak form is defined as

$$\begin{aligned}\int_\Omega v \frac{\phi^{n+1} - \phi^n}{\Delta t} d\Omega &= \int_\Omega v \left[-\frac{\partial}{\partial x_i}(\phi u_i)^n + \frac{\partial}{\partial x_j}\left(\frac{\partial k_j \phi}{\partial x_j}\right)^n\right] d\Omega \\ &\quad + \frac{\Delta t}{2} \int_\Omega v \left[u_k \frac{\partial}{\partial x_k}\frac{\partial}{\partial x_i}(\phi u_i)^n\right] d\Omega\end{aligned} \tag{2.34}$$

where υ is an arbitrary weighting function. The variation of ϕ is approximated by the standard finite element spatial discretisation as $\phi \approx \tilde{\phi} = \mathbf{N}\boldsymbol{\phi}$ where $\mathbf{N}$ is the shape function. The shape function $\mathbf{N}$ also replaces the arbitrary weighting function. $\mathbf{N}$ is defined as $\mathbf{N} = [N_1, N_2, ..., N_n]$ and $\boldsymbol{\phi} = [\phi_1, \phi_2, ..., \phi_n]$. In order to explicitly conserve the flux and the variables all terms are integrated by parts and using Galerkin weighting gives

$$\begin{aligned}\int_\Omega \mathbf{N}^\mathbf{T}\mathbf{N}\left(\frac{\boldsymbol{\phi}^{n+1}-\boldsymbol{\phi}^n}{\Delta t}\right)d\Omega \;=\; &+\int_\Omega \frac{\partial \mathbf{N}^\mathbf{T}}{\partial \mathbf{x}_i}\mathbf{N}\left\{\phi u_i\right\}^n d\Omega \\ &-\int_\Gamma \mathbf{N}^\mathbf{T} n_i \mathbf{N}\left\{\widehat{\phi u_i}\right\}^n d\Gamma \\ &-\int_\Omega \frac{\partial \mathbf{N}^\mathbf{T}}{\partial \mathbf{x}_j}\frac{\partial \mathbf{N}}{\partial \mathbf{x}_j}\left\{\boldsymbol{k_j}\boldsymbol{\phi}\right\}^n d\Omega \\ &+\int_\Gamma \mathbf{N}^\mathbf{T} n_j \mathbf{N}\left\{\frac{\widehat{\partial k_j \phi}}{\partial \mathbf{x}_j}\right\}^n d\Gamma \\ &-\frac{\Delta t}{2}\int_\Omega \frac{\partial \mathbf{N}^\mathbf{T}}{\partial \mathbf{x}_k}u_k\frac{\partial \mathbf{N}}{\partial \mathbf{x}_i}\left\{\phi u_i\right\}^n d\Omega \\ &+\frac{\Delta t}{2}\int_\Gamma \mathbf{N}^\mathbf{T} n_k u_k \mathbf{N}\left\{\frac{\widehat{\partial u_i \phi}}{\partial \mathbf{x}_i}\right\}^n d\Gamma\end{aligned} \tag{2.35}$$

where Γ denotes the boundary domain of Ω. The face flux terms have been approximated by a numerical flux, denoted by $\{\widehat{.}\}$. Assuming the numerical flux can be determined, then this equation is valid for any domain divided into non-overlapping continuous elements. In the LCG method, this equation is used between individual elements. This process is equivalent to treating the global domain as a group of elemental sub-domains, each with its own time-dependent Neumann boundary conditions prescribed at each timestep. The application of the equation at the elemental level allows for an element-by-element solution process, removing the necessity of assembling a global matrix prior to establishing the solution.

The numerical face flux may be determined using only a small post-processing calculation, as opposed to DG methods which utilise extra equations to determine the interface flux, with flux continuity often determined using Lagrangian multipliers [67]. With the introduction of Neumann type boundary flux conditions, nodal values of the fluxes are required. Nodal values of convection fluxes can be calculated at the nodes, however both the diffusive fluxes and the flux due to the stabilisation term are constant

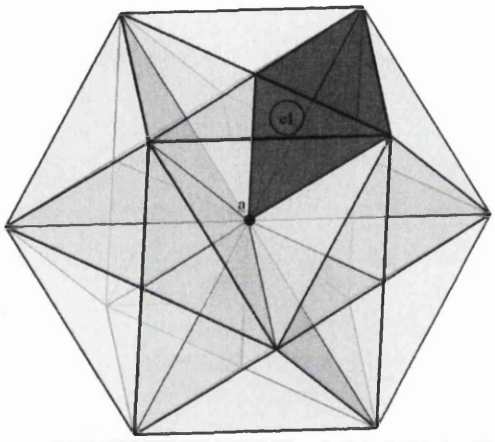

Figure 2.3: Flux crossing a common face between two tetrahedral elements.

over the element. Therefore, the nodal values of these fluxes are determined by averaging the values over the connected elements. Although averaging techniques such as volume (3D) or area (2D) weighting the gradients may be utilised, a simple averaging approach is used in order to reduce complexity. This averaging approach (Figure 2.3) for the diffusive flux component of node a is given as

$$\left(\frac{\partial \phi}{\partial x_i}\right)_a = \frac{1}{Ne} \sum_{e=1}^{Ne} \left(\frac{\partial \phi}{\partial x_i}\right)_e \tag{2.36}$$

where Ne denotes the number of contributing elemental values e. Once the nodal values are obtained, the following condition (Figure 2.4) is enforced

$$(Fn)_{e1} = (Fn)_{e2} \tag{2.37}$$

The numerical flux can be treated in a consistent form as outlined in Equation 2.36 or a lumped approach may be employed as used in [63]. Due to the solution of elemental discrete equations, multiple solutions at a node are obtained. Thus, in order to achieve a unique solution, a simple arithmetic mean of the nodal values obtained from the different elements is undertaken. This continuous solution can then be used for determining the numerical flux during the following time step.

It can be clearly visualised that the LCG method and the global Galerkin (GG) method will provide the same steady state solution since any difference due to the mass matrix will vanish at steady state. In the case where the individual elements are of identical

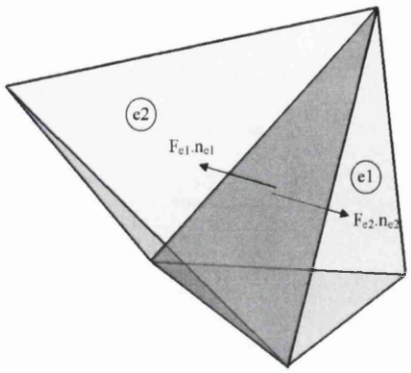

Figure 2.4: Element contributions to global node a

size, the LCG method will also provide an identical solution in a transient case. In a transient problem where an unstructured mesh is employed, a correction factor may be required in order to produce an identical solution for internal nodes. At an internal node, in principle the equal and opposite fluxes introduced at the interfaces of the elements will cancel each other when the solution is averaged over a node. The only difference between the GG and the LCG equations described here lies in the use of the mass matrix employed. In order for the LCG method to produce the same results to that of the continuous Galerkin method, a correction factor, based upon this difference, must be implemented [66, 86]. In the lumped mass matrix case, the correction factor ψ, is applied to the mass matrix term on the RHS and is of the form

$$\psi = \left(Ne \left[\mathbf{M} \right]^{-1} - \left[\mathbf{M_e} \right]^{-1} \right) \tag{2.38}$$

where Ne is the number of connected elements and $[\mathbf{M}]$ and $[\mathbf{M_e}]$ are the nodal components of the global mass matrix and LCG element mass matrix respectively. The correction factors can be determined at a preprocessing stage for cases involving the Eulerian frame of reference, noting that ψ is identical for all the three steps if the explicit CBS scheme is employed. The above correction is especially important when transient problems are solved, in order to ensure that the method converges to the identical solution provided by the global Galerkin method. Along external nodes, the LCG method will produce a globally conservative solution whereas the global Galerkin method is not globally conservative unless Neumann boundary conditions are enforced. Thus, at an exterior node the solutions are not identical.

With the locally conservative Galerkin (LCG) spatial discretisation outlined in the case of a simple transport equation, the characteristic based split algorithm can now be

presented.

2.6 The Characteristic Based Split Scheme

The characteristic based split (CBS) scheme has its origins in the split originally introduced by Chorin [88, 89] for the study of incompressible flow using the finite difference method. The work of Zienkiewicz and Codina [68,69] extended the split using the characteristic-Galerkin technique in order to model incompressible and compressible fluid dynamics. The scheme has been since employed in solving a wide range of problems, from aeronautical and solid mechanics to shallow water flows.

The CBS algorithm utilises a fractional step involving a split to circumvent the LBB (Ladyzhenskaya-Babuska-Brezzi) restriction. Thus avoiding restrictions on the shape functions N for the velocity and pressure components. For the explicit artificial compressibility form of the CBS scheme (CBS-AC), the three main steps can be described as:

1. Determine a preliminary solution for the auxiliary intermediate velocity field.
2. Solve for the pressure field using the intermediate velocity variables.
3. The final step involves determining a corrected version of the velocity field.

In the literature, there are two possible splits employed (Split A or Split B) [83] with Split A outlined, and used, above. The difference between the two splits is the treatment of the pressure term in the momentum equation. In Split A, the pressure terms (p^{n+1} and p^n)are removed from the momentum equation before determining the intermediate velocity field, whereas in Split B, only partial removal of pressure terms (p^{n+1} terms only) occurs.

2.6.1 Temporal Discretisation

The momentum equation given in Equation 2.8 contains both pressure and velocity components. Removal of the pressure term from this equation provides the basis for Step 1 of the CBS scheme. This removal means that the remaining equation is of a similar nature to that of the transport equation, making the characteristic-Galerkin

method readily applicable. The introduced split has the additional benefit of increasing the pressure stability of the scheme. This stems from the introduction of the second-order pressure term which reduces pressure oscillations.

For convenience, the momentum equation is repeated below.

$$\frac{\partial U_i}{\partial t} + \frac{\partial}{\partial x_j}(u_j U_i) = -\frac{\partial p}{\partial x_i} + \frac{1}{Re}\frac{\partial \tau_{ij}}{\partial x_j} \tag{2.39}$$

Time discretisation is undertaken using the forward time difference approximation and the characteristic-Galerkin procedure to give

$$\begin{aligned} \frac{U_i^{n+1} - U_i^n}{\Delta t} &= -\frac{\partial}{\partial x_j}(u_j U_i)^n - \frac{\partial p^{n+\theta_2}}{\partial x_i} + \frac{1}{Re}\frac{\partial \tau_{ij}^n}{\partial x_j} \\ &\quad - \frac{\Delta t}{2} u_k \frac{\partial}{\partial x_k}\left[-\frac{\partial}{\partial x_j}(u_j U_i)^n - \frac{\partial p^{n+\theta_2}}{\partial x_i} + \frac{1}{Re}\frac{\partial \tau_{ij}^n}{\partial x_j}\right] \end{aligned} \tag{2.40}$$

which can be rearranged as

$$\begin{aligned} \frac{U_i^{n+1} - U_i^n}{\Delta t} &= \left[-\frac{\partial}{\partial x_j}(u_j U_i)^n + \frac{1}{Re}\frac{\partial \tau_{ij}^n}{\partial x_j}\right] \\ &\quad - \frac{\Delta t}{2} u_k \frac{\partial}{\partial x_k}\left[-\frac{\partial}{\partial x_j}(u_j U_i)^n + \frac{1}{Re}\frac{\partial \tau_{ij}^n}{\partial x_j}\right] \\ &\quad - \frac{\partial p^{n+\theta_2}}{\partial x_i} + \frac{\Delta t}{2} u_k \frac{\partial}{\partial x_k}\left(\frac{\partial p^{n+\theta_2}}{\partial x_i}\right) \end{aligned} \tag{2.41}$$

Assuming the relationship

$$U_i^{n+1} = U_i^n + \Delta U_i^* + \Delta U_i^{**} \tag{2.42}$$

then the auxiliary variables ΔU_i^* and ΔU_i^{**} can be defined from Equation 2.42 as

$$\Delta U_i^* = \Delta t\left[-\frac{\partial}{\partial x_j}(u_j U_i)^n + \frac{1}{Re}\frac{\partial \tau_{ij}^n}{\partial x_j}\right] - \frac{\Delta t^2}{2} u_k \frac{\partial}{\partial x_k}\left[-\frac{\partial}{\partial x_j}(u_j U_i)^n + \frac{1}{Re}\frac{\partial \tau_{ij}^n}{\partial x_j}\right] \tag{2.43}$$

$$\Delta U_i^{**} = -\Delta t \frac{\partial p^{n+\theta_2}}{\partial x_i} + \frac{\Delta t^2}{2} u_k \frac{\partial}{\partial x_k}\left(\frac{\partial p^{n+\theta_2}}{\partial x_i}\right) \tag{2.44}$$

where Equation 2.43 forms the basis for Step 1 of the CBS scheme and Equation 2.44 the basis for Step 3. In the above equation

$$\frac{\partial p^{n+\theta_2}}{\partial x_i} = (1-\theta_2)\frac{\partial p^n}{\partial x_i} + \theta_2 \frac{\partial p^{n+1}}{\partial x_i} \tag{2.45}$$

but in the fully explicit CBS scheme, $\theta_2 = 0$, thus the relationship simply becomes

$$\frac{\partial p^{n+\theta_2}}{\partial x_i} = \frac{\partial p^n}{\partial x_i} \tag{2.46}$$

Removing third order and higher terms, the equation for Step 1 can be rewritten in its final semi-discrete form as

$$U_i^* = U_i^n + \Delta t \left[-\frac{\partial}{\partial x_j}(u_j U_i)^n + \frac{1}{Re}\frac{\partial \tau_{ij}^n}{\partial x_j}\right] + \frac{\Delta t^2}{2} u_k \frac{\partial}{\partial x_k}\frac{\partial}{\partial x_j}(u_j U_i)^n \tag{2.47}$$

since $\Delta U_i^* = U_i^* - U_i^n$. Employing the relationships from Equations 2.42 and 2.46 in Equation 2.44, Step 3 becomes

$$U_i^{n+1} = U_i^* - \Delta t \frac{\partial p^n}{\partial x_i} + \frac{\Delta t^2}{2} u_k \frac{\partial}{\partial x_k}\left(\frac{\partial p^n}{\partial x_i}\right) \tag{2.48}$$

The pressure can be determined from the continuity equation, which is repeated below

$$\frac{1}{\beta^2}\frac{\partial p}{\partial t} + \frac{\partial U_i^{n+\theta_1}}{\partial x_i} = 0 \tag{2.49}$$

where

$$U_i^{n+\theta_1} = (1-\theta_1)\, U_i^n + \theta_1 U_i^{n+1} = \theta_1 \Delta U_i - U_i^n \tag{2.50}$$

where $\theta_1 > 0$ is essential for pressure stability. Here $\theta_1 = 1$ is used. Replacing ΔU by the known variable ΔU_i^* and substituting into Equation 2.49 the semi-discrete form of Step 2 can be given as

$$p^{n+1} = p^n - \Delta t \left(\beta^2\right)^n \left[\frac{\partial U_i^n}{\partial x_i} + \frac{\partial \Delta U_i^*}{\partial x_i} - \Delta t \frac{\partial}{\partial x_i}\left(\frac{\partial p^n}{\partial x_i}\right)\right] \tag{2.51}$$

Details concerning the artificial compressibility parameter β will be outlined later on in this chapter in section 2.6.4.

2.6.2 Spatial Discretisation

Introducing the weak form of the three semi-discrete equations (2.47, 2.51 and 2.48) as

$$\begin{aligned}\int_\Omega \upsilon U_i^* d\Omega \;=\; & \int_\Omega \upsilon U_i^n d\Omega + \int_\Omega \upsilon \Delta t \left[-\frac{\partial}{\partial x_j}(u_j U_i)^n + \frac{1}{Re}\frac{\partial \tau_{ij}^n}{\partial x_j}\right] d\Omega \\ & + \int_\Omega \upsilon \frac{\Delta t^2}{2} u_k \frac{\partial}{\partial x_k}\frac{\partial}{\partial x_j}(u_j U_i)^n d\Omega\end{aligned} \tag{2.52}$$

$$\int_\Omega \upsilon p^{n+1} d\Omega = \int_\Omega \upsilon p^n d\Omega - \int_\Omega \upsilon \Delta t \left(\beta^2\right)^n \left[\frac{\partial U_i^n}{\partial x_i} + \frac{\partial \Delta U_i^*}{\partial x_i} - \Delta t \frac{\partial}{\partial x_i}\left(\frac{\partial p^n}{\partial x_i}\right)\right] d\Omega \tag{2.53}$$

$$\int_\Omega \upsilon U_i^{n+1} d\Omega = \int_\Omega \upsilon U_i^* d\Omega - \int_\Omega \upsilon \Delta t \frac{\partial p^n}{\partial x_i} d\Omega + \int_\Omega \upsilon \frac{\Delta t^2}{2} u_k \frac{\partial}{\partial x_k}\left(\frac{\partial p^n}{\partial x_i}\right) d\Omega \tag{2.54}$$

where υ is an arbitary weighting function. After integrating by parts, Equation 2.52 becomes

$$\begin{aligned}\int_\Omega \upsilon U_i^* d\Omega &= \int_\Omega \upsilon U_i^n d\Omega \\ &- \Delta t \int_\Omega \frac{\partial \upsilon}{\partial x_j}\left[-(u_j U_i)^n + \frac{1}{Re}\tau_{ij}^n\right] d\Omega \\ &+ \Delta t \int_\Gamma \upsilon n_j \left[-(u_j U_i)^n + \frac{1}{Re}\tau_{ij}^n\right] d\Gamma \\ &- \frac{\Delta t^2}{2}\int_\Omega \frac{\partial \upsilon}{\partial x_k}\hat{u}_k \frac{\partial}{\partial x_j}(u_j U_i)^n d\Omega \\ &+ \frac{\Delta t^2}{2}\int_\Gamma \upsilon n_k \hat{u}_k \frac{\partial}{\partial x_j}(u_j U_i)^n d\Gamma\end{aligned} \tag{2.55}$$

Although discontinuous trial functions may be employed within the CBS-LCG scheme, in this work the variables are approximated by the standard finite element spatial discretisation as:

$$u_i \approx \tilde{u_i} = \mathbf{N}\mathbf{u_i} \quad \text{and} \quad p \approx \tilde{p} = \mathbf{N}\mathbf{p} \tag{2.56}$$

where $\mathbf{N}$ are the shape functions. Introducing the locally conservative Galerkin spatial discretisation and replacing the arbitrary weighting function υ with the Galerkin weighting $\mathbf{N}$, Equation 2.55 becomes

$$\begin{aligned}\int_\Omega \mathbf{N}^\mathbf{T}\mathbf{N}\{\mathbf{U}_i\}^* d\Omega &= \int_\Omega \mathbf{N}^\mathbf{T}\mathbf{N}\{\mathbf{U}_i\}^n d\Omega \\ &+ \Delta t \int_\Omega \frac{\partial \mathbf{N}^\mathbf{T}}{\partial \mathbf{x}_j}\mathbf{N}\{\mathbf{u}_j\mathbf{U}_i\}^n d\Omega \\ &- \Delta t \frac{1}{Re}\int_\Omega \frac{\partial \mathbf{N}^\mathbf{T}}{\partial \mathbf{x}_j}\left(\frac{\partial \mathbf{N}}{\partial \mathbf{x}_j}\{\mathbf{u}_i\}^n + \frac{\partial \mathbf{N}}{\partial \mathbf{x}_i}\{\mathbf{u}_j\}^n - \frac{2}{3}\delta_{ij}\frac{\partial \mathbf{N}}{\partial \mathbf{x}_k}\{\mathbf{u}_k\}^n\right) d\Omega \\ &- \Delta t \int_\Gamma \mathbf{N}^\mathbf{T} n_j \mathbf{N}\{\mathbf{u}_j\mathbf{U}_i\}^n d\Gamma \\ &+ \Delta t \frac{1}{Re}\int_\Gamma \mathbf{N}^\mathbf{T} n_j \mathbf{N}\{\hat{\boldsymbol{\tau}}_{ij}\}^n d\Gamma \\ &- \frac{\Delta t^2}{2}\int_\Omega \frac{\partial \mathbf{N}^\mathbf{T}}{\partial \mathbf{x}_k}\hat{u}_k \frac{\partial \mathbf{N}}{\partial \mathbf{x}_j}\{\mathbf{u}_j\mathbf{U}_i\}^n d\Omega \\ &+ \frac{\Delta t^2}{2}\int_\Gamma \mathbf{N}^\mathbf{T} n_k \hat{u}_k \mathbf{N}\left\{\frac{\partial \widehat{\mathbf{u}_j\mathbf{U}_i}}{\partial \mathbf{x}_j}\right\}^n d\Gamma\end{aligned} \tag{2.57}$$

where the face flux terms have been replaced by nodal values of the numerical fluxes as denoted by $\{\widehat{\cdot}\}$. In matrix form

$$\begin{aligned}\mathbf{M}_1\{\mathbf{U}_i\}^* &= \mathbf{M}_1\{\mathbf{U}_i\}^n \\ &\quad + \Delta t\left[\mathbf{C}_1\{\mathbf{u}_j\mathbf{U}_i\}^n - \mathbf{K}_1 - \{\mathbf{f}_1\} + \{\mathbf{f}_2\} + \mathbf{K}_1^{\mathbf{CG}}\{\mathbf{u}_j\mathbf{U}_i\}^n + \{\mathbf{f}_3\}\right]\end{aligned} \tag{2.58}$$

where the matrices are defined (for 3D) in Appendix A.

In Step 2, discretisation is undertaken in the same manner. Beginning from Equation 2.53 and after substitution of the Galerkin weighting and integration by parts the expression for Step 2 becomes

$$\begin{aligned}\int_\Omega \mathbf{N}^\mathbf{T}\mathbf{N}\{\mathbf{p}\}^{n+1}\,d\Omega &= \int_\Omega \mathbf{N}^\mathbf{T}\mathbf{N}\{\mathbf{p}\}^n\,d\Omega \\ &\quad + \Delta t\left(\beta^2\right)^n\int_\Omega \frac{\partial \mathbf{N}^\mathbf{T}}{\partial \mathbf{x}_i}\mathbf{N}\{\mathbf{U}_i^n + \Delta\mathbf{U}_i^*\}\,d\Omega \\ &\quad - \Delta t\left(\beta^2\right)^n\int_\Gamma \mathbf{N}^\mathbf{T}\mathbf{N}n_i\{\mathbf{U}_i^n + \Delta\mathbf{U}_i^*\}\,d\Gamma \\ &\quad - \Delta t^2\left(\beta^2\right)^n\int_\Omega \frac{\partial \mathbf{N}^\mathbf{T}}{\partial \mathbf{x}_i}\frac{\partial \mathbf{N}}{\partial \mathbf{x}_i}\{\mathbf{p}\}^n\,d\Omega \\ &\quad + \Delta t^2\left(\beta^2\right)^n\int_\Gamma \mathbf{N}^\mathbf{T}\mathbf{N}n_i\left\{\widehat{\frac{\partial \mathbf{p}}{\partial \mathbf{x}_i}}\right\}^n d\Gamma\end{aligned} \tag{2.59}$$

Or in matrix form:

$$\mathbf{M}_2\{\mathbf{p}\}^{n+1} = \mathbf{M}_2\{\mathbf{p}\}^n + \Delta t\left(\beta^2\right)^n\left[\mathbf{C}_2\{\mathbf{U}_i + \Delta\mathbf{U}_i^*\}^n - \{\mathbf{f}_4\} - \mathbf{K}_2\{\mathbf{p}\} + \{\mathbf{f}_5\}\right] \tag{2.60}$$

The discretised velocity correction Step 3 is determined from Equation 2.54, which is repeated for clarity.

$$\int_\Omega v U_i^{n+1} d\Omega = \int_\Omega v U_i^* d\Omega - \Delta t\int_\Omega v\frac{\partial p^n}{\partial x_i}d\Omega + \frac{\Delta t^2}{2}\int_\Omega v u_k\frac{\partial}{\partial x_k}\left(\frac{\partial p^n}{\partial x_i}\right)d\Omega \tag{2.61}$$

After integration by parts and substitution of the nodal approximations and Galerkin weighting, the expression becomes

$$\begin{aligned}\int_\Omega \mathbf{N}^\mathbf{T}\mathbf{N}\{\mathbf{U}_i\}^{n+1}\,d\Omega &= \int_\Omega \mathbf{N}^\mathbf{T}\mathbf{N}\{\mathbf{U}_i\}^*\,d\Omega \\ &+ \Delta t\int_\Omega \frac{\partial \mathbf{N}^\mathbf{T}}{\partial \mathbf{x}_i}\{\mathbf{p}\}^n\,d\Omega \\ &- \Delta t\int_\Gamma \mathbf{N}^\mathbf{T}\mathbf{N}n_i\{\mathbf{p}\}^n\,d\Gamma \\ &- \frac{\Delta t^2}{2}\int_\Omega \frac{\partial \mathbf{N}^\mathbf{T}}{\partial \mathbf{x}_k}\hat{u}_k\frac{\partial \mathbf{N}}{\partial \mathbf{x}_i}\{\mathbf{p}\}^n\,d\Omega \\ &+ \frac{\Delta t^2}{2}\int_\Gamma \mathbf{N}^\mathbf{T}\mathbf{N}\hat{u}_k n_k\left\{\widehat{\frac{\partial \mathbf{p}}{\partial \mathbf{x}_i}}\right\}^n d\Gamma \end{aligned} \tag{2.62}$$

This can be rewritten in matrix form as

$$\mathbf{M}_3\{\mathbf{U}_i\}^{n+1} = \mathbf{M}_3\{\mathbf{U}_i\}^* + \Delta t\left[\mathbf{C}_3\{\mathbf{p}\}^n - \{\mathbf{f}_6\} - \mathbf{K}_3\{\mathbf{p}\}^n + \{\mathbf{f}_7\}\right] \tag{2.63}$$

2.6.3 Final CBS-AC Equations

The fully discretised steps are summarised below. With the use of the LCG method for the spatial discretisation, these equations are valid over an element which is comparable to treating the global domain as a number of interconnected sub-domains. This allows for an element-by-element solution strategy. In order to establish a globally continuous solution the nodal values are averaged over the element contributions within each step. As highlighted in the previous section, the face fluxes may be treated as continuous or lumped. Within the thesis the lumped approximation has been employed.

Step 1: The determination of an intermediate velocity field U_i^* using the modified momentum equation.

$$\begin{aligned}\mathbf{M}_1\{\mathbf{U}_i\}^* &= \mathbf{M}_1\{\mathbf{U}_i\}^n \\ &+ \Delta t\left[\mathbf{C}_1\{\mathbf{u}_j\mathbf{U}_i\}^n - \mathbf{K}_1 - \{\mathbf{f}_1\} + \{\mathbf{f}_2\} + \mathbf{K}_1^{CG}\{\mathbf{u}_j\mathbf{U}_i\}^n + \{\mathbf{f}_3\}\right]\end{aligned} \tag{2.64}$$

Step 2: Calculation of the pressure field

$$\mathbf{M}_2 \{\mathbf{p}\}^{n+1} = \mathbf{M}_2 \{\mathbf{p}\}^n + \Delta t \left(\beta^2\right)^n [\mathbf{C}_2 \{\mathbf{U}_i + \Delta \mathbf{U}_i^*\}^n - \{\mathbf{f}_4\} - \mathbf{K}_2 \{\mathbf{p}\}^n + \{\mathbf{f}_5\}] \quad (2.65)$$

Step 3: Velocity Correction

$$\mathbf{M}_3 \{\mathbf{U}_i\}^{n+1} = \mathbf{M}_3 \{\mathbf{U}_i\}^* + \Delta t [\mathbf{C}_3 \{\mathbf{p}\}^n - \{\mathbf{f}_6\} - \mathbf{K}_3 \{\mathbf{p}\}^n + \{\mathbf{f}_7\}] \quad (2.66)$$

2.6.4 Artificial Compressibility and Local Time-Stepping

The use of artificial compressibility (AC) allows for a fully explicit CBS scheme for computing incompressible flows. Artificial compressibility introduces a parameter β which replaces the compressible wave speed c within the continuity of mass equation. This is an advantage in problems where c becomes very large, which imposes severe time step restrictions on the solution procedure.

The value of β can be given as a constant throughout the domain, but in the recommended approach which is adopted in this work, β is determined locally, based on both convective and diffusive time-step restrictions [77, 78, 83]. This gives not only a scheme which is suitable for different Reynolds numbers but more importantly it accommodates different flow regimes (convection and diffusion dominated) within a problem at a particular Reynolds number. In this work the relation

$$\beta = max(\epsilon, u_{conv}, u_{diff}) \quad (2.67)$$

is employed, The constant ϵ ensures that β does not approach zero, and typically takes the value of $0.1 \leq \epsilon \leq 0.5$. , ν_{conv} is the local convective velocity and ν_{diff} is the local diffusive velocity. These velocities are calculated from the non-dimensional relations [77],

$$u_c = \sqrt{u_i u_i} \quad (2.68)$$

$$u_d = \frac{h}{2Re} \quad (2.69)$$

where h is the local element size and Re is the Reynolds number. The local element size h is defined based upon the local nodal values within an element. The value of h_i for a local node is defined in 3D as

$$h_i = \frac{3V_e}{A_{opp}} \tag{2.70}$$

where V_e is the volume of the element and A_{opp} denotes the opposite face area. In 2D, the value of h_i for a local node is defined by

$$h_i = \frac{3A_e}{L_{opp}} \tag{2.71}$$

where A_e is the area of the element and L_{opp} denotes the opposite edge length. The local element size h is calculated using

$$h = min(h_i) \quad i = 1, N \tag{2.72}$$

where N is the number of nodes within the element.

Since the value of β varies throughout the domain, local time stepping is employed in order to accelerate convergence to a local steady state. The local elemental time step can be determined by

$$\Delta t_e = min(\Delta t_c, \Delta t_d) \tag{2.73}$$

where the convective component of the local time step is defined as

$$\Delta t_c = \frac{h}{max(\sqrt{u_i u_i} + \beta)} \tag{2.74}$$

The local element time step utilises the maximum value of the convective velocity determined from the four local node values (in 3D). The diffusive component can be determined by

$$\Delta t_d = \frac{h^2 Re}{2} \tag{2.75}$$

Once the elemental values of Δt have been determined, the nodal values are calculated by

$$\Delta t_p = min(\Delta t_e) \quad e = 1, 2, .., Ne \tag{2.76}$$

where Ne represents the number of connected elements.

With the use of an artificial compressibility parameter and local time-stepping, a steady state solution may be determined. In order to recover the transient solution, an additional component is required within the outlined CBS scheme.

2.6.5 Recovery of the Transient Solution

The local time stepping procedure outlined in the previous section may be regarded as an iterative mechanism or pseudo time stepping mechanism. In order to determine a transient solution, a true transient term is added to the momentum equation. With the momentum equation split over Step 1 and Step 3 the true transient term may be added to either. In this work the true transient term is added to the velocity correction step in Step 3. This results in the modified form (from Equation 2.66)

$$\mathbf{M}_3 \{\mathbf{U}_i\}^{n+1} = \mathbf{M}_3 \{\mathbf{U}_i\}^* + \Delta t \left[\mathbf{C}_3 \{\mathbf{p}\}^n - \mathbf{f}_6 - \mathbf{K}_3 \{\mathbf{p}\}^n + \mathbf{f}_7 - \frac{\Delta \mathbf{U}_i^\tau}{\Delta \tau}\right] \tag{2.77}$$

where $\Delta \tau$ is the real time step. $\Delta \mathbf{U}_i^\tau$ can be calculated using the backward differentiation formulae

$$\Delta \mathbf{U}_i^\tau = \frac{\mathbf{U}_i^n - \mathbf{U}_i^{m-1}}{1} \tag{2.78}$$

for a first order backward implicit scheme (BDF1). For a second order backward implicit scheme (BDF2)

$$\Delta \mathbf{U}_i^\tau = \frac{3\mathbf{U}_i^n - 4\mathbf{U}_i^{m-1} + 1\mathbf{U}_i^{m-2}}{2} \tag{2.79}$$

and finally for a third order backward implicit scheme (BDF3)

$$\Delta \mathbf{U}_i^{\tau} = \frac{11\mathbf{U}_i^n - 18\mathbf{U}_i^{m-1} + 9\mathbf{U}_i^{m-2} - 2\mathbf{U}_i^{m-3}}{6} \tag{2.80}$$

In the above equations the nth term denotes the solution from the previous pseudo time step and mth term denotes the solution from the respective mth real time level. Due to the implicit nature of the three alternatives, no time step restrictions are placed on the real time step. Only the BDF1 and BDF2 equations produce A-stable solutions. With the introduction of the real time stepping term within the CBS scheme, an additional restriction is placed upon the determination of the artificial compressibility parameter β. This modified β can be determined from

$$\beta = max(\epsilon, u_{conv}, u_{diff}, u_{real}) \tag{2.81}$$

where the real time velocity component is calculated using

$$u_{real} = \frac{h}{\Delta\tau} \tag{2.82}$$

Since the backward difference formula schemes are not self starting, solutions must be determined for the prerequisite number of previous real time steps. Within this work, these values are determined by use of a steady state solution to approximate the required time instance.

2.7 Convergence

The L_2 norm of the velocity field was used to determine whether the steady state had been achieved. It gives the norm of the velocity difference between the $n+1$ and n pseudo time level and is normalised by the Euclidean norm of the velocity at time level $n+1$.

$$\|e\|_{L_2} = \sqrt{\frac{\sum_{i=1}^{Np} \left(\|u\|_i^{n+1} - \|u\|_i^n\right)}{\sum_{i=1}^{Np} \left(\|u\|_i^{n+1}\right)}} \tag{2.83}$$

where Np represents the total number of points within the domain. Steady state has been achieved when the L_2 residual norm of the velocity has reduced to 10^{-5} or less.

2.8 Spalart-Allmaras Turbulence Model

If the flow displays turbulent properties, then a steady state solution is no longer possible due to the unsteady nature of turbulence. In order to ensure a steady state solution can be determined, it is possible to employ the Reynolds Averaged Navier Stokes equations (RANS). These turbulence models were developed to account for (part of) the turbulence unsteadiness statistically. There are a number of possible turbulence models that can be employed. Within this work, the Spalart-Allmaras (SA) one equation model is used [82]. This model replaces the laminar viscosity with a Reynolds averaged viscosity. The use of a turbulence model avoids the requirement for highly refined mesh resolutions which would be necessary in order to carry out direct numerical solution (DNS). This avoids the issue of excessively high computational cost needed by DNS due to the high mesh resolution. Early one equation models were implicit in nature, which can increase computational resources compared to an explicit method. The Spalart-Allmaras one equation model, however, produces a local turbulence model. Therefore the equation at one point does not depend on the solution from other points, and the turbulence model is explicit. Due to its explicit nature, it can easily be implemented within the fully explicit CBS scheme.

The SA model also has several additional advantages. The model allows for a relatively smooth transition from laminar to turbulent conditions which is of importance within the study of blood flow. In arteries such as the human carotid, the flow is typically laminar. In diseased arteries, a local narrowing may induce turbulence, thus a model that allows for a smooth laminar-turbulent transition is necessary. Stability of the method is enhanced through the inclusion of a wall destructive mechanism. This term depends on the proximity to the wall, and diminishes as the distance is increased. This precludes a large source term affecting stability throughout the domain, as it is localised to the near-wall region.

The SA model is applied as a fourth step within the characteristic based split scheme outlined within this chapter. In order to incorporate the turbulent viscosity a modification must also be made to Step 1. With the introduction of a RANS model, all solution variables are time-averaged quantities.

2.8.1 Modified Intermediate Velocity Field Calculation

In order to include the turbulent viscosity, a modification is made to the momentum equation, specifically the diffusive component in Step 1. The original shear component

τ_{ij} is replaced with $\tau_{ij} + \tau_{ij}^R$ where the first part represents the laminar shear stress as before and τ_{ij}^R represents the additional Renolds stress tensor. The Reynolds stress tensor τ_{ij}^R is introduced by Boussinesq's assumption as

$$\begin{aligned} \tau_{ij}^R &= -\rho\overline{u_i' u_j'} \\ &= \mu_t \left(\frac{\partial \bar{u}_i}{\partial x_j} + \frac{\partial \bar{u}_j}{\partial x_i} - \frac{2}{3}\frac{\partial \bar{u}_k}{\partial x_k}\delta_{ij} \right) - \frac{2}{3}\rho\kappa\delta_{ij} \end{aligned} \tag{2.84}$$

where $\bar{u}_j$ is the time-averaged velocity components, δ_{ij} is the Kronecker delta, $\mu_t \equiv \rho\nu_t$ is the turbulent eddy dynamic viscosity that is the positive scalar coefficient and the turbulent kinetic energy $\kappa = 0$ is assumed in this study.

After noting that all velocity components are now time-averaged, the overbars are now dropped from the equations. In order to introduce the Reynolds stress tensor term into Step 1, only a small correction in the coefficient of the shear stress term is required. Thus, no significant computational code modifications are required. The turbulent eddy viscosity ν_t can be calculated using

$$\nu_t = \hat{\nu} f_{\hat{\nu}1} \tag{2.85}$$

where $\hat{\nu}$ is the modified turbulent eddy viscosity and the coefficient $f_{\hat{\nu}1}$ is

$$f_{\hat{\nu}1} = X^3/(X^3 + c_{\hat{\nu}1}^3) \tag{2.86}$$

and the constant $c_{\hat{\nu}1} = 7.1$.

$$X \equiv \hat{\nu}/\nu \tag{2.87}$$

In order to non-dimensionalise the turbulent variables, two additional relationships to the ones outlined in Section 2.2.1 are required. These are given as

$$\nu_t^* = \frac{\nu_t}{\nu_\infty} \qquad\qquad \hat{\nu} = \frac{\hat{\nu}}{\nu_\infty} \tag{2.88}$$

and therefore the shear stress tensor becomes

$$\tau_{ij} + \tau_{ij}^{R} = \frac{1 + \nu_t^*}{Re}\left(\frac{\partial \mathbf{u}_i}{\partial \mathbf{x}_j} + \frac{\partial \mathbf{u}_j}{\partial \mathbf{x}_i} - \frac{2}{3}\delta_{ij}\frac{\partial \mathbf{u}_k}{\partial \mathbf{x}_k}\right) \tag{2.89}$$

2.8.2 Transport Equation of the Modified Turbulent Eddy Viscosity

The use of a transport equation to model the turbulent eddy kinematic viscosity allows for easier determination compared to computation of the turbulent dissipation rate ϵ and kinetic energy κ. The $\kappa - \epsilon$ models require finer resolution near a wall as well as having convergence issues due to the source terms employed [82]. The transport equation for the modified turbulent eddy viscosity variable $\hat{\nu}$ is defined as

$$\frac{\partial \hat{\nu}}{\partial t} + \underbrace{\frac{\partial \hat{\nu} u_i}{\partial x_i}}_{\text{convection}} = \underbrace{\frac{1}{\sigma_{\hat{\nu}}}\left[\left(\frac{\partial}{\partial x_i}\left(\nu + \hat{\nu}\right)\frac{\partial \hat{\nu}}{\partial x_i}\right) + c_{b2}\left(\frac{\partial \hat{\nu}}{\partial x_i}\right)^2\right]}_{\text{Viscous diffusion}} - \underbrace{c_{w1} f_w \left(\frac{\hat{\nu}}{y}\right)^2}_{\text{destruction}} + \underbrace{c_{b1}\hat{S}\hat{\nu}}_{\text{production}} \tag{2.90}$$

From the work undertaken by Spalart and Allmaras [82], the values of the constants were chosen as follows: $\sigma_{\hat{\nu}} = 2/3$, $c_{b2} = 0.622$ for the viscous diffusion term and $c_{b1} = 0.1355$ for the production term. These values were calibrated from the free shear flow version of the model. Within the production term, the magnitude of the vorticity S is replaced by a modified vorticity function in order to maintain its log-layer behaviour all the way to the wall. The modified function $\hat{S}$ is calculated using

$$\hat{S} \equiv S + (\hat{\nu}/k^2 y^2) f_{\hat{\nu}2} \tag{2.91}$$

where y is the distance from the nearest wall, $k = 0.41$. $f_{\hat{\nu}2}$ is calculated from

$$f_{\hat{\nu}2} = 1 - X/(1 + X f_{\hat{\nu}1}) \tag{2.92}$$

and S, the magnitude of the vorticity, is determined using

$$S = \sqrt{\left(\frac{\partial \mathbf{u}_2}{\partial \mathbf{x}_1} - \frac{\partial \mathbf{u}_1}{\partial \mathbf{x}_2}\right)^2 + \left(\frac{\partial \mathbf{u}_3}{\partial \mathbf{x}_1} - \frac{\partial \mathbf{u}_1}{\partial \mathbf{x}_3}\right)^2 + \left(\frac{\partial \mathbf{u}_3}{\partial \mathbf{x}_2} - \frac{\partial \mathbf{u}_2}{\partial \mathbf{x}_3}\right)^2} \tag{2.93}$$

In the boundary layer, the blocking effect of the wall acts upon the flow at a distance due to the pressure term. This acts as the main destructive mechanism for the Reynolds shear stress. The destructive term in the transport equation consists of $-c_{w1}(\nu_t/y)^2$ which was determined via dimensional analysis. c_{w1} is calculated using $c_{w1} = c_{b1}/k^2 + (1+c_{b2}/\sigma_{\hat{\nu}})$. The choice of f_w comes from algebraic models [82] where the mixing length plays an important role in the near-wall region. The mixing length $l = \sqrt{\nu_t/S}$. Since f_w must be non-dimensional, a convenient approach utilises the square of l/ky, which gives

$$r = \nu_t/\hat{S}k^2y^2 \tag{2.94}$$

Any dimensionally correct term comprised of ν_t, y, S that reduces to $-c_{w1}k^2u_r^2$ is appropriate for f_w although the relationship

$$f_w = g\left[\frac{1+c_{w3}^6}{g^6+c_{w3}^6}\right]^{1/6} \tag{2.95}$$

is employed in this scheme, where $u_r = Sky$ is the friction velocity, $c_{w3} = 2$ and g is defined by

$$g = r + c_{w2}(r^6 - r) \tag{2.96}$$

and $c_{w2} = 0.3$. In the log layer, both r and f_w are equal to 1 and decrease in the outer region. The influence of the vorticity within the destructive term is given in Figure 2.5. Two values of the vorticity were chosen (small = 0.001 s^{-1}, large = 3000 s^{-1}). The distance to the wall y for any node i is calculated simply by examination of the designated wall nodes using a loop comparison mechanism. This is outlined along with its parallel implementation within the following chapter.

2.8.3 Non-dimensional Form of the Transport Equation

The non-dimensional form of the transport equation is used within this work. Using the non-dimensional relationships outlined in Sections 2.2.1 and 2.8.2, the non-dimensional form of the transport equation (after dropping asterisk notation) is defined as

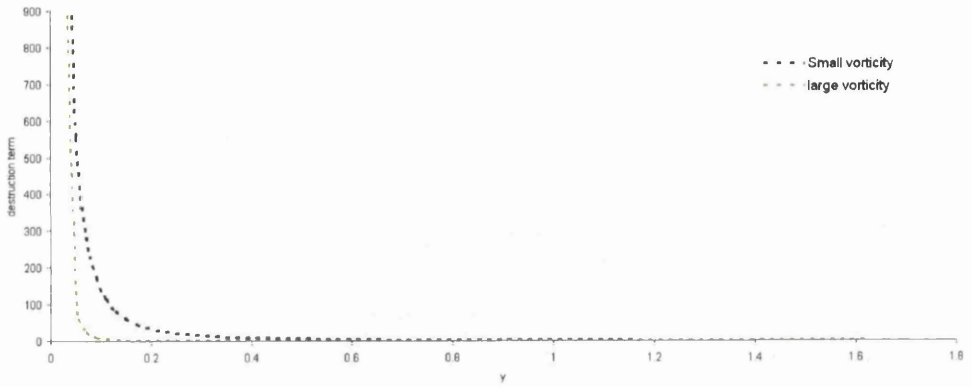

Figure 2.5: Influence of the vorticity on the destructive term away from the wall

$$\frac{\partial \hat{\nu}}{\partial t} + \frac{\partial \hat{\nu} u_i}{\partial x_i} = \frac{1}{Re\sigma_{\hat{\nu}}} \left[\left(\frac{\partial}{\partial x_i} (1 + \hat{\nu}) \frac{\partial \hat{\nu}}{\partial x_i} \right) + c_{b2} \left(\frac{\partial \hat{\nu}}{\partial x_i} \right)^2 \right] - \frac{c_{w1} f_w}{Re} \left(\frac{\hat{\nu}}{y} \right)^2 + c_{b1} \hat{S} \hat{\nu} \quad (2.97)$$

The non-dimensional form of the remaining parameters is unchanged except for

$$\hat{S} \equiv S + \frac{1}{Re} \frac{\hat{\nu}}{(ky)^2} f_{\hat{\nu}2} \quad (2.98)$$

and

$$r = \frac{1}{Re} \frac{\hat{\nu}}{\hat{S}(ky)^2} \quad (2.99)$$

2.8.4 Discretised Transport Equation

From the non-dimensionalised form of the transport equation in Equation 2.97, the weak form is introduced as

$$\begin{aligned} \int_\Omega v \frac{\partial \hat{\nu}}{\partial t} d\Omega + \int_\Omega v \frac{\partial \hat{\nu} u_i}{\partial x_i} d\Omega &= \int_\Omega v \frac{1}{Re\sigma_{\hat{\nu}}} \left[\left(\frac{\partial}{\partial x_i} (\nu + \hat{\nu}) \frac{\partial \hat{\nu}}{\partial x_i} \right) + c_{b2} \left(\frac{\partial \hat{\nu}}{\partial x_i} \right)^2 \right] d\Omega \\ &+ \int_\Omega v \left[- \frac{c_{w1} f_w}{Re} \left(\frac{\hat{\nu}}{y} \right)^2 + c_{b1} \hat{S} \hat{\nu} \right] d\Omega \end{aligned} \quad (2.100)$$

After integration by parts, introduction of the characteristic Galerkin time discretisation and substitution of the spatial discretisation and Galerkin weighting, the expression once higher order terms are ignored becomes

$$
\begin{aligned}
\int_\Omega \mathbf{N}^\mathbf{T}\mathbf{N}\left\{\frac{\Delta\hat{\boldsymbol{\nu}}}{\Delta \mathbf{t}}\right\} d\Omega \;=\; & + \int_\Omega \frac{\partial \mathbf{N}^\mathbf{T}}{\partial \mathbf{x}_i}\left\{\hat{\boldsymbol{\nu}}\mathbf{u}_i\right\} d\Omega \\
& - \int_\Gamma n_i \mathbf{N}^\mathbf{T}\mathbf{N}\left\{\hat{\boldsymbol{\nu}}\mathbf{u}_i\right\} d\Gamma \\
& - \frac{\Delta t}{2}\int_\Omega \frac{\partial \mathbf{N}^\mathbf{T}}{\partial \mathbf{x}_k}\hat{u}_k\frac{\partial \mathbf{N}}{\partial \mathbf{x}_i}\left\{\hat{\boldsymbol{\nu}}\mathbf{u}_i\right\} d\Omega \\
& + \frac{\Delta t}{2}\int_\Gamma \mathbf{N}^\mathbf{T}\mathbf{N}n_k\hat{u}_k\left\{\widehat{\frac{\partial \hat{\boldsymbol{\nu}}\mathbf{u}_i}{\partial \mathbf{x}_i}}\right\} d\Gamma \\
& - \frac{1}{Re\sigma_{\hat{\nu}}}\int_\Omega \frac{\partial \mathbf{N}^\mathbf{T}}{\partial \mathbf{x}_i}(1+\hat{\nu})\frac{\partial \mathbf{N}}{\partial \mathbf{x}_i}\left\{\hat{\boldsymbol{\nu}}\right\} d\Omega \\
& + \frac{1}{Re\sigma_{\hat{\nu}}}\int_\Gamma \mathbf{N}^\mathbf{T}\mathbf{N}n_i(1+\hat{\nu})\left\{\widehat{\frac{\partial \hat{\boldsymbol{\nu}}}{\partial \mathbf{x}_i}}\right\} d\Gamma \\
& + \frac{c_{b2}}{Re\sigma_{\hat{\nu}}}\int_\Omega \mathbf{N}^\mathbf{T}\left(\frac{\partial \mathbf{N}}{\partial \mathbf{x}_i}\left\{\hat{\boldsymbol{\nu}}\right\}\right)^2 d\Omega \\
& - \frac{\Delta t c_{b2}}{2Re\sigma_{\hat{\nu}}}\int_\Omega \frac{\partial \mathbf{N}^\mathbf{T}}{\partial \mathbf{x}_k}\hat{u}_k\left(\frac{\partial \mathbf{N}}{\partial \mathbf{x}_i}\left\{\hat{\boldsymbol{\nu}}\right\}\right)^2 d\Omega \\
& + \frac{\Delta t c_{b2}}{2Re\sigma_{\hat{\nu}}}\int_\Gamma \mathbf{N}^\mathbf{T}\mathbf{N}n_k\left\{\widehat{\frac{\partial \hat{\boldsymbol{\nu}}}{\partial \mathbf{x}_i}}\right\}^2 d\Gamma \\
& + c_{b1}\int_\Omega \mathbf{N}^\mathbf{T}\mathbf{N}\hat{S}\left\{\hat{\boldsymbol{\nu}}\right\} d\Omega \\
& - \frac{\Delta t}{2}c_{b1}\int_\Omega \frac{\partial \mathbf{N}^\mathbf{T}}{\partial \mathbf{x}_k}\hat{u}_k\hat{S}\mathbf{N}\left\{\hat{\boldsymbol{\nu}}\right\} d\Omega \\
& + \frac{\Delta t}{2}c_{b1}\int_\Gamma \mathbf{N}^\mathbf{T}\mathbf{N}n_k\hat{u}_k\hat{S}\left\{\widehat{\hat{\boldsymbol{\nu}}}\right\} d\Gamma \\
& - \frac{c_{w1}f_w}{Re}\int_\Omega \mathbf{N}^\mathbf{T}\mathbf{N}\left\{\frac{\hat{\boldsymbol{\nu}}}{\mathbf{y}}\right\} d\Omega \\
& - \frac{\Delta t}{2}\frac{c_{w1}f_w}{Re}\int_\Omega \frac{\partial \mathbf{N}^\mathbf{T}}{\partial \mathbf{x}_k}\hat{u}_k\mathbf{N}\left\{\frac{\hat{\boldsymbol{\nu}}}{\mathbf{y}}\right\} d\Omega \\
& - \frac{\Delta t}{2}\frac{c_{w1}f_w}{Re}\int_\Gamma \mathbf{N}^\mathbf{T}n_k\hat{u}_k\mathbf{N}\left\{\frac{\widehat{\hat{\boldsymbol{\nu}}}}{\mathbf{y}}\right\} d\Gamma \qquad (2.101)
\end{aligned}
$$

since the residual on the boundaries can be neglected [83], the shortened matrix form is

$$\begin{aligned}\mathbf{M}^{SA}\{\hat{\nu}\}^{n+1} &= \mathbf{M}^{SA}\{\hat{\nu}\}^{n} \\ &+ \Delta t\left[\mathbf{C}_1^{SA} - \mathbf{K}_1^{SA} - \mathbf{f}_1^{SA} - \mathbf{K}_2^{SA} + \mathbf{f}_2^{SA} + \mathbf{K}_3^{SA}\right] \\ &+ \Delta t\left[\mathbf{K}_4^{SA}\{\hat{\nu}\} + \mathbf{K}_5^{SA}\left\{\frac{\hat{\nu}^2}{y}\right\} - \mathbf{K}_6^{SA} - \mathbf{K}_7^{SA}\right]\end{aligned} \tag{2.102}$$

2.8.5 Local Timestepping and Artificial Compressibility β Modification

With the introduction of the turbulence equation, additional restrictions are imposed on the local time step and the artificial compressibility parameter. These restrictions are dependent upon the non-dimensional relationships

$$\beta = max(\epsilon, u_{conv}, u_{diff}, u_{real}, u_{turb}) \tag{2.103}$$

where u_{turb} is defined by

$$u_{turb} = max\left(c_{b1}\hat{S}, \frac{1+\hat{\nu}}{\mathrm{Re}\sigma_{\hat{\nu}}h^2}, \frac{c_{b2}\hat{\nu}}{\mathrm{Re}\sigma_{\hat{\nu}}h^2}, \frac{c_{w1}f_w\hat{\nu}}{\mathrm{Re}y^2}\right) \times h \tag{2.104}$$

The local time step is automatically modified through the modification in β.

2.8.6 Real Time Stepping

In order to recover the transient solution, a true transient term is added to the transport equation using the procedure outlined in Section 2.6.5. In order to maintain continuity between both of the true transient terms the same backward difference formula is implemented in each case. The second order backward implicit transient term is given as

$$\Delta\hat{\nu}^{\tau} = \frac{3\hat{\nu}^{n} - 4\hat{\nu}^{m-1} + 1\hat{\nu}^{m-2}}{2\Delta\tau} \tag{2.105}$$

where the nth term denotes the solution from the previous pseudo time step and mth term denotes the solution from the respective mth real time level as before.

2.9 Boundary Conditions

In order to complete a problem specification, initial and boundary conditions must be defined. The free stream values are imposed as the initial conditions within the domain unless otherwise specified. Pressure boundary conditions are imposed at the end of Step 2 and the velocity boundary conditions are imposed at the end of Step 3. Within this thesis a number of boundary conditions are employed. Both general boundary conditions such as no-slip conditions and more specific boundary conditions are employed. In order to model blood flow problems both Womersley profiles and Windkessel boundary conditions are used and are outlined within their respective section. The numerical solution to the Helmholtz equation can also be used. At boundaries that represent solid geometries such as an arterial wall the no-slip condition is imposed. This involves the specification of the velocity components as zero.

The symmetric boundary condition is imposed through calculation of the magnitude of the velocity at the face and imposing a zero velocity normal to the face, while simultaneously reallocating the velocity in the tangential directions.

2.9.1 Turbulence Boundary Conditions

The value of the modified turbulent kinematic eddy viscosity $\hat{\nu}$ must be prescribed at an inlet. In this work a small value for $\hat{\nu}$ is applied, a value of $\hat{\nu} = 1 \times 10^{-5}$ was found to be suitable. This is less than the $\nu/10$ limit recommended by Spalart and Allmaras [82] and large enough to avoid numerical errors creating negative $\hat{\nu}$ values near the edge of the boundary layer. This is essential since the exact solution cannot be negative at any point. This small value was also employed as an initial condition within the domain for the same reason. At the outlet $\hat{\nu}$ was unprescribed. At the wall $\hat{\nu} = 0$, and this is also true for symmetrical boundary conditions.

With the use of non-uniform transient flow profiles as is outlined in Section 2.9.2, an inlet surface will experience a period of reverse flow across a portion of its surface. The same is true of an outlet which would experience a section acting as an inlet during that time. In order to apply the necessary turbulent boundary conditions, a calculation to designate inlet *nodes* is undertaken within each real time step. These nodes may be either at the inlet or outlet face. Once the nodes are designated, the condition $\hat{\nu} = 1 \times 10^{-5}$ is applied. The remaining outlet *nodes* are unprescribed.

2.9.2 Womersley Velocity Profiles

There are several possible flow profiles that can be employed within the field of blood flow modelling for the inflow and outflow boundaries. Since the flow is assumed to be unsteady and fully developed, a Hagen-Poiseuille flow profile, which assumes fully developed steady flow in a circular channel, would be inappropriate for this problem. On the other hand, a Womersley profile, which assumes fully developed unsteady flow is widely used in the field [19,24,41,90–92]. Another alternative would be to use measured velocity profiles captured using MRI and phase contrast measurements. However, this was not possible in this work and thus a velocity profile based on a Womersley solution is used. The Womersley profile is a 2D linear viscous solution of the Navier-Stokes equations for cylindrical tubes. A mapping procedure must be undertaken to map the flow profile to a non-circular cross section, introducing a small error dependent on the non-circularity of the inlet/outlet.

The Womersley profile can be reconstructed either from a flow rate waveform or from a centreline velocity waveform. Both are outlined in the following sections before the mapping procedure is described along with the optional combing technique that is proposed to obtain an optimal inflow direction. The velocities in the radial and tangential direction are initially assumed to be zero although the combing technique may introduce small velocities in these directions. Once reconstructed, the velocity components are imposed at the end of Step 3 within the CBS scheme.

2.9.2.1 Flow Rate Waveform

In order to determine an appropriate Womersley profile, the inflow/outflow boundary surface area must be calculated. From this value, it is then possible to determine the idealised radius R of the vessel. Starting with the flow waveform (Figure 2.6), which can be represented by a Fourier series as

$$Q(t) = \Re \sum_{n=0}^{N} B_n \exp^{i\omega_n t} \tag{2.106}$$

where Q is the flow rate, B_n and $\omega_n = 2\pi n\omega_0$ are the amplitude and angular frequency of the nth harmonic of the flow waveform. N is the number of harmonics and t is time. The axial component of the velocity profile can then be constructed using [93]

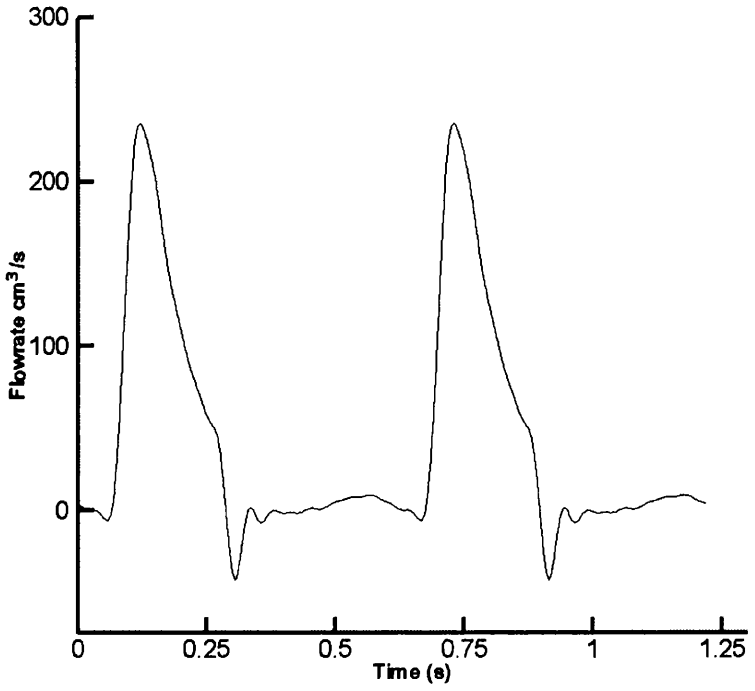

Figure 2.6: The aorta inlet transient flow profile for two heart beats

$$\mathbf{u}(\mathbf{x},t) = \frac{2B_0}{\pi R^2}\left[1-\frac{r(\mathbf{x})}{R}\right] + \Re\left(\sum_{n=1}^{N}\left\{\frac{2B_n}{\pi R^2}\left[\frac{1-\frac{J_o\left(\alpha_n\frac{r(\mathbf{x})}{R}i^{3/2}\right)}{J_o\left(\alpha_n i^{3/2}\right)}}{1-\frac{2J_1\left(\alpha_n i^{3/2}\right)}{\alpha i^{3/2}J_o\left(\alpha i^{3/2}\right)}}\right]\right\}\exp^{i\omega_n t}\right) \quad (2.107)$$

where $\alpha = R\sqrt{\omega_n/\nu}$ is the Womersley number, $i = \sqrt{-1}$, the imaginary number, J_0 and J_1 denote Bessel functions of the first kind, zero and first order respectively, ν the kinematic viscosity, $\Re()$ the real part, and $r(\mathbf{x})$ is the distance between a point $\mathbf{x}$ and the axis of the cylinder.

2.9.2.2 Maximum Velocity Waveform

To construct the Womersley profile from the centreline velocity waveform, the following expression is used [2]

$$\mathbf{u}(\mathbf{x},t) = \Re\left(\sum_{n=1}^{N}\frac{B_n}{i\omega_n}\left[1-\frac{J_0\left(i^{3/2}r(\mathbf{x})\sqrt{\omega_n/\nu}\right)}{J_0\left(i^{3/2}R\sqrt{\omega_n/\nu}\right)}\right]e^{i\omega_n t+\phi_n}\right) \quad (2.108)$$

Harmonic	freq. (Hz)	Amplitude	phase (rad)
0	0	126.88125	0.00000
1	1.63548	219.04800	-1.59841
2	3.27097	156.06450	3.04933
3	4.90645	80.25450	1.81371
4	6.54193	57.64425	1.22483
5	8.17742	56.19338	-0.107859
6	9.81290	25.00121	-1.55024
7	11.44840	17.10540	-1.40587
8	13.08390	24.24746	-2.93862
9	14.71940	8.16308	1.45781
10	16.35480	10.90725	2.74547
11	17.99030	12.69634	0.490823
12	19.62580	2.756033	-2.48452
13	21.26130	5.983050	-0.254379
14	22.89680	5.026950	-2.84223
15	24.53230	2.558115	0.376408

Table 2.1: Harmonics utilised to construct the Womersley profile. [2]

Here B is the amplitude and ϕ is the phase. A transient cardiovascular flow profile can be obtained through addition of sinusoidal harmonics. In theory the exact representation of a transient flow would require an infinite number of harmonic profiles, however in practice it is possible to achieve sufficient accuracy with only a few harmonics. Table 2.1 depicts the harmonics obtained from a Fourier analysis of a measured aortic velocity waveform [2].

2.9.2.3 Mapping procedure

Given a triangulated inflow/outflow boundary surface, for general 3D problems, the mapping involves the following steps:

- Determination of the centroid of the surface, calculated as the average of the coordinate values of the nodes. This step is carried out by using the following expression

$$\bar{\mathbf{x}} = \frac{1}{A} \sum_{i=1}^{n_{\text{node}}} \mathbf{x}_i A_i \tag{2.109}$$

  where $\bar{\mathbf{x}}$ is the centroid coordinates, A is the total area of the surface, n_{node} is the number of nodes on the surface and A_i is the nodal projection of the area of the

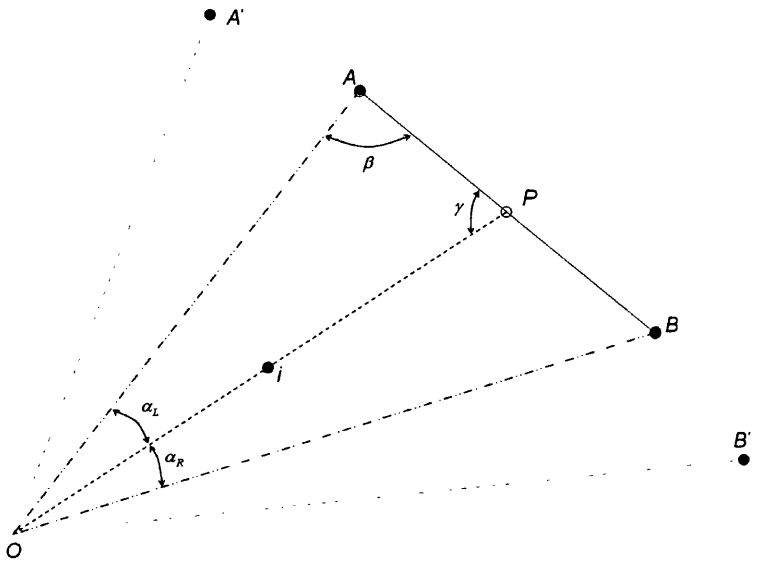

Figure 2.7: Finding the imaginary boundary node for an interior node i

triangular faces connected to node-i. Once the centroid is obtained, the surface is translated such that the centroid is the origin.

- When the normal unit vector of the inflow/outflow boundary surface is not coinciding with any of the unit vectors of the global Cartesian coordinates, a local ortho-normal coordinate system is constructed on the surface, employing the unit normal vector, unit tangential vector and unit bi-tangential vector as its basis. The origin of the local coordinate system here coincides with the centroid of the surface.

- Transform the local Cartesian coordinates of each node into local polar coordinates.

- Calculate the normal radius for each interior node. This is done by first identifying the two boundary nodes A and B that form the smallest value of α (see Figure 2.7). From the vectors OA and AB determine β. It is now possible to find γ. Using the absolute radius of boundary node A (R_l), a linearly interpolated radius (R_i) of an imaginary boundary node P can be found using

$$R_i = R_l \frac{\sin\beta}{\sin\gamma} \tag{2.110}$$

This imaginary boundary node P is on the same line OP that connects the interior node with the centroid.

- Based on the radius of the imaginary boundary node, the normalised radius (r_{norm})

Figure 2.8: Typical velocity profiles at the inflow boundary

of the interior node i can be calculated as $r_{\text{norm}} = r/R_i$. If r_{norm} does not coincide with a previously determined $r(\mathbf{x})$ then it is necessary to perform an interpretation to determine the velocity at the interior point using

$$u = u_1 + \lambda(u_2 - u_1) \tag{2.111}$$

where u_1 and u_2 represent known velocity values at two $r(\mathbf{x})$ points which lie either side of the required datum, and λ is the determined linear distance from the required point to the u_1 point.

A typical velocity profile calculated using the above procedure for an arbitrary inlet is shown in Figure 2.8.

2.9.2.4 Combing Refinement

In the situation where the arterial cross-section varies significantly the vessel wall faces may not be orthogonal to the inlet or outlet. In this case, it may be necessary to use a combing technique to adjust the velocity vectors in order to avoid parasitic flow separation. The combing technique, which can be seen as an alternative to the introduction of mesh extensions such as cylinders, can be outlined (see Figure 2.9) as follows:

- Compute the normal vectors to the wall on outlet/wall shared nodes (green arrows).
- From the normal vectors, determine the tangental vectors to the wall in the shared nodes (blue arrows).
- Set the initial vectors for the remaining outlet nodes as the outlet normal (red arrows)

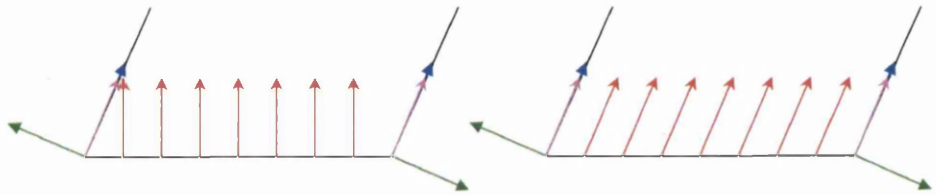

Figure 2.9: Combing Procedure shown in 2d with exaggerated non-orthogonal wall/inlet angle. Arrows represent vector directions. a) pre-combing b) post-combing

- Perform iterations similar to Laplace smoothing, with the shared node normals (pink arrows) being fixed at their initial values, until normals are combed
- Once combed, the velocity vectors are scaled in order to maintain the original flow rate across the arterial cross-section

2.9.3 Finite Element Solution of the Helmholtz Equation

While the Womersley profile may be mapped to non-circular cross-sections, an alternative method may be employed to determine the velocity profile where significant deviation has occurred. This numerical solution assumes a constant cross-sectional area along a straight pipe to determine the solution. The cross-section is not required to be circular. In straight pipe flow, the Navier-Stokes equations reduce to a single linear parabolic inhomogeneous PDE with respect to the axial velocity component $u(x, y, t)$

$$\frac{\partial u}{\partial t} + \nu \frac{\partial^2 u}{\partial x_1^2} + \nu \frac{\partial^2 u}{\partial x_2^2} = \frac{1}{\rho} \frac{\partial p(t)}{\partial x_3} \tag{2.112}$$

Since the PDE is linear, the pressure and solution can be represented by a Fourier series (assuming $\frac{\partial p(t)}{\partial x_3}$ is periodic).

$$\frac{\partial p(t)}{\partial x_3} = \sum_{n=-\infty}^{+\infty} \left(\frac{\partial \tilde{p}}{\partial x_3} \right)_n e^{i\omega_n t} \tag{2.113}$$

where $\omega_n = 2\pi n/T$. Examining the harmonics individually and representing the velocity $u(x, y, t) = \tilde{u}(x, y) e^{i\omega_n t}$ gives

$$i\omega\tilde{u} + \nu\frac{\partial\tilde{u}}{\partial x_1} + \nu\frac{\partial\tilde{u}}{\partial x_2} = \frac{1}{\rho}\frac{\partial\tilde{p}}{\partial x_3} \tag{2.114}$$

This is the Helmholtz equation, and ignoring ˜ may be rewritten as

$$\frac{\partial^2 u}{\partial x_1} + \frac{\partial^2 u}{\partial x_2} + k^2 u = f \tag{2.115}$$

where $k^2 = \frac{i\omega}{\nu}$ and $f = \frac{1}{\eta}\frac{\partial p}{\partial x_3}$. The numerical solution can now be determined using the Finite Element method and noting that on the boundary $u = 0$.

2.9.4 Windkessel 3-Element Model

Windkessel models [94–96] are used to describe the load faced by the heart in pumping blood through the arterial system and are used to relate the blood flow to the blood pressure. The arterial system is characterised in terms of the parameters found within the model, such as peripheral resistance and arterial compliance. A simple Windkessel model describes the arterial system in terms of a closed hydraulic circuit, which consists of a water pump connected to a partially filled chamber. When the water pump is activated the water enters the chamber and the air is compressed which in turn pushes the water back to the pump. The compression of air within the chamber is used to model the elasticity of an artery and its contractible actions within the cardiac cycle. This is known as arterial compliance. Peripheral resistance describes the resistance experienced as the water leaves the chamber to return to the pump. This peripheral resistance simulates the resistance to the blood flow through the arterial network into decreasing arterial diameters. Windkessel elements are typically represented with an electrical analogue as shown in Figure 2.10.

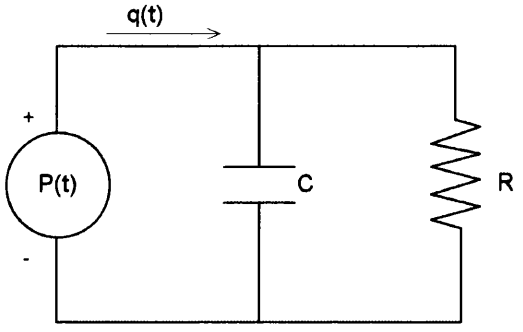

Figure 2.10: 2-Element Windkessel Model.

In the figure, $P(t)$ is the electric potential which corresponds to the blood pressure within the arterial system. $q(t)$ is the current within the electrical system and characterises the blood flow within the arteries. R is the resistance of the resistor and C is the capacitance of the capacitor, which correspond to the aforementioned peripheral resistance and arterial compliance respectively. In the 3-element Windkessel model an additional resistor is added to the electrical circuit as shown in Figure 2.11 in order to simulate the resistance to the blood flow due to the aortic valve.

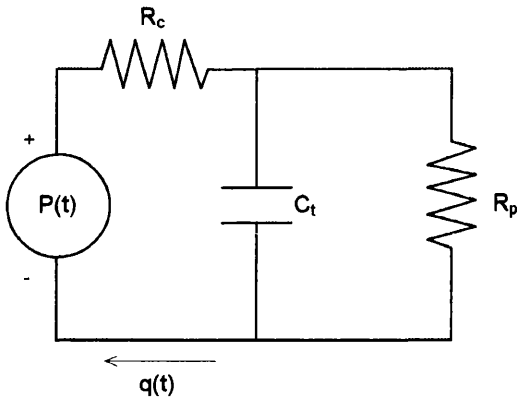

Figure 2.11: 3-Element Windkessel Model.

The 3-element Windkessel equation is expressed as

$$\frac{1}{R_t}\frac{\partial p}{\partial t} = \left(\frac{R_c}{R_p} + 1\right)\frac{q}{R_c C_t} - \frac{\partial q}{\partial t} - \frac{p}{R_c R_p C_t} \tag{2.116}$$

The total peripheral resistance of the truncated branch $R_t = R_c + R_p$. For each truncated artery the values of R_c, R_p and C_t must be provided. It is then possible to determine R_t a flow division must be specified. This flow division is based upon the cubic area of the outlet. R_t can be calculated for each truncated artery as

$$R_t = \frac{\overline{p} a_i^3}{\overline{q} a_t^3} \tag{2.117}$$

where $\overline{q}$ is the mean flow rate entering the common carotid artery, $\overline{p}$ is the mean pressure in time at the common carotid inlet. a_i is the area of the truncated outlet and $a_t = \sum_{i=1}^{N_t} a_i$ where N_t is the total number of truncated arteries (in this case, 2).

The Windkessel boundary condition imposes a pressure boundary condition through numerical solution of Equation 2.116. Using the total flow rate for the outlet during

Artery	R_c [kg cm^{-4}s^{-1}]	R_p [kg cm^{-4}s^{-1}]	C_t [10^{-3} cm^{4}s^{2}kg^{-1}]
Right Internal Carotid Artery	80.5	313.0	4.8
Right External Carotid Artery	77.8	315	4.8
Left Internal Carotid Artery	80.5	313.0	4.8
Left External Carotid Artery	77.8	315	4.8

Table 2.2: Windkessel parameters

the current and previous time step along with pressure at the nth time level, a value for p^{n+1} is calculated and this value is applied uniformly to the outlet surface.

$$\frac{1}{R_t}\frac{p^{n+1}-p^n}{\Delta t} = \left(\frac{R_c}{R_p}+1\right)\frac{q^n}{R_cC_t} - \frac{q^n-q^{n-1}}{\Delta t} - \frac{p^n}{R_cR_pC_t} \tag{2.118}$$

The pressure condition is imposed at the end of Step 2. The parameters for the internal and external carotid artery obtained from [97, 98] are shown in Table 2.2.

2.10 Derived Haemodynamic Wall Parameters

Numerical modelling of the blood flow in the carotid artery bifurcation is of interest with regard to the genesis and diagnosis of atherosclerotic plaques. In the study of aortic aneurysms the interest is towards both high wall shear stress (due to aneurysm rupture) and low or oscillating wall shear stress (aneurysm growth) [56]. It is apparent from clinical observations that atherosclerotic disease typically occurs at locations of complex haemodynamics such as arterial bifurcations, or regions of high curvature. Low or oscillatory shear stresses have been previously associated with atherogenesis [18–25]. On the other hand, high shear stress has been shown to induce mechanical and/or chemical mechanisms that work in concert to provide atheroprotective effects [30].

High oscillation in shear stress or disturbed flow conditions, however, have been shown to induce inflammatory pro-atherogenesis effects such as monocyte adhesion [26–28]. Derived harmodynamic wall parameters which are based on wall shear stress analysis are utilised in order to provide information on locally occurring flow conditions over the cardiac cycle. From the work of Bots *et al*, increased carotid artery intima-media thickness (IMT) is an indicator of atherogenesis [36]. The relationship between IMT and derived haemodynamic parameters for the common carotid artery (CCA) was quantified by the work of Vermeersch *et al* [37].

In the following subsections six haemodynamic parameters are outlined. These are the time-averaged wall shear stress, the temporal and spatial gradients of the wall shear stress and three parameters used to define the flow based upon its directional behaviour with time, namely the oscillating shear index, wall shear stress angle deviation and wall shear stress angle gradient.

2.10.1 Wall Shear Stress

Low wall shear stress (WSS) is one of the indicators to the location of atheroma. The traction vector $\mathbf{t}$ is calculated from the Cauchy stress tensor $\boldsymbol{\sigma}$ and the surface normal vector $\mathbf{n}$ using

$$\mathbf{t} = \boldsymbol{\sigma} \cdot \mathbf{n} \tag{2.119}$$

The surface traction vector $\mathbf{t_s}$ is calculated from

$$\mathbf{t_s} = \mathbf{t} - (\mathbf{t} \cdot \mathbf{n})\mathbf{n} \tag{2.120}$$

The time-averaged wall shear stress (WSS), τ_{abs}, is expressed as

$$\tau_{abs} = \frac{1}{T} \int_0^T \|\mathbf{t_s}\| \, dt \tag{2.121}$$

2.10.2 Oscillating Shear Index

The oscillatory shear index (OSI) originally introduced in [18] and adapted for general three dimensional use in [99] is used to quantify the transient shear stress dynamics experienced by the endothelial cells. The OSI is a ratio of the absolute wall shear stress and the mean wall shear stress. The mean wall shear stress is calculated as the magnitude of the time-averaged surface traction vector τ_{mean} which is defined as

$$\tau_{mean} = \left\| \frac{1}{T} \int_0^T \mathbf{t_s} dt \right\| \tag{2.122}$$

and the oscillatory shear index is defined by [99]

$$OSI = \frac{1}{2}\left(1 - \frac{\tau_{mean}}{\tau_{abs}}\right) \tag{2.123}$$

The oscillatory shear index will always lie within the range $0 \leq OSI \leq 0.5$ and does not take into account the magnitude of the shear stress vectors, it only accounts for WSS directions. The OSI quantifies the amount of time a point experiences flow away from the predominant axial direction such as cross or reverse flow within a cycle. The fraction given by the mean and absolute values of the shear stress varies from 0 to 1, i.e. 0 occurs when there is 180 degrees of variation over the cycle and 1 indicates there is no variation over the time period in question.

Although the clinical threshold for the OSI leading to a substantially increased risk of atherosclerotic lesions has not yet been fully determined, a correlation between the oscillating shear stress and the predisposition of lesion development has been reported [100, 101].

2.10.3 Wall Shear Stress Temporal Gradient

The wall shear stress temporal gradient (WSSTG) is calculated by determining the temporal gradient between instantaneous wall shear stresses for every consecutive time step and storing the maximum value.

$$WSSTG_i = \max\left(\frac{\partial \|\mathbf{t_s}\|_i}{\partial t}\right) = \max\left(\frac{\|\mathbf{t_s}\|_i^{n+1} - \|\mathbf{t_s}\|_i^{n}}{\Delta t}\right) \tag{2.124}$$

where i is the spatial point in question and $0 < t < T$.

2.10.4 Wall Shear Stress Spatial Gradient

The time-averaged wall shear stress spatial gradient (WSSG) is intended to identify the areas of locally disturbed flow. $\nabla \mathbf{t_s}$ is an asymmetric tensor with components acting in different directions at a given time point. The magnitudes of the diagonal components of $\nabla \mathbf{t_s}$ dominate [102, 103], thus the time-averaged WSSG is defined as [104]

$$\text{WSSG} = \frac{1}{T}\int_0^T \sqrt{\left(\frac{\partial \tau_x}{\partial x}\right)^2 + \left(\frac{\partial \tau_y}{\partial y}\right)^2 + \left(\frac{\partial \tau_z}{\partial z}\right)^2}\, dt \tag{2.125}$$

where τ_x is the x-coordinate component of the instantaneous shear stress vector $\mathbf{t_s}$. Since both positive and negative gradients contribute to atherogenesis, the absolute value of the instantaneous WSSG is employed [102, 103]. High WSSG values indicate sustained acceleration and deceleration of the flow.

2.10.5 Wall Shear Stress Angle Deviation

The oscillatory shear index (OSI) not necessarily always provide a good indication of atherogenesis [37]. In order to back up the OSI prediction, another directional quantity called wall shear stress angle deviation (WSSAD) can be employed. This is used to summarise the spatial variation of the mean shear stress direction. It can be used to evaluate the varying flow directions if adjacent surface nodes are approximately equidistant. It is defined as

$$\text{WSSAD} = \frac{1}{T}\int_0^T \left(\frac{1}{A_i}\int_S \phi_i dA_i\right) dt \tag{2.126}$$

where A_i represents the control volume surface area, which is defined as the sum of the connected element areas for node i and ϕ_i is defined as

$$\phi_i = \arccos\left(\frac{\boldsymbol{\tau}_i \cdot \boldsymbol{\tau}_j}{\|\boldsymbol{\tau}_i\| \cdot \|\boldsymbol{\tau}_j\|}\right) \tag{2.127}$$

where $\boldsymbol{\tau}_i$ represents the surface stress vector at the point of interest and $\boldsymbol{\tau}_j$ denotes the surrounding surface stress vectors. $j = 1 : n$ where n is the number of connected points to i.

2.10.6 Wall Shear Stress Angle Gradient

The time-averaged wall shear stress angle gradient (WSSAG) is employed as a mesh independent wall shear stress directional parameter [103]. It is defined as

$$\text{WSSAG} = \frac{1}{T}\int_0^T \left|\frac{1}{A_i}\int_S \nabla\phi_i dA_i\right| dt \tag{2.128}$$

As a time-averaged parameter it can identify locally high values of WSSAG which are sustained over the cardiac cycle. High WSSAG can be an indicator of atherogenesis [40].

2.11 Chapter Summary

The Navier-Stokes equations have been presented within this chapter along with the necessary relationships for non-dimensionalising the governing equations. The conservative form of the Navier-Stokes equations was applied within this thesis. From the non-dimensionalised form of the Navier-Stokes equations the characteristic based split (CBS) scheme was constructed. The CBS scheme outlined in detail was discretised temporally using the characteristic Galerkin method and spatially using the locally conservative Galerkin (LCG) method. In order to model problems that involve turbulent regions, the Reynolds averaged Navier Stokes (RANS) are modelled using the Spalart-Allmaras one equation model. The Spalart Allmaras model is outlined as an additional step within the CBS scheme. In order to complete the problem specification the application of initial and boundary conditions for the velocity, pressure and modified turbulent kinematic eddy viscosity variables was discussed. Finally, the chapter concluded with a discussion on derived haemodynamic wall parameters for utilisation within the study of blood flow. The scheme utilised is fully explicit through use of an artificial compressibility technique making the scheme suitable for parallel implementation as shall be discussed in the next chapter.

Chapter 3

Computational Program Overview

3.1 Introduction

The purpose of this chapter is to provide an overview of the computational implementation of the locally conservative Galerkin variant of the characteristic based split scheme with artificial compressibility. The entire code was written in FORTRAN 90 and parallel implementation was undertaken using Message Passing Interface (MPI).

The computational code may be viewed as having three components. These are namely: preprocessing, the main processing stage and finally the post-processing section. The solution procedure utilises an element-by-element approach, with a number of successive operations carried out using the *do loop* procedure. Within the computational code, it is necessary to do the traditional processing steps a serial code would undertake as well as parallel-specific steps. This is also true with regards to mesh construction, as shall be outlined in section 3.2.2. The parallel implementation, as mentioned, utilises MPI in a single program multiple data (SPMD) format.

3.2 Parallelisation

3.2.1 Overview

Parallelisation allows for the running of domains of greater mesh refinement or domains of greater size that would take an impractical length of time on a serial machine. When considering the field of biomedical problems, and in particular patient-specific problems, this makes parallelisation especially important, since not only is detailed study of a problem essential but also a timely solution is sought.

Parallelisation can be considered in its simplest form as division of the problem into a number of smaller problems, with each problem handled by a certain processor. Parallelisation can also be employed to split a task into a number of tasks allocated over a number of processors.

In addition to a reduction in the size of the domain to determine per processor, parallel implementation also reduces the time required for access to memory. This can lead to a greater than linear speedup as the number of processors increases. This is due a reduction in the overall size of the arrays, considered on a per processor basis. Thus, access calls to different sections of an array will require less time to complete. This also applies when considering the various memory storage options, namely each processors cache levels (Cache 1, Cache 2 etc) and local machine level memory (RAM). Examined over the entire distributed machine network, a greater percentage of information is retained within the fastest memory access levels (local processor cache), which can also have a speed increase influence. It is important to note that any speed up due to memory parallelisation is dependent upon these factors and as such is very problem specific. Smaller arrays may increase speed up, however a negative influence can be encountered due to badly ordered arrays.

Within the processing stage of the CBS scheme, a number of variables must be communicated between the processors in order to transfer information on one sub-domain to the next in order to link the sub-domains into the original sized domain. Only information concerning the interface (shared) nodes is transferred between the inter-connected domains. This is an effective means of parallelisation, in that only the interface nodal data is communicated and only to the patch that requires the information. This minimises data transfer. This is illustrated in Figure 3.1 for a domain that has been decomposed into four sub-domains or processor patches.

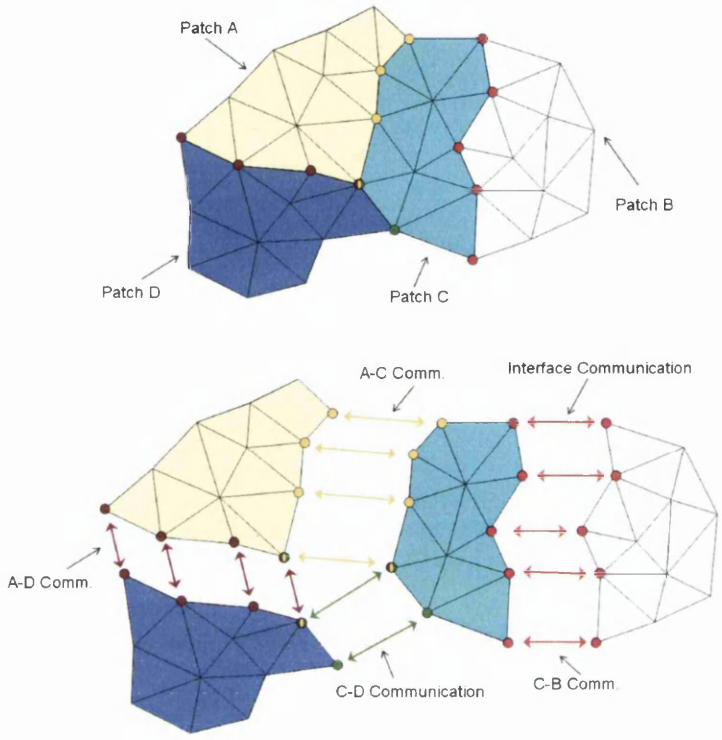

Figure 3.1: Communication between sub-domains.

In order to pass this information between sub-domains, the Message Passing Interface (MPI) library is employed. Originally developed in 1994 it has since become the *de facto* standard for distributed memory systems. With the MPI-2.2 standard published in Sept 2009, the quality is consistently expanding and improving. The standard covers topics from one-sided communications, point-to-point message transfer to environmental management and input/output control. The library is suitable for implementation with C,C++ and Fortran. MPI allows the usage of distributed memory machines as opposed to shared memory parallelisation (OpenMP). The advantage of MPI is that it allows for greater scalability with the removal of the shared memory requirement although it may be slower than OpenMP across an individual multi-processor machine that has shared memory. The MPI library allows for parallel input/output to or from a single storage file. However, within this work an alternative option has been utilised. The individual processor patch information is stored within patch-specific versions for each filetype as explained within section 3.2.2.

The decision for the choice of information transfer between sub-domains is important, since communication time between sub-domains is relatively slow when compared to communication between local processor and local RAM. Thus, while communication

between sub-domains is occurring the processors may be sitting idle, reducing the speed increase offered by parallelisation. Transfer time can be reduced with several management steps. The setup of the distributed memory system is a key factor. Communication speed is defined by interconnect throughput, latency, and messaging rate. Several popular interconnects for high performance computing (HPC) are InfiniBand and Myrinet. Myrinet is employed in this work to reduce communication time. Transfer time can also be reduced through keeping the amount of data transferred to a minimum hence the use of MPI and a single program multiple data (SPMD) format. The requirement of keeping communication to a minimum to avoid excessive time penalties means that certain tasks or programs are less parallelisable. An example of these less optimal techniques would be standard implicit solvers. However, the matrix free explicit scheme outlined in Chapter 2 is fully parallelisable in a simple manner.

3.2.2 Domain Splitting

The decision for each processor to be assigned computational responsibility for an individual sub-domain (SPMD) required the construction of the sub-domains. Two techniques can be employed: either each sub-domain can be constructed from scratch or a serial mesh can be split into the number of required sub-domains. In this work, a serial mesh is split into a number of required sub-domains. The use of an existing mesh is one of the benefits of this decision. In addition, this ensures conformity of the mesh independent of the number of processors utilised in the analysis and removes the requirement of constructing the mesh for each run. Conformity of the mesh allows for comparison between various processor runs which is essential in understanding the speed increase offered by parallelisation.

Standard serial code input consists of a mesh file, boundary flag file, an optional velocity boundary data file, an optional restart file and a parameter file. Before use of the CBS code, the sub-domain specific files must be created.

The serial mesh file is first processed using domain decomposition software. A basic domain decomposition software may be employed in 2D, or for 3D applications using a METIS based domain decomposition software. METIS (also known as Serial Graph Partitioning and Fill-reducing Matrix Ordering) from Karypis Labs, University of Minnesota, utilises a number of algorithms to partition a mesh [105]. ParMETIS is the parallel library implementation of METIS. The METIS library works by introducing a split that minimises the number of shared data points within the domain. The methods employed by METIS do not necessarily produce sub-domains that are contiguous.

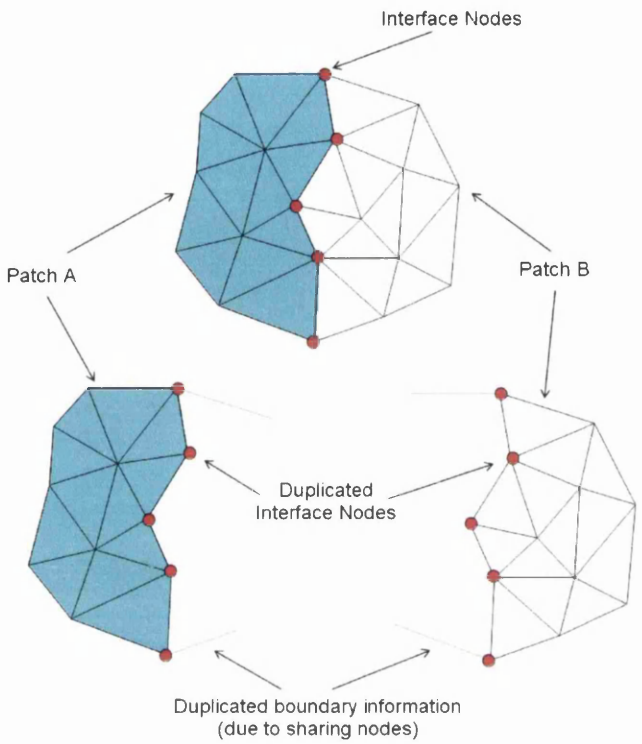

Figure 3.2: Domain Splitting in preparation for the parallel CBS program.

Using the decomposition software, the serial mesh file is divided into individual mesh files that are now specific to each processor or patch. While a serial mesh file would contain information on all nodes, element construction and boundary face information; the individual mesh file contains information on the local nodes, elements and boundaries as well as their corresponding global identities. As well as decomposing the serial mesh file into parallel variants, an additional input file is created for each patch. This is because the parallel implementation requires that certain data be communicated across patches. This input file contains data each patch needs to know on which nodes' information to pass and to which processor. This information must be passed in a specific order. This allows information stored on a local shared node to be passed and collected without recourse to its global identity. The global identity information stored within the patch mesh files is not utilised by the main CBS program and is merely stored for future reconstruction of the global domain at the post-processing stage once computation is finished, and only if required.

In Figure 3.2, an example of domain decomposition is provided for the simplest case. The domain is split into two patches for running in parallel on two processors. Five interface nodes are duplicated across the inter-connected domains. In addition, boundary

information is duplicated where interface nodes are involved. This requirement is due to the boundary information being face based rather than nodal. Each boundary face entry is composed of the face nodes, the element number in which the face resides and a flag to specify what the boundary denotes (e.g. no slip or horizontal velocity = 1 and all others = 0). This is of importance when conflicting boundary face flag information is provided such as in a lid-driven cavity flow problem around the lid corners. In order to maintain concurrency, this boundary information is shared and the program can then determine which boundary flag has dominance. From the initial serial mesh containing 25 elements and 19 nodes, two patches, with 12 nodes each, one containing 12 elements and the other containing 13 elements have been created. While there is now data transfer overhead from the 5 interface nodes, the number of elements has been halved. Although a small increase in the total number of nodes has occurred due to the duplication, this will clearly result in a speed increase for the CBS program. Actual realistic situations are investigated in section 3.7.

Parallel decomposition of the optional velocity boundary data files is also undertaken at the preprocessing stage prior to actual running of the main CBS program. Again, the local patch variant of the velocity file will only contain data relevant to the local patch. The velocity boundary data files contain pointwise data along with global node data. Decomposition of the file leads to a local node list of applicable nodes along with the velocity values for those points. During this stage, the mesh file generated using METIS is supplemented, with the addition of boundary information which is relevant to the local patch (as mentioned in Figure 3.2). The original METIS split separates the serial boundary data and distributes it according to its attached element. Thus, any element residing in patch A with boundary face B will automatically gain boundary data on boundary face B in patch A. Patch C which shares boundary nodes with boundary B will not gain information automatically on boundary B. This stage would also copy the relevant data on boundary B in Patch A to Patch C.

The mesh files produced by METIS also contain information regarding the inter-connected faces in the boundary file. It treats the interface as an external surface, with the boundary flag component of the boundary array detailing the correspondingly connected sub-domain. This information is not required by the CBS program and is discarded. This reduces the size of the initial boundary array information within the parallel CBS code reducing memory and data processing requirements. With these steps complete, the input files are prepared and the main CBS code can be utilised.

3.2.3 Parallel Setup and Information Transfer

In general a parallel program will consist of a master node and a number of slave nodes. The master node will delegate tasks to the slave nodes before collecting the resulting information and passing on to the next stage of the program. However, in the CBS code employed, the master node initialises the slave nodes but all calculations occur on the slave nodes. This reduces the overhead of each task.

The outline of the parallel implementation can be found in Figure 3.3. In this figure, example information transfer commands are highlighted. Information on all MPI subroutines used can be found in Appendix B. Only minimal difference exists between the master node and any slave node, with this difference due to the decision to store certain data parameters in a single file which is only accessed by the master node. In essence, the parallel code performs identically to the serial code with the addition of message transfer at specific points to link the sub-domains. Otherwise the parallel program acts as multiple copies of the serial code each running its own sub-domain problem. The master node was also chosen to output certain data such as convergence rates to file. The master node was chosen because it is the only guaranteed node in use, not because this data was located only on the master node.

The sequence of events undertaken in general form will now be outlined, with data on the pre-processing, processing or post-processing stage given in the following sections. The events specific to the parallel implementation can be found within the respective section.

3.3 Preprocessing

As mentioned previously, a number of input files are read into the program. These input files consist of mesh information, boundary flag data, a parameters file, optional restart file and optional velocity profile data file. With a problem split into a number of sub domains, the relevant files have been prepared for the respective processor. In the case of the turbulence code an additional input file may be read in. This additional file contains the minimum distance to the wall for all nodes within the domain. The restart files option allows for previous data runs to be resumed. These restart files are generated at the end of the processing loop, and are local to the individual patch. Thus, in serial only one restart file would be created, but in parallel N number of files would be generated for N number of processors. These restart files contain data on

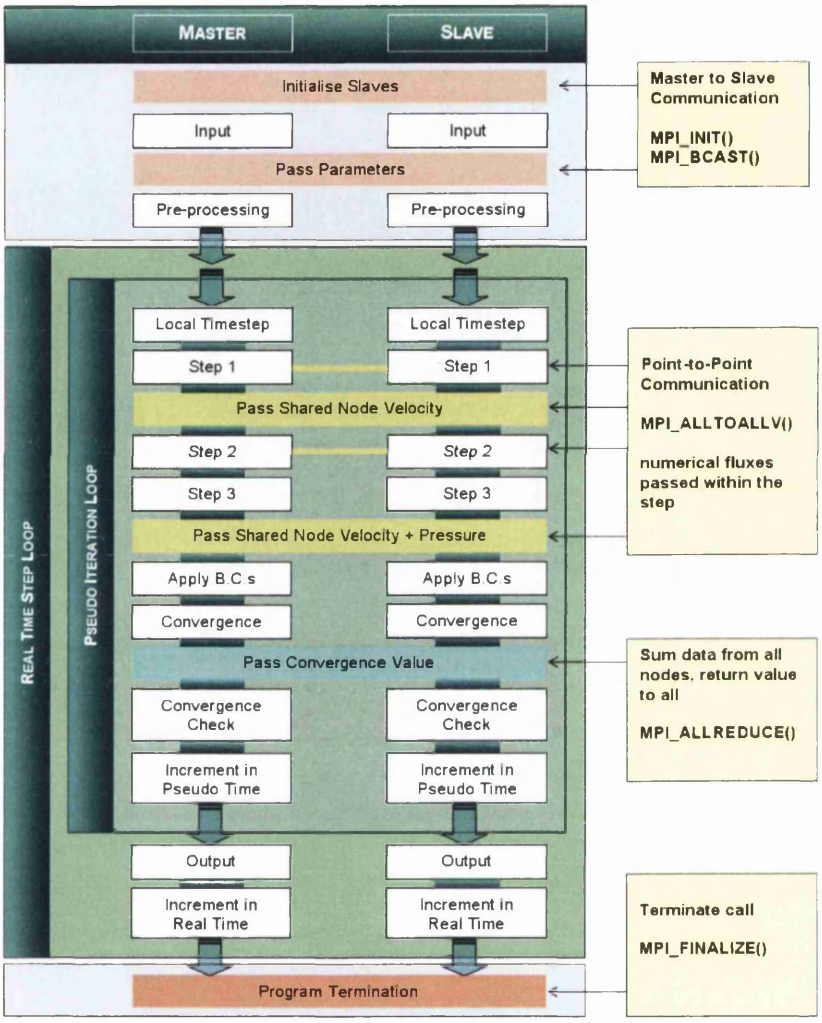

Figure 3.3: Parallel implementation within the CBS (laminar) program

the variables for the previous N real time steps (for transient problems). The value of N is equal to the order of the backward difference formula employed. This setup avoids communication transfer by keeping data needed by a processor localised to the processor.

In a serial code, if an input file is incomplete or missing, the program can terminate either by design or by compiler error detection. In parallel this must be designed into the program. There are several different cases of potential errors. In case 1, an optional file such as a restart or velocity boundary file is only available to some processors. Thus information must be passed to ensure conformity, e.g. the number of velocity profiles matches between domains. In case 2, a more serious fault occurs when an end-of-file is

reached unexpectedly in one patch. Without an error passing mechanism the parallel program would segment due to the remaining processors continuing onwards until the next MPI call. At this point they would then wait for the processor patch which would never get to that stage. In case 3, all processors have the required files but more sub-domains exist than there are allocated processors. All three cases require the program to terminate successfully. Therefore, while a serial code can avoid explicit error detection, a parallel version requires more explicit checks at various stages within the preprocessing stage of the codes.

The remaining input files, namely the boundary flag information and parameters file (small data files) are not decomposed. Instead these files are read in only by Processor 1 and distributed to the remaining processors. This has the benefit of allowing easy modification of these files without needing to replicate data. Parameters listed within the parameters file include information on free stream values along with time step information and program enabling options.

When input of data is complete, arrays are initialised and filled with initial values if the restart file is unavailable. In the next stage, boundary face information is then processed. Here the process splits the boundary face array into a point array and a boundary side function specific array. This allows the processing stage to run with greater efficiency. It is during this splitting that boundary information flags are analysed to determine which is appropriate for every point, i.e. in the situation of conflicting information due to two different flags being applicable to the same node. The side function specific array is required for situations such as the Windkessel model and symmetric boundary conditions. In order to apply this array as a boundary condition, it is necessary to communicate a small amount of information at the pre-processing stage. An example of such data would be the area of the tagged Windkessel boundary, in order to establish the total area of the outlet in question. In both the point based array and the side function array, the boundary flag codes are collated into two arrays, with their size dependent upon the number of flags employed. These two tiny arrays control access to the larger arrays, further reducing computational cost.

Following boundary definition within the program, the variables are non-dimensionalised (see Section 2.2.1) using data from the parameter file. Prior to the processing stage, a number of calculations may be undertaken within the pre-processing stage due to the Eulerian framework employed. These calculations can be undertaken using a loop-over-element type situation in the case of determination of the elemental shape function derivatives and calculation of the directional cosine components of each element face normal (along with it's respective area or length depending on 2D/3D). As such,

these variables are stored (albeit separately) in element arrays. Other calculations are undertaken in a loop-over-element style but also include the loop-over-point manner. These calculations include determination of the lumped-mass matrix and local element size, and as such requires communication between neighbouring sub-domains. These values are stored in nodal arrays (local element size) or elemental arrays (lumped mass matrix).

If the turbulent version of the code is implemented then additional calculation may be required to determine the shortest distance to the wall for each node. After initial calculation, these values are stored (dimensionalised) within a file, such that it is only necessary to calculate these values once. Calculation within the parallel implementation requires a degree of communication across all patches in order to gather data on all wall nodes. Parallel implementation increases the speed of calculation for this task by only needing to check its local nodes. This check loops over all non-wall nodes within the local domain and checks all wall nodes to determine the shortest distance. Wall nodes are immediately designated as having zero distance to the wall. There are better and faster ways of calculating wall distance. However, for the sake of simplicity this direct method is utilised.

The final task of the pre-processing component of the CBS code is initialisation of any additional arrays needed within the processing component and determination of which nodes to count when considering the convergence check. The necessity of the nodal count is due to parallel implementation. With a serial code all nodes would be counted, however in parallel, interface nodes have been duplicated, thus, one of the copies must be ignored in order to maintain consistency, independent of the number of processors employed.

3.4 Processing

This is the main component of the CBS program and the section that consumes the vast percentage of runtime. Due to the nature of the CBS-AC scheme, this section is comprised of two timestepping loops. For an outline of the processing stage, the reader is referred to Figure 3.3. The first (outer) loop concerns the real-time step which contains the second (inner) pseudo-time step loop. This pseudo-time step acts as iterative looping until a local steady-state convergence check tolerance is achieved before proceeding either to the next real-time step or to the completion of the CBS code.

The first task within the iterative loop concerns the reallocation of variables. Old values of the pressure and velocity components from the previous iterative loop are transferred from their respective current storage array into the designated old values array. These arrays are nodal based. Once complete, the calculations for the current iterative cycle can begin. The local time step value for each node is determined using values from the previous pseudo time step.

The intermediate velocity field can then be determined in Step 1. Step 1 begins with the determination of the numerical flux values for the diffusion which requires point-to-point message transfer. The convective component of the numerical flux may be determined locally, without message transfer. It then proceeds on an element-by-element basis storing the element value of the solution within the velocity variable nodal array. Once all elements are processed, simple averaging is undertaken to produce a global solution. This involves data transfer of the shared nodes between sub-domains.

With the global solution of the intermediate velocity established, Step 2 and the determination of the pressure field is undertaken. Again, the numerical flux must be determined prior to the element-by-element solution process. At the end of Step 2 pressure boundary conditions are optionally employed, an example of which is the Windkessel boundary condition.

Step 3 is the final part of the laminar CBS scheme, and works in the manner outlined in Steps 1 and 2. During this step, the intermediate velocity field is corrected and updated. Velocity specific boundary conditions (b.c.) are imposed after Step 3. These boundary conditions can consist of symmetrical b.c., Womersley velocity profiles or static b.c. such as no-slip conditions.

An additional step, Step 4, is undertaken within the turbulent variant of the CBS code employed. This step requires the determination of the turbulence transport equation. After Step 4, turbulence specific boundary conditions are imposed. These boundary conditions require the code to determine, using the velocity, which nodes are acting as an inlet point. In the case of imposed Womersley profiles, this may be determined once per real-time step, and stored in a suitable nodal array.

Once all the steps outlined above have been undertaken a steady-state convergence check is necessary to determine whether the iterative cycle is complete. This check is performed by calculation of an L_2 norm of the velocity. Individual sub-domain values are determined for the summations, before this information is exchanged. This allows the convergence check value to be determined locally while representing the global value. As

such, each individual processor can then determine whether to proceed to the next real-time step or begin the next iterative cycle. The convergence check process is outlined in Equations 3.1 to 3.3

$$h_k = \sum_{i=1}^{N} (U_i^{n+1} - U_i^n)^2 \tag{3.1}$$

$$g_k = \sum_{i=1}^{N} (U_i^{n+1})^2 \tag{3.2}$$

$$L_2 = \sqrt{\frac{\sum_{k=1}^{Np} h_k}{\sum_{k=1}^{Np} g_k}} \tag{3.3}$$

where k represents the processor patch number, N the local number of nodes to be counted, Np the number of processors and h_k and g_k represent individual patch summations for the L_2 norm components. Therefore, each processor will determine its individual h_k and g_k component and Equation 3.3 is then used.

If the convergence tolerance has been achieved, then the iterative cycle is complete for the real-time step under consideration. Therefore the data (pressure, velocity and turbulence variable) is output to a data file for future post-processing. Optional output includes the generation of restart files which contain the data from the previous two completed real-time cycles. As mentioned, each output file is local to the patch and unique within the global context. This avoids the complications of parallel output to a single storage file through additional MPI routines.

The final task within each real-time step loop is the reallocation of the velocity and turbulence variables in order to store the previous cycle's data. If the number of real-time steps required is reached then the program will terminate, otherwise a new iterative cycle will begin.

3.5 Post-Processing

In order to provide flexibility, post-processing of the calculated variables (velocity, pressure, turbulence) is undertaken by a separate program once the CBS code has been completed. Post-processing is undertaken by reading in the previously stored data. In this manner, the data can be stored in binary format which reduces the

storage requirements. Post-processing enables the output of data in a format suitable for visualisation and determination of required derived variables such as haemodynamic wall parameters, drag coefficient etc. Post-processing was also implemented in the same parallel manner.

3.6 Run-Time analysis of the LCG method

With the LCG variant of the CBS-AC scheme outlined, this section provides information regarding the influence of employing the locally conservative Galerkin method. This method has the advantage of explicit variable and flux conservation between elements. This advantage requires a small post-processing stage to recover continuous nodal solutions for the flux. Work by Thomas *et al* 2008 [65] examined LCG execution times in comparison to the global Galerkin (GG) method for the pure diffusion problem, finding implicit LCG to be the most rapid. Comparing the explicit LCG to explicit GG variants, it was found that explicit GG provided a more rapid technique. However, with the small computational times (0.09 seconds Vs 0.06 seconds in one case), computational access/transfer times could have had an undue influence.

In order to test the LCG variant of the CBS-AC scheme, the lid-driven cavity flow problem for $Re = 100$ is examined. A two-dimensional unstructured mesh consisting of 2667 linear triangular elements and 1401 nodes was used (Figure 3.4). The time taken to converge to the steady state solution for both methods in given in Table 3.1. Two systems were utilised to ensure the results were compiler and environment independent. The first system consisted of the linux operating system, Intel FORTRAN compiler and Intel Xeon Quad-core 3.6Ghz processor, the second system consisted of the windows operating system, Compaq FORTRAN compiler and Intel Quad-core 3Ghz processor. In each case the test was repeated 5 times to ensure reproducibility of the results. A total of 2100 iterations are required to achieve the prescribed convergence tolerance. The median run time values are given in graphical form in Figure 3.5.

From the table, it is apparent within each test variant, there is conformity in the run time duration. It is also clear that the system chosen influences the outcome of this test, which indicates that the run time of both methods is relatively similar as shown in Figure 3.5. This can be explained via the way in which the construction of the LCG program is carried out. Additional computations are minimised within the LCG method by storing additional information. Prior to the start of each step, the elemental values of the flux are determined. These are then averaged to produce nodal values. The elemental calculation

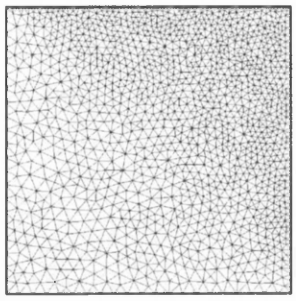

Figure 3.4: Test case mesh for GG Vs LCG run time duration analysis

Run	System	Method	Time (s)
1	1	GG	7.595969
2	1	GG	7.596415
3	1	GG	7.581628
4	1	GG	7.612094
5	1	GG	7.592439
1	2	GG	8.296875
2	2	GG	8.296875
3	2	GG	8.328125
4	2	GG	8.312500
5	2	GG	8.328125
1	1	LCG	8.156205
2	1	LCG	8.163457
3	1	LCG	8.162019
4	1	LCG	8.168987
5	1	LCG	8.156018
1	2	LCG	7.656250
2	2	LCG	7.609375
3	2	LCG	7.640625
4	2	LCG	7.609375
5	2	LCG	7.593750

Table 3.1: Test 1. Run time comparison between the LCG method and the GG method

is required by both the LCG and GG methods within the element *do-loop*, thus the only difference is the determination of the nodal values. However, when considering the convection and diffusion components of Step 1, the nodal values can be combined during the nodal flux averaging stage, avoiding this step which must be undertaken within the GG elemental do-loop. It is this trade-off of reducing calculations within the element do-loop for the LCG method relative to the GG loop, while adding and averaging of elemental values, which results in similar run times. Memory array storage may also play a small role due to the element-by-element nature of the LCG method versus the global assembly of the global Galerkin method. The simple averaging step to establish a

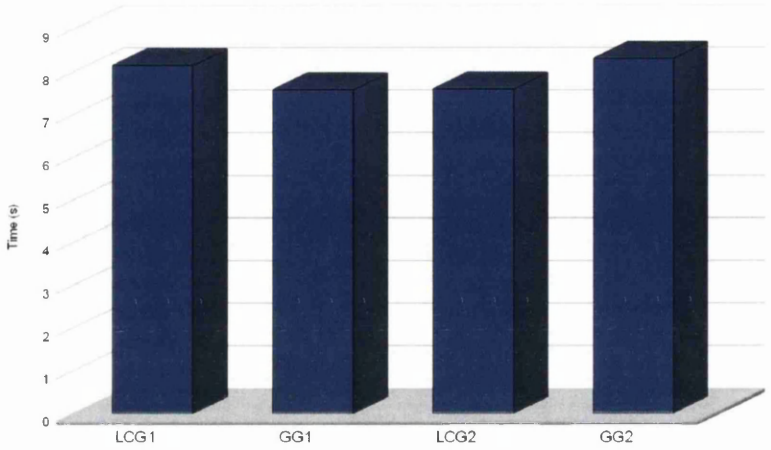

Figure 3.5: LCG and GG Run time durations

continuous solution across the domain in the LCG method is comparable, computational wise, to the global solution phase of the GG method. It is important to note here that in the LCG method, only one operation is performed per node in comparison to three operations per node in the GG method.

A second problem is examined in order to check mesh influence on the test. The domain in this test consisted of a structured mesh of 28,800 linear triangular elements and 14,641 nodes. Within the processing stage of the CBS code 500 pseudo iterations are completed. The results for the test are given in Table 3.2. The same two systems are used in this test.

From Table 3.2 it is clear that the results of the second test are in agreement with the findings from the first test. Thus, increasing the number of elements within the domain by a factor of ten has not altered the outcome. Performance can be further improved within the LCG CBS scheme through the bandwidth optimisation of array specification for the element-by-element solution approach.

3.7 Parallel Run-Time and Optimisation

In order to validate the parallel implementation, a comparison was made between calculated variables from the serial and parallel implementations. This was achieved by utilisation of a program to read the corresponding output files and determine the maximum difference between the two implementations for each variable. From this analysis it was determined that both implementations produced identical solutions

Run	System	Method	Time (s)
1	1	GG	20.289278
2	1	GG	20.269228
3	1	GG	20.256045
4	1	GG	20.484112
5	1	GG	20.299036
1	2	GG	21.468750
2	2	GG	21.437500
3	2	GG	21.437500
4	2	GG	21.437500
5	2	GG	21.468750
1	1	LCG	21.981202
2	1	LCG	21.824658
3	1	LCG	21.869068
4	1	LCG	21.958441
5	1	LCG	21.826935
1	2	LCG	19.406250
2	2	LCG	19.390625
3	2	LCG	19.406250
4	2	LCG	19.359375
5	2	LCG	19.390625

Table 3.2: Test 2. Run time comparison between the LCG method and the GG method.

to within 1×10^{-10} orders of magnitude. This is expected due to truncation errors experienced during the respective calculations.

In order to achieve optimal usage of the code, work was undertaken at the Barcelona Supercomputing Center, Spain. Optimisation and run-time analysis was undertaken using CEPBA Tools [106]. These tools consist of both instrumentation and visualisation tools for analysis purposes. Paraver was utilised as a performance visualiser based on traces generated when running the CBS code. Performance analysis was undertaken on both the local computations within the code and message transfer protocols. This analysis indicated that the code was performing admirably, with no single processor performing excessive calculation which would cause the remaining processors to remain idle. This load balancing is essential in order to achieve a suitable speed increase. In addition, use of CEPBA Tools resulted in a reorganisation of storage arrays which together with some minor algorithm improvements reduced the calculation time. This increased the speed of the code by 6% in the laminar case and 13% in the turbulent version.

While the load balancing of the program itself is suitable, the program is highly dependent on the domain decomposition of the mesh. Thus the CBS code is dependent

Processor	Time (s)	Total Shared Nodes	Max Shared Nodes (%)	Speedup (%)	Efficiency (%)
1	157.055	0	0.0	100.0	100.0
2	79.154	121	1.6	198.4	99.2
4	40.044	241	3.3	392.2	98.1

Table 3.3: Run time analysis for the Intel quad-core machine.

upon METIS. In order to investigate the potential speed increase by utilising parallel processing, three meshes are investigated.

The first mesh consists of a regular structured mesh in two dimensions consisting of 28,800 linear triangular elements and 14,641 nodes. This mesh was chosen since optimal load balancing can be achieved through equal partition of the mesh. In order to assess the scalability of the software on multiple architectures, this analysis was performed on multiple systems. The first system considered consisted of a quad-core Intel Q9600 3Ghz machine with 4GB of RAM. This system allows for investigation on a system of shared memory rather than distributed memory. The test was undertaken in the linux system environment using the Intel FORTRAN compiler. Parallel run times were investigated for 2 and 4 processors, and compared to serial data runs. In order to assess the speed up from parallelisation, the time taken to undertake pre-processing and processing (which involved 5,000 iterations and data output to file) was recorded. Five data runs were undertaken in each case, with the median value recorded in Table 3.3. This data is represented in graphical form in Figure 3.6.

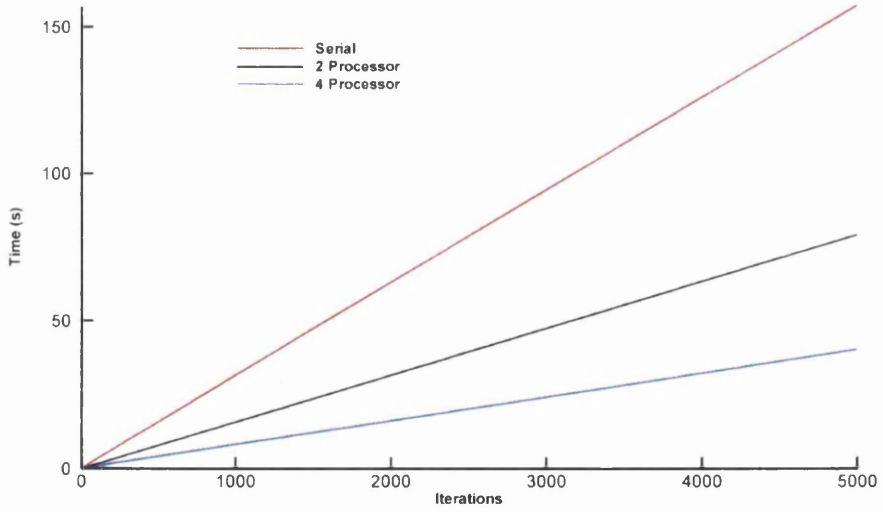

Figure 3.6: Run time duration for the Intel Quad-core Computer.

From the table, it can be clearly seen that near linear speed up occurs when increasing

Processor	Time (s)	Total Shared Nodes	Max Shared (%) Nodes (%)	Speedup (%)	Efficiency (%)
1	276.445	0	0.0	100.0	100.0
2	138.269	121	1.6	199.9	100.0
4	70.528	241	3.3	392.0	98.0
8	35.011	481	8.2	789.6	98.7
16	17.727	717	13.3	1559.5	97.5
32	10.023	1189	19.8	2758.1	86.2

Table 3.4: Run time analysis for the AMD Athlon Cluster.

the number of processors. Included within the table is information on the total number of shared nodes within the domain, along with the maximum percentage of shared nodes within a local sub-domain. From these values, it can be seen that efficiency decreases marginally with increasing inter-patch communication. However, in order to fully assess parallel impact more data points are required. The second architecture employed consists of distributed memory machines with up to 32 2Ghz AMD Athlon processors arranged within a small linux cluster. Intel FORTRAN compilers were again employed.

From the run time durations in Table 3.4 the CBS code speed up is close to linear until information transfer becomes excessive, in this case for the 32 processor run. In the 32 processor run, the increase in computational resources is offset by a diminished return. Not only is communication a factor, but also since shared nodes are duplicated by definition, additional calculation must be undertaken compared to the serial case. Due to the inclusion of the preprocessing stage and output of information to file within the timed analysis, it is possible to conclude that the parallel arrangement of these components is suitable and does not hinder the parallel efficiency of the code. From the efficiency results that was obtained from the cluster durations and the Intel quad-core, the influence of shared vs distributed memory is minimal.

The second test of the parallelisation technique consists of a more realistic scenario. A three dimensional unstructured mesh of a patient-specific aorta was decomposed into a number of patches. The original (serial) mesh consisted of 475,637 linear tetrahedral elements and 89,753 nodes. The observed run time durations for one, four, eight, sixteen and thirty two processors are recorded in Table 3.6 and represented graphically in Figure 3.7. The maximum shared percentage S_p is calculated using the following equation,

$$S_p = max\left(P_{comm}/P_{node}\right)_i \qquad \text{wherei} = 1, \text{N} \tag{3.4}$$

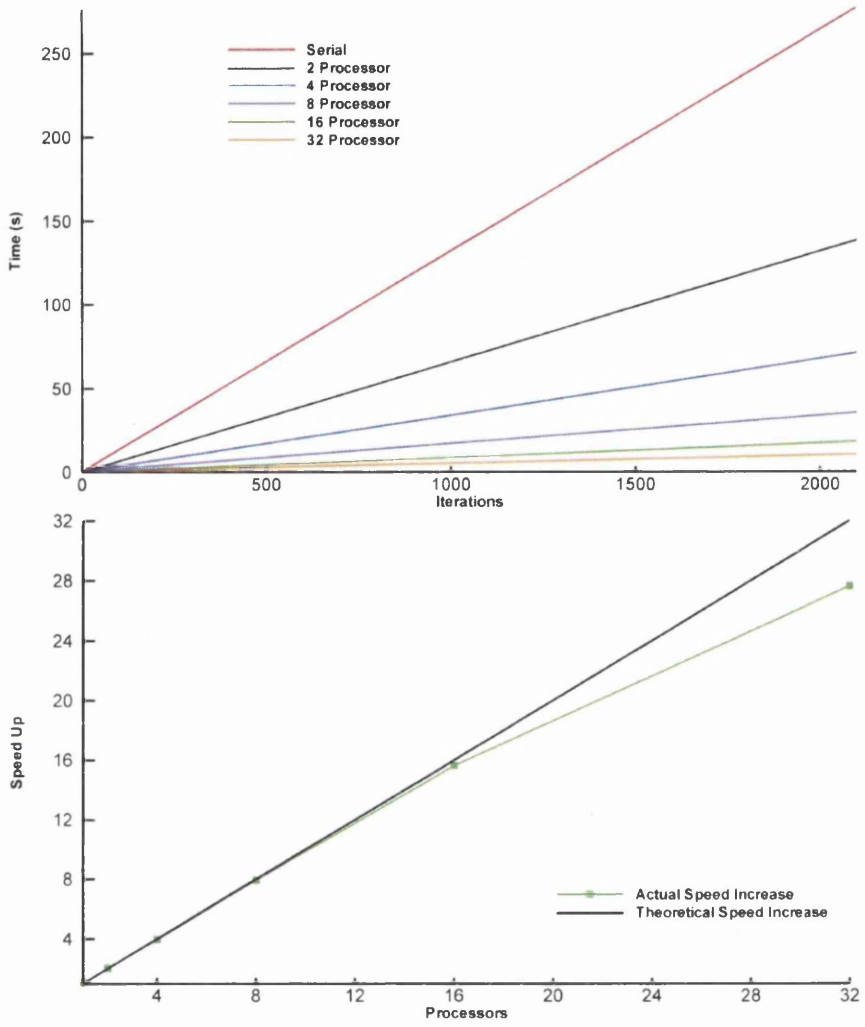

Figure 3.7: Run time duration for the AMD Athlon Cluster.

where N represents the the total number of patches, P_{comm} the number of interface nodes within the patch and P_{node} the total number of nodes within the patch. The recorded time duration includes 500 iterations within the processing stage, the convergence check was undertaken every ten iterations. In order to provide an understanding of METIS based domain decomposition, the patch distribution for varying processor totals is given in Figure 3.8 and the number of elements per patch is given in Table 3.5. The patch with the most elements is highlighted in dark grey and the patch containing the least number of elements in light grey. The range can be calculated simply as the difference between these two numbers. The number of wasted units W is calculated using

$$W = \sum_{i=1}^{N} (P_{max} - P_i) \tag{3.5}$$

where P_{max} denotes the maximum number of elements within the patches and P_i the number of elements in patch i. The maximum percentage of wasted units is calculated by $100 \times (P_{min}/W)$ where P_{min} represents the minimum number of elements within the patches.

Figure 3.8: Parallel Test 2. METIS decomposition of the aorta for each parallel run. a) 4 Patch b) 8 Patch c) 16 Patch d) 32 Patch

In Figure 3.8, alternating colours are used to represent different patches within the

Processor	4 Patch	8 Patch	16 Patch	32 Patch
1	105085	59276	30008	15150
2	122880	60089	29648	15469
3	121391	61699	30566	14428
4	126281	60307	29853	14794
5		57713	29577	15403
6		60497	30886	15214
7		52512	30018	14900
8		63544	29504	14503
9			24747	12803
10			30004	14454
11			30439	14505
12			30712	15143
13			30912	13409
14			27457	15599
15			31225	13546
16			30081	16284
17				15304
18				14634
19				15286
20				15352
21				15113
22				15450
23				15666
24				15921
25				15338
26				15486
27				15390
28				15425
29				15060
30				11320
31				13760
32				15528
Range	21196	11032	6478	4964
Wasted Units	29487	32715	23963	45451
Max Wasted Unit (%)	71.9	33.7	27.0	10.9

Table 3.5: Number of elements per patch for each parallel run in the aorta test case.

Processor	Time (s)	Total Shared Nodes	Max Shared Nodes (%)	Speedup (%)	Efficiency (%)
1	1645.162	0	0.0	100.0	100.0
4	527.786	2311	7.8	311.7	77.9
8	222.327	5527	15.9	740.0	92.5
16	81.119	11619	33.1	2028.1	126.8
32	38.531	19177	52.0	4269.7	133.4

Table 3.6: Run time analysis for aorta on the AMD Athlon Cluster.

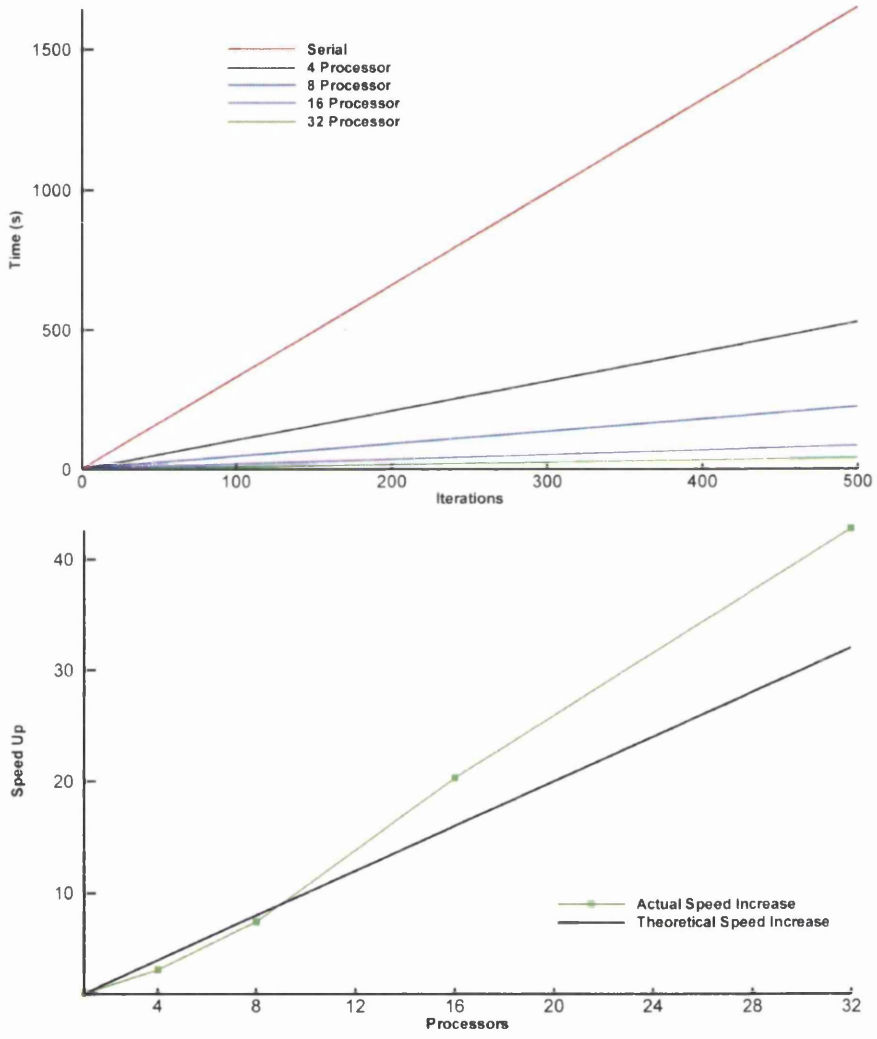

Figure 3.9: Parallel Test 2. Parallel implementation on a patient-specific aorta a) Run time duration b) Speed Increase

domain. In this case there are no divided sub-domains within the domain and any colour repetition denotes different processor patches. From this figure, and Table 3.5, it is clear

that METIS, while minimising shared nodes, can partition meshes such that one or more patches contains a markedly smaller number of elements (and nodes) than the remaining patches. In the table, the range in the local number of elements is examined. Comparison of these values with the run time efficiencies in Table 3.6 does not provide any insight. However, if it is assumed that each element is worth one computational unit then it is possible to determine the number of wasted units. The processor with the highest number of elements will take longer than a patch with smaller number of elements. This difference represents that processor's idle time or wasted units. The number of elements has been examined here as loop-by-element forms the majority of the computational cost. They are therefore a good indicator of true idle times within each processor. In general,the total number of wasted units increases with the number of processors which would be expected. This is due to even small variations causing a greater number of processors to become idle. However, in the sixteen processor run a markedly smaller number of wasted units occurs. Although as an average per processor, the number of wasted units is almost identical to the thirty two processor run. Examination of the allocation of these wasted units over the patches reveals that these wasted units are more adversely affected when the processor numbers are smaller. In the four processor case 71.9% of the wasted units occur within one of the processors. In contrast, in the thirty two processor run a maximum of 10.9% of the wasted units occur within one processor. This is a clear issue of load balancing and its resulting impact on the run time durations. The smaller wastage percentages indicate improved load balancing. With improved load balancing, as the number of processors is refined, greater than linear speed up has occurred in the sixteen and thirty two processor cases, as clearly shown in Figure 3.9(b). This is due to the memory speed up efficiencies mentioned previously in Section 3.2.1. From Table 3.6, it can be seen that in a three dimensional case, information transfer has increased (up to 52% of local patch nodal information transferred). However, this increase has not influenced run time efficiency. This is due to the loop-over-element components dominating. Since it is clear that METIS based decomposition has a strong influence on overall parallel processing efficiency, a third parallel test has been undertaken.

The third test consisted of a larger problem which allowed higher scaling tests to be performed. A three dimensional mesh of a patient-specific human carotid artery was decomposed using a METIS based partitioner. This unstructured mesh consists of 5,672,955 linear tetrahedral elements and 973,010 nodes. For this test, run time duration was defined as the preprocessing and processing stages, with 600 iterations being conducted within the processing component. The computing facilities (MareNostrum) available to the Barcelona Supercomputing Center were used for this analysis. The

machine architecture consisted of an IBM BladeCentre JS21 Cluster containing dual core IBM PowerPC 970MP 2.3Ghz processors (10,240 CPU's in total). The code was compiled using the IBM FORTRAN compiler. The METIS decomposed patch distribution is given in Figure 3.10 for the 16, 32, 64 and 256 partitioned patches. From the figure it is initially clear to see that the partitioner is minimising communication transfer through the choice of cuts employed. As the number of partitions increases the choices for the location of the necessary cuts is no longer clear and reliance is placed on the decomposition algorithm. The run time data can be found in Table 3.7 and Figure 3.11.

Figure 3.10: Parallel Test 3. METIS decomposition of the carotid for the parallel runs. a) 16 Patch b) 32 Patch c) 64 Patch d) 256 Patch

From the table, it can be seen that information transfer has further increased (up to

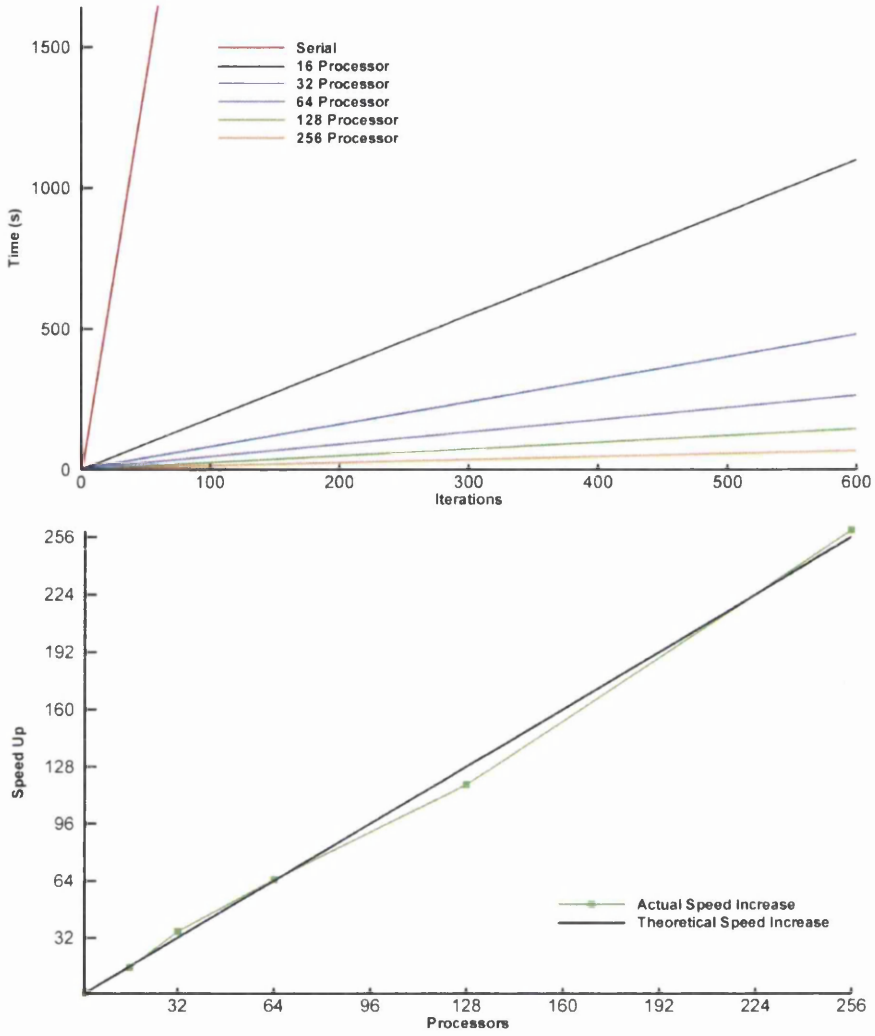

Figure 3.11: Parallel Test 3. Patient-specific carotid on the MareNostrum Supercomputer a) Run time duration b) Speed Increase

85% of local patch nodal information transferred). However, this increase has still not influenced run time efficiency and loop-over-element components remain dominant. Hence, the variations in run time efficiency are likely due to load balancing effects, rather than excessive message transfer! A speed up greater than linear is observed in half the recorded values, with general linear scaling evident in Figure 3.11(b). The serial result in Figure 3.11(a) has been ignored in order to allow suitable scaling to visualise the parallel runs. From the figure it is clear that a timely solution can be returned as the number of processors increases.

From the multiple architecture testing that employed both two dimensional and three

Processor	Time (s)	Total Shared Nodes	Max Shared (%) Nodes (%)	Speedup (%)	Efficiency (%)
1	16844.211	0	0.0	100.0	100.0
16	1099.138	55,087	17.3	1532.5	95.8
32	478.181	90,231	26.6	3522.6	110.1
64	261.692	144,202	43.2	6436.7	100.6
128	143.325	200,166	55.3	11752.5	91.8
256	64.934	264,648	85.7	25940.5	101.3

Table 3.7: Run time analysis for the MareNostrum.

dimensional meshes, the scaling efficiency of the code using parallelisation is virtually linear with increasing number of processors.

3.8 Summary

The outline of the implementation of the computational algorithm has been presented in this chapter for the preprocessing, processing and post-processing components of the code. In order to allow timely solutions to problems such as patient-specific blood flow modelling, a technique for the parallelisation of the serial code was introduced. The parallelisation scheme outlined allowed the CBS code to scale linearly as the number of processors was increased. The code has been tested on the MareNostrum supercomputer in order to confirm this scaling up to 256 processors. The author believes that this scaling to continue to higher number of processors although these have not been tested. A number of factors influence the scalability of the CBS code and thus it was noted that a limit of diminishing returns can affect this scaling when considering too large processor numbers on a relatively small mesh. The use of a METIS based domain decomposition method on unstructured meshes means that the choice of the number of sub-domains can influence the scaling of the code. From testing, it is clear that, while suitable to produce linear scaling, the METIS based method can have adverse load balancing issues. These issues are mesh and processor number dependent, although a configuration can be tested prior to usage if optimum scaling is required. While load balancing could be a small issue, a speed up is still encountered in every case outlined. The best efficiency encountered was 133%, altogether only one result was less than 92% in all of the three dimensional runs. Keeping the amount of information transferred to a minimum can increase speed up efficiency although this effect is dependent upon the relative weight of the computational cost of internal patch calculation.

Chapter 4

Test Cases

4.1 Introduction

In this chapter the locally conservative Galerkin (LCG) method is applied to a number of problems for which the solution is known. This allows for a rigourous assessment of the performance of the outlined explicit LCG-CBS scheme in both two and three dimensional problems. The first is that of the steady state problem of incompressible fluid flow within a lid-driven cavity. A lid-driven cavity problem is investigated over a range of Reynolds numbers ($0 \leq \mathrm{Re} \leq 5000$) for a two dimensional problem before analysis is undertaken upon a three dimensional mesh. The results from the LCG scheme are compared to both experimental benchmark data [1] and to the continuous or global Galerkin (GG) method.

The second problem investigated to assess the transient behaviour of the LCG scheme is that of transient incompressible flow past a cylinder for a Reynolds number of 100. This problem was modelled in two dimensions. This is a well known problem that is widely used for the assessment of numerical methods. In order to assess the performance of the LCG method, the solution from this problem is compared to the results obtained from the global Galerkin method.

The third problem is that of transient flow within a three dimensional pipe. This test is similar to the modelling conditions applied to a patient-specific problem in later chapters. A Womersley profile is applied to both the inlet and outlet. The results from the LCG scheme are compared to those of the GG scheme. The final problem is that of turbulent flow past a backward facing step at a Reynolds number of 3025. This problem

is utilised to assess the SA turbulence model incorporated within the LCG-CBS scheme. The results are compared to those of the continuous Galerkin method.

4.2 Lid-Driven Cavity Flow

The problem considered is the incompressible fluid flow in a lid-driven cavity. This problem is a standard test case and comparison of the velocity profiles can be made with well known benchmark data [1]. The cavity geometry is defined as a square (2D) or cube (3D) with unit length. No-slip boundary conditions are applied to the left, right and bottom walls and the flow inside the cavity is generated by the motion of the top surface, which travels in the horizontal direction. In the three dimensional case, the two remaining walls are subjected to a symmetrical boundary condition. The three dimensional geometrical and boundary conditions are given in Figure 4.1 along with the two and three dimensional meshes used. The two dimensional mesh consists of 10,596 linear triangular elements and 5,515 nodes, while the three dimensional mesh consists of 514,297 linear tetrahedral elements and 92,405 nodes. Both contain refinement around the solid walls.

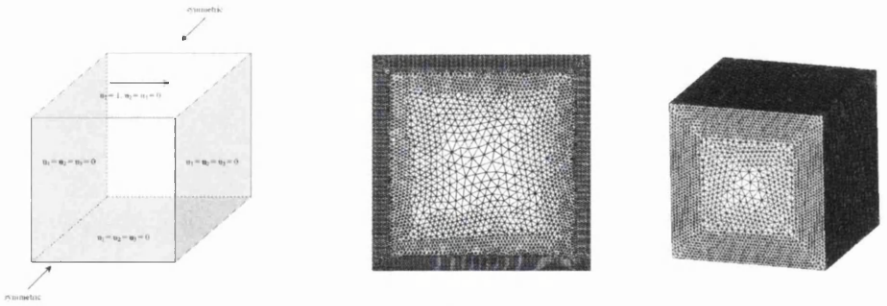

(a) Geometry and boundary conditions (b) 2D Mesh (c) 3D Mesh

Figure 4.1: Flow in a lid-driven cavity

The two dimensional lid-driven cavity problem is investigated for Re = 100, 1000, 3200 and 5000. The qualitative results are given in Figure 4.2 and 4.3. The pressure distribution is given in Figure 4.2 for the four Reynolds cases and Streamtrace plots are given in Figure 4.3. The contours are generally smooth and without oscillations.

To provide a quantitative evaluation of the performance of the LCG scheme, the horizontal velocity component u_1 along the vertical centreline and the vertical velocity component u_2 along the horizontal centreline are compared with the benchmark solution

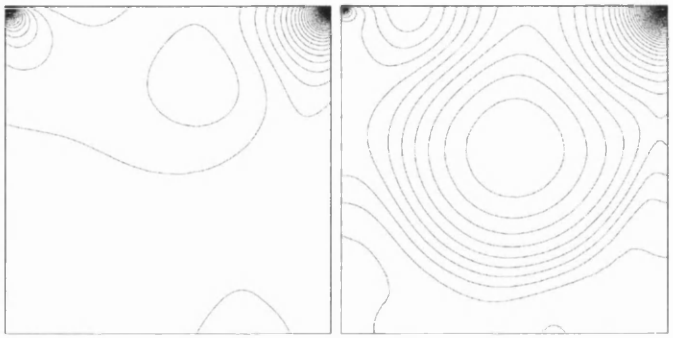

(a) $Re = 100$ (b) $Re = 1000$

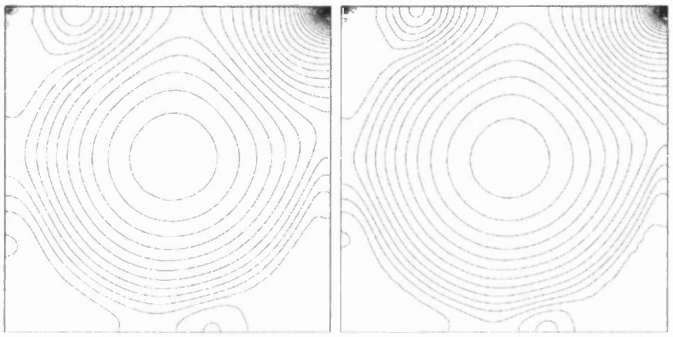

(c) $Re = 3200$ (d) $Re = 5000$

Figure 4.2: Flow in a lid-driven cavity. Pressure contours

by Ghia *et al* [1]. The quantitative evaluation for the chosen Reynolds numbers are given in Figures 4.4 and 4.5. From the figures, it is clear that excellent agreement is obtained between the LCG and GG schemes and there is good agreement between the numerical and benchmark solutions.

Figure 4.6 shows the results obtained for the three dimensional lid-driven cavity flow problem at a Reynolds number of 400. Figure 4.6(a) shows the comparison of the u_1 velocity distribution along the mid-vertical line with the numerical benchmark solution of Ghia et al [1]. It can be seen that the LCG results obtained are in excellent agreement with the benchmark solution. Figure 4.6(b) shows the comparison of the u_3 velocity distribution along the mid-horizontal line with the benchmark solution and it is also in excellent agreement with the benchmark solution.

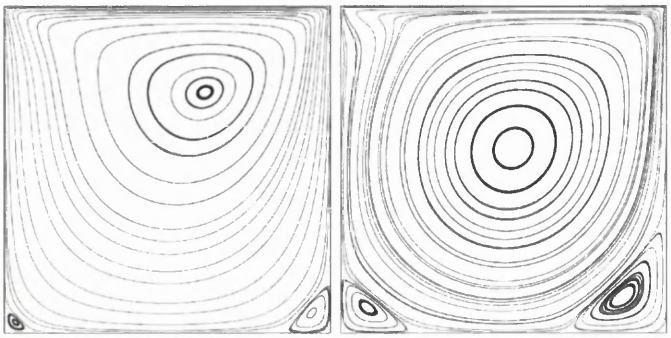

(a) $Re = 100$ (b) $Re = 1000$

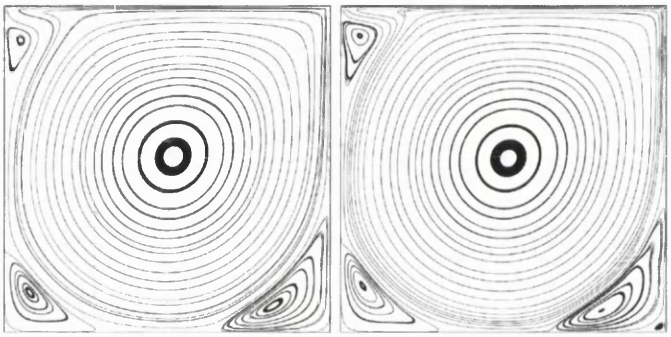

(c) $Re = 3200$ (d) $Re = 5000$

Figure 4.3: Flow in a lid-driven cavity. Streamtrace Contours

4.3 Flow around a cylinder Re=100

This two dimensional problem is a popular test case for validating the transient part of numerical schemes [77–79, 83, 107, 108]. Problem geometry and boundary conditions can be found in Figure (4.7). The computational domain is $16D$ in length and $8D$ in width. The cylinder centroid is located at a distance of $4D$ from the inlet and along the horizontal centre line. At the inlet boundary, the horizontal and vertical velocity components are prescribed as unity and zero respectively. At the outlet boundary, the pressure is specified as zero. Slip conditions are imposed at the top and bottom of the domain. No-slip conditions are prescribed on the cylinder. Initial horizontal velocity is unity and both the initial vertical velocity and pressure are zero. A single unstructured mesh was used in this study. It contains 19,650 linear triangular elements and 9988 nodes. This mesh has been designed using previous knowledge on the formation of the unsteady wake and subsequent vortex shedding to refine specific regions [109, 110]. The real time-step size utilised is 0.1 and simulations were carried out to a real non-dimensional time of 200.

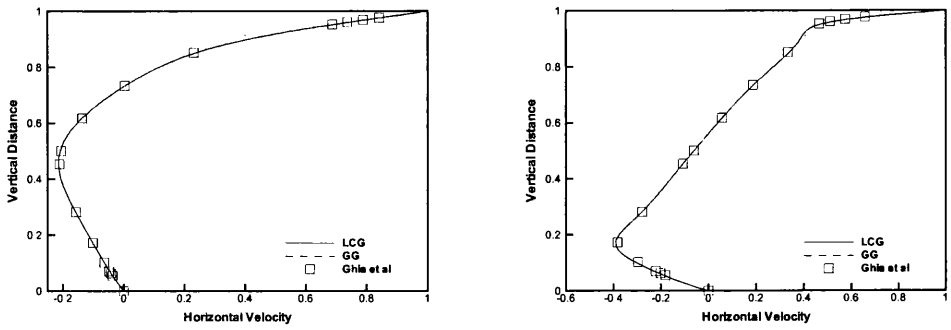

(a) $Re = 100$ (b) $Re = 1000$

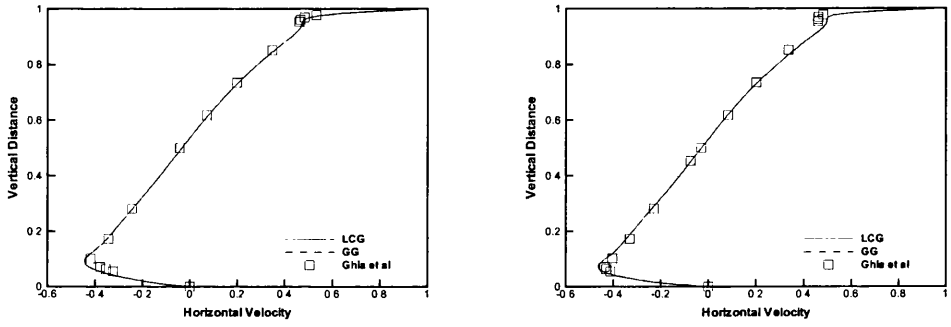

(c) $Re = 3200$ (d) $Re = 5000$

Figure 4.4: Flow in a lid-driven cavity. Comparison with Ghia *et al* [1] of u_1 velocity distribution along the vertical centreline

The distribution of the velocity components u_1 and u_2 along with the pressure p are given in Figure 4.8 for the non-dimensional time instance of 150. A quantitative analysis is given in Figure 4.9. Here, the real-time history of the lift and drag coefficients are presented, along with the variation of the vertical velocity component at the central exit point. Examining in detail the real time interval of $130 < t < 150$, the GG results are included for comparison. The three parameters demonstrate excellent agreement between the LCG and GG methods. Both methods predicted a Strouhal number of 0.17088, which has an error of 2.5% compared to the experimental value of 0.1666 [109]. A more accurate solution would be possible with a larger refined wake region.

4.4 Pipe

This problem considers the three dimensional transient flow through a straight pipe. A Womersley profile is applied to both the inlet and the outlet, and a no-slip condition

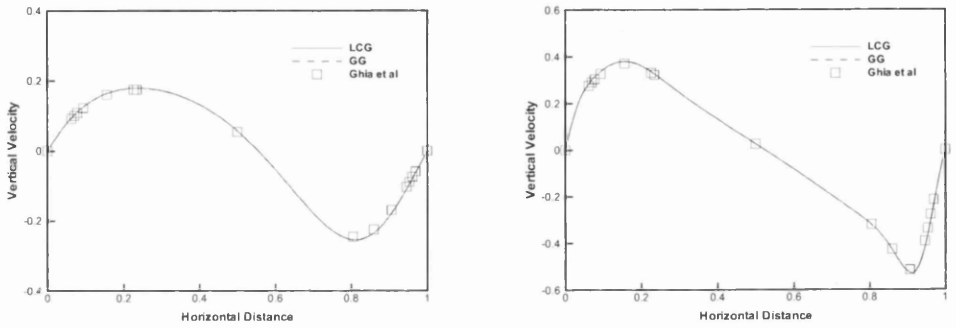

(a) $Re = 100$ (b) $Re = 1000$

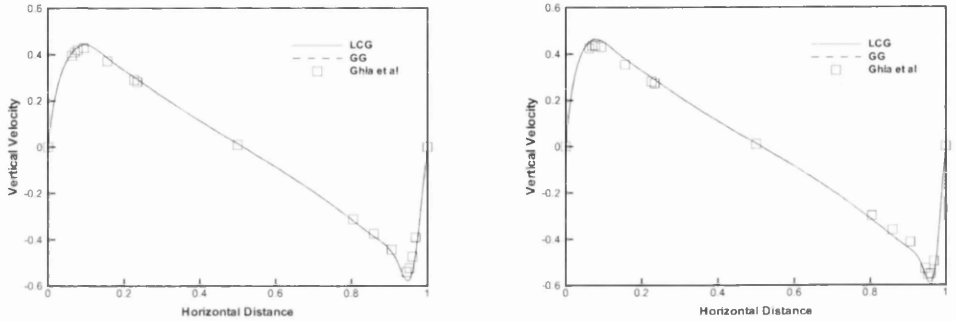

(c) $Re = 3200$ (d) $Re = 5000$

Figure 4.5: Flow in a lid-driven cavity. Comparison with Ghia *et al* [1] of u_2 velocity distribution along the vertical centreline

is applied to the wall of the pipe. The mesh geometry is given in Figure 4.10. The pipe radius was 0.3cm and the length was 3.5cm. The mesh consisted of 169,666 linear tetrahedral elements, 30,088 nodes and 6 boundary layers. The Womersley profile was constructed using the aortic waveform (as outlined in Section 2.9.2.2) and was scaled in order to achieve a peak centreline velocity of 66cm/s. The cycle was discretised into 240 time steps.

In order to examine the transient solution, two time instances are identified. A mid acceleration time instance (pre peak systole) and a peak flow time instance (at peak systole). The velocity vectors at peak flow for the LCG and GG methods are shown in Figure 4.11 for five slices. A cross-section along the pipe length is given in Figure 4.12 for the pressure distribution during the mid acceleration time instance. As can be seen from the two figures, the LCG and GG results show excellent agreement. In order to examine the difference quantitatively, the central point within the domain was employed. The transient velocity waveform for this node is given in Figure 4.13. Again,

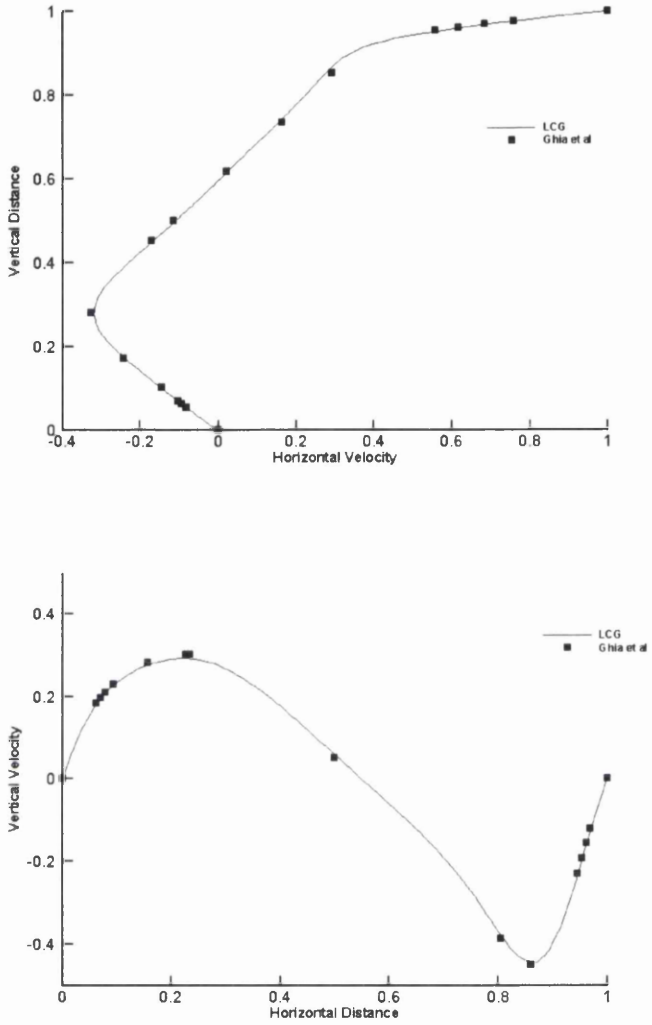

Figure 4.6: Flow in a 3D lid-driven cavity at $Re = 400$. (a) comparison of horizontal velocity distribution along mid-vertical line with Ghia et al. and (b) comparison of vertical velocity distribution along mid-horizontal line with Ghia et al.

the differences between the two methods are too small to separate the solutions (being of the order 1×10^{-8}).

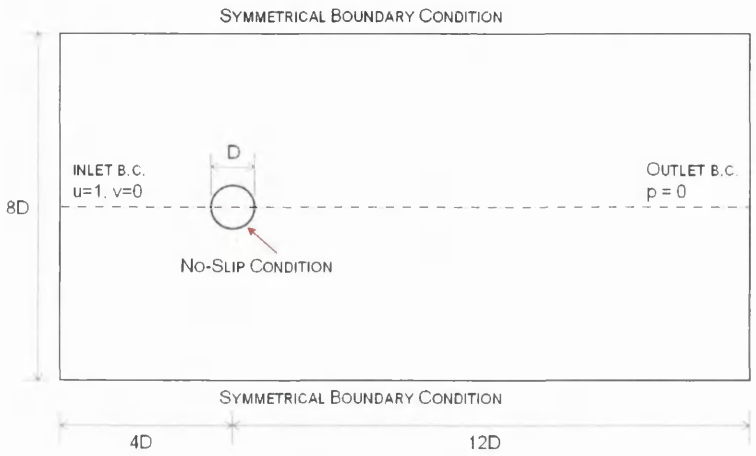

(a) u_1 velocity contours

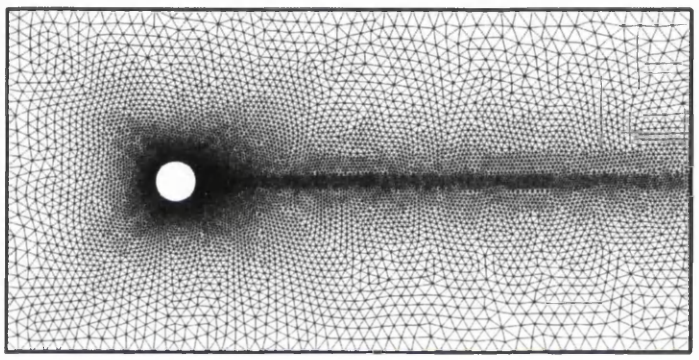

(b) u_2 velocity contours

Figure 4.7: Unsteady flow past a circular cylinder at $Re = 100$. a) Geometry and boundary conditions. b) Unstructured mesh used in the computations.

4.5 Backward Facing Step

This is a standard test case which is commonly used for testing turbulent flow models. This test problem includes a recirculation region downstream of the step and the resulting complex flow patterns allows for an analysis of the suitability of the turbulence model. The problem definition and non-uniform structured mesh used is shown in Figure 4.14. The mesh used consisted of 13,650 linear triangular elements and 7,021 nodes. The mesh has been refined close to the wall region and is relatively coarse along the centreline of the domain.

The velocity profiles at two selected downstream sections (2L and 4L from the step location) are given in Figure 4.15. As can be seen, the LCG and GG methods are in excellent agreement at both the selected locations. The u_1 velocity component contours

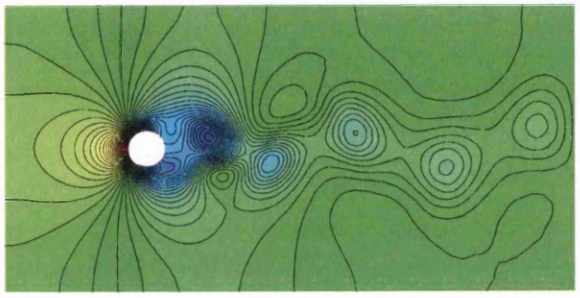

(a) Pressure contours

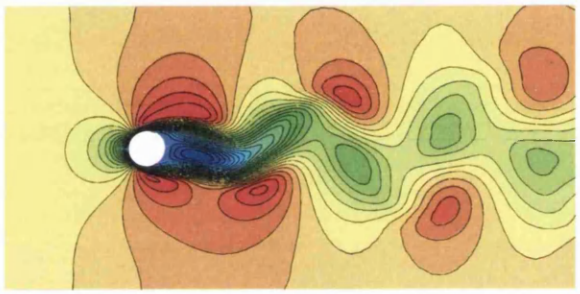

(b) Horizontal velocity contours

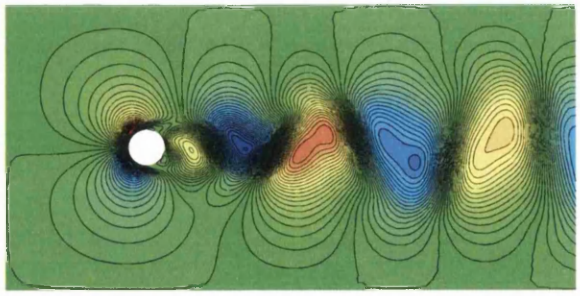

(c) Vertical velocity contours

Figure 4.8: Unsteady flow past a circular cylinder at $Re = 100$. Computed solution at a non-dimensional real time of 150

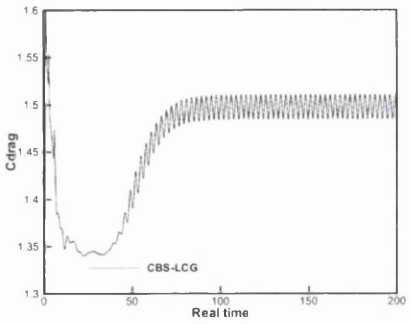

(a) Full history of drag coefficient c_d

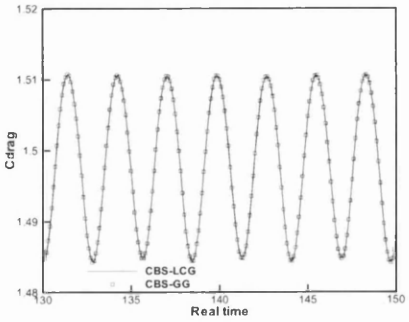

(b) Comparison of c_d

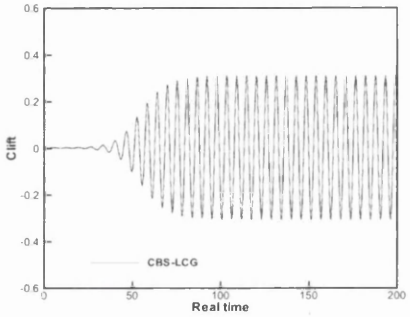

(c) Full history of lift coefficient c_l

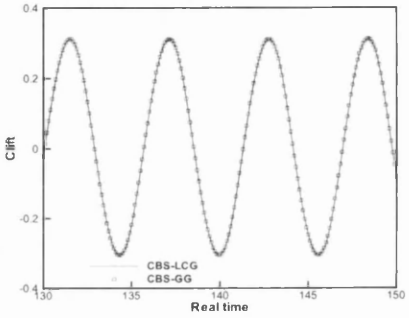

(d) Comparison of c_l

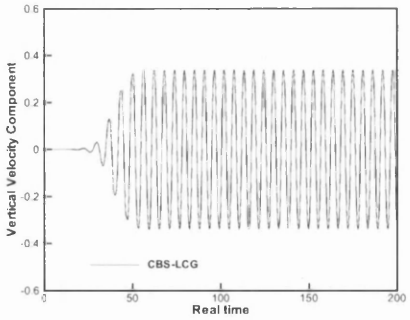

(e) Vertical velocity component u_2 at central exit

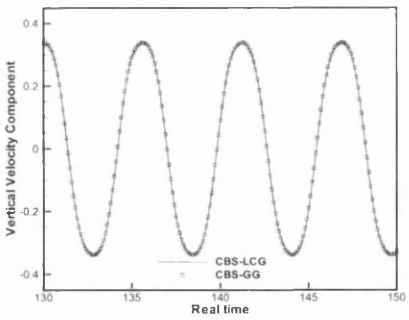

(f) Comparison of u_2 at exit

Figure 4.9: Unsteady flow past a circular cylinder at $Re = 100$. Computed coefficients of the drag and lift, and computed vertical velocity component at central exit point. All are plotted as a function of the non-dimensional, real time.

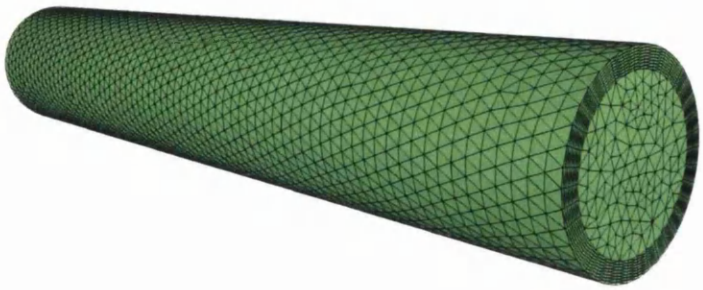

Figure 4.10: Straight 3D pipe mesh geometry

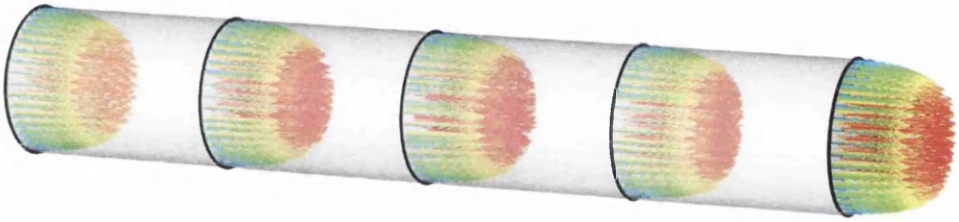

(a) LCG

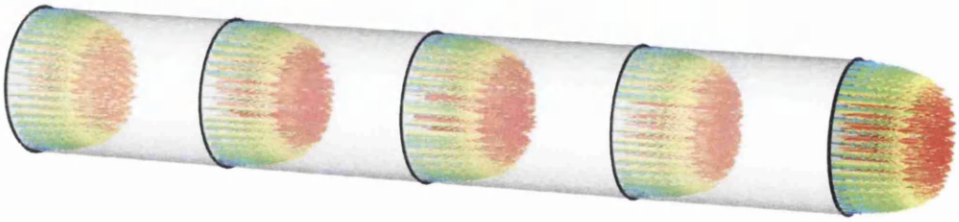

(b) GG

Figure 4.11: Flow in a 3D pipe. Velocity vectors at five slices during peak flow

are given in Figure 4.16 along with the pressure and $\hat{\nu}$ contours from the LCG run. As can be seen, the recirculation region downstream of the step is predicted. The LCG and GG results are again in good agreement.

4.6 Summary

This chapter has examined both steady state and transient cases, as well as laminar and turbulent problems. Both three dimensional and two dimensional problems on structured and unstructured meshes have been examined. The rigorous testing demonstrates that the LCG variant of the CBS scheme is in excellent agreement with the continuous Galerkin method for all of the problems outlined.

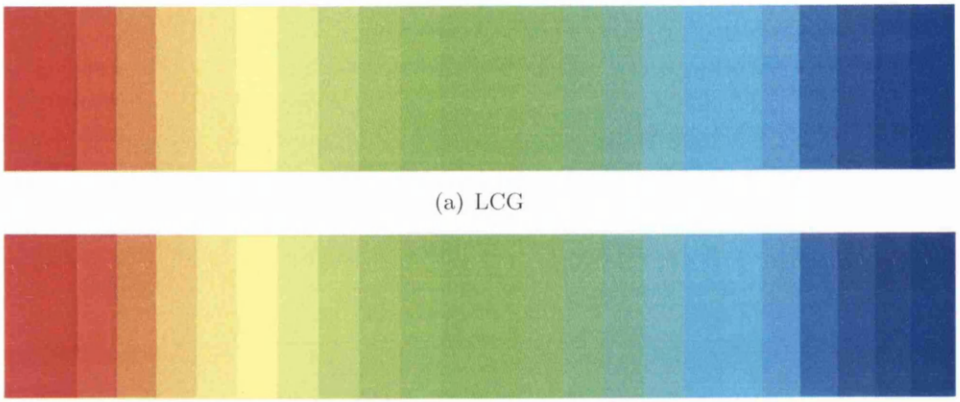

(a) LCG

(b) GG

Figure 4.12: Flow in a 3D pipe. Pressure distribution within the pipe at the mid acceleration time instance

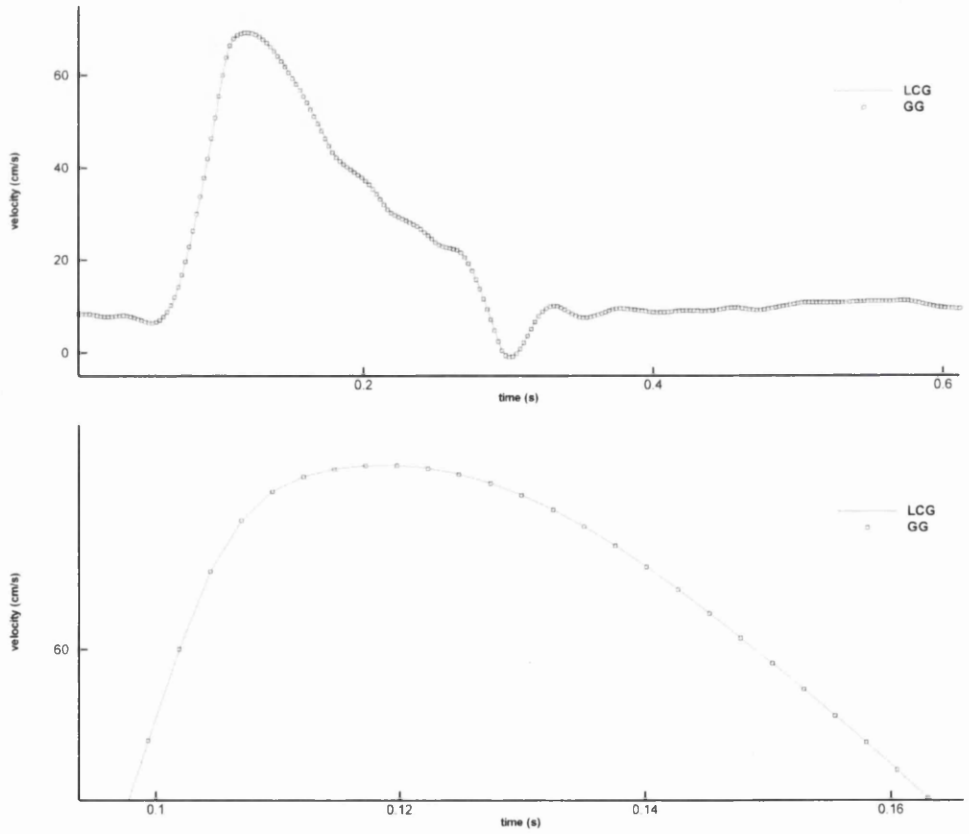

Figure 4.13: Flow in a 3D pipe. a) Velocity profile at the centroidal node during one cardiac cycle b) Detailed view of peak systole

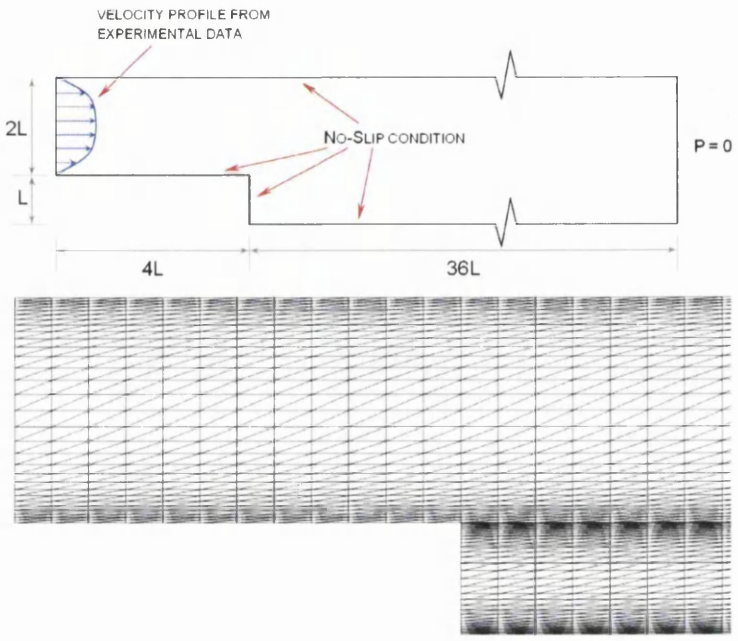

Figure 4.14: Turbulent flow over a backward facing step at Re=3025. a) Problem definition b) Mesh used, 13,650 elements and 7,021 nodes.

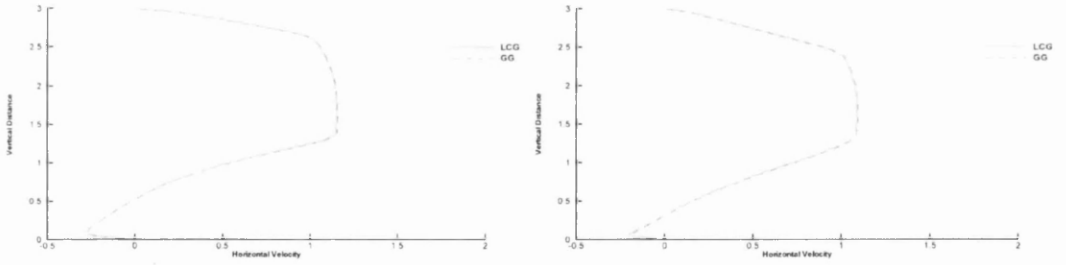

Figure 4.15: Turbulent flow over a backward facing step at Re=3025. Velocity profiles downstream of the step at a distance of a) 2L b) 4L

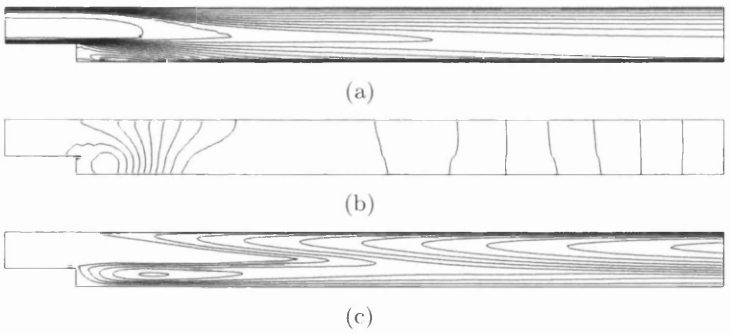

Figure 4.16: Turbulent flow over a backward facing step at Re=3025. Contours within the domain from the LCG run a) u_1 velocity b) Pressure c) $\hat{\nu}$

Chapter 5

Patient-Specific Meshing

5.1 Introduction

This chapter is intended to provide a short overview of the techniques used in the construction of the patient-specific meshes utilised in the following chapters. The author is indebted to Dr. Igor Sazonov from Swansea University for his mesh processing work and to Singleton Hospital (Swansea, UK), Morriston Hospital (Swansea, UK) and the Royal Wolverhampton Hospital (Wolverhampton, UK) in providing the necessary scans which were used.

5.2 Mesh Recovery

The arterial geometries were recovered from sets of standard CT scans without contrast enhancing angiography. The CT scan resolution was 0.877×0.877 mm in the slice plane and 1 mm between the slices from Morriston Hospital and the Royal Wolverhampton Hospital scan resolution was 0.35×0.35mm in the slice plane and 0.5mm between the slices. The scan sets consisted of approximately 500-600 slices from Wolverhampton Hospital and 400 from Morriston Hospital.

In order to extract the arterial geometry, the AMIRA software (Mercury Computer Systems, Chelmsford, MA, USA) is used for region segmentation and initial surface mesh generation. However, it is difficult to precisely distinguish the interface between the lumen and the wall using AMIRA. Therefore some additional manual interaction is

necessary on almost every slice. In Figure 5.1 an example of an AMIRA segmentation, post manual intervention, for a left carotid artery is given. With the interest for this example being atherosclerotic plaque formation, the reconstruction only needs the carotid bifurcation and sufficient arterial length either side.

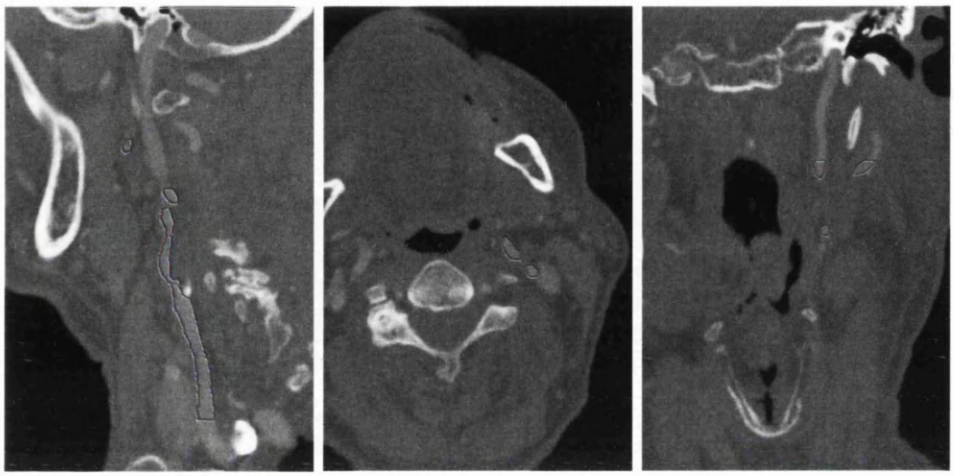

Figure 5.1: AMIRA segmentation of a left carotid artery. a) Sagittal b) Axial c) Coronal.

From the initial surface obtained using AMIRA, the surface is refined using the in-house software developed by Dr. Sazonov. Using the example of an aortic reconstruction from the data provided by Morriston Hospital, the initial surface mesh from AMIRA is given in Figure 5.2(a). The initial processing of the STL file concerns isolating the domain needed for numerical simulation. Thus the arterial components that are not required are clipped and removed. At the clipped sections, which for the aortic problem consists of the one inlet and four outlets, a surface mesh is constructed. This surface is approximately orthogonal to the axis of the artery at the cut location. The surface mesh now consists of the vessel walls and relevant inlet/outlet triangles as shown in Figure 5.2(b).

The initial surface mesh obtained is not smooth and contains a significant number of very short edges (marching cubes). To improved the quality of the surface mesh, the mesh contraction method described in [111, 112] is applied. This contraction method reduces the shortest edge into a point. For a plane surface, such as an outlet or inlet, this is straightforward. For a non-planar surface (the artery vessel), the procedure is a little more complex. Here, the shortest edge must be contracted to a midpoint that should be moved and placed at the original surface. If the mid point is not relocated, then the surface mesh may shrink locally. After application of the contraction method, the topology around the new point is improved by swapping edges containing the new point unless the new point is a ridge point. Ridge points are the nodes separating the

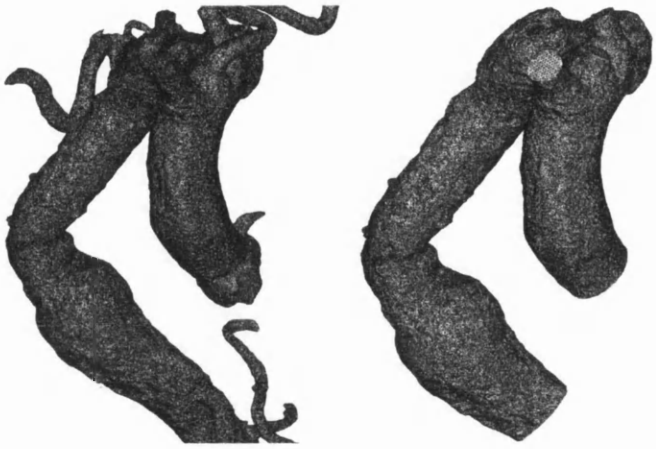

Figure 5.2: a) The initial surface mesh created by use of AMIRA b) Numerical domain after outlet/inlet meshing has been introduced.

vessel wall and inlet/outlet plane. Ridge point topology is improved based upon the number of wall edges and the number of inlet/outlet edges connected to the point. The mesh is then smoothed around the new point using Taubing smoothing [113] to avoid the mesh from shrinking. This contraction process is aborted when there are no edges shorter than a tolerance length. After the process is complete, the quality of the surface triangles has improved and the surface mesh is smoother.

5.3 Boundary Layer and Volume Mesh Construction

The next stage is to create boundary layers in order to resolve the high near-wall velocity gradients. To construct these layers, the surface mesh nodes are projected inward and points are placed at a specific distance in the direction of the inward surface normal. A new inside surface mesh is constructed from these new points, creating a surface mesh with the same topology as the outer wall surface mesh. Prisms are then formed between corresponding surface faces. Multiple prismatic layers can be formed in this way. To generate the volume mesh inside the structured layers, every prism is first divided into a number of shorter prisms. To do this, every edge connecting the two triangles is divided into shorter sides using geometrical progression with smaller size edges placed close to the wall. Then, every prism is the divided into three tetrahedra. The geometrical progression employed is determined by the following technique.

Let d be the mean size of the surface element face and the inner prismatic layer thickness be $d \times f$ where f is a diminishing factor. The thickness of a prismatic layer from inside

No of layers (N)	f	D/d	f^N
3	0.8105	2.00	0.5324
4	0.7413	2.00	0.3020
5	0.7090	2.00	0.1792
6	0.6921	2.00	0.1099
7	0.7067	2.20	0.0881
8	0.7191	2.38	0.0715
9	0.7297	2.54	0.0587
10	0.7390	2.69	0.0486
11	0.7472	2.84	0.0405
12	0.7546	2.97	0.0341

Table 5.1: Table of prismatic layer properties.

the geometry to the solid surface is reduced by a factor f progressively. Thus the total depth D of the boundary layer (comprised of N layers) is defined as:

$$D = df + df^2 + df^3 + ... + df^N \tag{5.1}$$

with df^N being the thickness of the layer adjacent to the wall. In order to produce a solution, either D or f must be specified. For meshes involving less than 6 boundary layers, the total depth was defined as $D = 2d$. For meshes with more than six boundary layers, the factor f is defined using the equation

$$f = \frac{N^a}{N^a + 1} \tag{5.2}$$

where $a = 0.452$ was chosen to provide continuity for a six layered mesh between the two techniques. The distribution employed allows for a smooth transformation between the inner unstructured mesh and the boundary layer mesh.

Table 5.1 depicts the prismatic layer distribution for increasing N. The thinnest prismatic layer has a thickness of df^N. Thus the f^N column in the table quantitively highlights the increasing density of the mesh at the solid surface. Figure 5.3 illustrates the boundary layer mesh distribution used in the present study against cumulative distance (depth) from the inner mesh. The depth is defined relative to the average surface element size d.

The resultant mesh for a twelve boundary layer geometric progression is shown in Figure 5.4. With the construction of boundary layers, the inlet and outlet surfaces of the

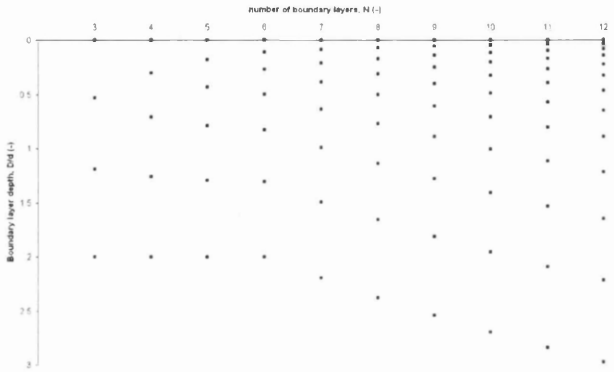

Figure 5.3: Flow through a patient-specific carotid bifurcation. For a mesh with N prismatic layers, the cumulative inter-layer depths (relative to d).

geometry also now contains these structured layers. Beyond the inner structured layer surface, the surface mesh at inlet/exit is generated using the unstructured methodology referred to as stitching method [114]. This provides a high quality surface mesh at inlet/exit, as shown in Figure 5.4. The volume tetrahedron mesh of the remaining domain is generated using the Delaunay triangulation method described in [115, 116].

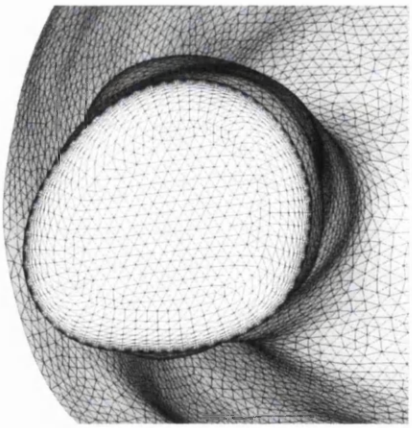

Figure 5.4: Closeup of an external carotid artery mesh outlet with boundary layers.

5.4 Summary

This chapter dealt briefly with the methods employed in the reconstruction of the arterial geometry from patient CT scans. The techniques for improving the initial surface mesh provided by AMIRA were outlined along with the construction of the boundary layers.

These techniques were used for the construction of the meshes utilised within in the following chapters.

Chapter 6

Preliminary carotid bifurcation study

6.1 Introduction

This chapter presents the preliminary investigations undertaken on a small patient-specific carotid geometry. The patient-specific mesh was utilised to determine the appropriate parameters for the general patient-specific studies in the following chapters. The healthy patient-specific carotid bifurcation geometry was constructed from a set of anonymous CT images provided by Singleton Hospital. The CT scan consisted of 390 axial slices from the thorax to the nasal passage. The mesh geometry is shown in Figure 6.1.

6.2 Convergence

One of the primary aims of these investigations was to determine both the spatial and temporal detail required for mesh converged solutions. To do this, a number of sensitivity studies were carried out. Since part of the carotid bifurcation analysis will involve the study of derived haemodynamic parameters, the convergence study examines two factors to determine whether convergence has been achieved. The first factor used is the maximum wall shear stress and the second is the time-averaged wall shear stress. The relative convergence error is defined by

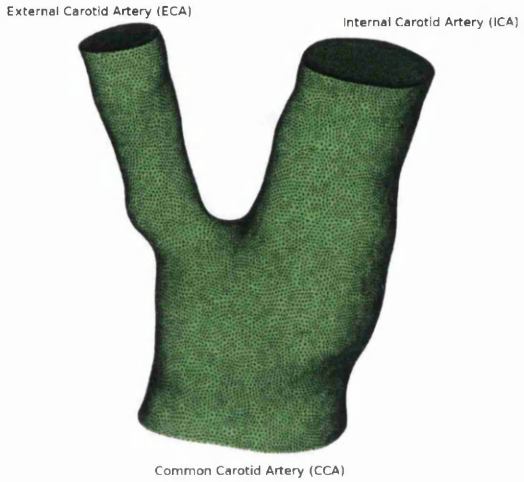

Figure 6.1: Patient 01 right carotid bifurcation

$$\text{error} = \frac{\max\left(\tau_{abs}\right)_i - \max\left(\tau_{abs}\right)_j}{\max\left(\tau_{abs}\right)_i} \tag{6.1}$$

for the time-averaged wall shear stress, in which τ_{abs} is the time-averaged wall shear stress (WSS) and is defined in Section 2.10.1. The subscripts i and j refer to consecutive meshes i and j respectively.

6.2.1 Mesh Convergence Analysis

To investigate mesh convergence and the influence of boundary layers on the wall shear stress solution, ten meshes were employed. Nine of the grids contained boundary layers and one without them. The number of elements within the mesh ranged from 1,465,562 linear tetrahedral elements for the non boundary layered mesh to 2,453,723 elements for the 12 boundary layered mesh. The mesh details are summarised in Table 6.1, with selected mesh detail outlined in Figure 6.2.

For this study, the blood dynamic viscosity and density were taken to be $\mu = 0.035$ g $\text{cm}^{-1}\text{s}^{-1}$ and $\rho = 1.0$ g/cm^3 respectively. The flow division between the ICA and the ECA varies in the literature from constant ratios 56:44, 61:39, 63:37 and 67:33 [25,117, 118] to non-uniform ratios in time [119]. While WSS patterns between individuals are influenced by geometry and flow rate differences, Milner *et al* [117] concludes that the geometry is the key influence. Thus, to simplify the boundary conditions, we assumed an ICA flow rate of 60% and an ECA flow rate 40% of the total CCA flow rate. The

Mesh	Boundary Layers	Number of Elements	Number of Nodes
1	0	1,465,562	254,848
2	3	1,498,712	261,399
3	4	1,689,792	292,467
4	5	1,808,064	312,326
5	6	1,926,336	332,185
6	7	1,960,429	339,028
7	8	2,058,619	355,172
8	9	2,180,947	375,715
9	11	2,359,644	405,803
10	12	2,453,723	421,608

Table 6.1: Patient 01 right carotid Mesh details.

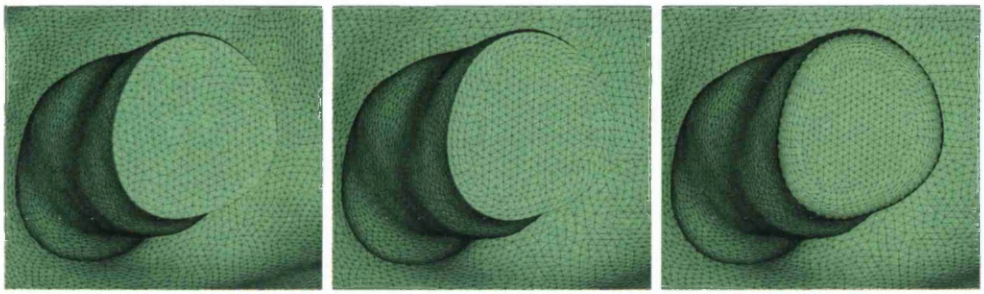

Figure 6.2: Patient 01 right external carotid artery outlet. a) Mesh 1 (purely unstructured) b) Mesh 2 (3 boundary layers) c) Mesh 10 (12 boundary layers)

velocity profile was constructed from the harmonics given in Table 2.1. These harmonics are derived from a fast fourier transform of a measured aortic velocity waveform [2]. The final profile was scaled to give the desired maximum velocity which for this preliminary study was 66cm/s. The period of the cardiac cycle was 0.61144 seconds (98 beats per minute).

Figure 6.3 shows the mesh convergence for the maximum wall shear stress within the domain (Figure 6.3(a)) and the peak time-averaged wall shear stress (Figure 6.3(b)). From the maximum wall shear stress plot, it is clear that after the introduction of the structured boundary layers the maximum wall shear stress steadily converges towards a solution. The rate of convergence is more clearly visible in Figure 6.3(b). While a decreasing gradient of the curve with increasing number of elements is expected, there is rapid variation of time-averaged wall shear stress at two points. The first is as going from the unstructured mesh to the three layer mesh. The sudden change near the mesh with the three structured layers is due to the change in topology from purely unstructured mesh to structured layers close to the wall. The second rapid change (between the six/seven boundary layer meshes) is a result of change in the approach

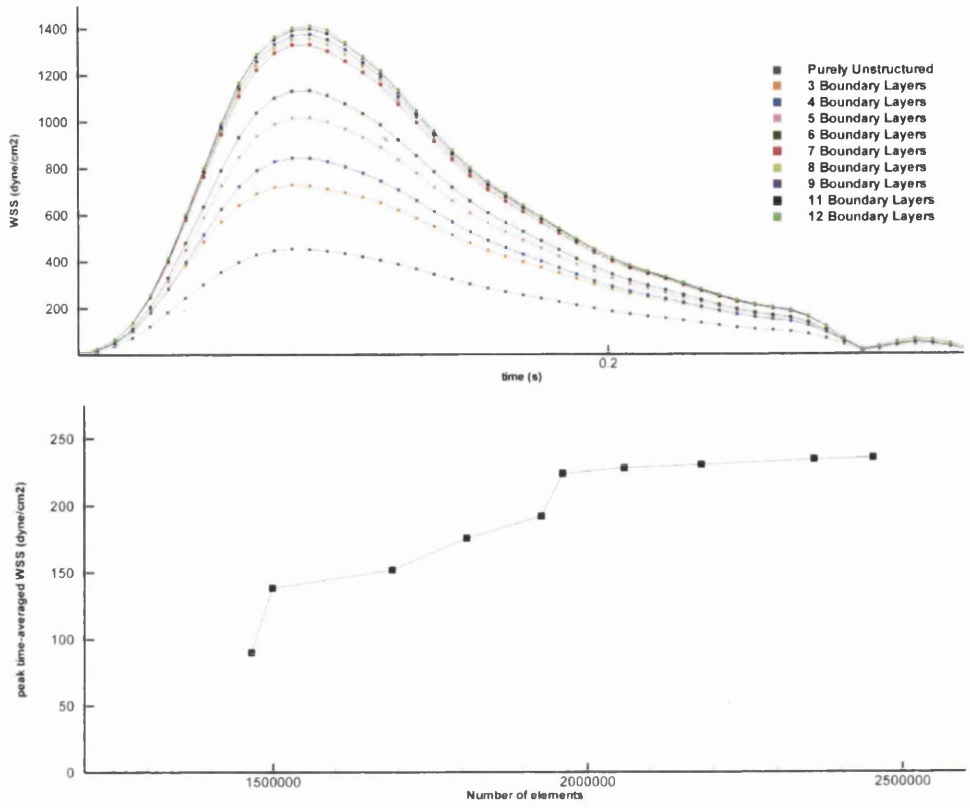

Figure 6.3: Patient 01 right mesh convergence analysis. a) Maximum wall shear stress (dyne/cm^2) b) peak time-averaged wall shear stress (dyne/cm^2)

to construct the boundary layer mesh. With the use of an expanding boundary layer depth, the inner volume mesh must be recalculated. On the grids containing six or less boundary layers, the same inner volume mesh is employed and any convergence in the solution is due to the structured layer refinement. As the number of boundary layers is increased it becomes necessary to increase the overall boundary layer depth to ensure a smooth transition in the element size from the structured layer to the inner mesh. To provide quantitative results, the relative convergence error between the eleven and twelve layer grids was 0.6% for maximum wall shear stress (WSS) and only 0.5% for peak time-averaged WSS. Examining the relative error for the nine and twelve layer grids, the maximum WSS error was 2.5% and peak time-averaged WSS error was 2.1%. Comparing the six and twelve layer grids, the relative convergence error was 19.5% (maximum WSS) and 18.4% for peak time-averaged WSS. From this mesh convergence analysis, the number of boundary layers employed should be greater than nine to reduce the relative convergence error below a threshold of 2.5%. To obtain the best accuracy in the remaining preliminary studies, the mesh with twelve layers consisting of 421,608

nodal points and 2,453,723 linear tetrahedral elements was chosen.

6.2.2 Time Discretisation Convergence

To test for time convergence the cardiac cycle was discretised into 60, 100, 120, 200 and 240 time steps. This convergence study was undertaken on the same problem outlined in the previous section using the twelve layer mesh. The results of the sensitivity study are given in Figure 6.4. From the figure, it is clear that good agreement exists after the peak in all but the 60 time step case. Prior to the instance of peak flow, there is greater discrepancy between the solutions. There is close agreement between the 200 and 240 time step cases demonstrating sufficient refinement in the time discretisation has occurred. Examining the peak time-averaged wall shear stress graph, it is clear that a typical convergence pattern has emerged, with decreasing gradient as the number of time steps is refined. However, it is clear that differences between the peak time-averaged wall shear stress values is small. Comparing the 60 time step case to the 240, the relative error is only 1.9%. In the comparison of the 120 case to the 240, the difference is 0.7%. For the overall maximum wall shear stress the difference between 60 and 240 is negligible, although if examined point-wise the difference is approximately 5%. From the analysis, the number of time steps was chosen to be 120 as this kept the maximum point-wise difference to approximately 2.4%. While it is necessary to utilise a sufficient number of real time steps to ensure convergence, the penalty due to over refinement is minimal. The increase in real time steps only marginally influences the run time of the problem due to the corresponding decrease in pseudo iterations as the number of real time steps is increased. Depending on the problem, increasing the number of real time steps may actually decrease computational run duration.

6.2.3 Real Time-stepping Order of Approximation

To examine the choice of order of approximation (Section 2.6.5) for the real time step term in Step 3 of the artificially compressibly CBS scheme , the twelve layer boundary mesh was again employed together with a carotid artery centreline velocity waveform given by the harmonics in Table 6.2. The resulting waveform is given in Figure 6.5. The harmonics were reconstructed from the single patient data in Figure 3 of Holdworth *et al* [120]. The four complete cycles were examined mathematically by a colleague (Dr Sazonov) to reproduce a typical waveform profile that did not lose data by artificial smoothing. The amplitude is scaled to produce the desired flow rate which for this

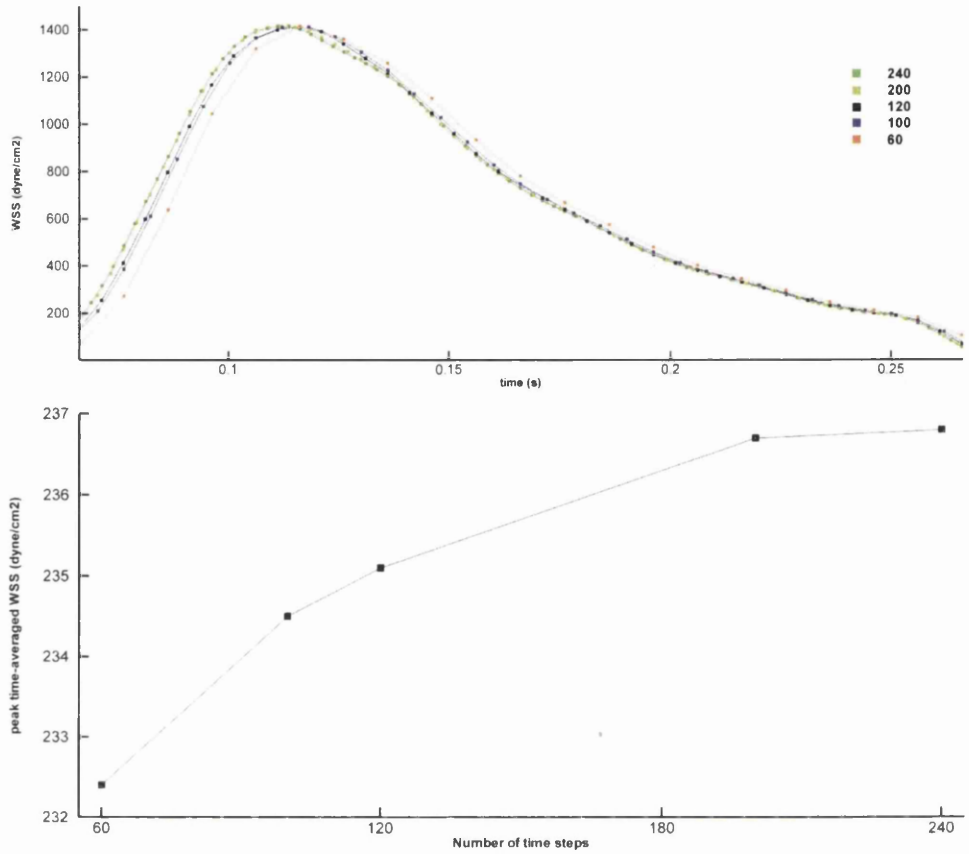

Figure 6.4: Patient 01 right time convergence analysis. a) Maximum wall shear stress (dyne/cm^2) b) peak time-averaged wall shear stress (dyne/cm^2)

problem was a mean flow rate of Q=4.5cm^3/s. This corresponded to a peak velocity of 89cm/s at the centroid of the inlet surface. The period of the cardiac cycle was 0.9195 seconds, with 65 beats per minute. Since the cycle is 33% longer than the previously used cycle and a greater peak velocity the decision was taken to use 240 real time steps. The flow division in this case was chosen to be 75:25 between the ICA and the ECA [119]. This flow division was chosen as an extreme alternative to the 60:40 split mentioned previously.

The transient maximum wall shear stress distribution for the 1st, 2nd and 3rd order backward implicit schemes is given in Figure 6.6. From the plot it is clear that all three display close agreement. The quantitative analysis is given in Table 6.3. From the table, the visual agreement shown in the figure is maintained. The maximum relative error is only 0.33%. What is not obvious from the results highlighted is the advantage that 2nd or 3rd order backward difference schemes possess in this situation. For the problem examined the total number of iterations required to obtain the complete transient cycle

Harmonic	freq. (Hz)	Amplitude (cm)	phase (rad)
0	0.0000000	46.926373	0.0000000
1	1.0875476	21.524133	-1.1757456
2	2.1750952	17.614591	-1.6399569
3	3.2626427	12.147710	-2.4126155
4	4.3501903	6.7678515	-2.5923204
5	5.4377379	9.0132960	-2.8654415
6	6.5252855	8.0155307	2.5792239
7	7.6128331	4.4200926	2.0271286
8	8.7003806	3.5711419	1.9278901
9	9.7879282	3.4320565	1.3878100
10	10.875476	2.3272178	0.77936298
11	11.963023	1.4287817	0.62628156
12	13.050571	1.5817702	0.35279629
13	14.138119	1.2964663	-0.36075375
14	15.225666	0.71691449	-0.75219771
15	16.313214	0.64928471	-0.87984983
16	17.400761	0.55890994	-1.4506194
17	18.488309	0.35656742	-1.8778747
18	19.575856	0.27656662	-2.0518077
19	20.663404	0.25371520	-2.4611692
20	21.750952	0.18540847	-2.9991421
21	22.838499	0.11846889	3.0061654
22	23.926047	0.10273053	2.7403593
23	25.013594	0.077012238	2.2301464
24	26.101142	0.049128254	1.9239422

Table 6.2: Harmonics utilised to construct the Sazonov carotid waveform

was less in both cases when compared to the 1st order run. Indeed, the 3rd order scheme possessed a similar advantage over the 2nd order scheme. Compared to the second order run, the 1st order required a total of 117% iterations. The 3rd order run, conversely, required only 90%. As part of the computational setup, a minimum of one hundred pseudo iterations must be completed for every time step. If this number was reduced, the differences between the 1st, 2nd and 3rd order runs would most likely have further increased. From both the negligible differences in the run time results and the overall run time duration, it is clear that 3rd or even 2nd order can possess significant advantages.

Order	Overall maximum WSS	peak time-averaged WSS
1	2077.8	356.2
2	2075.7	356.9
3	2077.3	357.4

Table 6.3: Real time step order convergence analysis. WSS in dyne/cm^2

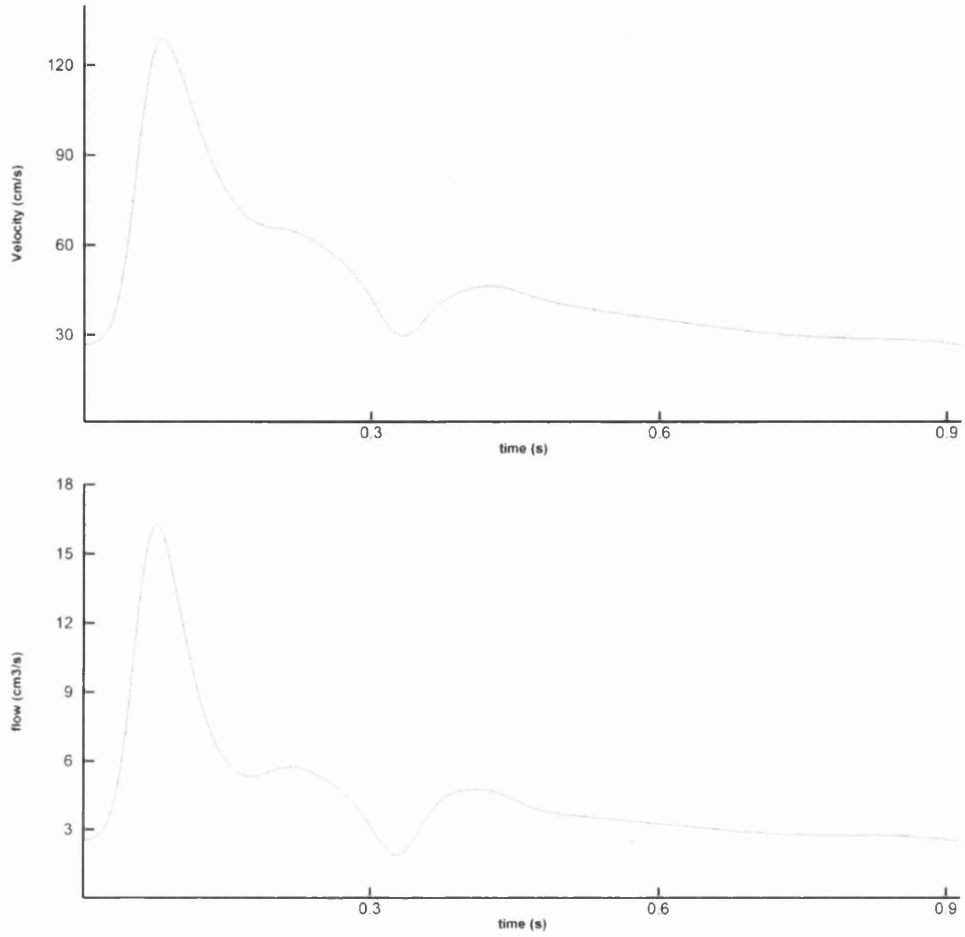

Figure 6.5: Sazonov carotid waveform. a) Resultant centreline velocity (cm/s) b) Resultant transient flow rate (cm^3/s)

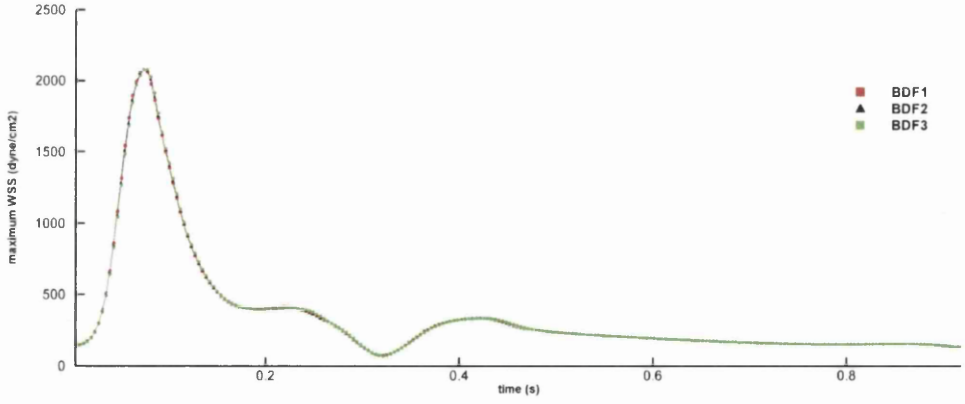

Figure 6.6: Patient 01 right real time step order analysis.

6.3 Results

The results obtained from the use of the measured aortic waveform (Case 1) and the Sazonov carotid waveform (Case 2) are given in this section. The two cases utilise very different waveforms, resultant flow rates and flow divisions. Since the differences are flow based any similarities in the results between the two cases highlights the influence of geometry and any differences highlight the importance of flow in modelling of a healthy patient specific carotid.

6.3.1 Time-Averaged Wall Shear Stress

The time-averaged wall shear stress distribution is shown in Figure 6.7. From the figure, it is obvious that there is an excellent agreement between the time-averaged WSS distributions of Case 1 and 2 within the external carotid artery (ECA) and the common carotid artery (CCA). A high time-averaged WSS is found near the apex, with a localised region experiencing a maximum peak time-averaged WSS of 235 dyne/cm^2 in Case 1 and 357 dyne/cm^2 in Case 2. The apex experiences time-averaged WSS values between 60-150 dyne/cm^2 in Case 1 and 60-170 dyne/cm^2 in Case 2. This demonstrates the increased flow rate of Case 2 has on the maximum time-averaged WSS while this influence is reduced in the apex region. This region is closer to the inner wall of the external carotid artery which is in agreement with the results of Younis *et al* [41], who examined three patient-specific geometries and found this region experienced values of between 60-100 dyne/cm^2 with a small region experiencing values over 100 dyne/cm^2. Downstream of the bifurcation, the ECA experiences a second region of elevated time-averaged WSS values. The Case 1 localised maximum is 100 dyne/cm^2 whereas the corresponding Case 2 value has increased by 20%.

The majority of the CCA experiences less than 5 dyne/cm^2 in Case 1 which would indicate a possible region of atherogenesis, this is in good agreement with the work of Papathanasopoulou *et al* [20] which found low time-averaged WSS in the carotid bulb. In Case 2 the majority of the CCA experiences less than 10 dyne/cm^2, but only a small region experiences less than 5 dyne/cm^2. In the Case 1 ECA, small regions also experience a time-averaged WSS value less than 10 dyne/cm^2 and this is true for significant regions of the ICA. In the higher flow case, no regions in either the ECA or the ICA experience values less than 10 dyne/cm^2. Indeed in the ICA, the values are significantly higher than Case 1 (for example 90 dyne/cm^2 versus 25 dyne/cm^2). However, the distribution pattern within the ICA in Case 1 and Case 2 does display

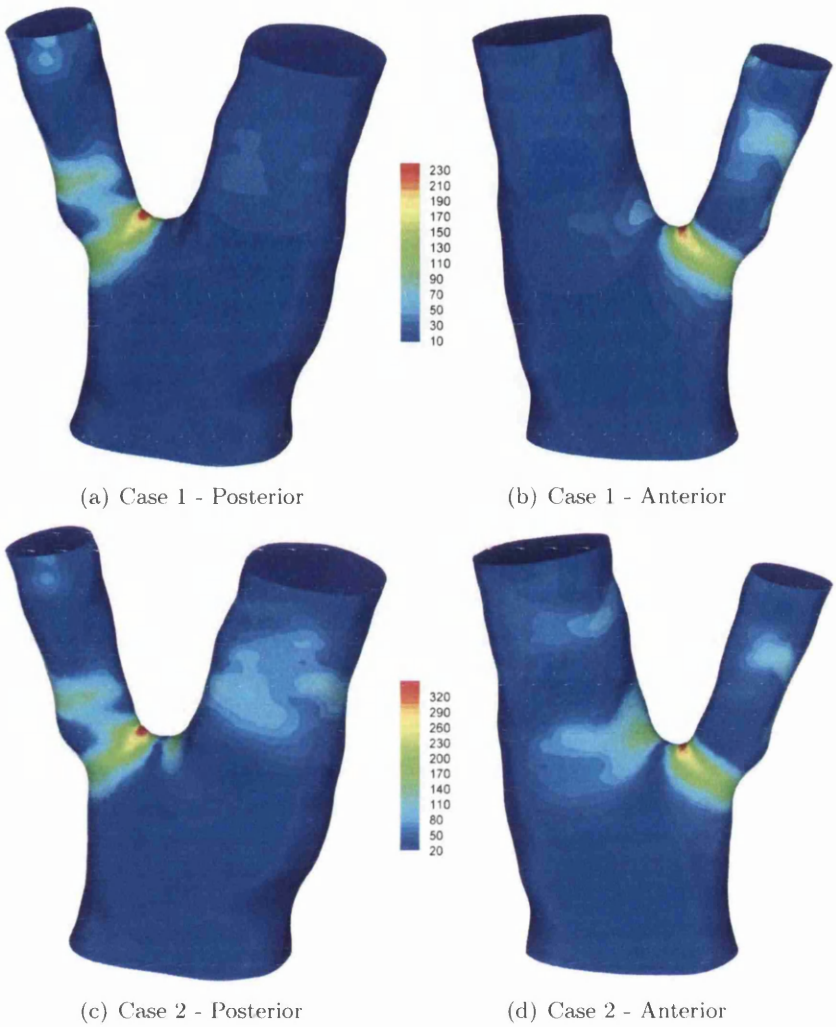

(a) Case 1 - Posterior (b) Case 1 - Anterior

(c) Case 2 - Posterior (d) Case 2 - Anterior

Figure 6.7: Flow through Patient 01 right carotid bifurcation. Time-averaged Wall Shear Stress (dyne/cm^2) distribution within the carotid bifurcation.

similarities, although the range is greater in the higher flow case. From the time-averaged WSS values it is clear that while altering the flow rate and flow division has an influence on the resulting magnitudes of the wall shear stress, geometry has a overriding influence on the distribution.

6.3.2 Oscillating Shear Index

The oscillatory shear index (OSI) distribution for both cases is shown in Figure 6.8. From the plot, the OSI distributions in Case 1 and Case 2 appear substantially different.

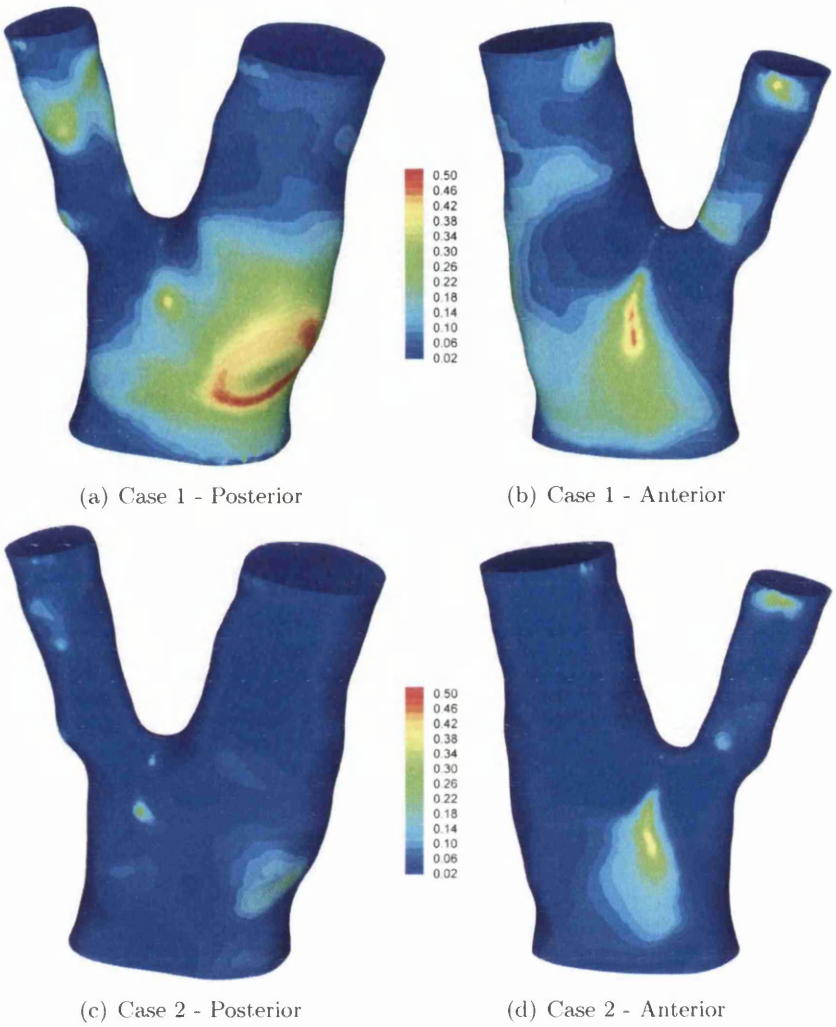

(a) Case 1 - Posterior (b) Case 1 - Anterior

(c) Case 2 - Posterior (d) Case 2 - Anterior

Figure 6.8: Flow through Patient 01 right carotid bifurcation. Oscillating Shear Index distribution within the carotid bifurcation.

However, the regions that display high OSI in Case 1 display elevated values in Case 2. The OSI value is dependent upon the oscillatory nature of the flow and is thus more dependent upon the flow waveform imposed. With the flow in Case 1 experiencing a period of reverse flow, the oscillatory nature of the flow is greater than in the Sazonov waveform case which does not. In Case 1, it can be seen that a region within the CCA displays a high OSI value, indicating a region where atherosclerotic plaque is expected to form. This region is farthest from a local narrowing of the CCA and is along the outer wall, which is in close agreement with the findings of Kaazempur-Mofrad *et al* [21]. In Case 2, this region displays only mildly elevated (0.1-0.15) values decreasing the indicated potential for plaque to form due to oscillatory shear. However, the region

corresponds to a region of low (<5dyne/cm^2) time-averaged WSS. Cheng *et al* [29] found that the atherosclerotic plaque composition was dependent on whether the lesion experienced low shear stress or oscillating shear stress. The low shear stress plaque composition contained more "destabilising" components such as lipids and macrophages. In Case 2, the highest (0.39) OSI values are obtained below the apex on the CCA wall. This corresponds to high OSI values from Case 1. This region also experiences low time-averaged WSS. However, the work of Cheng *et al* [29] suggests the potential plaque formation in this region would contain less "destabilising" components. There are also several smaller regions of elevated OSI values on the ECA in Case 1, although these values are reduced in Case 2.

6.3.3 Wall Shear Stress Temporal Gradient

The wall shear stress temporal gradient (WSSTG) over the cycle has also been investigated here (Figure 6.9). The Case 1 model predicts values of maximum WSSTG of less than 2500 dyne/cm^{2}s for all of the CCA and less than 3500 dyne/cm^{2}s for all but a small region of the ICA. The highest values of WSSTG occur around the entrance to the ECA and the apex, with these values exceeding 40000 dyne/cm^{2}s. These WSSTG results for the CCA compare favourably to the work of Younis *et al* [41]. In Case 2, the model predicts a large region in the CCA experiencing less than 2500 dyne/cm^{2}s. However, a small region in the CCA experiences a maximum WSSTG of 9000 dyne/cm^{2}s. The region of highest WSSTG values correspond between the cases. In the higher flow case, the WSSTG values exceed 58000 dyne/cm^{2}s. The distribution of WSSTG corresponds well with the values of the time-averaged WSS for both cases, although the value range is greater for the WSSTG. These results are typical of those found in the work of Kaazempur-Mofrad *et al* [21] which studied four patients, finding close correlation between WSS and WSSTG for most instances but not all, and WSSTG values exceeding 40000 dyne/cm^{2}s were encountered. Once again, the results point to the entrance to the ECA as athero-protective region and the downstream CCA arterial wall as a region for potential atherogenesis.

6.3.4 Wall Shear Stress Spatial Gradient

The time-averaged wall shear stress spatial gradient (WSSG) is intended to identify the areas of locally disturbed flow. High WSSG values indicate sustained acceleration and deceleration of the flow. The WSSG distribution is given in Figure 6.10. It can be seen

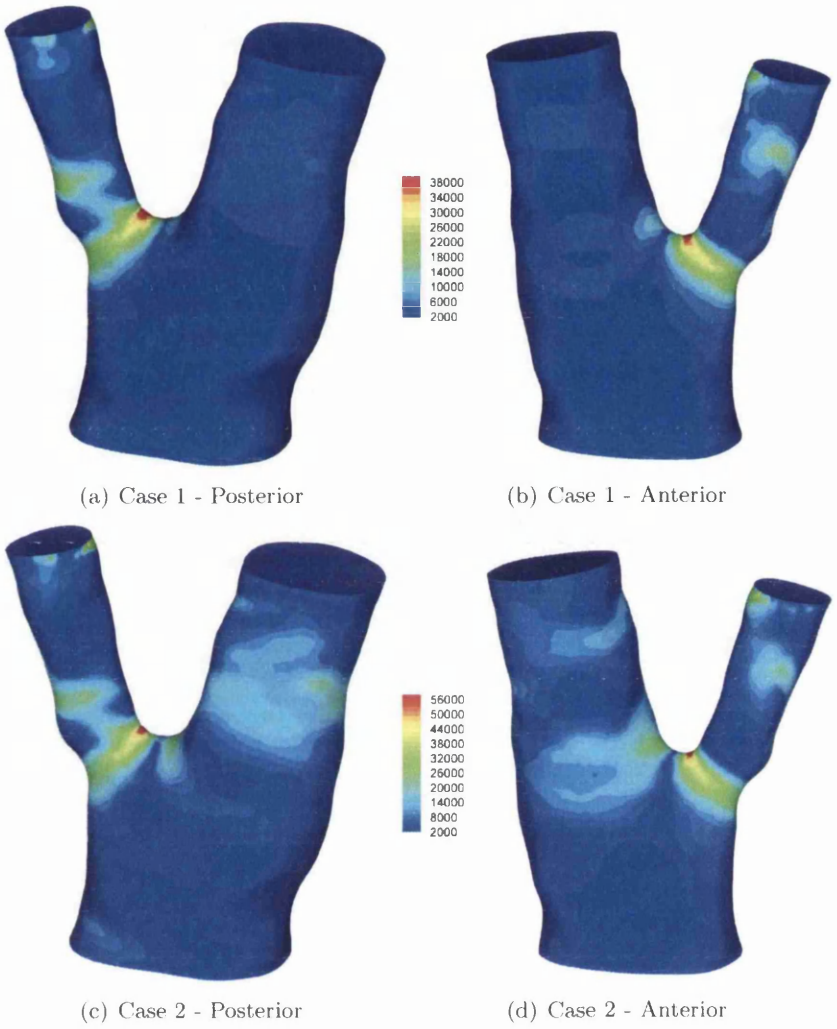

(a) Case 1 - Posterior (b) Case 1 - Anterior

(c) Case 2 - Posterior (d) Case 2 - Anterior

Figure 6.9: Flow through Patient 01 right carotid bifurcation. WSSTG (dyne/cm^{2}s) distribution within the carotid bifurcation.

that the wall shear stress gradient is greatest near the apex in the ECA, and displays a visible correlation with the time-averaged WSS distribution in general for both cases. In Case 2, the distribution within the ICA does display differences. While the region displays elevated time-averaged WSS values, only low WSSG values are predicted. The work of Vermeersch *et al* [37] found a negative correlation between WSSG and carotid artery intima-media thickness (IMT) in the CCA, thus a low WSSG (and low time-averaged WSS) value would be indicative of increased IMT in that region and a high WSSG (and WSS) value would be indicative of decreased IMT thickness near the high WSSG value locality. In Case 1 the peak WSSG value predicted was 370454 dyne/cm^3, while the predicted peak WSSG for Case 2 was 561345 dyne/cm^3. An increase of 52%

which compares faviourably to the 50% increase in the peak centreline velocity between the two cases.

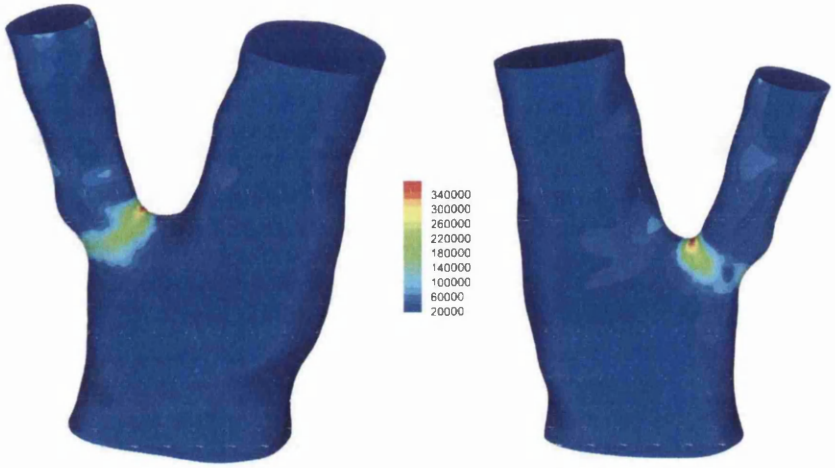

(a) Case 1 - Posterior (b) Case 1 - Anterior

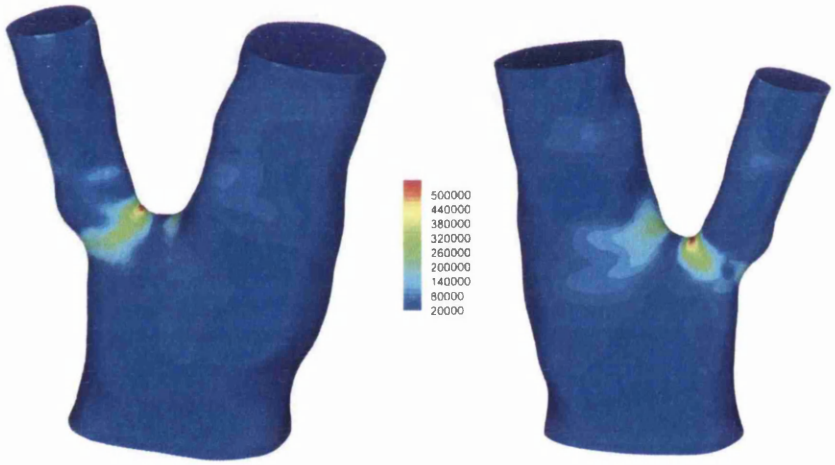

(c) Case 2 - Posterior (d) Case 2 - Anterior

Figure 6.10: Flow through Patient 01 right carotid bifurcation. WSSG (dyne/cm^3) distribution within the carotid bifurcation.

6.3.5 Wall Shear Stress Angle Deviation

In order to back up the OSI prediction, we have calculated another directional quantity called wall shear stress angle deviation (WSSAD). In both cases, the highest values of WSSAD (Figure 6.11) occur at the apex between the ECA and ICA and elevated values extend upstream of the divider along the outer wall of the CCA. On the anterior outer wall of the CCA, the elevated WSSAD region corresponds to a region of high or elevated

OSI in both cases, although this region is less pronounced in Case 1. On the posterior wall of the CCA there is a small region that also corresponds to a region of elevated OSI (0.3-0.4) in both cases although the location has altered marginally. Elsewhere in the domain, low WSSAD values are predicted in both cases. The peaks at the entrance and exits are the results of imposing the velocity profiles and they are ignored here.

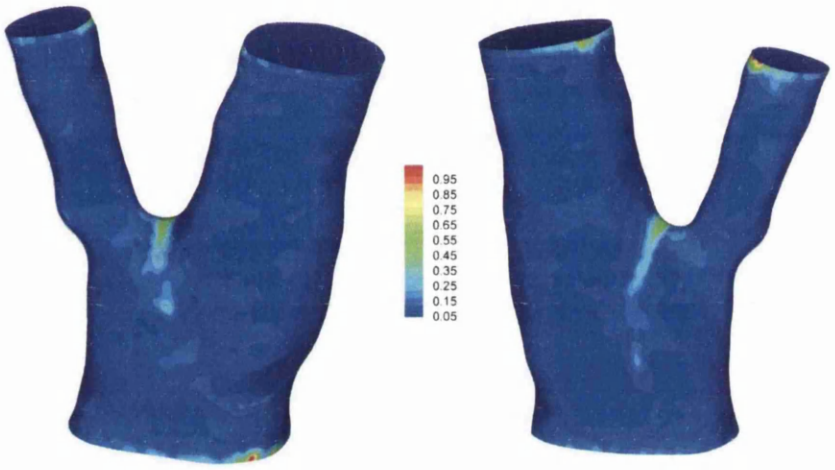

(a) Case 1 - Posterior (b) Case 1 - Anterior

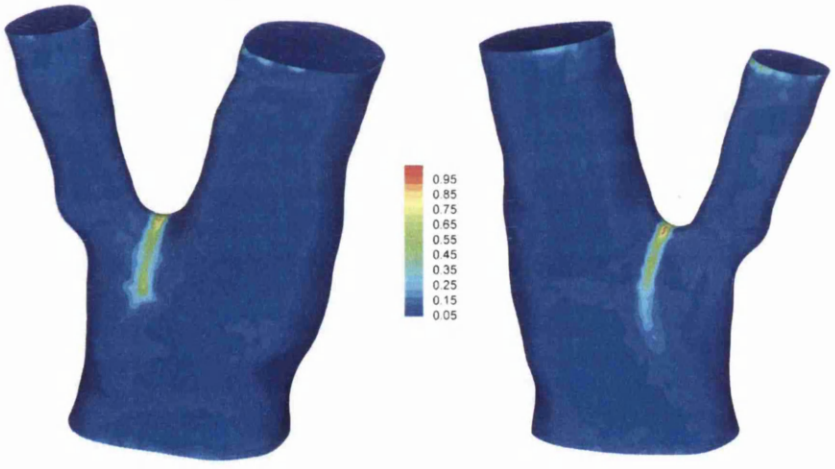

(c) Case 2 - Posterior (d) Case 2 - Anterior

Figure 6.11: Flow through Patient 01 right carotid bifurcation. WSSAD (rad) distribution within the carotid bifurcation.

6.3.6 Wall Shear Stress Angle Gradient

High time-averaged magnitude of wall shear stress angle gradient (WSSAG) values can be an indicator of atherogenesis [40]. Time-averaged magnitude WSSAG values are

shown in Figure 6.12. WSSAG closely correlates with the WSSAD, indicating the surface nodes are approximately equidistant. A region of high WSSAG occurs at the flow divider, where entry to the ICA and ECA begins in good agreement with [104], and elevated values of WSSAG extend away from the divider along the CCA. This is in good agreement with available studies [40]. Statistical correlation between WSSAG and IMT by Vermeersch *et al* [37] found a positive correlation in both the ICA and the CCA, thus a high WSSAG value would indicate an increased IMT value and a low WSSAG would indicate a correspondingly low IMT value within the CCA and ICA. The peaks at the entrance and exits are the results of imposing the velocity profiles and they are ignored here.

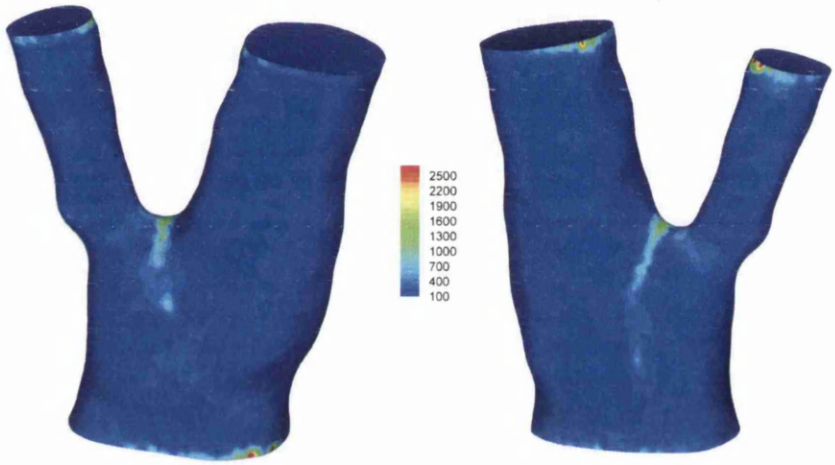

(a) Case 1 - Posterior (b) Case 1 - Anterior

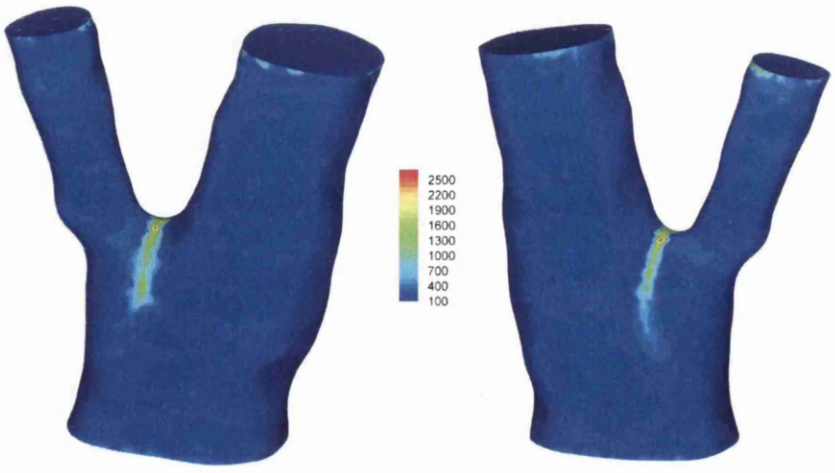

(c) Case 2 - Posterior (d) Case 2 - Anterior

Figure 6.12: Flow through Patient 01 right carotid bifurcation. WSSAG (rad/cm) distribution within the carotid bifurcation

6.4 Discussions

As mentioned previously, haeomdynamic wall parameters are intended to indicate regions of potential atherosclerosis and have been correlated with arterial intima-media thickness in the carotid artery [36,37,121]. Although wall parameters and atherosclerosis are linked, to what extend they are reliable is still a open question. This is one of the reasons why all the six parameters have been provided together to make an assessment.

Since haemodynamic wall parameters WSS, WSSTG and WSSG are negatively correlated with intima-media thickness (IMT), it appears that the outer wall of the CCA region is the potential region for IMT increase. It is also apparent from the previous works that high WSS is atheroprotective but can be responsible for remodelling of endothelial cells. Thus, the increase in IMT could start at the interface between high and low WSS regions. In the present study, the maximum time-averaged WSS of 235 dyne/cm^2 in Case 1 and 357 dyne/cm^2 (Case 2) occurred at the flow divider. It is also obvious that a region close to the apex and the inner wall of the ECA is an athero-protected region due to extremely large WSS values.

It is also clear from past studies that, high values of the parameters OSI, WSSAD and WSSAG are indicative of regions of atherogenesis. Referring to Case 1, the OSI indicates a region experiencing low WSS is at risk of atherogenesis. Smaller regions also exhibit elevated OSI and correspond to regions of low WSS (<5 dyne/cm^2). In Case 2, the OSI parameter is less indicative and the time-averaged WSS values are higher. Only a small region experiences mildly elevated OSI and low time-averaged WSS. As mentioned previously, this could indicate a region of more vulnerable plaque formation. This region is located at the region of highest OSI in Case 1. The WSSAD and the WSSAG parameters are in close agreement with each other in both cases, and exhibit elevated values at the flow divider and regions extending from the apex. Away from the apex the WSSAD and WSSAG parameters show elevated values which correspond to the margins of regions of elevated OSI. With the three parameters not indicating the same regions, it is necessary to remember that the work of Vermeersch *et al* [37] found that the OSI showed a better statistical correlation to increased IMT than the WSSAG parameter for the CCA. Whilst high values for the WSSAD and WSSAG parameters occur at the apex itself, high WSS values would preclude atherogenesis.

Examining the results in combination, low values for WSS, WSSTG and WSSG, elevated values for WSSAD and WSSAG along with high OSI indicate a potential region of atherogenesis in the common carotid artery. The high values for WSS, WSSTG and WSSG indicate a region near the flow divider experiencing atheroprotective influences,

which along with low OSI would indicate that the high WSSAD and WSSAG values are perhaps misleading (false positive) and as such should be considered with caution. Within the ECA, the indicators are less conclusive, with only elevated levels of OSI found in regions of low WSS, WSSG and WSSTG. Within these regions the WSSAD and WSSAG values are also low, lowering the potential for atherosclerosis development here.

From the six haemodynamic wall parameters presented for both cases it is clear that geometry provides an overriding influence on the parameter distribution. The most significant differences between the two methods occurred in the OSI distribution. This parameter is linked to directional changes in the flow away from the mean direction. Even in the OSI distribution, the differences are related to magnitude rather than locational changes. While only elevated OSI values are recorded in the posterior wall CCA for Case 2, the region is centralised on the region of high OSI from Case 1. From this preliminary study, the chosen velocity profile should closely approximate the actual velocity profile if good approximation of the magnitudes of wall shear stress are required. An example of where this would be required is in the flow through a stenosis. Distribution-wise, an idealised velocity profile may be employed for further study of local geometrical influences, while comparison with ultrasound data can be utilised to confirm predicted velocity values.

6.5 Summary

In this chapter a number of sensitivity studies were undertaken as part of a preliminary investigation into a patient-specific carotid bifurcation. The mesh convergence study indicated the need for at least 9 structured boundary layer meshes to resolve the near-wall high velocity gradient to within a WSS tolerance of 2.5%. A real time step order analysis demonstrated that all three backward difference formulae produced solutions that are in good agreement. However, as the order was increased the run time duration decreased, since fewer iterations overall were required. Finally, the chapter concluded by examining the six haemodynamic wall parameters and their distribution within the domain for two flow cases. The first case had an aortic waveform with a peak velocity at the inlet of 66cm/s and the second had a carotid waveform with a peak velocity of 91cm/s. From the derived haemodynamic wall parameter analysis, a region on the posterior wall of the CCA is predicted to experience potential atherosclerotic plaque formation in both cases. In the carotid waveform case, the region is predicted to be smaller but the plaque composition would contain more "destabilising" components

such as lipids and macrophages due to the presence of low shear stresses and reduced oscillatory shear. In contrast, the region in Case 1 is predicted to experience high oscillatory shear along with low shear stress. From the two flow cases examined on the same carotid, it is apparent that the geometrical features of the vessel provide the dominant factor for the induction of the local wall shear stresses distribution.

Chapter 7

The carotid bifurcation - an arterial geometry study

7.1 Introduction

In the current chapter the carotid bifurcations from three patients are examined. With the previous finding that geometry provides a strong influence on the developed wall shear stress and associated derived haemodynamic parameters, the intention of this chapter is to examine local geometrical influences. In order to do this, the Sazonov carotid waveform is used for the flow modelling in each case and a 60:40 flow division is applied for each internal and external carotid artery. The anonymous CT scans were provided by Royal Wolverhampton Hospital. The number of slices in each set ranged from 510 to 564. The mesh geometries are provided in Figure 7.1. All of the mesh geometries contained 10 structured boundary layers. The mesh for Patient 2 right carotid consisted of 6,934,199 linear tetrahedral elements and 1,185,109 nodes. The right carotid mesh for Patient 3 consisted of 6,111,472 elements and 1,047,301 nodes. The left carotid in Patient 4 had a more complicated and longer structure and the reconstructed mesh consisted of 13,124,417 elements and 2,239,739 nodes.

From Figure 7.1, it can be seen that the geometries for the right carotids of Patient 2 and 3 display some of the standard features expected within a carotid bifurcation. Namely, the internal carotid artery (ICA) diameter is greater than that of the external carotid artery (ECA) and in the Patient 3 right carotid the ICA narrows after the bifurcation (carotid sinus or bulb feature). The Patient 3 right carotid displays a smooth transition along its entire length (within the domain), whereas the Patient 2 right carotid has a

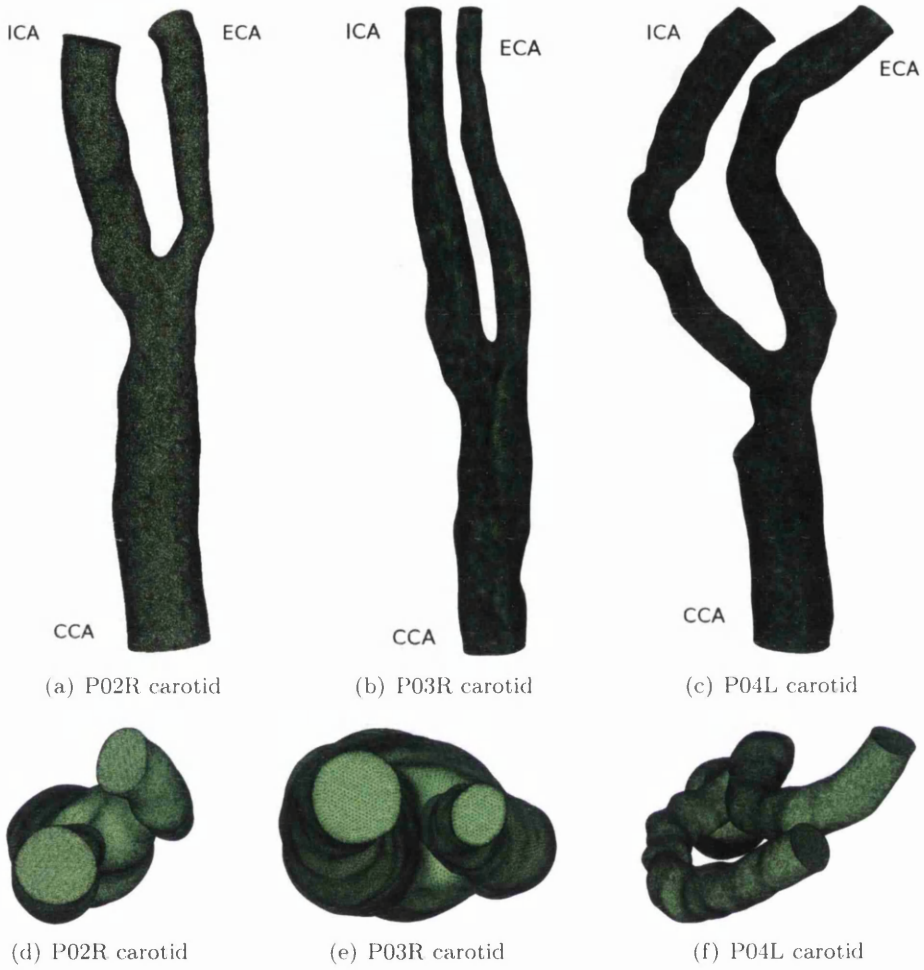

(a) P02R carotid (b) P03R carotid (c) P04L carotid

(d) P02R carotid (e) P03R carotid (f) P04L carotid

Figure 7.1: Carotid Mesh Geometries for Patient 2 right (P02R), Patient 3 right (P03R) and Patient 4 left (P04L).

sharp feature downstream of the bifurcation in the ECA. The left carotid in Patient 4 displayed less regular features due to calcification which can be clearly seen immediately upstream of the bifurcation.

As mentioned previously, the flow division between the ICA and ECA was chosen to be 60:40. Womersley velocity profiles were applied to both the inlet and the two outlets. The inlet mean flow rate for Patient 2 was set to $4.5\text{cm}^3/\text{s}$, which produced a peak velocity at the inlet of 96cm/s. This was chosen based on the accompanying ultrasound data which had a peak velocity of 87cm/s in the CCA although the radius and location were not known. Thus, while the ultrasound data was available, its usefulness was marginal. The mean flow rate at the inlet for Patient 4 was also chosen to be $4.5\text{cm}^3/\text{s}$ which gave a peak inlet velocity of 71cm/s which again was similar to the ultrasound

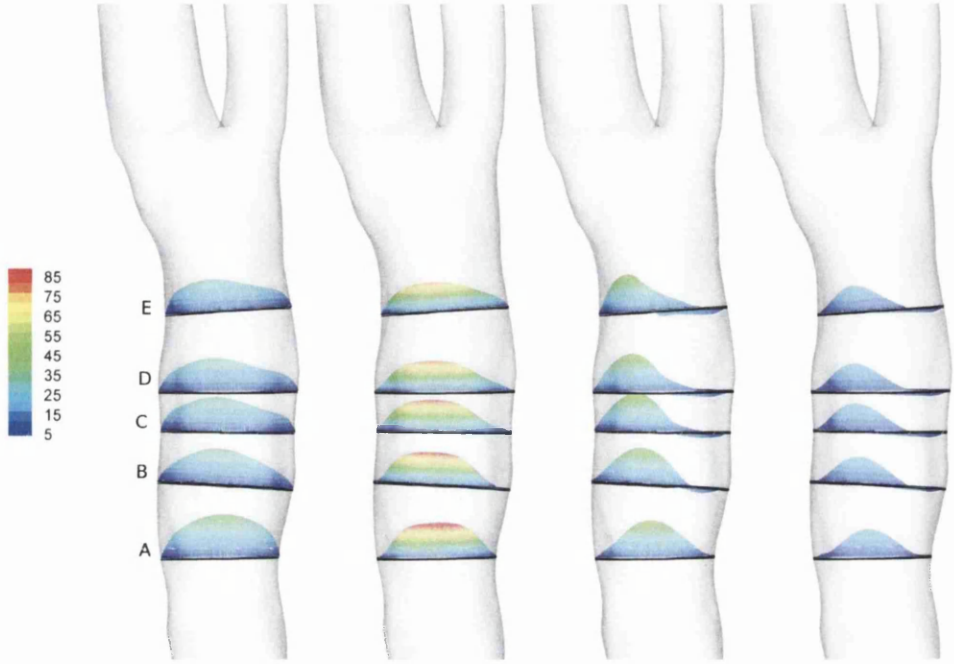

(a) Mid Accl. (b) Peak (c) Mid Decel. (d) Dicrotic notch

Figure 7.2: P03R. 3d velocity distribution within five slices (cm/s)

data of 73cm/s. There was no ultrasound data for Patient 3, so a peak centreline velocity of 101cm/s was assumed as this fell in the middle of the range (68-171cm/s) found by Holdsworth *et al* [120]. The cardiac cycle was decomposed into 240 real time steps in each case.

7.2 Flow Visualisation

As the flow enters the domain and traverses the common carotid artery (CCA) towards the bifurcation, minor geometrical features in the arterial wall of P03R alters the velocity profile within the CCA. This is shown in Figure 7.2 for four selected time instances. These are mid acceleration, peak flow, mid deceleration and the minimum flow between first and second systole peaks (dicrotic notch). The flow profile at second peak systole displays the same features as first peak systole. From the plot, the velocity profile at slice A displays only a slight deviation (during mid acceleration) from a Womersley profile. By slice B, however, geometrical features on the left lateral wall (righthand side as viewed) and the effect of bifurcation have induced a flow separation within the artery. This separation is clearly seen to develop over the four time instances in Figure

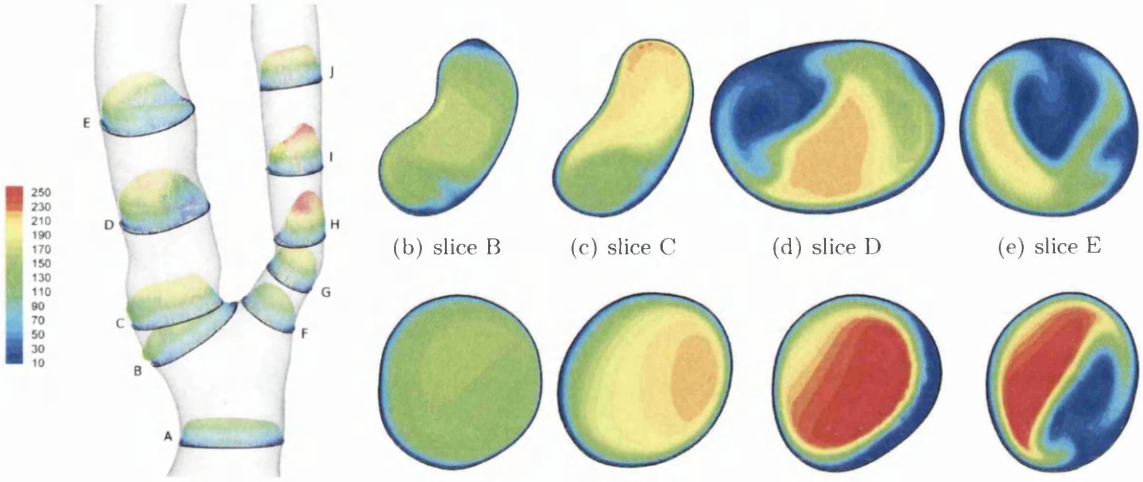

(a) Peak flow (b) slice B (c) slice C (d) slice D (e) slice E

(f) slice F (g) slice G (h) slice H (i) slice I

Figure 7.3: Flow at the bifurcation of P02R during peak flow. a) 3D slice representation at peak flow, b) to f) Velocity magnitude and distribution at the respective slice.

7.2. After second peak systole, flow is unidirectional. Within the same region, the velocities predicted are reduced across almost all time instances (outside accelerating flow). The peak velocity obtained during mid acceleration for the selected slices was 44.3 cm/s. This rises to 95.4 cm/s during peak flow. This indicates the increase in arterial diameter from the inlet due to the reduced (from 101 cm/s) velocity predicted. The peak value within the dicrotic notch instance was 23.1 cm/s.

The flow distribution within the CCA for P02R and P04L does not contain comparable recirculation zones and maintains a Womersley profile until the bifurcation. As the flow from the CCA enters the bifurcation, a region of complex flow is expected. Examining the P02R bifurcation during peak flow (Figure 7.3), it is possible to see the flow has split and many of the velocity profiles are increasingly skewed towards one wall in the ECA and ICA due to the curvature effects from the wall with progression downstream. The maximum predicted velocity magnitude in the ECA is 259cm/s for the selected slices and 271cm/s overall. These values are in close agreement with the recorded ultrasound results for the patient (Figure 7.4). In the ultrasound, the peak velocity in the cardiac cycle varies from 250cm/s to 280cm/s. The peak predicted velocity in the ICA (214cm/s) is higher than the ultrasound value of 181cm/s. However, the difference between the values is reduced closer to the bifurcation. From the obtained values, the choice of 60:40 flow division is acceptable.

Figure 7.5 gives the in-plane velocity vector distribution for the eight selected slices. While the flow remains unidirectional proximal to the bifurcation in the ECA, this is

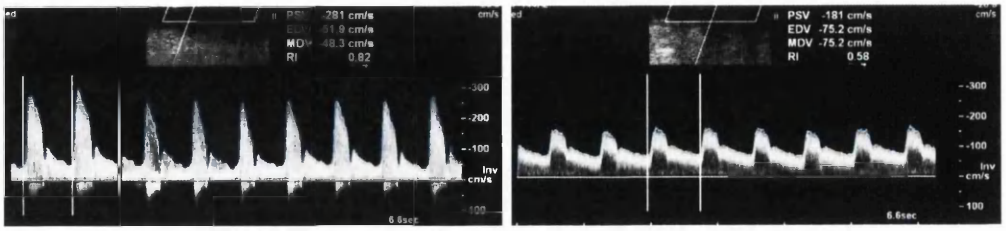

Figure 7.4: P02R Ultrasound proximal to the bifurcation a) ECA b) ICA

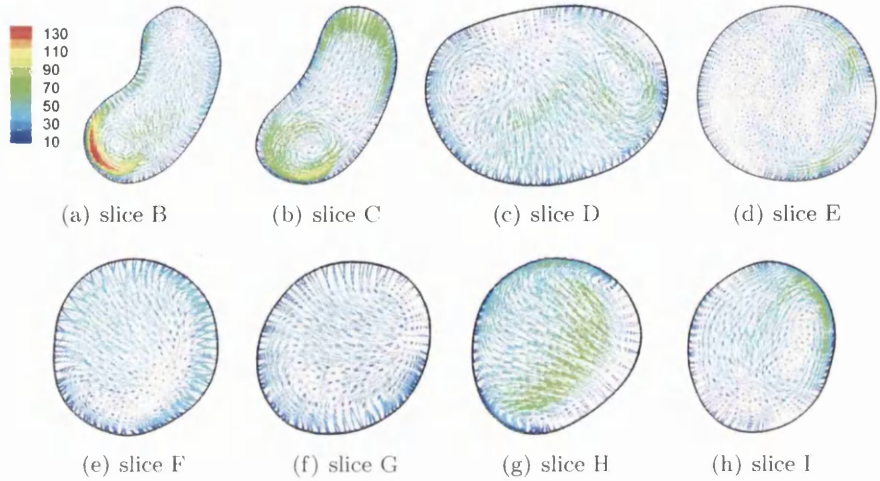

(a) slice B (b) slice C (c) slice D (d) slice E

(e) slice F (f) slice G (g) slice H (h) slice I

Figure 7.5: Flow at the bifurcation of P02R during peak flow. In-plane velocity vectors at eight cross sections (see Figure 7.3 for labels B-I).

not the case in the ICA. This is clearly visible in slice B and C where the vortex has a peak in-plane velocity of 137.4cm/s along the outer wall of the artery. The disturbed nature of the flow in the ICA is maintained during progression downstream, although in a reduced form. In the ECA the reverse is true, with the in-plane recirculation increasing further downstream from the bifurcation, due to the curvature of the artery. Peak in-plane velocity in the ECA is 64.4cm/s in slice I.

At the mid acceleration time instance (not shown), the in-plane velocities are much reduced (26cm/s in slice B) and the vortex present in slice B and C is yet to emerge. Elsewhere, the in-plane velocity distributions are in good agreement with those at the peak flow time instance. During the mid deceleration time instance, the in-plane velocity distribution is in good agreement with the peak flow time instance for all slices. The peak in-plane velocity within the vortex of slice B and C has reduced to 37cm/s. At the dicrotic notch this in-plane vortex velocity has reduced further to 8cm/s.

Moving from the bifurcation of P02R to the bifurcation in P03R, the flow distribution

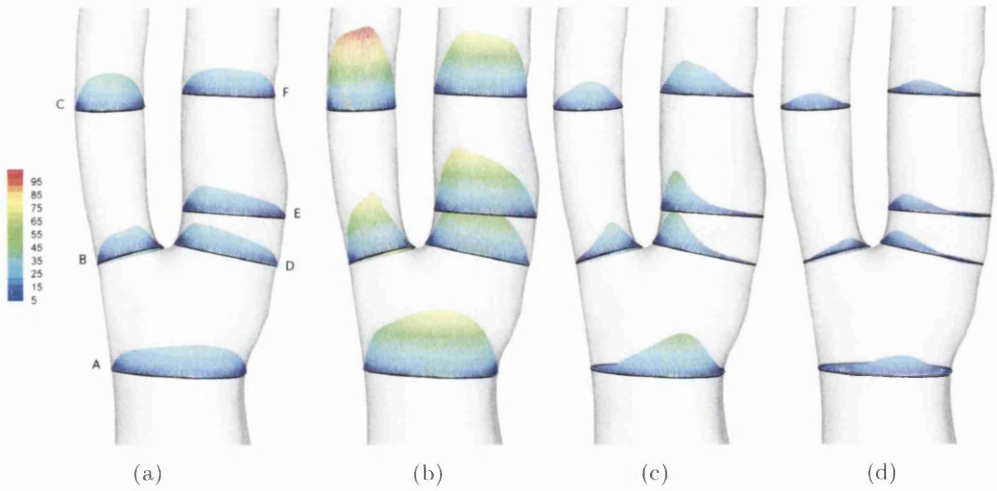

Figure 7.6: Velocity vectors at various flow phases for P03R. a) Mid acceleration b) Peak flow c) Mid deceleration d) Dicrotic notch

over the four time instances is given in Figure 7.6. From the figure, it can be seen that the transition between the CCA and the ICA/ECA is smooth due to the gentle curvature present. Flow in the ICA is higher along the inner wall and velocities are reduced along the outer wall. The same applies to the flow in the ECA. The distribution at each slice during the acceleration time instance is in good agreement with the respective peak flow time instance distribution. The velocity magnitudes at mid acceleration increase from 33cm/s in slice A (CCA) and slice E (ICA) to 45cm/s at slice C in the ECA. At peak flow, these values have increased to 79, 81 and 104 cm/s respectively. In contrast, in the deceleration phase and at the dicrotic notch the peak velocities are obtained within the ICA and CCA (both 52cm/s versus the 33cm/s in the ECA at mid deceleration).

Figure 7.7 displays the in-plane velocity vectors for slices A, B and D over the four selected time instances. In contrast to the flow patterns obtained for P02R, the in-plane velocity is minimal outside of the flow divider effect. The peak in-plane velocity predicted for P03R is 39cm/s compared to the 137cm/s predicted for P02R. Since there was no ultrasound data available for this patient, the velocities predicted cannot be quantified using patient-specific data.

The flow within the bifurcation region in P04L has more in common with P02R than P03R. The velocity magnitude and distribution for the mid acceleration time instance is given in Figure 7.8. From the figure, it can be seen that the flow has been skewed towards the inner wall of both the ICA and the ECA, whereas the flow upstream of the bifurcation in the CCA (slice A) is nearly parabolic. The peak velocity at this time

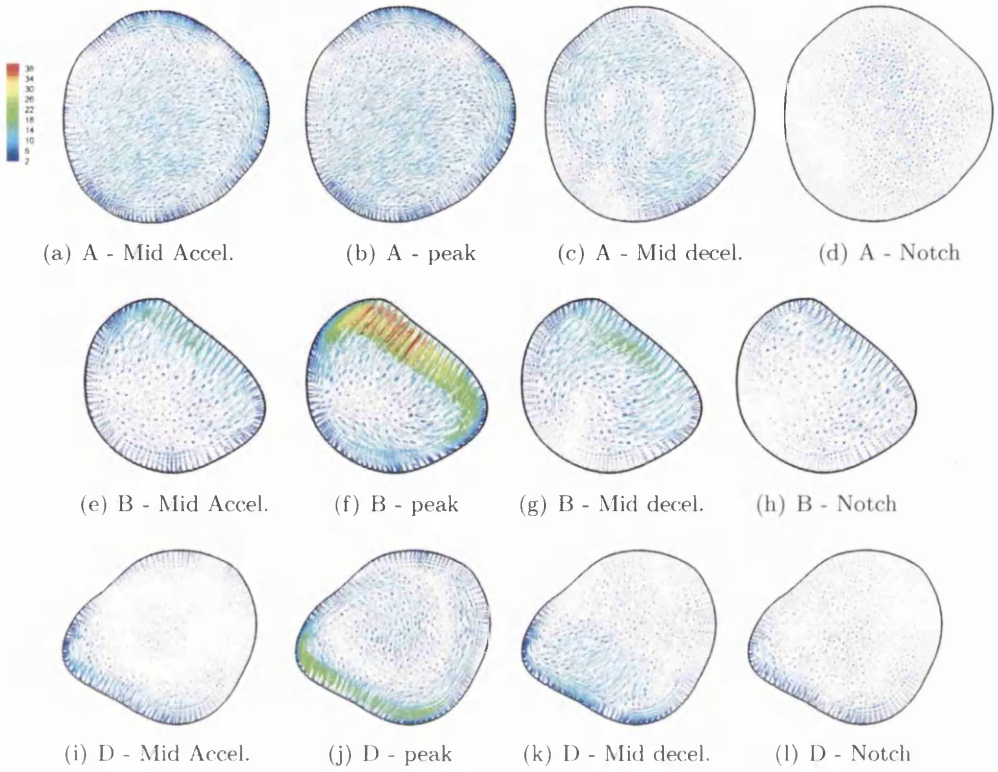

(a) A - Mid Accel. (b) A - peak (c) A - Mid decel. (d) A - Notch

(e) B - Mid Accel. (f) B - peak (g) B - Mid decel. (h) B - Notch

(i) D - Mid Accel. (j) D - peak (k) D - Mid decel. (l) D - Notch

Figure 7.7: Flow at the bifurcation of P03R during four time instances. In-plane velocity vectors at three cross sections

instance (for the selected slices) is 47cm/s at slice A, although slice B has a peak velocity of 44cm/s.

During peak flow (Figure 7.9), the skewing effect of the geometrical curvature is more pronounced. The maximum velocity in slice A has increased to 144cm/s. This value of 144cm/s in the CCA is high considering the peak inlet velocity is only 71cm/s due to the relatively large arterial diameter. The vessel diameter proximal to slice A is constricted by calcification. The ICA for this patient is rather narrow, relative to the ECA. As such, slice D in the ICA experiences the overall peak velocity for the selected slices, and all slices experience velocities greater than 140cm/s. A peak velocity of 164cm/s is predicted. While the ECA is relatively large the flow is concentrated by the curvature effects leaving 30-40% of slice F with velocities of <10cm/s. At the mid deceleration time instance, the flow is more uniformly distributed and the skewed nature of the flow in the ICA is reduced, although it is still present in slice D. Due to the larger cross sectional areas in the ECA at all three slices, the peak velocity values are significantly smaller than those of the ICA (90, 95 and 114cm/s in the ICA compared to 54, 58 and 34cm/s in the ECA).

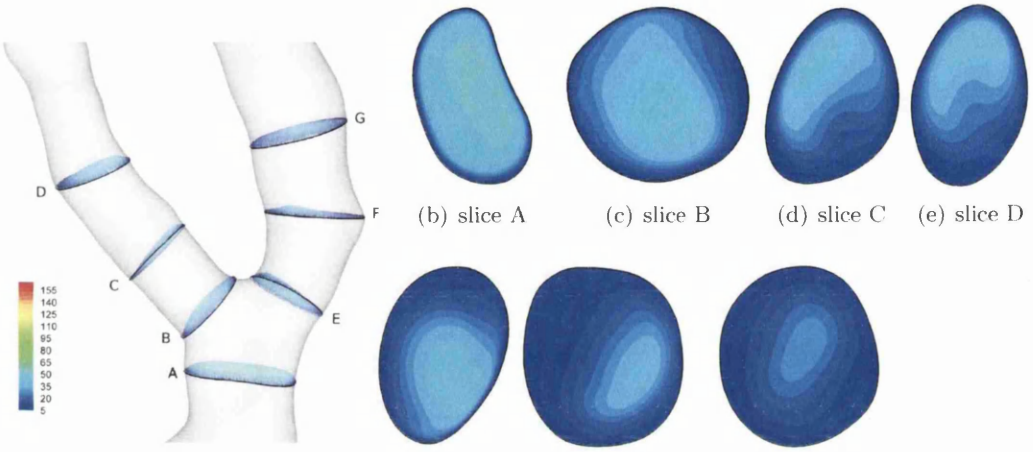

(a) Mid acceleration (b) slice A (c) slice B (d) slice C (e) slice D (f) slice E (g) slice F (h) slice G

Figure 7.8: Flow at the bifurcation of P04L during mid acceleration. a) 3D slice representation at peak flow, b) to h) Velocity magnitude and distribution at the respective slice.

From Figure 7.11 it can be seen that the flow in each of slices B, C and D contains an in-plane vortex, indicating the flow is swirling in a helical formation downstream of the bifurcation within the ICA. In contrast, the ECA flow demonstrates only minimal swirling effects proximal to the bifurcation and these are further reduced downstream. The swirling nature of the flow at the first systole peak is repeated at the mid deceleration phase in the ICA, whereas the ECA flow profile maintains only small in-plane velocities. During peak flow, the in-plane velocities in the ICA exceed 85cm/s in a large area of slice B. In contrast, only a small region exceeds 80cm/s with the majority experiencing an in-plane velocity of 40-50cm/s in the ECA slices. During the deceleration phase the in-plane velocities in the ECA reduce to less than 30cm/s. Peak in-plane velocity for this time instance is 64cm/s in the ICA. The predicted velocities in the ICA can be compared with ultrasound data for this patient, although no data on the ECA velocities was available. The ultrasound for the ICA proximal to the bifurcation is given in Figure 7.12. From the plot, the peak recorded velocity value was 169cm/s which is in good agreement with that of the peak in slice D of 164cm/s.

7.3 Haemodynamic Wall Parameter Investigation

The six haemodynamic wall parameters were investigated on the three carotid meshes and the results are presented in this section. The values obtained from the three

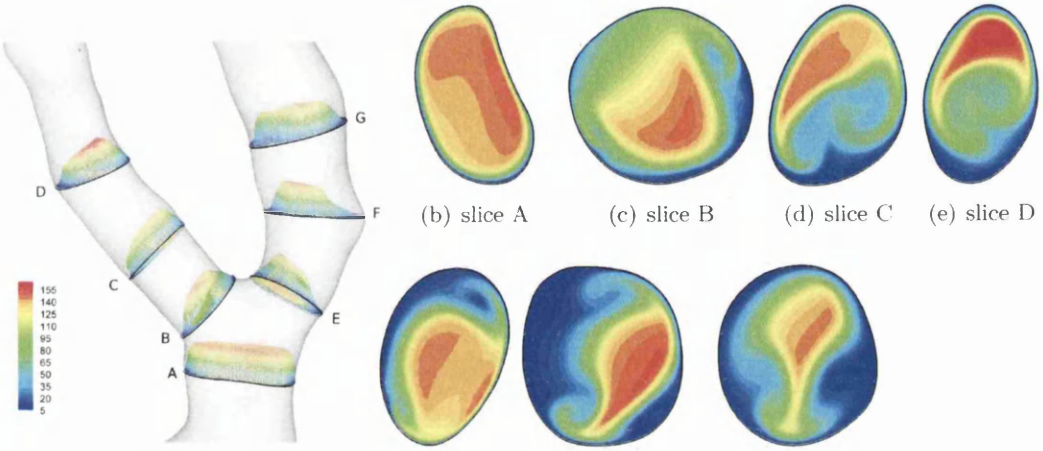

Figure 7.9: Flow at the bifurcation of P04L during peak flow. a) 3D slice representation at peak flow, b) to h) Velocity magnitude and distribution at the respective slice.

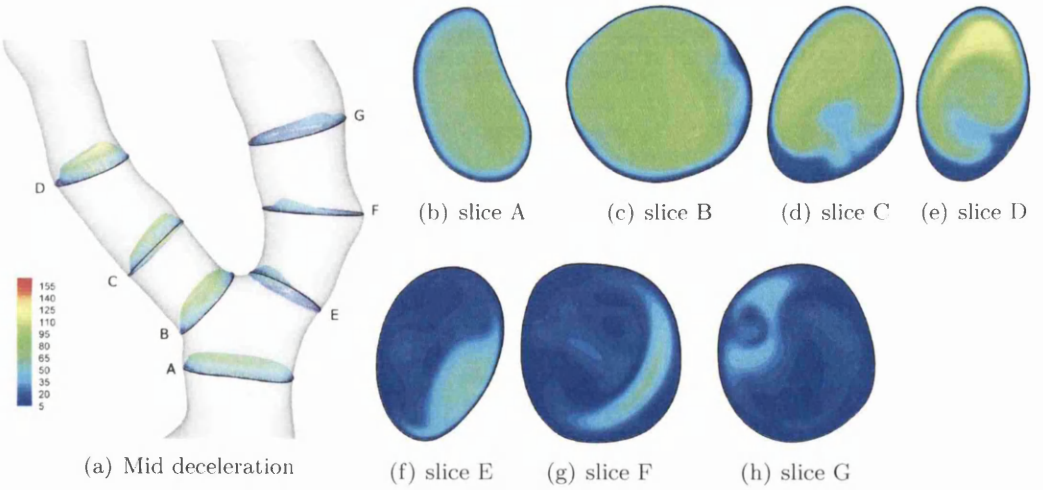

Figure 7.10: Flow at the bifurcation of P04L during mid deceleration. a) 3D slice representation at peak flow, b) to h) Velocity magnitude and distribution at the respective slice.

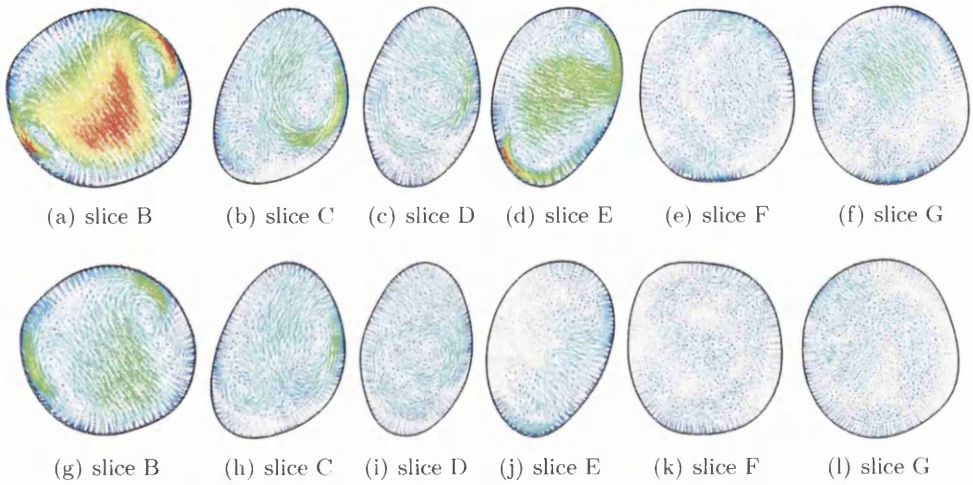

(a) slice B (b) slice C (c) slice D (d) slice E (e) slice F (f) slice G

(g) slice B (h) slice C (i) slice D (j) slice E (k) slice F (l) slice G

Figure 7.11: Flow at the bifurcation of P04L for two time instances. In-plane velocity vectors at six cross sections a) to f) are during peak flow and g) to l) are at mid deceleration.

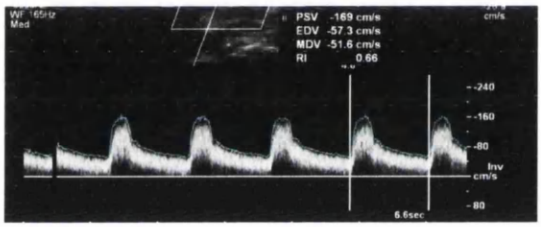

Figure 7.12: P04L Ultrasound in the ICA proximal to the bifurcation.

simulations are related to the observed flow patterns and compared between each carotid.

7.3.1 Time-averaged wall shear stress

The time-averaged wall shear stress (WSS) for the three carotid geometries is presented in Figure 7.13. From the figure, it is clear that the flow divider experiences high time-averaged WSS in all three carotid simulations. While the carotid of Patient 2 is predicted to experience a peak WSS at the apex just as the carotid simulations of Patient 1 in the previous chapter. The peak time-averaged WSS in P03R and P04L is located in the ECA and ICA respectively. In P02R, the peak time-averaged WSS is 467 dyne/cm^2. The point of maximum time-averaged WSS is closer to the inner wall of the ICA. A region of high time-averaged WSS extends upstream from the apex along the posterior wall and bisecting the CCA and ICA transition. This is due to the local narrowing or stenosis as shown in Figure 7.14(a) inducing the high velocity values in slice B and C. Within this

region, the time-averaged WSS ranges from 100-280 dyne/cm^2 away from the apex. The peak value of 467 dyne/cm^2 is located proximal to both the flow divider and the stenosis, inducing a higher time-averaged WSS than would otherwise be expected. Proximal to the flow divider, a band of high time-averaged WSS extends across the ECA entrance. Within this band, the time-averaged WSS values range from 100-180 dyne/cm^2, with a localised region experiencing a peak of 304 dyne/cm^2. These values and their location are in good agreement with the simulations of Patient 1 and the results of Younis *et al* [41]. Within the ECA itself, a secondary region of high time-averaged WSS values extend along the inner wall due to the curvature within the ECA itself and upstream of the divider. The angle of the ECA axis relative to the CCA axis for P02R is approximately 45 degrees, whereas the angle between the ECA and CCA axes for P03R is merely 5 degrees. These geometrical influences have skewed the flow entering the ECA such that high velocities are found proximal to the inner wall (as shown in slice G). This secondary region experiences time-averaged WSS values ranging from 100-250 dyne/cm^2 with a small region on the inner wall experiencing values exceeding 300 dyne/cm^2. Within the CCA, the time-averaged WSS values typically range between 10-25 dyne/cm^2 which is greater than the 5-10 dyne/cm^2 believed to stimulate an atherosclerosis inducing phenotype. A region corresponding to a narrowing by 15% of the upstream arterial diameter experiences elevated time-averaged WSS values exceeding 110 dyne/cm^2. Only in the CCA does a small region experience a time-averaged WSS of less than 5 dyne/cm^2. This is located approximately 1/3 of the distance from the inlet.

Examining the time-averaged WSS for P03R, the peak value, as mentioned, is obtained within the ECA. At the bifurcation itself, the localised peak time-averaged WSS is predicted to be 143 dyne/cm^2. The region of high WSS is located at the flow divider and closer to the inner wall of the ECA. Upon entering the ECA, the time-averaged WSS values are mildly elevated from less than 25 dyne/cm^2 to 40 dyne/cm^2. The peak time-averaged WSS predicted for P03R is 269 dyne/cm^2, proximal to a small local narrowing and influenced by arterial curvature. Over 50% of the ECA experiences time-averaged WSS values exceeding 50 dyne/cm^2. In contrast to P02R, a significant percentage (approx 40%) of the CCA experiences less than 5 dyne/cm^2 and virtually all values in CCA are less than 10 dyne/cm^2. A region distal to the flow divider and along the outer wall of the ICA also experiences time-averaged WSS of less than 5 dyne/cm^2 (as shown in pink in Figure 7.14(b)). This region extends to envelope the entire ICA apart from the inner wall, for the domain shown if a measure of less than 10 dyne/cm^2 is used as region of low time-averaged WSS. This is due to the flow favouring the inner wall of the ICA as can be seen in Figure 7.6 and no relevant in-plane recirculation (as demonstrated in slice D of Figure 7.7). The majority of the ICA experiences time-averaged WSS in

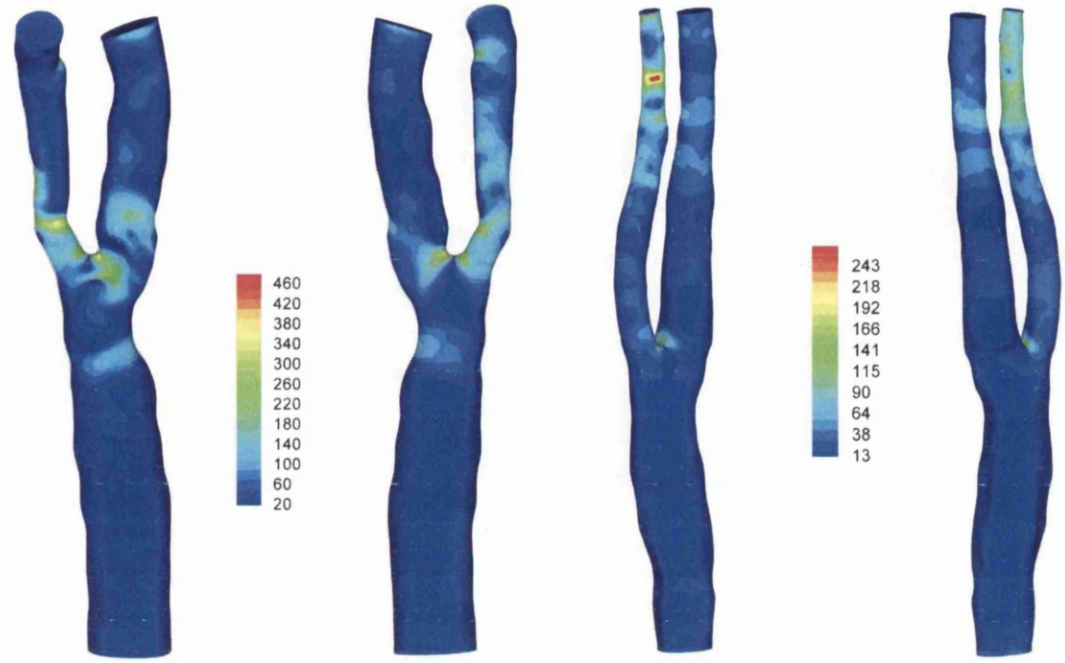

(a) P02R - Posterior (b) P02R - Anterior (c) P03R - Posterior (d) P03R - Anterior

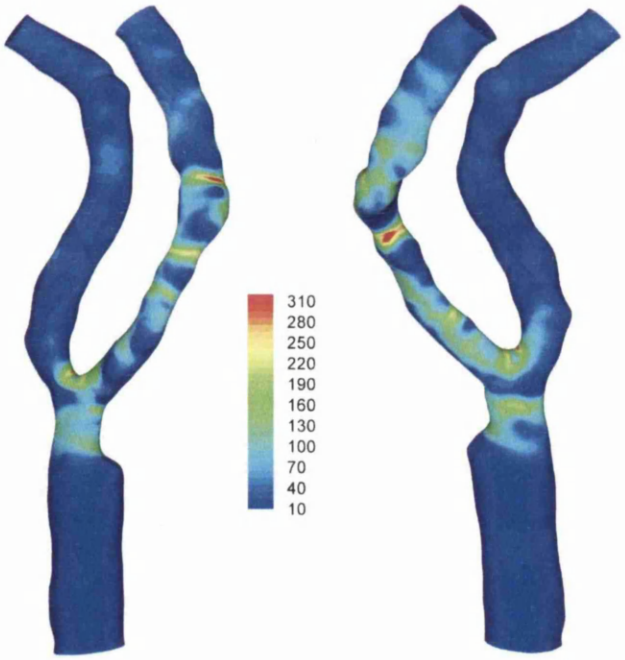

(e) P04L - Posterior (f) P04L - Anterior

Figure 7.13: time-averaged WSS distribution.

the range of 10-50 dyne/cm^2.

The time-averaged WSS distribution for P04L is also high at the apex. The bifurcation angles is similar to that of ECA of P02R. In this case, the angle between both the ICA to CCA and the ECA to CCA axis is approximately 40-45 degrees. The peak time-averaged WSS at the bifurcation is located nearer to the inner wall of the ECA and a localised region exceeds 250 dyne/cm^2. Whereas the ECA in P02R displays a band feature around the artery, no band of high WSS is present in P04L extending from the bifurcation. Instead, the high time-averaged WSS values extend along the inner wall, both proximally in the ECA and distally in the ICA. Regions of high time-averaged WSS are concentrated downstream of local narrowing. The peak time-averaged WSS of 318 dyne/cm^2 occurs in the ICA at a stenosis (30-35% change in diameter). A secondary peak of 298 dyne/cm^2 occurs downstream of this stenosis on the posterior wall. A majority of the ICA experiences elevated to high time-averaged WSS values, due to the relatively narrow width of the ICA compared to the ECA inducing both high and swirling flow. A small region within the ICA experiences a low time-averaged WSS of less than 5 dyne/cm^2. This region is located proximal and upstream of the stenosis. A significant region experiences this potentially atherosclerotic inducing low time-averaged WSS in the CCA. This region is located upstream of the calcified location given by slice A. The vast majority of the CCA of P04L experiences less than 10 dyne/cm^2. Although, proximal to the bifurcation, the time-averaged WSS values range from 100-180 dyne/cm^2 due to the calcification. In the ECA however, only a small region experiences this low time-averaged WSS (as given in pink by Figure 7.14(c)). Like the region predicted for P03R, this is along the outer wall. The majority of the ECA experiences between 10-25 dyne/cm^2.

Examining the three cases, the region of low WSS distal to the bifurcation and opposite the flow divider is seen in both P03R and P04L. This is in good qualitative agreement with that of Kaazempur-Mofrad *et al* [21] who found this occurred in three out of four patients. In their work, they theorised that the remaining patient did not experience a corresponding region of low shear stress due to a sudden constriction immediately distal to the bifurcation. P02R does experience a sudden constriction in the larger artery (ICA) such that no low shear stress region is induced. From the three cases, it is clear that while patient-specific geometrical features induce local variation, inter-patient comparison is also possible.

(a) P02R (b) P03R (c) P03R

Figure 7.14: Detail views of the time-averaged WSS distribution. Pink indicates regions of low time-averaged WSS believed be susceptible to an atherosclerosis inducing phenotype.

7.3.2 Maximum wall shear stress temporal gradient

The maximum wall shear stress temporal gradient (WSSTG) is given in Figure 7.15 for the three carotids. From the figure it is clear that the distribution of WSSTG is in good agreement with that of the time-averaged WSS distribution for P03R. However, the distributions within P02R and P04L contain significant differences. In P03R, only minor differences occur upstream of the stenosis in the ECA. At the apex, the peak predicted WSSTG is 15000 dyne/cm^2s. In the ECA, however, the WSSTG values exceed 10000 dyne/cm^2s in approximately 30% of the artery, with an overall predicted peak of 39000 dyne/cm^2s. In [21], values in excess of 40000 dyne/cm^2s are encountered in the diseased carotids. In the carotid of P02R, the regions of high time-averaged WSS correspond with regions of high WSSTG. Indeed, the peak values of both parameters occur in the same small region. The predicted peak value in the P02R carotid is 70100 dyne/cm^2s. Regions of WSSTG exceeding 40000 dyne/cm^2s extend proximal to the bifurcation into both the ICA and the ECA. At the ICA outlet, the high values are the result of imposing the flow profile and are ignored here. It is in the ICA that the most differences exist between the time-averaged WSS and WSSTG distributions. While the differences are localised to the ICA for P02R, significant differences exist between the two distributions in the carotid P04L for all three arteries. In the CCA, the majority experiences less than 2500 dyne/cm^2s which is in good agreement with [41]. In contrast only 10-15% of the ICA experiences a maximum WSSTG of less than 5000 dyne/cm^2s. In the ECA, this percentage is approximately 40-50%. At the bifurcation, the peak WSSTG value exceeds 40000 dyne/cm^2s, while the maximum predicted values occur in four small regions of the ICA. Each exceeds 85000 dyne/cm^2s, with the peak being

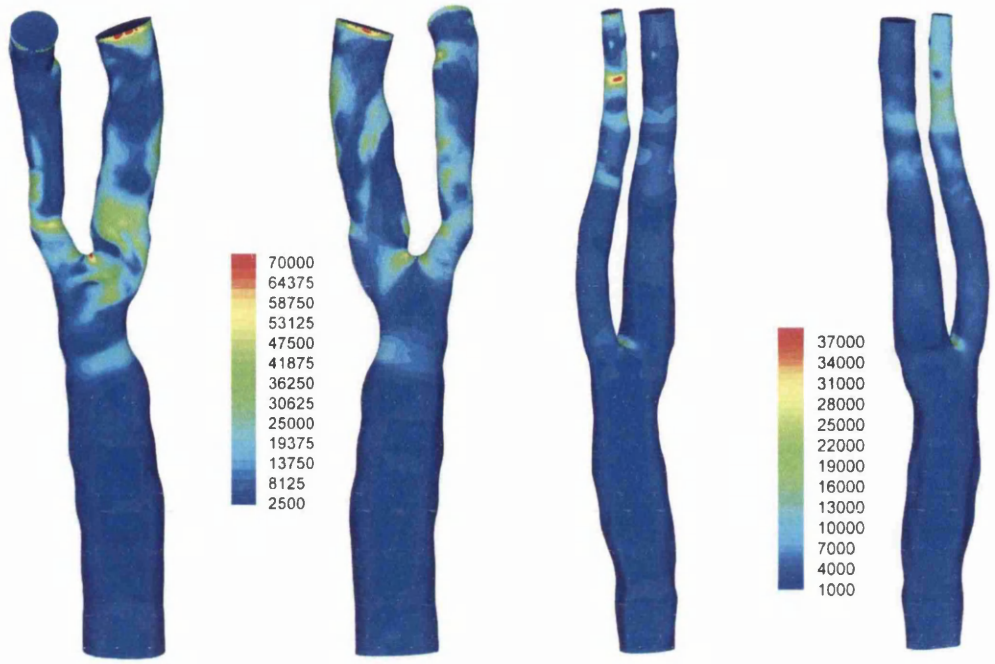

(a) P02R - Posterior (b) P02R - Anterior (c) P03R - Posterior (d) P03R - Anterior

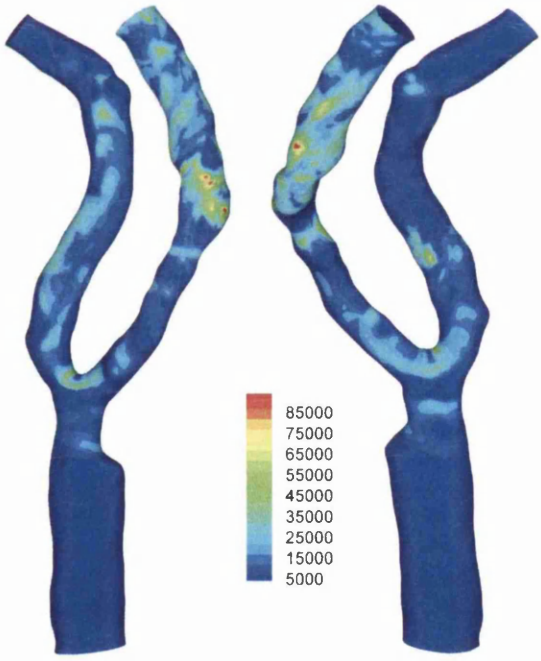

(e) P04L - Posterior (f) P04L - Anterior

Figure 7.15: Maximum wall shear stress temporal gradient (WSSTG) distribution in dyne/cm$^2 s$

95100 dyne/cm$^2 s$.

With the work of Vermeersch *et al* [37] finding a negative correlation between high WSSTG and intima media thickness for both the ICA and the CCA, the predicted WSSTG distributions for the three carotids indicate the CCA is at risk of increased intima media thickening since all experience low (defined as less than 2500 dyne cm$^{-2}s^{-1}$) WSSTG values. (70% in P02R, 95% in P03R and 65% in P04L). Outside of the CCA, the low time-averaged WSS regions of P03R and P04L also experience low WSSTG. Although in P03R the region of low WSSTG extends to envelope all of the distended ICA. Smaller regions of low WSSTG exist in the ICA and ICA of all three subjects and will be referred to further later.

7.3.3 Time-averaged wall shear stress spatial gradient

The time-averaged wall shear stress gradient (WSSG) for the three carotids is given in Figure 7.16. The distribution of WSSG displays many similarities between those of time-averaged WSS and WSSTG. However, there are also differences between the distributions as there were between time-averaged WSS and WSSTG. In P02R, the peak of 5.28×10^6 dyne/cm^3 is located at the point of maximum WSSTG and time-averaged WSS. In P03R the value predicted at the apex is less than that of P02R, with a reduction of 70% to 1.6×10^6 dyne/cm^3. At the stenosis within the ECA, the peak WSSG value is predicted to be 5.1×10^6 dyne/cm^3. Not only is this value comparable to that obtained within P02R, but both are located proximal to a local narrowing. In the carotid of P04L the peak WSSG value of 3.5×10^6 dyne/cm^3 is again proximal to a local narrowing. In P04L the peak corresponds to the secondary peak of time-averaged WSS. At the peak time-averaged WSS location, the WSSG value is high but only 70% of the peak WSSG value. Examining low WSSG values (pink regions denote less than 3000 dyne/cm^3) in Figure 7.17 it is clear that low WSSG values correspond to regions of low time-averaged WSS as expected, in both the CCA and distal to the flow divider along the outer wall.

WSSG is the third wall parameter that is negatively correlated to increased intima media thickness [37]. However, this correlation was only found in the CCA and not in the ICA. The ECA correlation was not examined. The work of Barbee *et al* [122] examined (using atomic force microscopy) the surfaces of living endothelial cells in a culture. They found that both shear stress and the spatial gradient of the wall shear stress induced alignment between the endothelial cells. With alignment, the smooth surface of unsheared cells was transformed into a surface exhibiting ridges extending in the direction of the flow

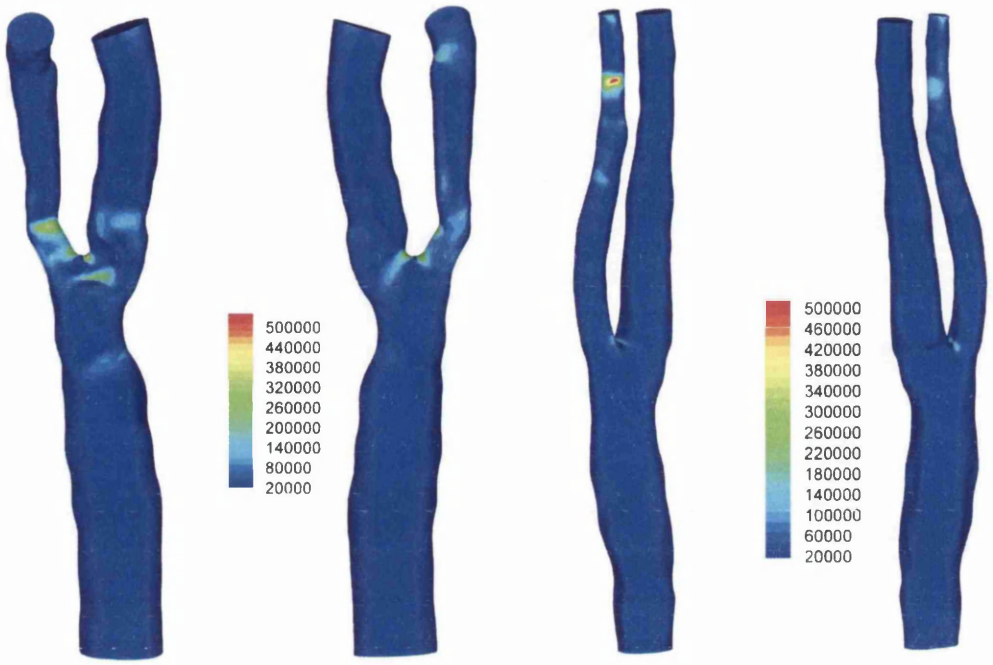

(a) P02R - Posterior (b) P02R - Anterior (c) P03R - Posterior (d) P03R - Anterior

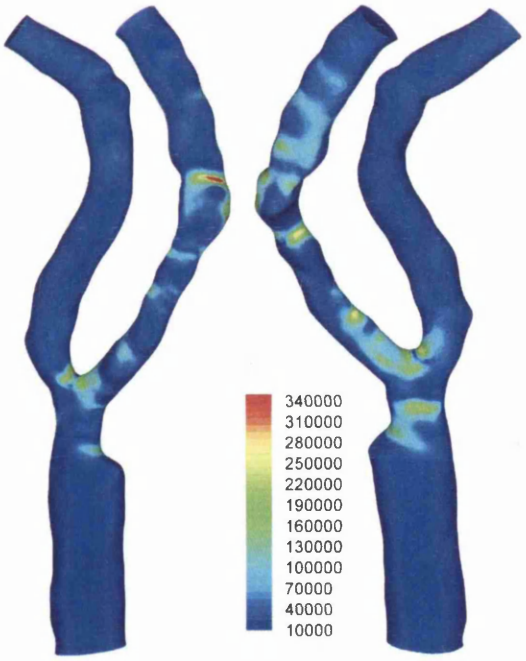

(e) P04L - Posterior (f) P04L - Anterior

Figure 7.16: Time-averaged wall shear stress spatial gradient (WSSG) distribution in dyne/cm^3

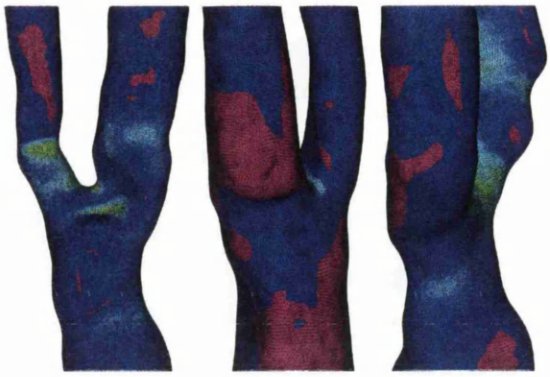

(a) P02R (b) P03R (c) P03R

Figure 7.17: Detail views of the time-averaged WSSG distribution. Pink indicates regions of low time-averaged WSSG believed be susceptible to an atherosclerosis inducing phenotype.

within 24 hours. Therefore, while no correlation was found for the subjects studied, the WSSG distribution within the ICA and ECA may still be relevant. While the work of Glor *et al* [19] found that while the WSSG distribution for a particular patient is highly reproducible on scans taken several weeks apart, the magnitudes were not. This also applied to time-averaged WSS and WSSTG. They concluded this is due to two factors. Accurate segmentation and meshing is required to capture these magnitudes, but also the waveform itself may alter significantly depending on condition of the patient.

7.3.4 Oscillating Shear Index

Figure 7.18 gives the distribution of the oscillating shear index for the three cases. In the CCA of P02R, the OSI values are minimal, with only a small region displaying mildly elevated values (0.05-0.11). This region corresponds to the only region within P02R displaying time-averaged WSS values of less than 5 dyne/cm^2. These values together with low WSSG and WSSTG (less than 1000 dyne/cm^3 and 1000 dyne/cm^{2}s respectively) indicate a potential region of atherogenesis. While the oscillating shear index at this point is low, atherosclerosis is believed to develop in regions of low or oscillatory shear stresses. As outlined in [29], the "destabilising" components within the plaque composition would be greater in low rather than oscillatory shear. A small region of elevated OSI extends from the flow divider along the anterior outer wall which is in good agreement with the results obtained for Patient 1. In the ECA, a region of high OSI extends from the inner wall of the sharp curvature downstream to the outlet. This wall region corresponds to low velocities within the flow due to the curvature skewing

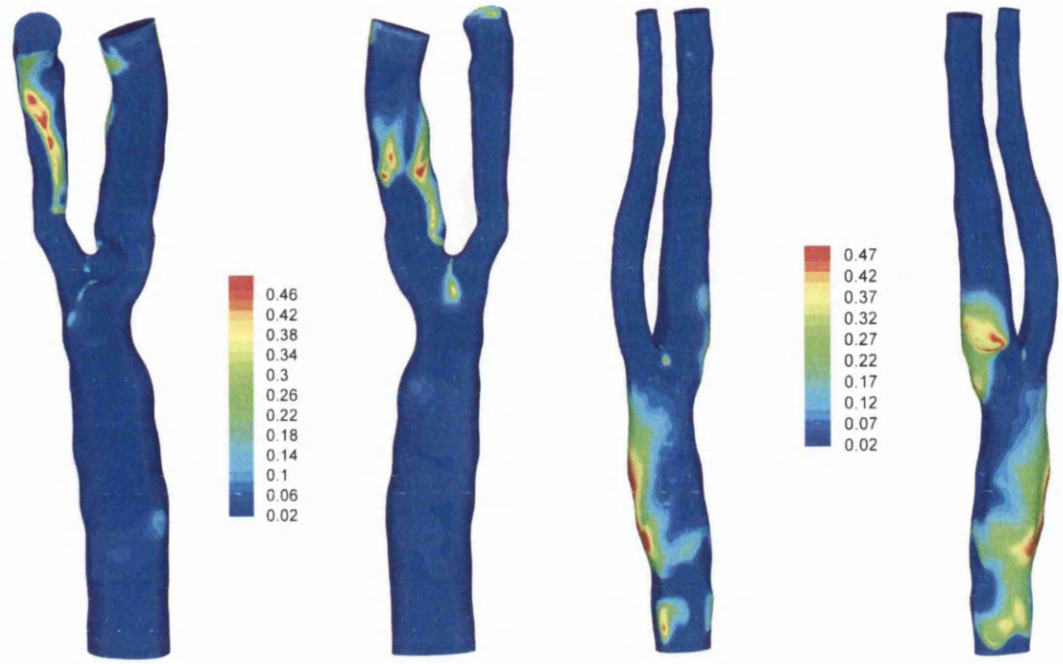

(a) P02R - Posterior (b) P02R - Anterior (c) P03R - Posterior (d) P03R - Anterior

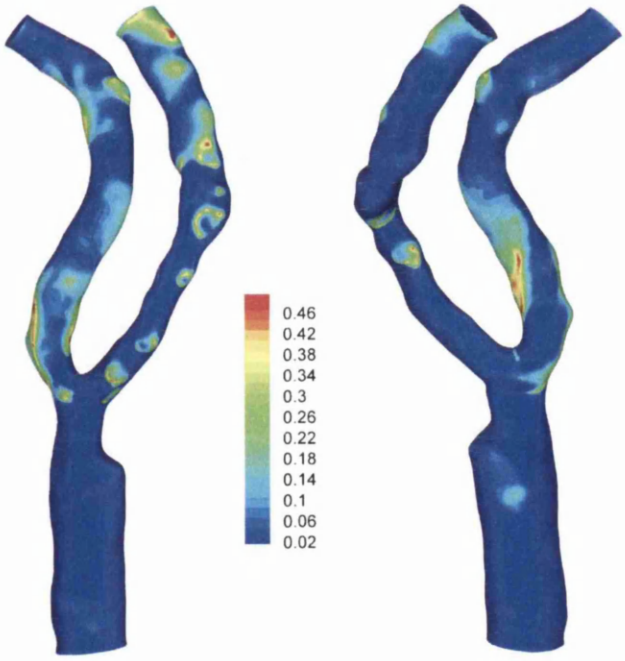

(e) P04L - Posterior (f) P04L - Anterior

Figure 7.18: Oscillating shear index (OSI) distribution (-)

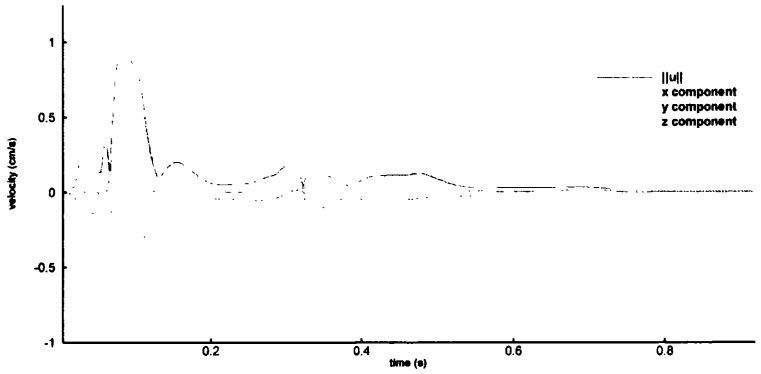

Figure 7.19: Velocity transient profile for node near high OSI region proximal to a stenosis in P02R

the flow to the outer wall, resulting in low (10-15 dyne/cm^2) time-averaged WSS. High OSI is also predicted within the ICA along the anterior wall. Again this corresponds to low velocities proximal to the wall (as can be seen in slice D and E). The high OSI region extends along the inner wall towards the stenosis proximal to the flow divider. A sample element close to the stenosis experiencing high OSI was selected, with the transient velocity profile recorded and presented in Figure 7.19 for the in-stream node. In the figure, a local transformation has been performed, with the Z component of the velocity normal to the wall surface. As can be seen that low oscillatory velocity is present at the sample node.

In P03R, the oscillating shear index is high in the majority of the CCA, while absent from the ECA due to the narrow width of the artery and it's relatively shallow curvature avoiding the induction of skewed or swirling flow. The regions of high OSI in the CCA correspond to regions of low or reverse flow as shown in Figure 7.2. As in the CCA, the region in the ICA experiencing high OSI is distal to a local narrowing and along the outer wall. This is in good agreement with that of [21]. This pattern of high OSI distal to a local narrowing is more obvious in the ICA of P04L (as shown in Figure 7.20). In the ECA however, the high OSI is the result of the flow separation which is visible in Figure 7.9. Together with a relatively wide arterial diameter results in low velocities and recirculation zones near both the inner and outer walls.

From the OSI distributions it is possible to see that there are two alternative explanations for high or elevated OSI. The first cause of predicted high OSI is due to a local narrowing, with the high OSI values obtained distal to the narrowing. The second cause of high OSI is arterial curvature, most likely encountered within the bifurcation region and may induce high OSI in either the inner wall of the curve or both, depending on the severity of flow separation caused by the curvature.

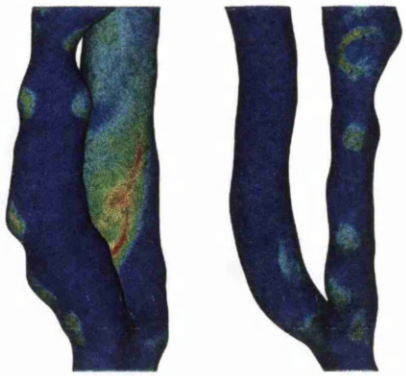

(a) OSI (b) WSSAD

Figure 7.20: Detail views of the oscillating indicators in the ICA of P04L.

7.3.5 Wall shear stress angle deviation and angle gradient

The distributions of wall shear stress angle deviation (WSSAD) and wall shear stress angle gradient (WSSAG) are virtually identical and hence shall both be discussed in this section. The distribution of WSSAD is presented in Figure 7.21 and WSSAG in Figure 7.22. From the figures it is clear that in contrast to the OSI parameter, only small elongated regions experience high or elevated WSSAD (and hence WSSAG). In the ICA of P04L these small regions correlate well with the OSI values as shown in Figure 7.20. In the CCA and extending into the ECA, small regions of elevated WSSAD are predicted. These correspond well to the outline of a region of high OSI. In the remainder of the CCA, WSSAD remains minimal. In P03R, only mildly elevated WSSAD values are predicted away from the flow divider. These elevated values are predicted along the anterior wall of the ICA prior to a local widening of the artery. Only low WSSAD is predicted within the CCA. Peak WSSAD values are predicted at the flow divider, which is in excellent agreement with that of P04L. The distribution of WSSAD in P02R contains significant regions of elevated or high predicted values. Three small regions are located near the flow divider. The first occurs at the apex as in the cases of P03R and P04L. The second and third occur proximal to the stenosis within the ICA entrance. Elevated regions also extend along the inner wall of the ECA downstream of the sharp curvature. In the CCA the WSSAD values are minimal which is in good agreement with P03R and P04L.

In order to understand the differences between the WSSAD/WSSAG distributions and OSI, it is worth considering what the respective parameter represents. While OSI is concerned with deviation of the flow direction from the historial mean shear stress direction at a node, the (time-averaged) WSSAD parameter is concerned with the

shear stress directions of the surrounding region at any time instance. Thus, the OSI parameter provides information on transient oscillation whereas the WSSAD parameter provides data on spatial oscillation in the region. Where the two parameters coincide in predicting elevated or high values then the oscillations are predicted to be both transient and spatial. High values of WSSAD and WSSAG may be considered normal at the flow divider as the flow is being directed into two different arteries. Glor *et al* [19] demonstrated that both qualitatively and quantitatively the parameters of OSI and WSSAD were highly reproducible (>90%) on scans taken weeks apart, ensuring that the predicted results for these parameters are relevant and reproducible.

7.3.6 In combination

In the previous subsections, the individual haemodynamic wall parameter distribution has been examined in its respective section. However, in order to assess potential regions of atherogenesis it is necessary to examine the derived parameters together to provide an overall assessment. While the patient carotids have been compared within the previous sections, it is worth considering each patient in turn for this assessment before contrasting between patients.

Beginning with P02R, only one small region experiences a time-averaged WSS of less than 5 dyne/cm^2. This region is located one third of the length from the inlet to the bifurcation within the CCA. Coincident with this low time-averaged WSS is mildly elevated OSI but the other parameters remain low. Together, this is indicative of a possible region of vulnerable plaque lesion formation. At the bifurcation, the stenosis across the entrance to the ICA experiences high time-averaged WSS although small regions of high OSI and WSSAD/WSSAG occur both upstream and downstream of the stenosis, indicating possible regions of further growth. The high time-averaged WSS values between 250-450 dyne/cm^2 indicate potential platelet thrombus formation [47], especially when considering that under exercise etc the WSS values can double [19]. Smedby [123] through the study of 237 femoral arteries determined that growth of a stenosis downstream was most likely. This tallies excellently with the high OSI/WSSAD region extending downstream (time-averaged WSS for this region less than 10 dyne/cm^2) from the stenosis and only small upstream regions of potential growth indicated. In the ECA the region of high OSI coincides with low WSSG, WSSTG and time-averaged WSS along with elevated WSSAD indicating another potential region of atherosclerotic plaque formation although due to high transient and spatial oscillations any lesion would likely be stable.

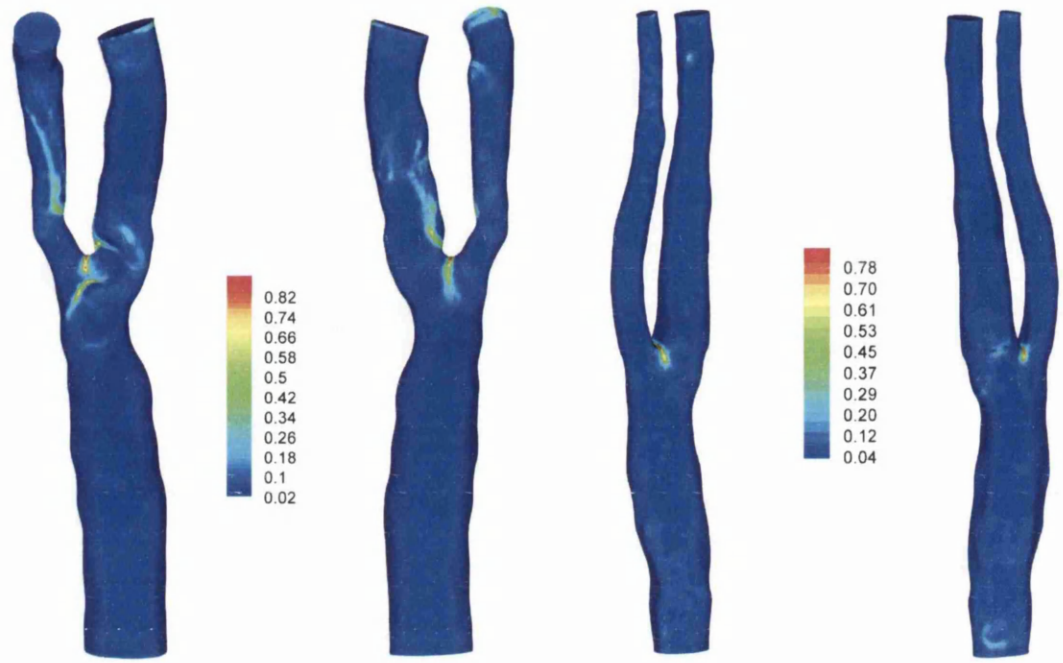

(a) P02R - Posterior (b) P02R - Anterior (c) P03R - Posterior (d) P03R - Anterior

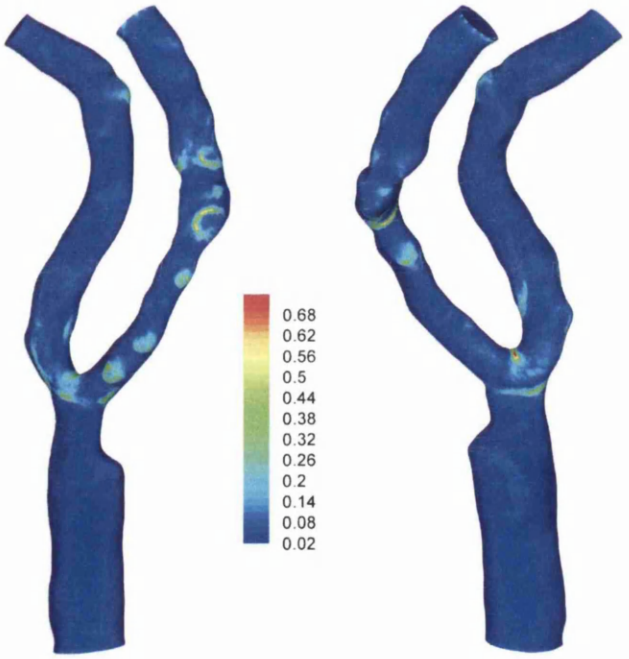

(e) P04L - Posterior (f) P04L - Anterior

Figure 7.21: Wall shear stress angle deviation (WSSAD) distribution (rad)

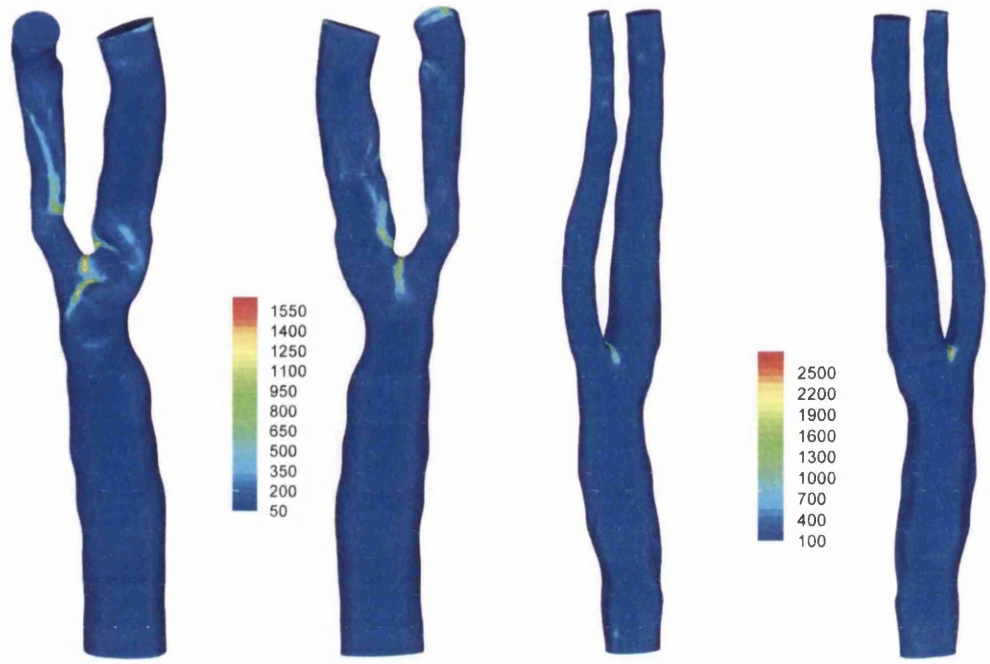

(a) P02R - Posterior (b) P02R - Anterior (c) P03R - Posterior (d) P03R - Anterior

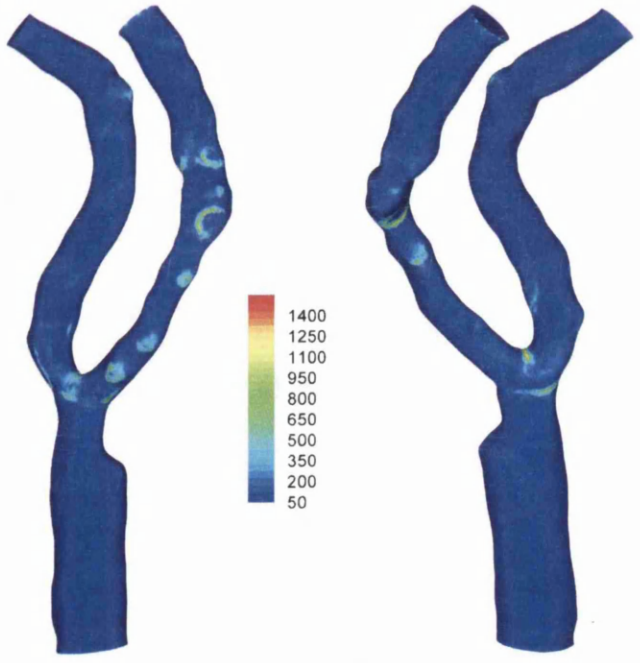

(e) P04L - Posterior (f) P04L - Anterior

Figure 7.22: Wall shear stress angle gradient (WSSAG) distribution (rad/cm)

P03R in contrast contains only minimal spatial oscillation (as defined by WSSAD and WSSAG), with the expected high values obtained at the flow divider. Transient oscillations are predicted due to flow separation along the outer wall of the ICA. This region is a potential region of atheroma due to low time-averaged WSS (less than 5 dyne/cm^2), WSSG and WSSTG. Spatial oscillation is negligible however, decreasing the likelihood of atherogenesis. In the CCA, significant regions experience high OSI and low time-averaged WSS, WSSG and WSSTG. WSSAD and WSSAG are again minimal, although within the CCA, Vermeersch *et al* [37] determined that OSI better correlated to increased IMT than WSSAG. Therefore this region has a greater likelihood of atherogenesis than that of the ICA region. In the ECA, the high time-averaged WSS, WSSG and WSSTG along with low OSI, WSSAD and WSSAG indicate a low potential for plaque formation.

The ICA in P04L contains numerous small regions of potential atherogenesis, as indicated by sustained spatial oscillations as well as transient oscillation. While almost all of these regions experience low time-averaged WSS, WSSG and WSSTG, the region along the posterior wall at the location of maximum curvature contains time-averaged WSS in excess of 40-50 dyne/cm^2, indicating that this region is subjected to athero-protective influences. At the bifurcation, elevated WSSAD and WSSAG values are predicted away from the apex along with high time-averaged WSS (150-190 dyne/cm^2) and low OSI due to the narrowing of the artery. The narrowing is due to calcification (visible on original CT data), which indicates the prior flow conditions that may have influenced initial atheroma are no longer present. Below the narrowing lies a significant region of low time-averaged WSS of less than 5 dyne/cm^2 indicating a region of potential expansion of the current plaque formation. With low OSI predicted for this region the lesions would likely consist of vulnerable plaque. In the ECA a region distal to the flow divider exhibits high OSI, mildly elevated WSSAD/WSSAG and low time-averaged WSS (less than 5 dyne/cm^2) as well as low WSSG and WSSTG. This is indicative of a potential region of atherogenesis.

With the study of only three carotid geometries it is possible to see factors that influence the distributions of the derived parameters. It is clear that a region distal to the flow divider is a potential region of atherosclerotic plaque formation (in 2 out of 3 of these carotids and 3 out of 4 in [21]). With the remaining artery already subjected to a stenosis proximal to this region the implications are even clearer. The CCA in all three subjects experienced relatively low time-averaged WSS although only a small region in P02R experienced less than 5 dyne/cm^2 compared to more significant regions in P03R and P04L. Flow within the ICA and ECA in general is disturbed and swirling, although this is reduced with smaller bifurcation angle differences between the relative arterial axes.

Downstream of the bifurcation, the time-averaged WSS, WSSG and WSSTG values tend to be higher (and locally significantly so) than in the CCA. At the bifurcation itself, the WSSAD and WSSAG values are expected to be high since flow is dividing between the ICA and ECA. A high time-averaged WSS, along with WSSG and WSSTG is expected at the apex although in all three carotids the location is not central and tends to either the ICA or ECA. While the apex value of time-averaged WSS is high, the peak location is dependent upon any stenosis present within the domain. If the stenosis is proximal to the bifurcation as it is in P02R, then the peak time-averaged values are significantly increased to potentially life threatening levels due to increased risk of rupture.

7.4 Summary

From the flow visualisation it is clear that the bifurcation induces complex flow patterns within the artery, with both swirling flow, flow separation and recirculation occurring. The angle of the bifurcation influences the degree of flow separation experienced downstream. Ultrasound data, where present, has been used as collaborative information to assess the suitability of the chosen assumptions of peak centreline velocity and flow division along with the use of Womersley profiles. The ultrasound data was in good agreement for the right internal/external carotid of Patient 2 and the left internal carotid of Patient 4. Data was unavailable for Patient 3. Finally, the haemodynamic wall parameters were investigated on the three carotids studied. The distributions and magnitudes of the parameters were compared between the three carotids and to other works, establishing both similarities as well as divergences between the carotids. This emphasises the need for patient-specific modelling with regard to wall shear stress analysis while allowing for possible local geometrical feature classification.

Chapter 8

Investigation of flow within a stenosed carotid

8.1 Introduction

In this chapter the flow through a diseased carotid is discussed. In the preliminary study of a carotid bifurcation, two alternative flow cases were assumed in order to assess their influence on the wall shear stress and its associated wall parameters for a healthy carotid geometry. In the current chapter, these flow assumptions are investigated on a diseased carotid. This carotid was chosen due to both the degree of stenosis but also due to it's location in relation to the bifurcation. In the previous chapter, the investigations on the three carotids revealed that potential atherogenesis would be expected in this region. From the four long carotid geometries presented in this thesis, 2 predict atherosclerotic plaque formation in this region and 2 already have a stenosis. While atherogenesis is believed to be induced by low or oscillatory shear stresses, the stenosis has already formed. As such, the atherosclerosis is well advanced and plaque formation is continuing under high wall shear stress. Within this geometry, possible rupture due to high WSS is also a factor to be considered. The aim of this chapter is to assess the importance of the flow assumptions both generally within the domain, but specifically around the stenosis.

The chapter has been split into several component sections. In the first section, the standard flow modelling assumptions of a 60:40 flow division are imposed. Since no ultrasound scan data was provided for this patient, the inlet flow was assumed to have a maximum velocity of 101 cm/s. This can be considered the baseline case and a

detailed examination of the flow conditions within the domain and resultant derived wall shear stress distributions are examined in this case. The second case assumed a reduced centreline velocity, giving a peak of 68cm/s. The third case takes into account the expected extra resistance within the ICA due to the stenosis and a flow division of 50:50 is imposed. A fourth case, involving an increased centreline velocity and altered flow division was also explored. Differences and similarities between the modified cases and the baseline will be highlighted.

8.2 Problem Outline

The Patient 03 left carotid geometry was reconstructed from a CT (Neck Contrast) scan taken in Royal Wolverhampton Hospital. The set consisted of 564 slices. Following previous mesh convergence studies only one detailed mesh was utilised to study the blood flow. This mesh consisted of 4,126,777 linear tetrahedral elements and 708,191 nodes with ten structured boundary layers. The left carotid of Patient 03 (P03L) has a stenosis within the internal carotid artery (ICA) immediately downstream of the bifurcation (Figure 8.1) The stenosis occludes approximately 65% of the ICA.

Figure 8.1: Patient 03 Left Carotid (P03L). Mesh Geometry.

8.3 First Case - Baseline

The maximum wall shear stress was analysed over one complete and one partial cycle to confirm that the results are representative of a generic cardiac cycle. The results obtained are shown in Figure 8.2. An overall peak WSS value of 3542 dyne/cm^2 was

predicted. Comparison between the two predicted peak WSS values in cycle one and cycle two is excellent. The percentage difference is only 0.008%. The only minor differences occur pre systole, therefore the results are representative.

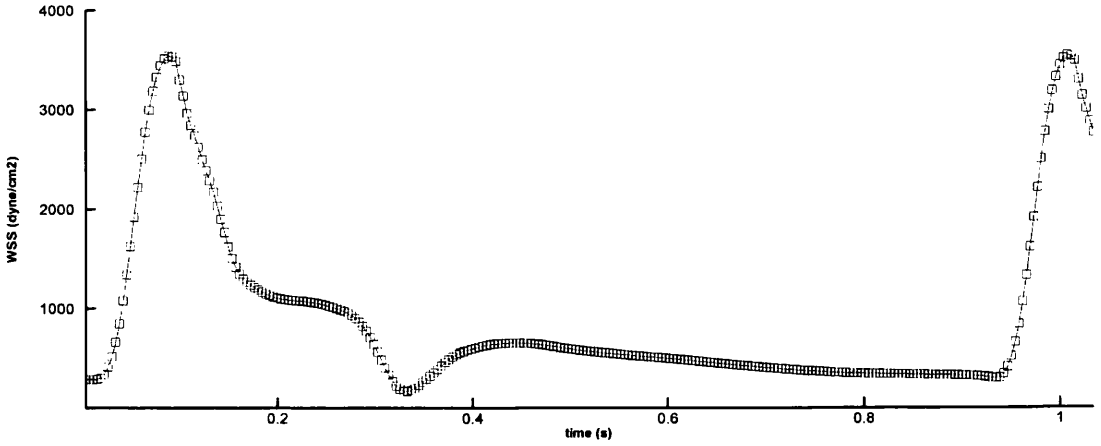

Figure 8.2: Patient 03 Left Carotid. Transient peak WSS values within the domain.

The maximum wall shear stress values for every time instance are located at the bifurcation (at the flow divider) and are distributed over three adjacent nodes. The instantaneous wall shear stress value distribution during representative phases of the cardiac cycle (mid acceleration, peak flow, mid deceleration) are near identical. To examine the complex flow within the stenosis and bifurcation in greater detail, the flow is visualised through a number of slices in Figure 8.3.

From the figure it is clear that the stenosis has a severe impact on the downstream flow, with flow separation visible until at least slice J. This is important since low WSS would be expected downstream of the stenosis, marking a potential region of further plaque formation. This would be in good agreement with Smedby [123] who found that plaque was more likely to grow downstream of a stenosis. Since it would be expected that the region experiencing flow separation is dependent upon the size and strength of the jet-like flow through the stenosis, it is necessary to examine this region in greater detail between the different flow cases. Within the CCA and ICA, the flow at mid acceleration and peak flow is typically well distributed within the slice, although in the ECA the flow is skewed towards the inner wall. This is reminiscent of P03R. It is during deceleration that the skewed nature becomes more obvious, with greater velocities found towards the inner wall in the ECA. To further establish the flow conditions within the ICA, the slices are now presented for three time instances. The mid accleration time instance in Figure 8.4, peak flow in Figure 8.5 and during deceleration in Figure 8.6. From the three figures, it is possible to see the evolution of the flow during systole.

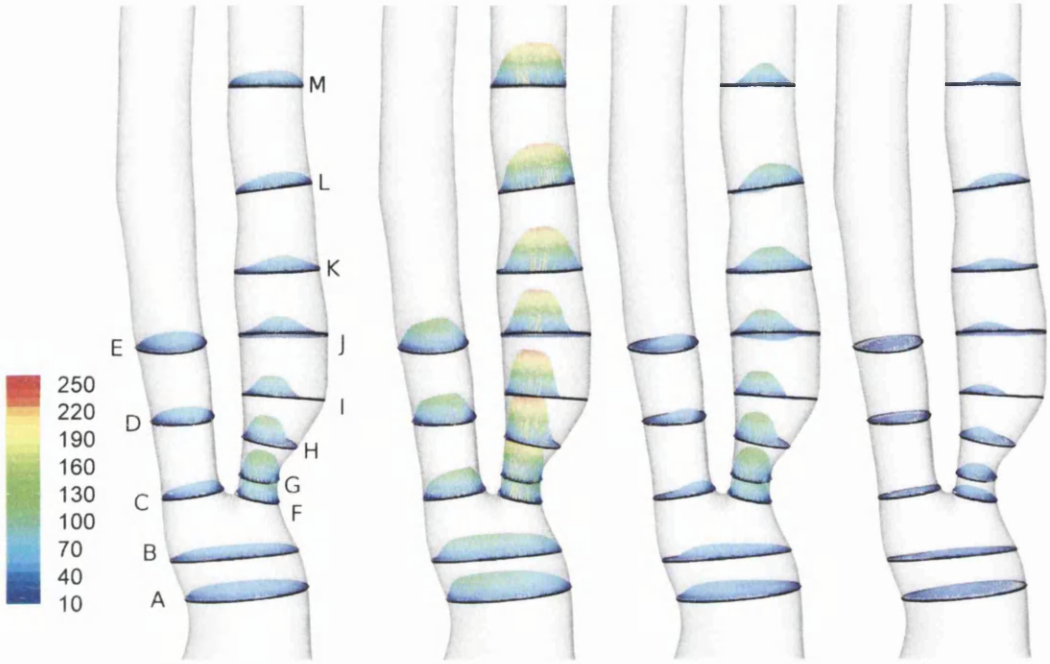

(a) Mid Accl. (b) Peak (c) Mid Decel. (d) Dicrotic notch

Figure 8.3: P03L. 3d velocity distribution within thirteen slices (cm/s).

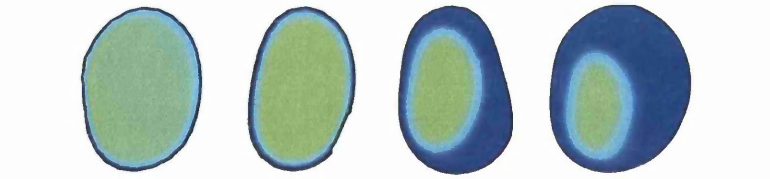

(a) slice F (b) slice G (c) slice H (d) slice I

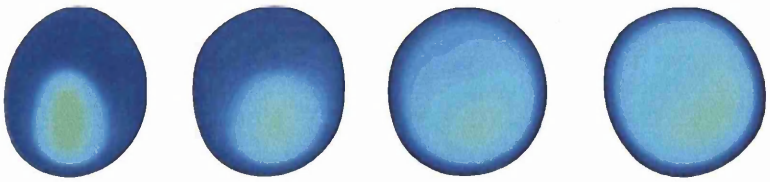

(e) slice J (f) slice K (g) slice L (h) slice M

Figure 8.4: Velocity magnitude at eight cross sections within the ICA of P03L at mid acceleration (cm/s).

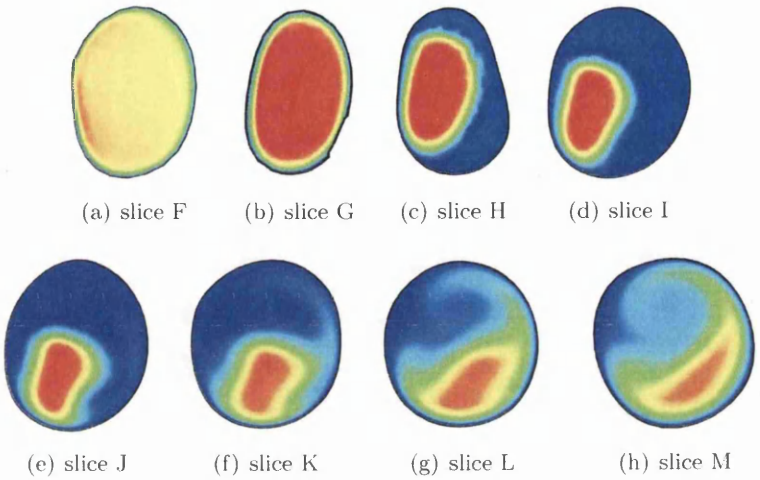

(a) slice F (b) slice G (c) slice H (d) slice I

(e) slice J (f) slice K (g) slice L (h) slice M

Figure 8.5: Velocity magnitude at eight cross sections within the ICA of P03L at peak flow (cm/s)

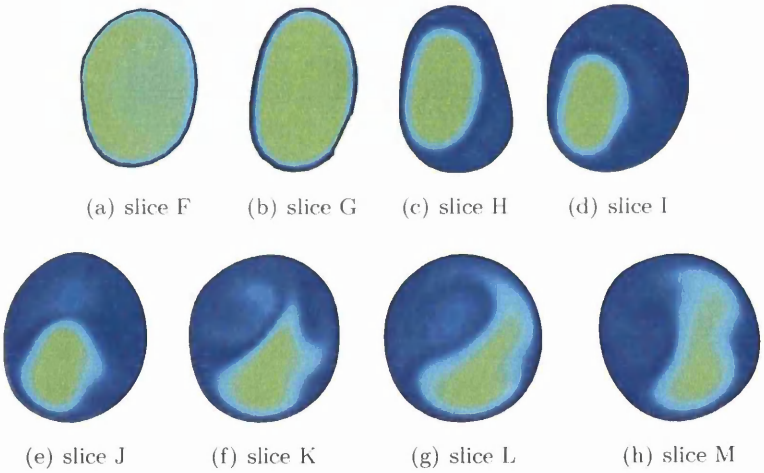

(a) slice F (b) slice G (c) slice H (d) slice I

(e) slice J (f) slice K (g) slice L (h) slice M

Figure 8.6: Velocity magnitude at eight cross sections within the ICA of P03L at mid deceleration (cm/s).

In the first time instance, flow maintains a strong jet from slice F to slice J before it begins to diffuse and by slice M reattachment has occurred. In contrast, during peak flow the length of the jet has extended such that it impacts the posterior wall and flow is skewed towards this wall even in slice M. During peak flow, the predicted overall peak velocity is 253cm/s within slice G, although even in slice M the velocity readily exceeds 200cm/s. Within the deceleration phase, the influence of the jet is still strong, although secondary flow is observed in all slices downstream of the stenosis. Figure 8.7 shows the in-plane velocity during peak flow. The high in-plane velocities in slice F are due

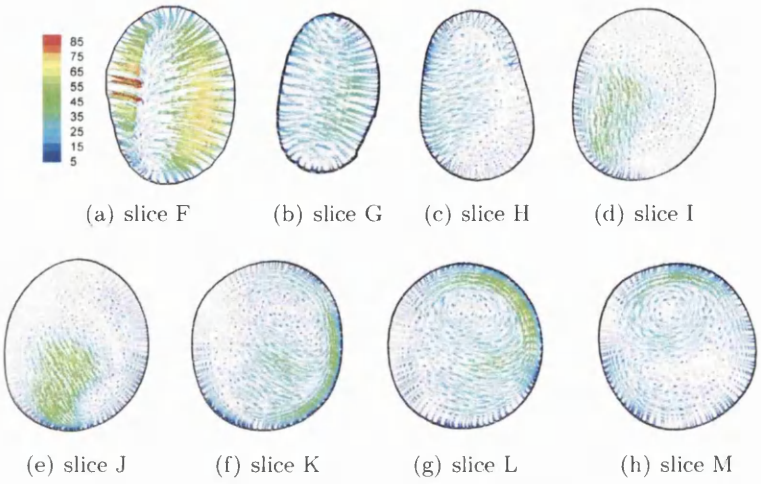

(a) slice F (b) slice G (c) slice H (d) slice I

(e) slice J (f) slice K (g) slice L (h) slice M

Figure 8.7: In-plane velocity vectors at eight cross sections within the ICA of P03L during peak flow (cm/s).

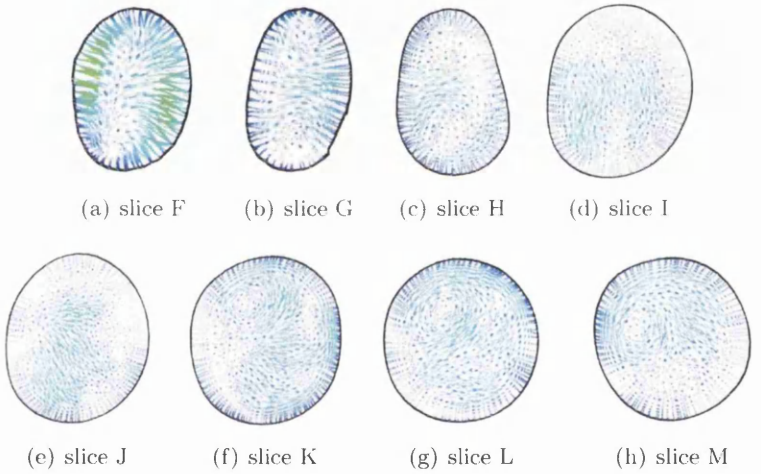

(a) slice F (b) slice G (c) slice H (d) slice I

(e) slice J (f) slice K (g) slice L (h) slice M

Figure 8.8: In-plane velocity vectors at eight cross sections within the ICA of P03L during mid deceleration (cm/s).

to flow being squeezed into the stenosis. Downstream of the stenosis, the in-plane plots reveal that the jet is at an angle to the artery axis, and is inducing a strong swirling vortex that becomes stronger and compressed the further downstream it goes. In slice L, the in-plane velocities induced by the vortex exceed 50cm/s. As can be seen in Figure 8.8 the helical flow pattern is still present during deceleration, although reduced, and will be virtually eliminated by the dicrotic notch. The in-plane velocities at this time instance rarely exceed 20-25cm/s. During the mid acceleration time instance the in-plane velocities away from the stenosis are much reduced (1-3cm/s) away from the jet location which is also typical of the values at the second peak systole time instance.

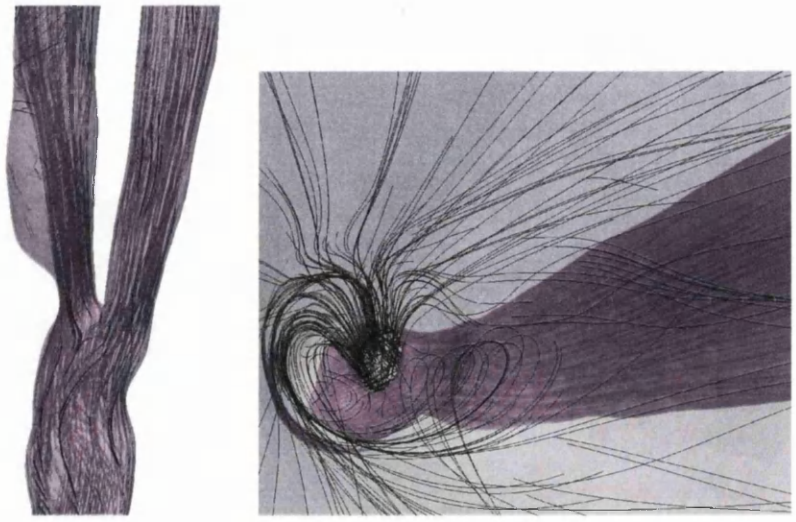

(a) (b)

Figure 8.9: P03L massless particle trajectories during peak systole. a) At the bifurcation b) From inside the ICA, view towards bifurcation

Over the entire cardiac cycle it is clear that the stenosis has a strong impact on inducing disturbed flow conditions within the ICA. In contrast, within the ECA the flow does not display any in-plane swirling effects and the in-plane velocities in slice D and E do not exceed 10cm/s during peak flow which is 80% less than those encountered within the ICA, downstream of the stenosis. In order to emphasise the influence of the stenosis on the flow field, and the three dimensional nature of the flow, a plot of particle paths is given in Figure 8.9. In the figure, the movement of massless particles within the flow field was recorded for 1/60th of a carotid cycle. The time instance shown is peak systole, with the movement for the 1/60th of a carotid cycle prior to systole displayed. As can be seen from the figure, only the ICA displays visible disturbed flow conditions, which is especially obvious when visualising the flow from inside the ICA itself.

The time-averaged WSS distribution is given in Figure 8.10 along with the oscillating shear index (OSI). As expected, the peak time-averaged WSS occurs at the flow divider, although closer to the ICA. The predicted peak of 805 dyne/cm^2 is exceptionally high and damaging. Upstream of the stenosis apex lies a band across the ICA of very high time-averaged WSS (400-500 dyne/cm^2). This is also greater than the 315 dyne/cm^2 that Holme *et al* [47] determined was sufficient to induce platelet activation and enhanced platelet thrombus formation. Immediately downstream of the stenosis lies a small region experiencing time-averaged WSS of less than 5 dyne/cm^2 and a bigger region experiencing less than 10 dyne/cm^2. This is indicative of potentially further plaque formation and corresponds to the region experiencing flow separation. Away

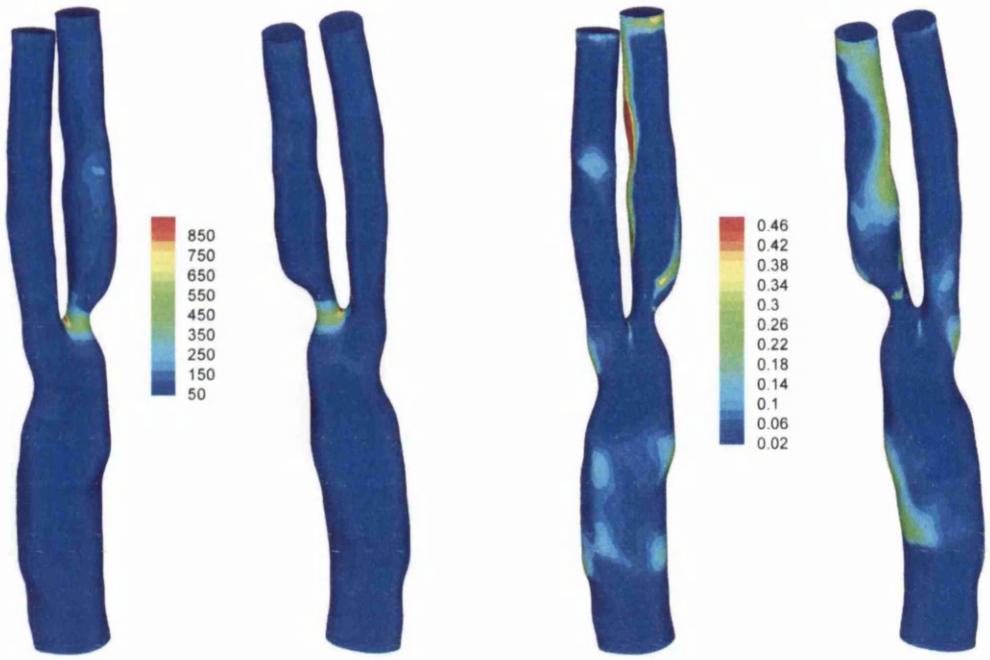

Figure 8.10: P03L a) time-averaged WSS (dyne/cm^2) Posterior b) time-averaged WSS (dyne/cm^2) Anterior c) OSI (-) Posterior d) OSI (-) Anterior

from the stenosis a majority of the ICA experiences between less than 40 dyne/cm^2 although regions experience values exceeding 100 dyne/cm^2 along the posterior wall. In the ECA the time-averaged WSS values range from 10-30 dyne/cm^2. In contrast, approximately 20% of the CCA is predicted to experience time-averaged WSS of less than 5 dyne/cm^2 with the remainder experiencing less than 25 dyne/cm^2. As in the three carotids in the previous chapter, the CCA typically experiences lower time-averaged WSS values compared to the ECA and ICA. The OSI distribution indicates that the regions experiencing low time-averaged WSS in the CCA are coincident with elevated OSI values. In the ICA, the regions of elevated or high OSI are extensive. A region extends from above the stenosis down the entire length of the inner wall to the ICA outlet. Another region of elevated OSI extends from near the stenosis apex along the outer wall of the ICA. In the ECA only a small region experiences elevated OSI although this is located distal to the flow divider along the outer wall which is reminiscent of the regions experiencing low time-averaged WSS in 2 out of 3 cases in the previous chapter and 3 out of 4 in [21]. This region experiences time-averaged WSS of between 5-7 dyne/cm^2.

The WSS gradient distributions are given in Figure 8.11. From the plot it is clear that

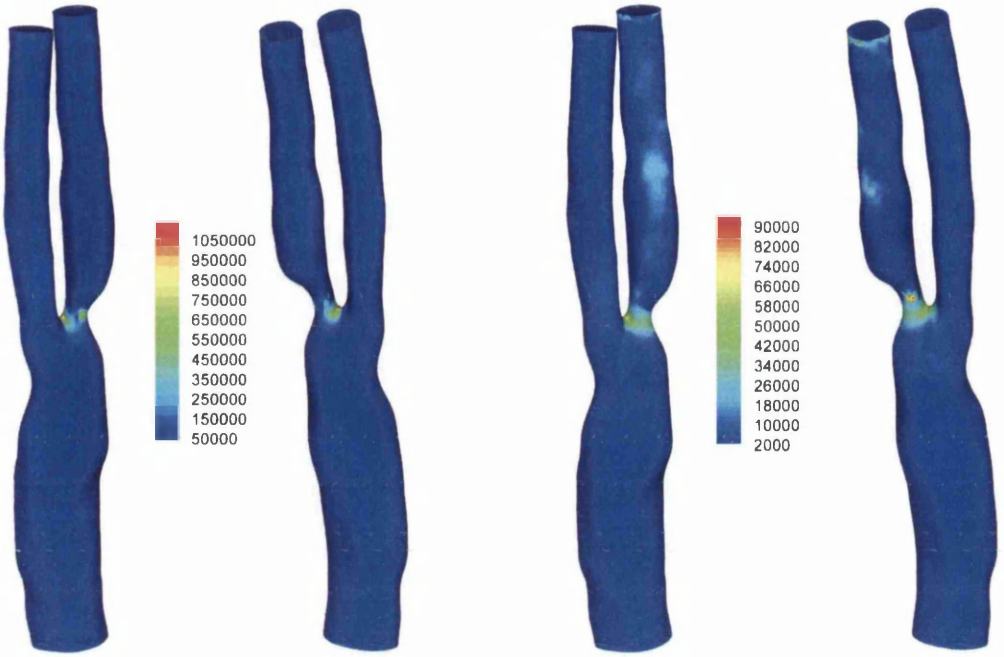

Figure 8.11: P03L a) WSSG (dyne/cm^3) Posterior b) WSSG (dyne/cm^3) Anterior c) WSSTG (dyne cm$^{-2}s^{-1}$) Posterior d) WSSTG (dyne cm$^{-2}s^{-1}$) Anterior

in general the distributions of WSSG and WSSTG are in agreement with that of time-averaged WSS. Although the peak of all three parameters occur in close proximity, the regions of high WSSG, WSSTG and time-averaged WSS are not entirely coincident. The peak predicted value of WSSG is higher than those of the three carotids in the previous chapter, being approximately 200% larger. The peak WSSTG value (93800 dyne cm$^{-2}s^{-1}$) on the other hand, is comparable to that of P04L which actually has a higher peak value. The difference in peak WSSG values can be explained by the presence of jet flow through the stenosis in this carotid.

The spatial oscillation parameters WSSAD and WSSAG for P03L are given in Figure 8.12. From the plots it is clear that spatial oscillation within the domain is centred on the bifurcation and the stenosis. While the flow divider experiences high WSSAD and WSSAG as in the previous three carotids, the location of peak WSSAG values does not coincide either with the peak WSSAD or the flow divider. The peak WSSAG of 4047 rad/cm is located close to the downstream side of stenosis apex on the anterior wall. This value represents a 48% increase over the previous maximum located in P03R. A band of high and elevated WSSAD extends along the outer wall proximal to the stenosis apex which is in good agreement with the WSSAG distribution. An elongated region

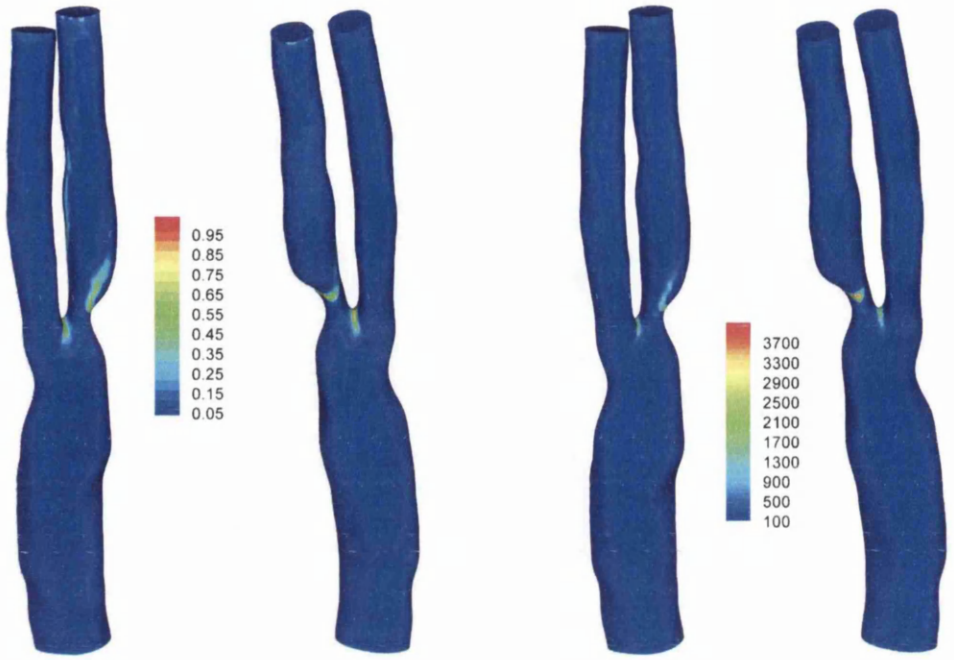

Figure 8.12: P03L a) WSSAD (rad) Posterior b) WSSAD (rad) Anterior c) WSSAG (rad/cm) Posterior d) WSSAG (rad/cm) Anterior

corresponding to the elevated OSI region extends upwards along the inner wall of the ICA. In the remainder of the domain, the spatial oscillation is minimal.

From the three oscillation parameters, it is clear that disturbed flow is found within the ICA, with both spatial and temporal oscillations encountered. With the flow separation inducing low time-averaged WSS immediately downstream of the stenosis, this indicates a potential for the stenosis to grow further in the downstream direction. Several small regions within the CCA experience low time-averaged WSS and elevated OSI making this a potential region of atheroma although WSSAD and WSSAG values are minimal. The high time-averaged WSS values are also a potential issue, either through inducing further platelet deposition, thrombus formation or possible rupture. With the baseline case detailed, the differences between applying different flow cases shall now be examined.

8.4 Second Case - Reduced Flow

The two chosen centreline velocities lie within the range recorded by Holdworth *et al* 1999 [120] from the recordings of 3520 human common carotid artery flow waveforms.

Figure 8.13: Patient 03 Left Carotid. Tracking nodes within the stenosis

The reduced centreline velocity of 68cm/s is at the lower end of the range. By reducing the flow rate, the magnitudes of all variables will also reduce. However, due to the non-linear relationship between wall shear stress and velocity, the decrease is more complex than a straight third reduction in line with the third reduction in the flow rate. In both the baseline case and the reduced flow case, the distribution of the maximum wall shear stress (and their nodal locations) are similar. The overall peak WSS has reduced by 41.9% to 2056.8 dyne/cm^2. The peak time-averaged WSS has reduced from 805 dyne/cm^2 to 444 dyne/cm^2, a decrease of 45%. This indicates that if accurate WSS values are required then the flow must be a good approximation to that actually experienced by the patient.

To examine the influence on the flow through the stenosis, three points were selected (shown in Figure 8.13). Point 1 is located where the stenosis is most severe, Point 2 is located downstream from Point 1 and Point 3 is located along the inner wall of the internal carotid artery. The three transient wall shear stress distributions for their respective node are given in Figure 8.14. From the figure, it is possible to see the both Point 1 and Point 2 display marked differences between the two cases. At Point 1 the peak (302.0 dyne/cm^2) is sharper and well defined, whereas the reduced flow peak (179.1 dyne/cm^2) is rounded. It is at Point 2 where the major differences emerge. Two distinct peaks are recorded in the baseline case, however only one smooth peak is recorded in the reduced flow case. The primary peak of 43.7 dyne/cm^2 and a subsidiary peak of 28.5 dyne/cm^2 is in contrast to the single peak of 16.5 dyne/cm^2, which is a difference of 62.2% and 42.1% respectively. The minimum wall shear stress value predicted in the baseline case is 0.48 dyne/cm^2. In the reduced flow rate case this value has actually increased by 85%. This is important when considering atherogenesis has been linked to low and oscillating shear stress. At Point 3, however, there is good agreement between the two transient profiles, apart from a small region at approximately 0.15 seconds. At the node, the peak WSS has decreased 36.8% to 326.1 dyne/cm^2. From the three datums, it is clear that the major influence of flow reduction at the stenosis is on the

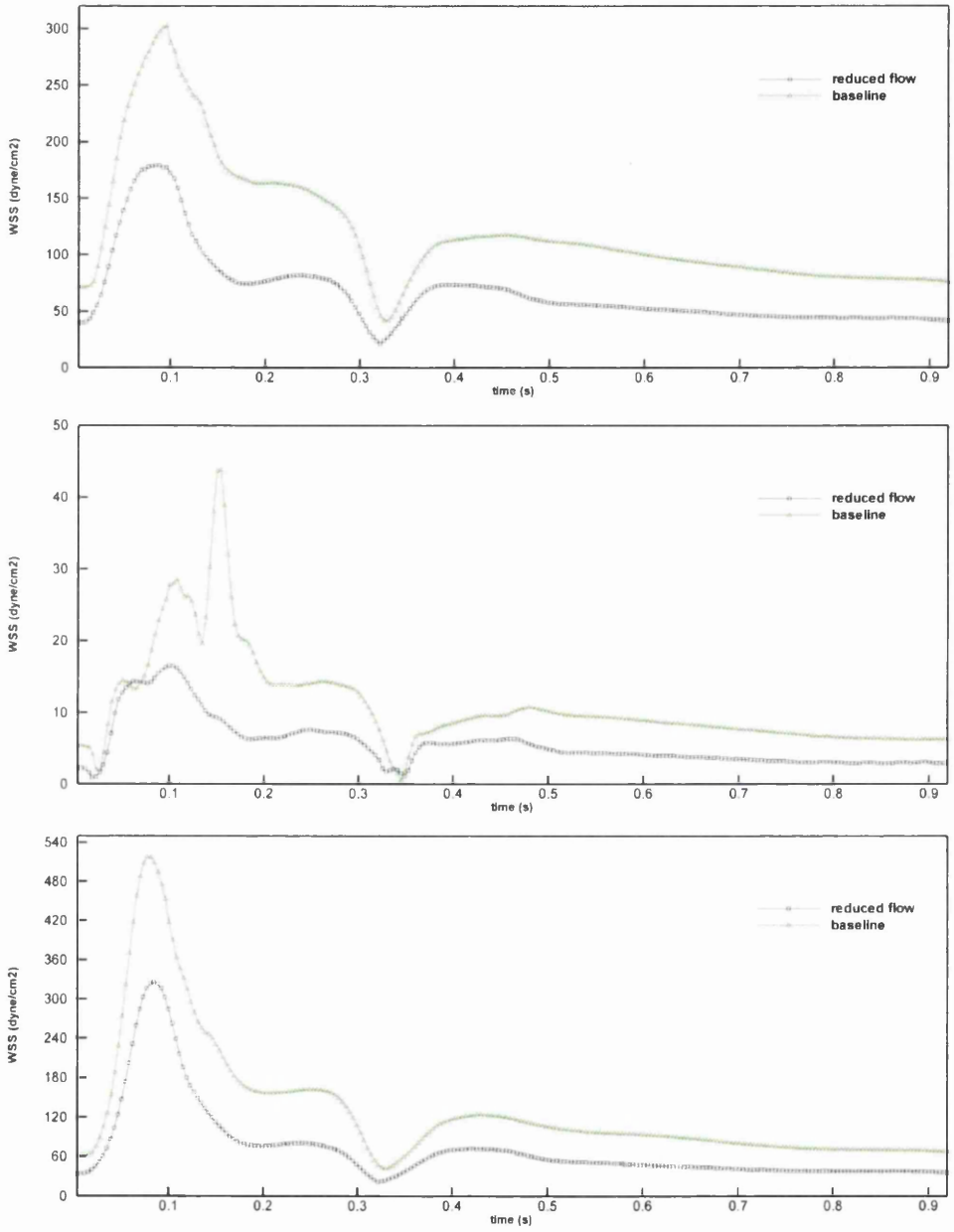

Figure 8.14: P03L. WSS transient profile comparison between the reduced flow case and the baseline for a) Point 1 b) Point 2 c) Point 3

Figure 8.15: Patient 03 Left Carotid. Tracking profiles within the ICA

outside wall of the internal carotid artery. This would be expected in a recirculation zone driven by the jet-like nature of the flow through the stenosis.

To further assess the impact on the wall shear stress in the ICA, three profiles along the vessel wall are examined downstream from the stenosis (as highlighted in Figure 8.15) for the four standard time instances. These profiles are presented in Figure 8.16. From the three plots it is clear that differences in distribution (rather than magnitude) are minimal across all four time instances. Some minor differences exist more than 1cm downstream of the stenosis. In Profile B, during the mid deceleration time instance the predicted WSS is decreasing from 1.2cm in the baseline case, although increasing in the reduced flow case. The opposite is true during peak flow. However, the differences between the baseline and reduced flow case do not appear to be major in these profiles. Since the flow rate should impact the flow separation downstream, the differences between the two cases should manifest more strongly within the oscillation wall parameters (OSI,WSSAD and WSSAG). Since there is excellent agreement between WSSAD and WSSAG for the profiles, only WSSAD is given along with OSI and time-averaged WSS in Figure 8.17. From the figure it is clear that while time-averaged WSS displays excellent agreement between both cases, there are distinct differences between OSI and WSSAD. This indicates that as expected, these variables display the most divergence and dependence upon the flow. However, having said that, the differences in WSSAD are relatively minor away from the stenosis. Proximal to the stenosis, the predicted WSSAD values display a change of up to 100%, although this divergence is local. In the OSI distribution it is apparent that the flow has had an impact, although differences are still relatively small.

To examine these differences qualitatively across the ICA, the detailed view of the OSI

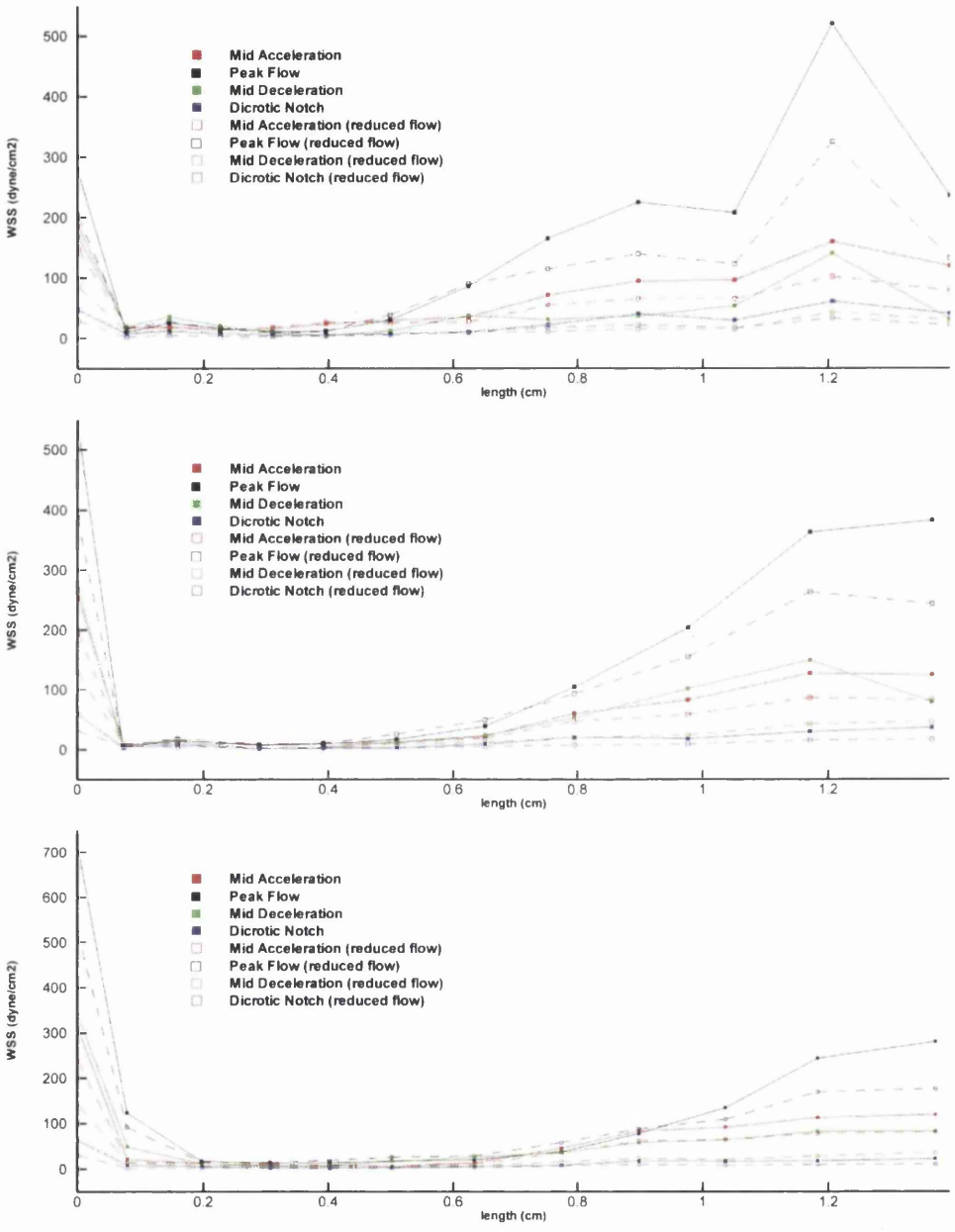

Figure 8.16: Patient 03 Left Carotid. WSS tracking profiles for a) Profile A b) Profile B c) Profile C

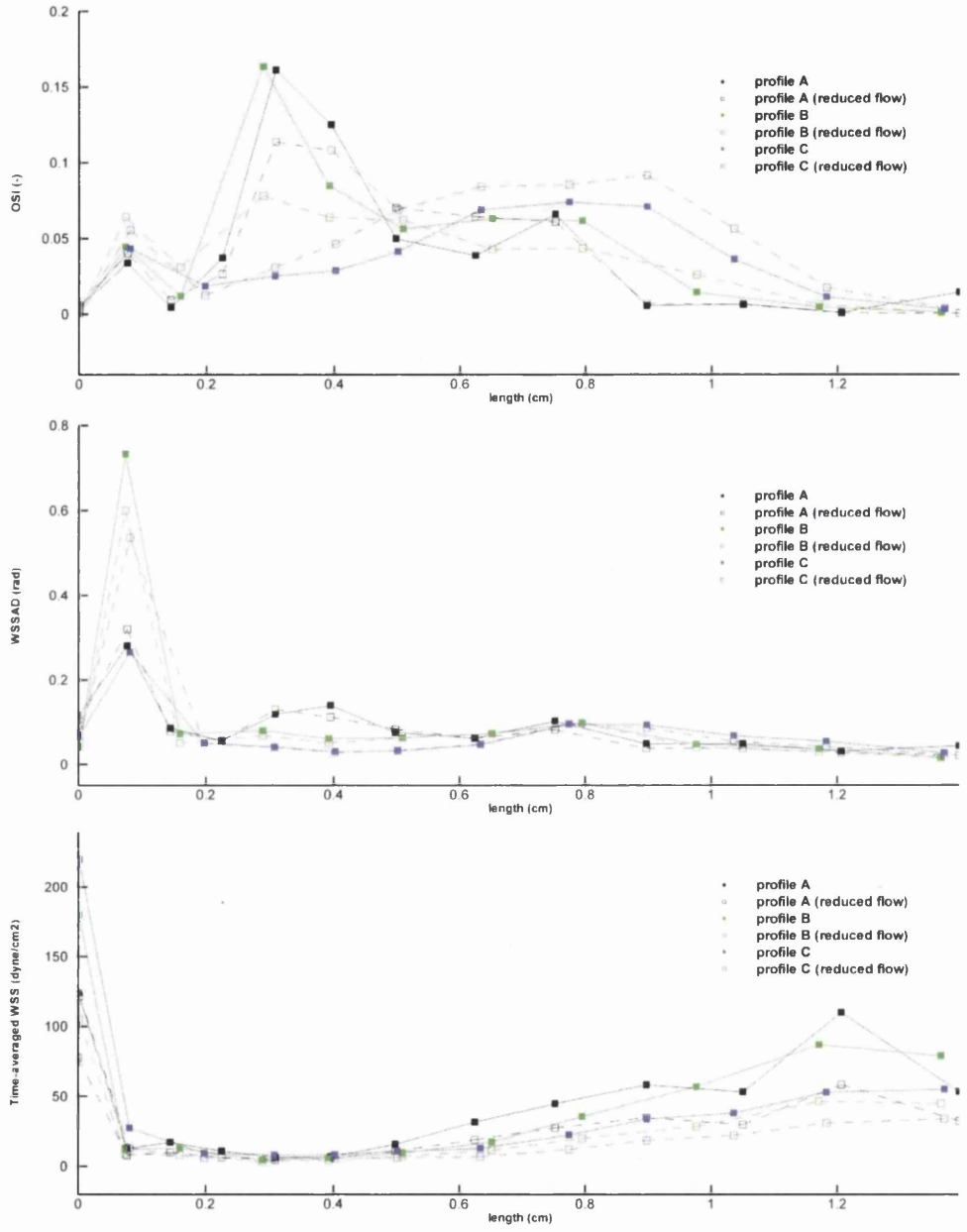

Figure 8.17: Patient 03 Left Carotid. Tracking profiles for a) OSI b) WSSAD c) Time-averaged WSS

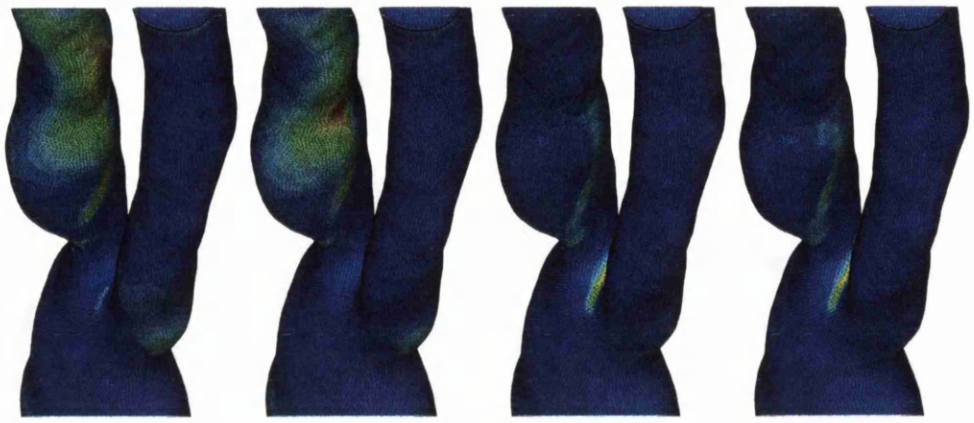

Figure 8.18: Patient 03 Left Carotid. Detailed view of oscillatory parameters in ICA a) OSI b) OSI (reduced flow) c) WSSAD d) WSSAD (reduced flow)

and WSSAD is presented in Figure 8.18. From the plot, it can be seen that the location of the elevated and high OSI region has been shifted and its extent is greater in the baseline case. In the WSSAD distributions the location of the band of elevated values extending from the stenosis has altered slightly although the magnitudes are still in excellent agreement within the band.

Overall, it can be considered that the reduced flow rate has not had significant influence on the final haemodynamic wall parameters even with the possible large variations point-wise such as in Figure 8.14. Also, the influence is greatest on the oscillatory shear index parameter due to it providing directional information only.

8.5 Third Case - Altered Flow Division

The third flow case assessed is that of the 50:50 flow division between the ICA and the ECA. The flow division has been altered to take into account the additional resistance to flow within the ICA due to the presence of the stenosis. The first point to note is that the peak time-averaged WSS has been reduced to 634 dyne/cm^2. The three points identified in Figure 8.13 are again utilised (Figure 8.19) to compare the point-wise differences of the transient WSS over the cardiac cycle around the stenosis. From the figure, it can be seen that only minimal differences are predicted along the inner wall at Point 3. In contrast, the outer wall points again display a marked difference between the two cases.

Figure 8.20 gives the three profiles as identified in the previous section. From the plot it can be seen that there is good agreement between both WSSAD and time-averaged

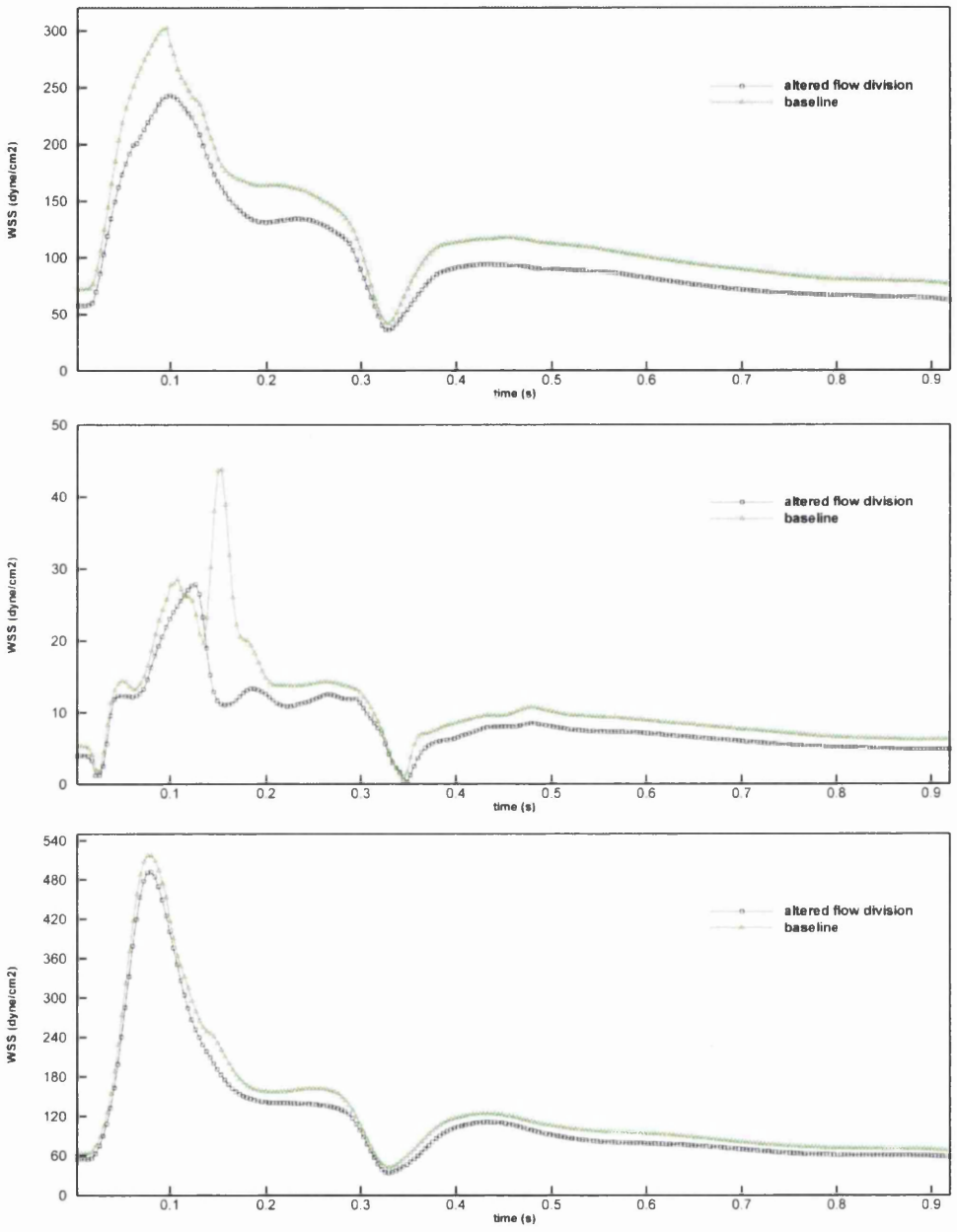

Figure 8.19: P03L. WSS transient profile comparison between the altered division case and the baseline for a) Point 1 b) Point 2 c) Point 3

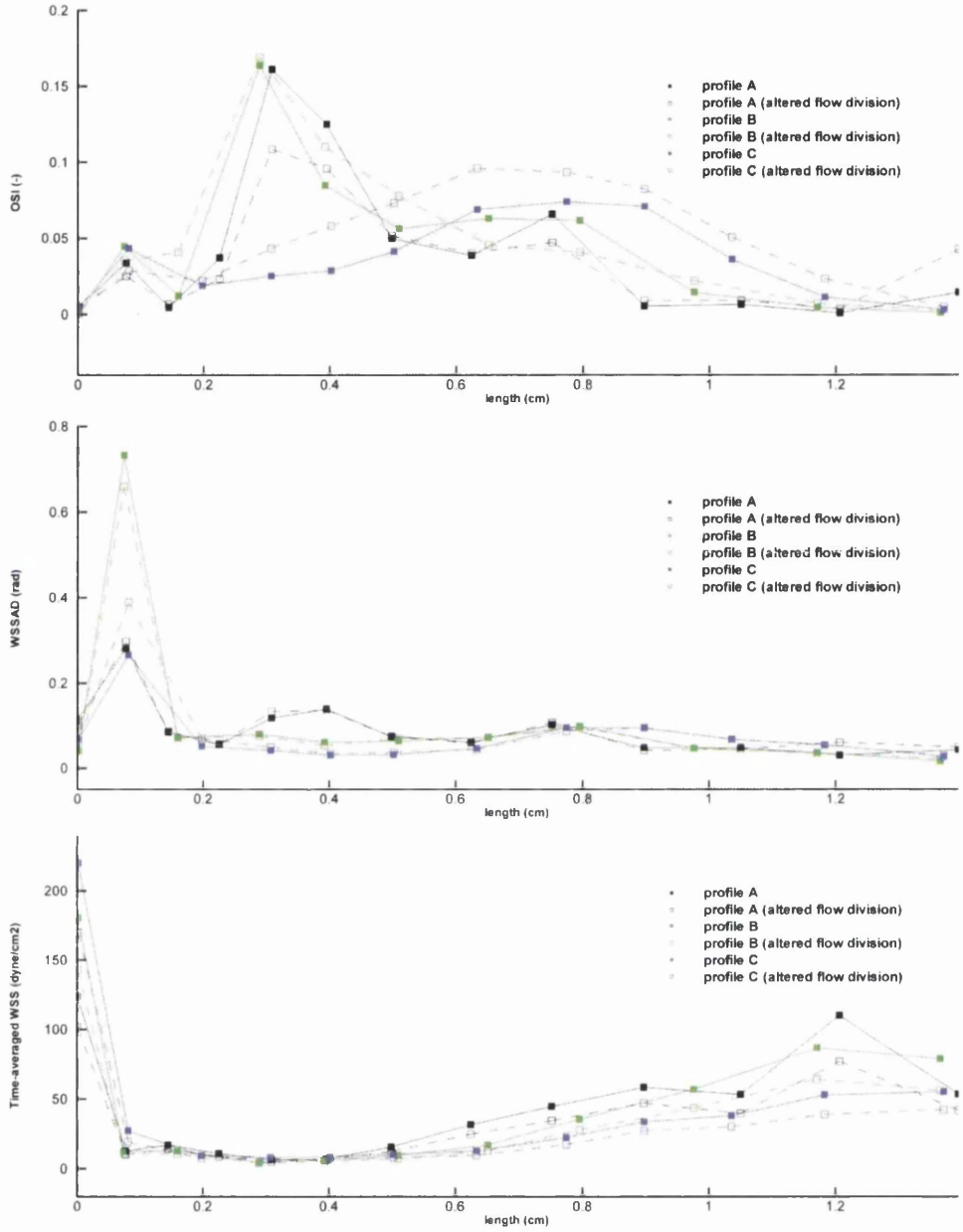

Figure 8.20: Patient 03 Left Carotid. WSS tracking profiles for a) OSI b) WSSAD c) Time-averaged WSS

WSS along the profiles. Differences are present within the OSI distribution, as before, although agreement has improved. Profile C displays the best correlation, while profiles A and B display relatively small differences.

The OSI and WSSAD for the altered flow division are given in Figure 8.21. The extent of the elevated and high OSI region is approximately the same in both the altered flow

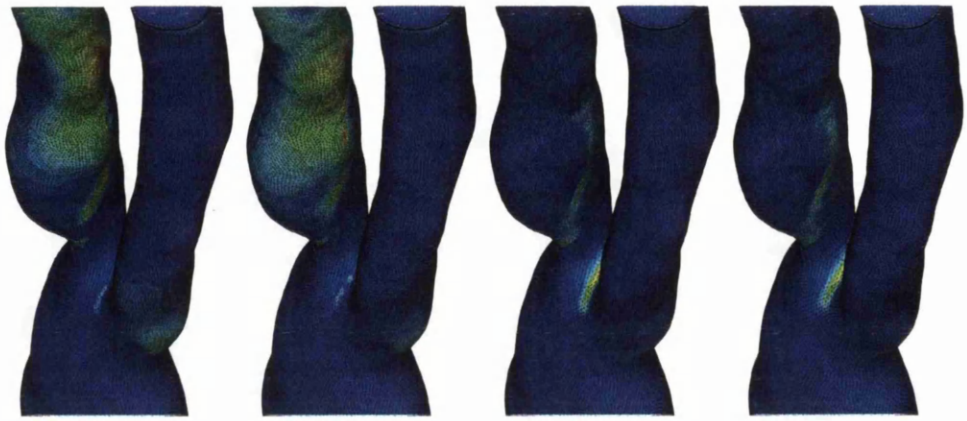

Figure 8.21: Patient 03 Left Carotid. Detailed view of oscillatory parameters in ICA a) OSI b) OSI (altered division) c) WSSAD d) WSSAD (altered division)

division case and the baseline. However, in the baseline, the region extends further towards the outlet. Whereas in the 50:50 flow division case, the region of elevated OSI extends further into the bulge downstream of the stenosis. Thus the flow division choice alters the location of predicted transient oscillations. In contrast, there is good agreement between the two WSSAD distributions, with only a minimal alteration in the band of elevated values.

From both this case and the reduced flow case it is apparent that only minimal differences exist between the derived haemodynamic wall shear stress parameter distributions within the ICA. Major differences do exist between the wall shear stress magnitudes as shall be discussed later.

8.6 Fourth Case - Increased flow and 50:50 flow division

Although the results in the previous two sections display only small variation in the wall parameter distributions, it is worth considering another case. In the fourth case the centreline velocity was increased to give a peak of 130cm/s and the flow division set at 50:50. This case was broadly in agreement with the baseline case. Indeed, the peak time-averaged WSS for this case was also 805 dyne/cm^2. Although again, the WSS point-wise differences remained. An increased centreline velocity was chosen to investigate the influence of turbulence on the predicted WSS parameters. The three previous cases were simulated satisfactorily using the laminar code. With the point-wise disturbance in the transient WSS distribution in the baseline case (see Figure 8.19) possibly indicating turbulent effects this case should reveal their influence. During the

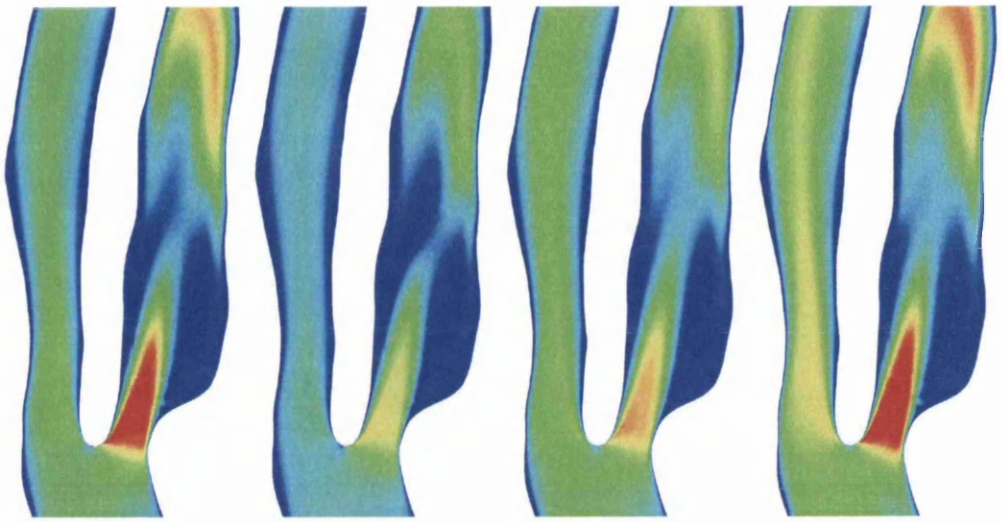

Figure 8.22: Patient 03 Left Carotid. Velocity contours in a vertical slice a) Baseline b) Reduced flow c) Altered division d) Increased flow and altered division

deceleration phase, there was a small region in the ICA that experienced a low amount of turbulence. The peak predicted turbulent viscosity was three orders of magnitude below that of the laminar viscosity. From these results, the stenosis is not sufficiently constricting to induce high turbulence. To provide a direct comparison between all four cases a vertical slice of the ICA is examined and presented for all four cases in Figure 8.22.

From the figure the jet within the two 50:50 cases appears to extend further into the ICA than that of the two 60:40 cases. This is due to the flow division altering the direction of the jet by approximately 5-10 degrees. This has, however, only a minor impact on the OSI distribution in both cases (as seen in Figure 8.21 for the altered flow division case).

8.7 Discussions

It can be seen in the four cases presented above that the geometry of the stenosis has an overriding influence on the resulting wall shear stress distribution along with associated wall parameters. However, the flow does present some minor influences downstream of the stenosis. One other case was examined although is not presented here. The case employed a Windkessel model for the outlet flow conditions. Under a steady state run, pre-systole, the model predicted a 57:41 split within a tolerance of a 2% mass flow

imbalance. With the flow division expected to change during the cardiac cycle, this is in good agreement with the choice of either a 50:50 split or the original 60:40 division.

Both the choice of flow division and peak centreline velocity have a very modest impact on the derived wall shear stress parameter distributions. In regions of flow separation, the influence is greatest on the transient oscillations parameter, OSI. In order to accurately assess the magnitudes of the wall shear stress parameters, the velocities found proximal to the stenosis/flow divider should be contrasted with ultrasound data. In the four flow cases in this chapter the peak time-averaged WSS ranged from 444 dyne/cm^2 to 805 dyne/cm^2. Perhaps more importantly, the band of high time-averaged WSS around the neck of the stenosis in the reduced flow case is predicted to experience between 190-240 dyne/cm^2. Whereas in the baseline case, the figures range from 400-500 dyne/cm^2. The reduced flow rate values are below the 315 dyne/cm^2 found to enhance platelet thrombus formation in Holme *et al* [47] while the baseline case exceeds this threshold. This is also true of the fourth case. In the third (altered flow division) case the predicted time-averaged WSS values coincide with the threshold, being between 300-350 dyne/cm^2.

With the eventual goal of this research being the development of a classification system to assess the severity of a stenosis, these flow investigations are valuable. If the classification system is to be determined based upon geometry alone, then the classification system would be incomplete and unable to predict accurately the proximal wall shear stresses at the stenosis. A number of flow cases should be analysed for each geometry, as this would allow a more accurate expectation of the wall shear stress values.

8.8 Summary

The flow through a stenosed ICA is analysed in this chapter, and the influence of flow on the resulting wall shear stress (and associated wall parameters) is investigated. From the analysis it is clear that for accurate determination of the wall shear stresses at the bifurcation, and more importantly at the stenosis, the model must be verified with clinical data. Ultrasound measurements of proximal velocities would be one method of achieving this, and require no extra effort on behalf of the radiologist. From the flow analysis in this chapter, any classification system based on localised geometry must also include a method of reasonably predicting the wall shear stress values. This is important for regions of high shear stresses such as within a stenosis. It was also determined that turbulence within the artery had negligible effect on the flow within the ICA, although in a more severe stenosis this may no longer be valid.

Chapter 9

Thoracic Aortic Aneurysm - Influence of a folded neck

9.1 Introduction

In this chapter a patient-specific thoracic aortic aneurysm (TAA) geometry with a folded neck is analysed. This is an unusual geometry and, as we see later, the folded neck will influence the flow within the geometry, producing patterns of wall shear stress (WSS) and oscillating shear index (OSI) different to that of regular or model TAAs.

9.2 Boundary Conditions and Mesh Geometry

The mesh was constructed as outlined in Chapter 5 from a set of CT scans provided by Morriston Hospital. The set consisted of 390 slices. For the numerical simulation, only the main aorta and short proximal sections of the left subclavian, left common carotid and brachiocephalic arteries was retained. The small vessels connected to the aortic arch were clipped and removed.

In order to examine the influences of the folded neck or kink on the blood flow and resulting wall shear stress distribution, the original geometry was modified and a second mesh was constructed with an artificially smoothed neck. This mesh was constructed from the original geometry, thus the only geometrical difference to the surface topology is in the folded neck region. Once the surface topology was suitably modified, the mesh

was completed with construction of suitable boundary layers and the inner volume mesh using the procedures described previously.

Three meshes with different resolutions, including one purely unstructured mesh were generated and tested to select the final mesh resolution. The final mesh was selected to represent minimal effect of mesh coarseness on the solution. The purely unstructured mesh was found unsuitable for wall shear stress (WSS) calculations, since insufficient refinement near the wall provided non-converged solutions of the WSS, as will be demonstrated in the following section. The structured layers used in the vicinity of the wall are intended to capture the high near-wall velocity gradient and thus produce an accurate representation of WSS. The final mesh (with kink) used contained 3,290,228 linear tetrahedral elements and 567,315 nodes and the no kink version contained 3,311,878 elements with 570,923 nodes. Both meshes contained ten structured layers close to the wall. The element size used on the wall is about 0.004 cm. The final mesh used for the kink and no kink cases are shown in Figure 9.1.

In this study, the flow was assumed to be Newtonian due to the relatively large size of the blood vessel. The blood dynamic viscosity and density are taken to be $\mu = 0.04$ g/cm s and $\rho = 1.0$ g/cm^3 respectively. The no-slip condition is applied on the vessel wall and assuming that the flow is unsteady and fully developed, Womersley velocity profiles were imposed on the inflow and outflow boundaries. For the outlet boundary conditions, the flow division of 66%, 17%, 10% and 7% is imposed on the descending aorta, brachiocephalic artery, left common carotid artery and left subclavian artery respectively. The flow waveform used for construction of the Womersley profiles is given in Figure 9.2. Each cardiac cycle was discretised into 240 time steps. For the turbulence boundary conditions, the transport quantity $\hat{\nu}$ is zero on the vessel walls and a small value (1×10^{-5}) is applied to the relevant inflow points, depending on the velocity profile at the current time step, of the inlet and outlet (reverse flow).

9.3 Maximum Wall Shear Stress

In order to assess the transient simulation and confirm that the inter-cycle variation was minimal, the maximum wall shear stress was examined. Two cardiac cycles were simulated. The maximum value of wall shear stress within the domain was recorded for every time instance, and the variation with time is given in Figure 9.3 for both the final meshes and the purely unstructured (with kink) mesh. The results obtained from

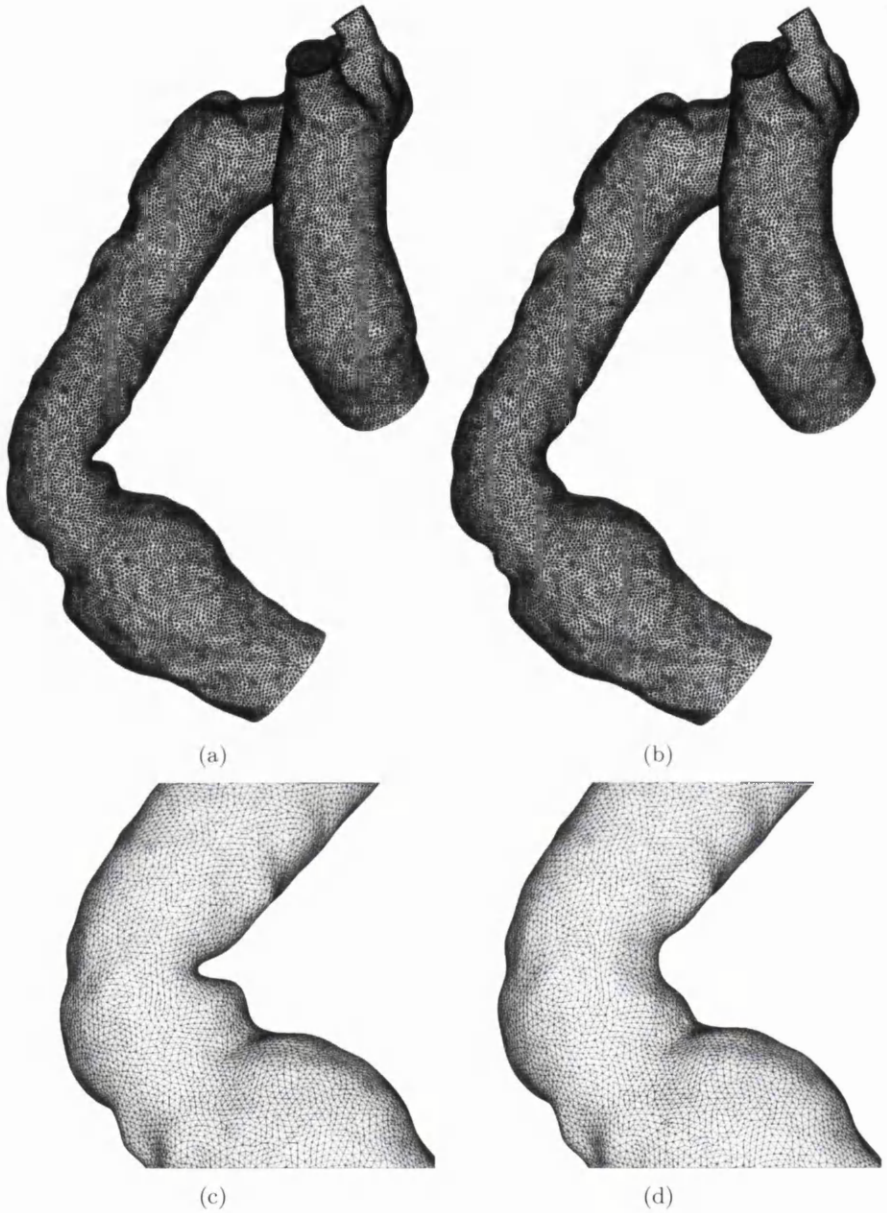

Figure 9.1: TAA patient geometry. a) With kink b) without kink c) with kink closeup d) no kink closeup

the purely unstructured mesh were included to demonstrate its unsuitability for this problem and the necessity of including boundary layer refinement.

From the figure, it can be seen that during the first cycle pre-systole, the domain is being flushed and that post-systole the maximal WSS displays inter-cycle repetition in all three meshes. However, the inter-cycle percentage deviation is bigger in the purely

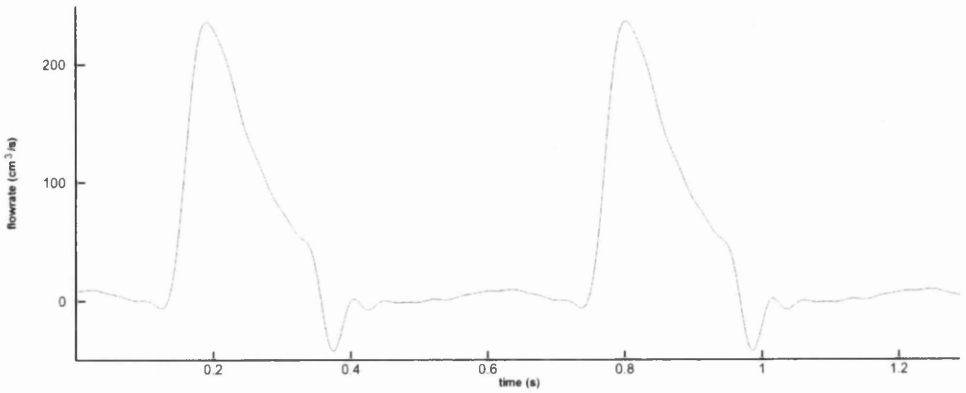

Figure 9.2: The aorta inlet transient flow profile for two heart beats

unstructured mesh. Due to the lack of near-wall refinement, the maximum wall shear stress prediction is significantly lower than in the refined equivalent mesh. A peak WSS value of 18.4 dyne/cm^2 was predicted from the purely unstructured mesh. However, in the refined meshes, the maximum instantaneous WSS value was 342.7 dyne/cm^2 for the with kink case and 136.4 dyne/cm^2 for the no kink case. The peak WSS in the refined (with kink) mesh is located at an abrupt spike within the cycle. Examining the second cycle results only, the maximum WSS values recorded over the cycle for both of the refined meshes occur in three distinct regions. The first is located proximal to the neck location and the second is within the aortic arch opposite the three arterial outlets (see Figure 9.4). The third region occurs near the inlet and is identical in both meshes due to its distance from the neck location. The regional distribution of the peak values is given in Figure 9.5. While the locations of the regions are similar, the second region exhibits a larger number of peak WSS values throughout the two cycles in the no kink mesh. In the no kink case 39.6% of the peak WSS values occur in this region. In the with kink case this decreases three-fold to 12.1%. Thus, the with kink case exhibits a far greater percentage of peak values within the neck region. This indicates the neck's influence not only on the maximum peak value overall, but also on the distribution of the maximum WSS in time.

With the region distribution examined, the maximum WSS within the two regions of interest is examined over the cardiac cycle. A representative point was chosen and the WSS magnitude tracked over the cycle and the results are given in Figure 9.6. For Region 2, an identical point could be chosen in order to provide a direct comparison. With the varying geometry in Region 1 however, only a central node within the region could be chosen for the representative node. Figure 9.7 shows the distribution of the max WSS locations within Region 1 in the with kink case. Also included in the analysis

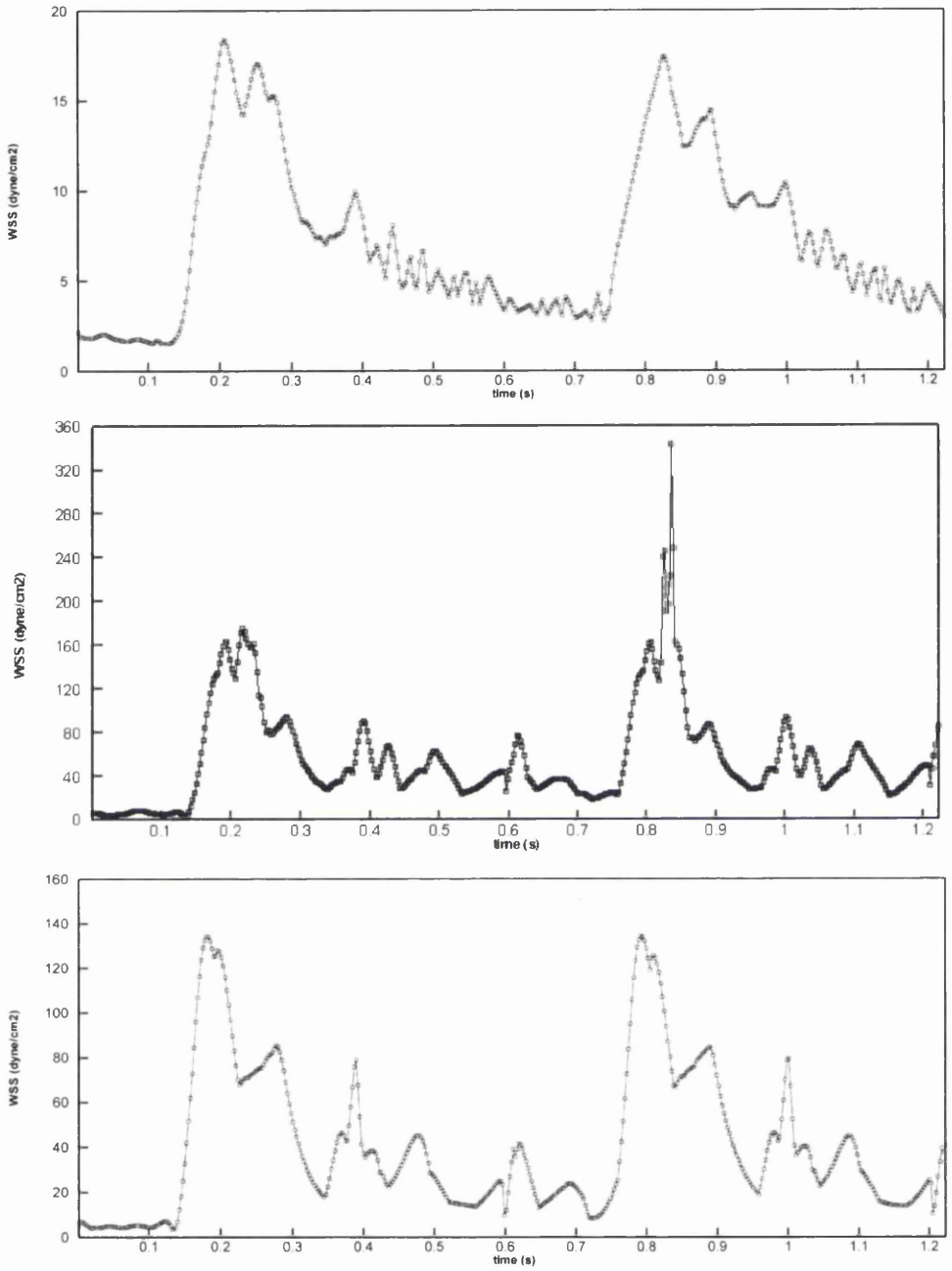

Figure 9.3: TAA maximum wall shear stress. a) Purely unstructured mesh (with kink) b) refined mesh (with kink) c) refined mesh (without kink).

is the node that experiences the overall peak WSS (as highlighted in Figure 9.7) and a corresponding location on the no kink mesh. From Figure 9.6(a), the influence of the folded neck is visible even within the aortic arch during diastole. Examining Figure 9.6(b), the transient distribution of the WSS values is markedly different. Within systole,

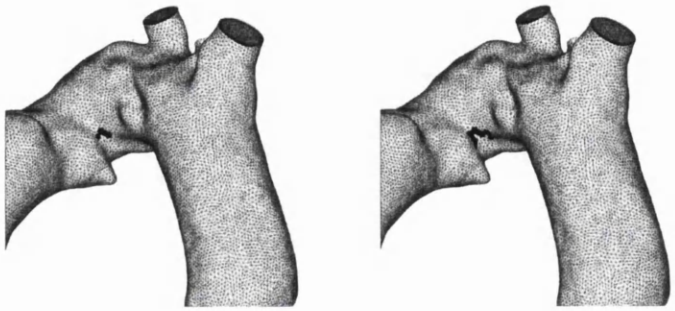

Figure 9.4: TAA Max WSS value distribution in Region 2. a) refined mesh (with kink) b) refined mesh (without kink)

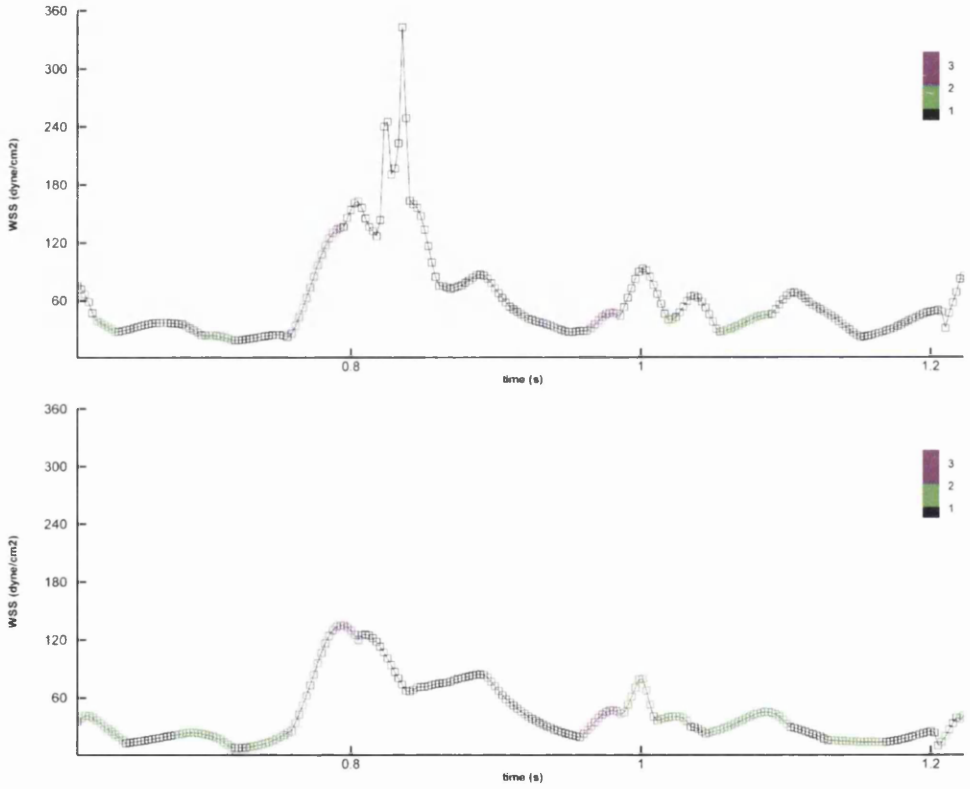

Figure 9.5: TAA Max WSS value distribution between regions. a) refined mesh (with kink) b) refined mesh (without kink).

which occurs around $t = 0.8$ seconds, the WSS values are lower in the with kink case compared to the no kink case. However, for the remainder of the cardiac cycle, the predicted WSS values are greater in the with kink case. Within the general oscillating nature, the overall peak WSS value recorded occurs at the dicrotic notch. The value of 93.1 dyne/cm^2 in the with kink case is 230% higher than the corresponding time value of

40.1 dyne/cm^2. Looking at the location downstream of the neck, only during systole are the values of WSS elevated in both the with kink and no kink cases. During systole the no kink WSS values display a smooth increase until a peak of 67.9 dyne/cm^2 is achieved before decreasing. In constrast, the with kink WSS values are short pulses with a minor peak of 119.0 dyne/cm^2 and a primary peak of 342.6 dyne/cm^2 before diminishing.

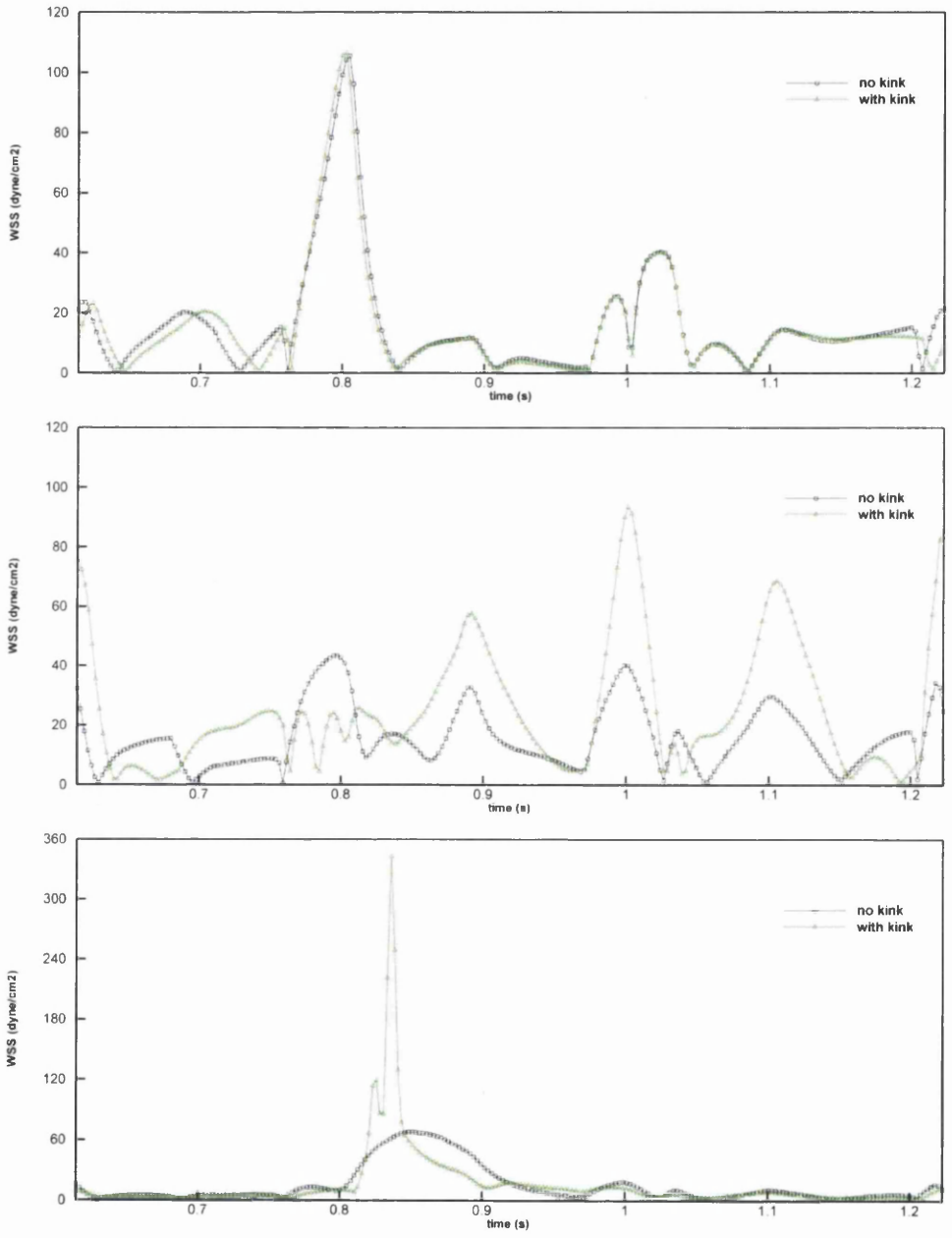

Figure 9.6: TAA WSS Point Tracking a) Region 2 b) Region 1 - in neck c) Region 1 - proximal distance downstream of neck.

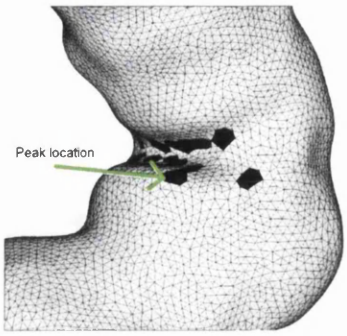

Figure 9.7: TAA Max WSS value distribution in Region 1 for the with kink refined mesh.

It is clear that the folded neck has an influence on the predicted wall shear stress, not only proximal to itself but also upstream within the aortic arch. Its influence is greatest, however, within the folded neck locality and downstream of the neck. In order to investigate the predicted WSS values, the flow within the domain shall be examined.

9.4 Flow within the domain

The flow within the cardiac cycle, is a rapidly evolving situation, as shown in Figure 9.8. In the figure, the streamlines at two time instances are presented. It is clear to see that the folded neck has a strong local influence, inducing greater complexity into the flow relative to the smoothed neck.

To quantitively capture the varying flow patterns in time, it is necessary to examine a number of time instances over the cardiac cycle. To capture the fluid dynamics during systole, the first time instance to be considered is the mid point within the acceleration phase and the second is at peak flow. The third instance is during the deceleration phase and the final time instance is within the dicrotic notch during full reverse flow. Based upon the maximum WSS data a fifth time point is also considered. This time instance being the point of the overall maximum WSS from the with kink case.

Two slices of the three dimensional domain were taken along the axis of the artery, as shown in Figure 9.9. These slices allow for flow investigation both upstream and downstream of the neck region. The first four time instances are shown in Figures 9.10 and 9.11.

Figure 9.10 displays the velocity vectors within the locality and downstream of the neck. During the acceleration phase only small values of the flow are found with 10.8 cm/s in

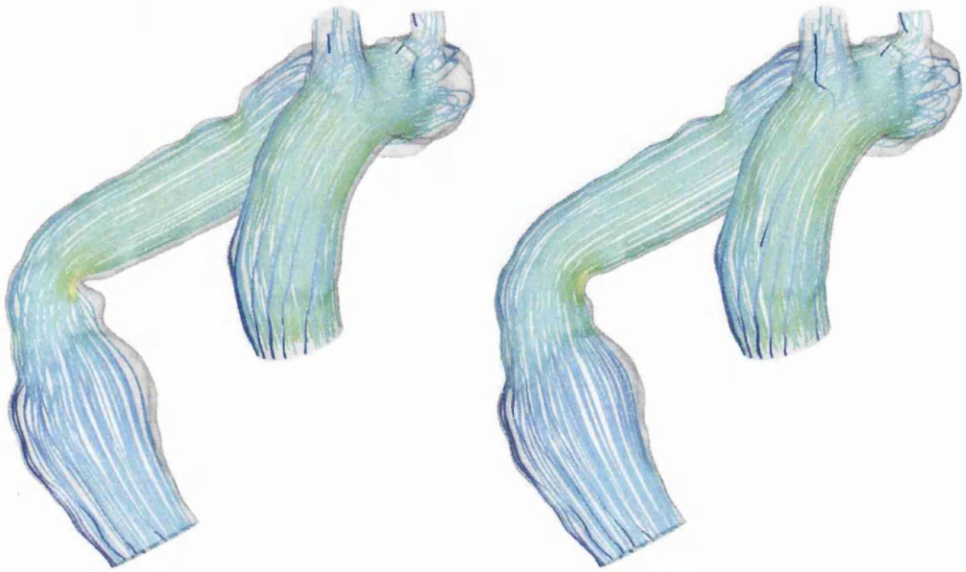

(a) peak systole

(b) peak systole

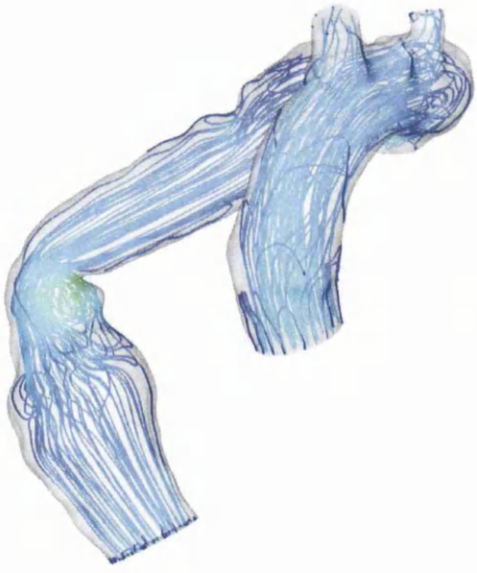

(c) mid deceleration

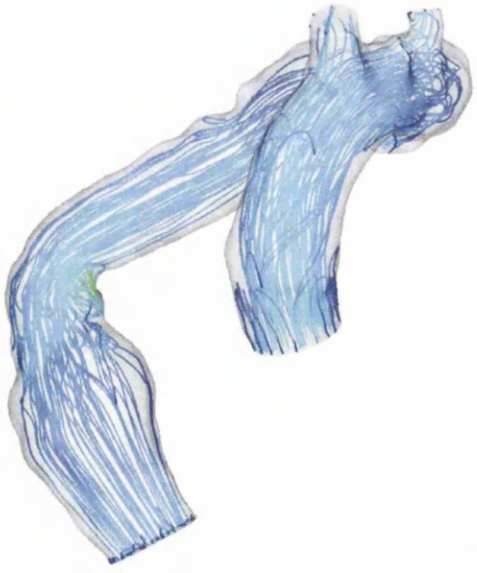

(d) mid deceleration

Figure 9.8: TAA Streamline visualisation for peak systole and mid deceleration

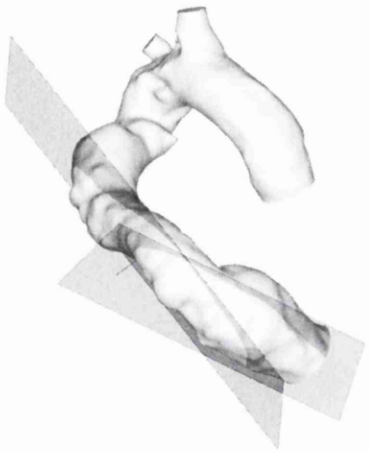

Figure 9.9: TAA Slice Visualisation.

the with kink case and 9.1 cm/s in the no kink case. The vortices are more pronounced in the with kink case although this is marginal. The influence of the folded neck is much more evident during peak flow where the velocity in the with kink case reaches 68.5cm/s proximal to the fold and the no kink velocity achieves a maximum of 48.3cm/s around the artificially smoothed neck. Due to the fold, the flow direction immediately downstream of the neck is towards the axis of the artery whereas in the no kink case the flow follows the vessel wall. This creates a region proximal to the vessel wall experiencing isolated flow downstream of the folded neck. On the opposite vessel wall, the velocities achieved are moderately influenced. Upstream of the neck the velocities experienced are lower in the no kink case ($\approx 7\%$). However, downstream the velocities experienced near the wall are greater ($\approx 20\%$).

During the deceleration phase, the main vortex has increased in size and contains a greater velocity (48.1cm/s) in the with kink case compared to the smaller vortex containing a max velocity of (23.7cm/s) for the no kink case. The location of the vortex has also altered. Instead of being located near the vessel wall proximal to the neck, it is more centrally located within the artery although due to its increased extent it also affects the region proximal to the fold. Upstream of the vortex, flow velocity is more uniform at approximately 9.5cm/s. This uniformity is present in the no kink case although the velocities tend to be greater 10-12cm/s. This uniformity extends throughout the remainder of the no kink domain. However, in the with kink case the vortex has induced a region of relatively stationary fluid $<$ 1cm/s whereas the no kink vortex merely reduces the velocities experienced to 5-6cm/s. Lower near-wall velocities will reduce the near-wall gradients and as such, the wall shear stress. Low wall shear stress is believed to induce growth within an aneurysm. Thus far during the acceleration,

Time Instance	Max Pressure wk	Max Pressure nk	Min Pressure wk	Min Pressure nk	Pressure Drop wk	Pressure Drop nk	Pressure Difference
Mid Acceleration	1219	1184	-7470	-7222	8688	8407	281.6
Peak	1519	2016	-9489	-8561	11008	10577	431.0
Peak WSS	3741	3762	-608	-599	4349	4361	-12.6
Mid Deceleration	4574	4695	-552	-579	5126	5275	-149.1
Full Reverse	5120	5207	-825	-880	5945	6087	-142.2

Table 9.1: TAA Slice pressure [dyne/cm^2] table for selected time instances. [wk - with kink, nk - no kink]

peak and deceleration phases the region downstream of the fold has experienced reduced velocity values while the fold itself has experienced increased velocities.

Within the dicrotic notch the flow experiences its maximum reversed flow. During this time instance the disturbed nature of the flow is again greater in the with kink case. Two vortices in the with kink case induce a maximum velocity of 28.0cm/s, whereas in the no kink case the predicted velocity is significantly smaller (12.8cm/s). However, in contrast to the other three time instances selected, the near-wall region downstream of the neck experiences higher velocities ($\approx$ 200%) in the with kink case. Along the opposite vessel wall the fluid is relatively stationary in the no kink case whereas the value of the velocity is 4-5cm/s in the with kink case. From these predicted values, the wall shear stress during reverse flow will be greater in the with kink case along the majority of the vessel wall highlighted.

With the influence of the fold in the neck examined downstream of its location, the upstream shall now be examined. Figure 9.11 and Table 9.1 give the pressure distribution for the same four time instances. During the acceleration phase, the difference in the pressure distribution is minimal upstream, however the pressure gradient increases downstream of the fold such that the final pressure difference between the two cases is 281.6 dyne/cm^2. The influence of the fold is greater during peak flow, with a larger negative pressure region proximal to the folded neck. In the no kink case the pressure is also negative in the region although the magnitude is smaller (-9502 dyne/cm^2 Vs -8561 dyne/cm^2). Pressure values upstream of the fold have also been influenced with a decrease ($\approx$ 17%) in the pressure gradient in the with kink case.

During the deceleration phase the the pressure gradient upstream is still reduced ($\approx$ 7%) in the with kink case. Downstream of the kink the major difference is due to the disturbed nature of the flow as seen in Figure 9.10 and described previously. The no kink case experiences a more uniformly distributed pressure field outside of the localised influence of the smoothed neck. The downstream influence is also evident within the

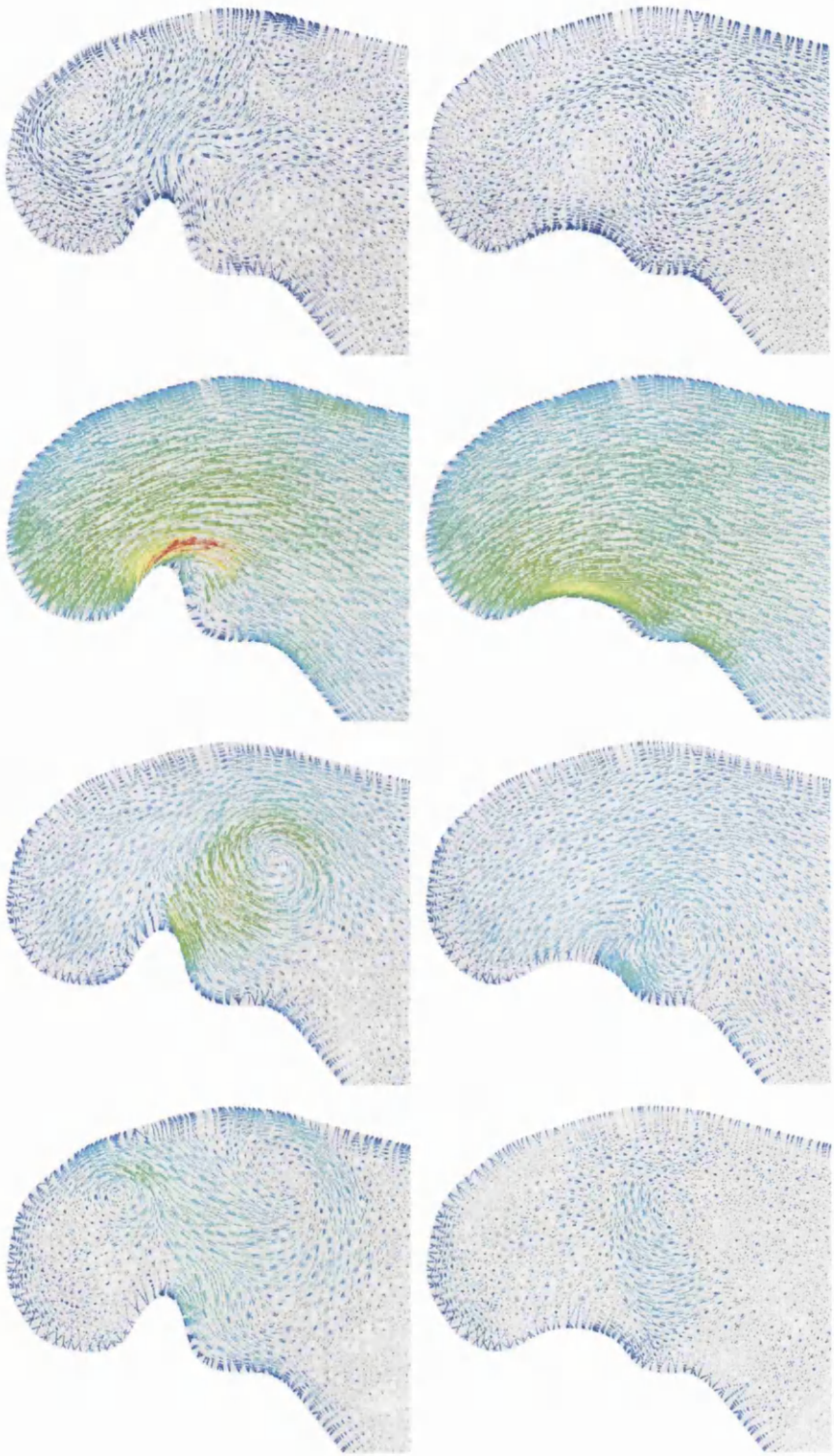

Figure 9.10: TAA Velocity Profiles a) Mid Acceleration (wk) b) Mid Acceleration (nk) c) Peak (wk) d) Peak (nk) e) Mid Deceleration (wk) f) Mid deceleration (nk) g) Full reverse (wk) h) Full reverse (nk). [wk - with kink, nk - no kink].

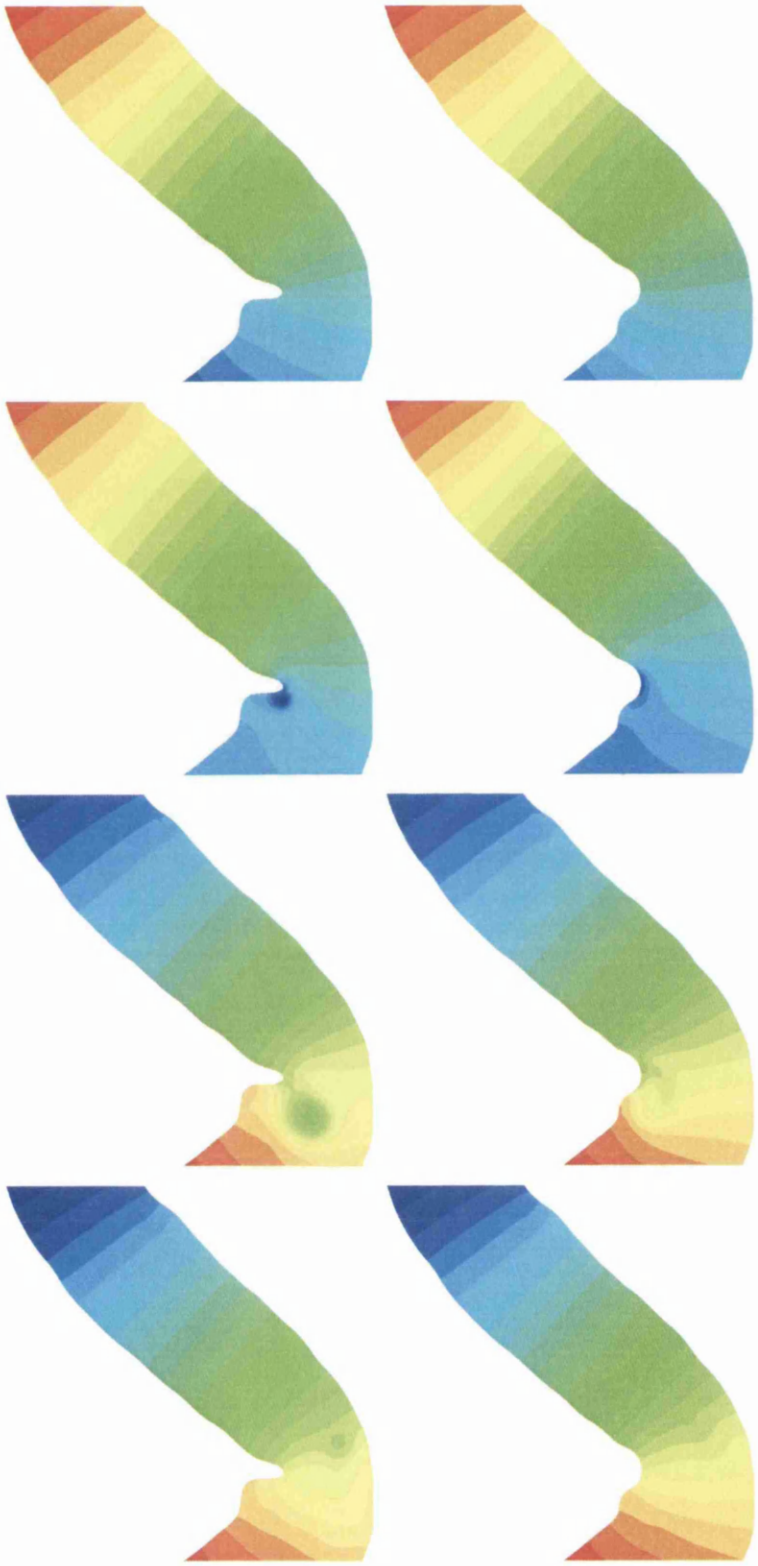

Figure 9.11: TAA Pressure [dyne/cm^2] Profiles a) Mid Acceleration (wk) b) Mid Acceleration (nk) c) Peak (wk) d) Peak (nk) e) Mid Deceleration (wk) f) Mid deceleration (nk) g) Full reverse (wk) h) Full reverse (nk). [wk - with kink, nk - no kink].

fourth time instance. The evenly distributed pressure field of the no kink case indicates a smooth velocity field throughout the slice. In the with kink case, their is still a difference in the upstream pressure gradient although it is now minor (2-3%). From the predicted pressure values, it is clear that the folded neck has an influence upstream of the neck, with the maximum influence occurring during peak flow. The pressure gradient differences indicate that while the distribution of the velocity field remains regular the magnitude differences in the velocities propagate upstream from the neck region.

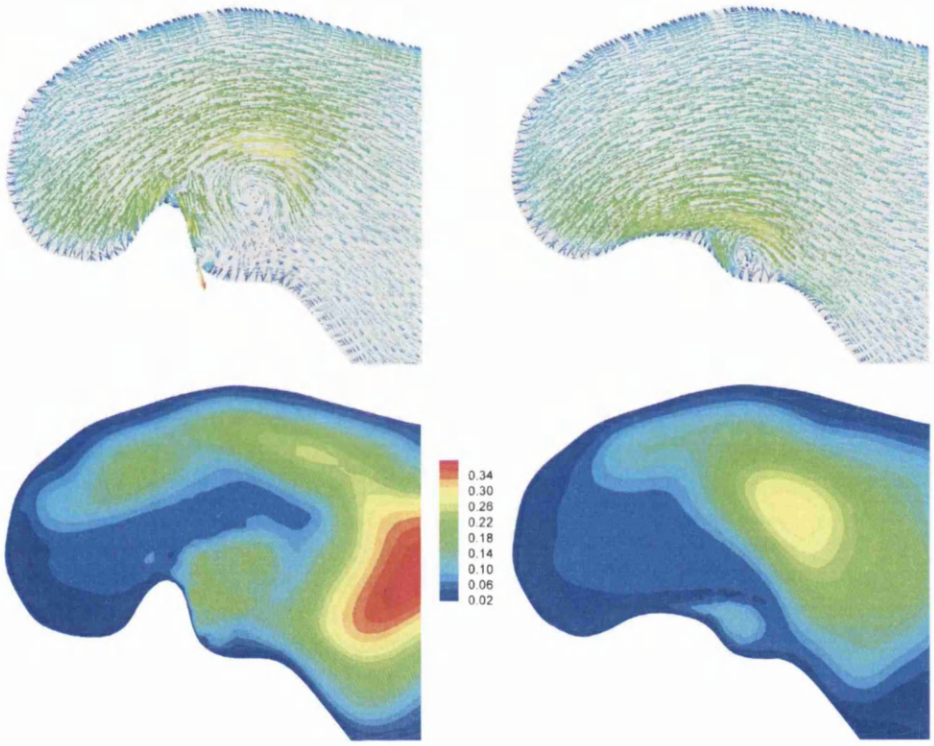

Figure 9.12: TAA Peak WSS time instance a) Velocity Distribution (wk) b) Velocity Distribution (nk) c) $\hat{\nu}$ (wk) d) $\hat{\nu}$ (nk). [wk - with kink, nk - no kink]

The fifth time instance examined was the instance of maximum wall shear stress in the with kink case. The predicted velocity distribution for this time instance is given in Figure 9.12 along with the the modified turbulent eddy kinematic viscosity field $\hat{\nu}$. From the figure, it is clear that the location of the turbulent vortex has induced a large near-wall velocity (64.1cm/s) in the with kink case. The elevated turbulent eddy kinematic viscosity values are proximal to the vessel wall in the with kink case. In the other time instances the gradient of $\hat{\nu}$ as it approaches the vessel wall is significantly less and more reminiscent of the gradient viewable in the no kink case. From these predicted values it is possible to conclude that the fold induces a larger turbulent intensity within the region ($\approx$ 200%) as well as altering it's distribution in the domain in order to produce

a negative outcome. The significantly increased peak WSS at this time instance is important due to high wall shear stress's possible influence on aneurysm rupture.

9.5 Instantaneous Wall Shear Stress

From the velocity and pressure field investigations for five specific time instances, it is clear the predicted solutions differ between the with kink case and the no kink case. The instantaneous wall shear stress distributions for the five instances are given in Figure 9.13. From the figure it is clear that the main influence of the folded neck is downstream of its location. During the acceleration phase, the the instantaneous wall shear stress magnitude is higher (55-80%) upstream of the neck but below the aortic arch although the WSS values are low. However, low WSS values are important when considering plaque formation and aneurysm growth. At peak flow, the values within the aforementioned region are similar in both cases. Differences between the two cases (ignoring downstream of neck) are situated within the aortic arch and the ascending aorta. Here the no kink values are again higher (for example 41.1 Vs 35.2 dyne/cm^2). At the neck itself the no kink maximum is predicted to be 119.0 dyne/cm^2 and the with kink 162.6 dyne/cm^2 a decrease of 27% in the no kink case. Downstream of the neck a band of elevated WSS values ($\approx$ 47 dyne/cm^2) encircles the aneurysm entrance in both cases. However, the location of the local maxima has altered considerably within the band. Within the aneurysm itself, the WSS distribution and magnitude is similar in both cases. During the deceleration phase, only local neck distribution differences exist between the two cases. Both have approximately identical maxima (82.2 dyne/cm^2 in the no kink case and 81.0 dyne/cm^2 in the with kink case). The same can be said of the time instance of maximum reverse flow. The fifth time instance highlights the regions of maximum wall shear stress within the with kink case. Upstream of the neck the differences between the WSS magnitudes is 10-20% although for small (5-10 dyne/cm^2) magnitudes only. At the kink itself, three small regions experience WSS values in excess of 150 dyne/cm^2 which is higher than the overall time and space maximum of 136.4 dyne/cm^2 in the no kink case. From the five time instances analysed, the distribution of WSS has been influenced both in the location and magnitude of the maximum WSS recorded, but also in the distribution of lower WSS values upstream of the fold itself. In the peak flow instance, the band of elevated WSS prior to entering the aneurysm is of importance due to its proximity to the aneurysm. With aneurysm growth weakness in the vessel wall may interact with the higher WSS values and lead to rupture.

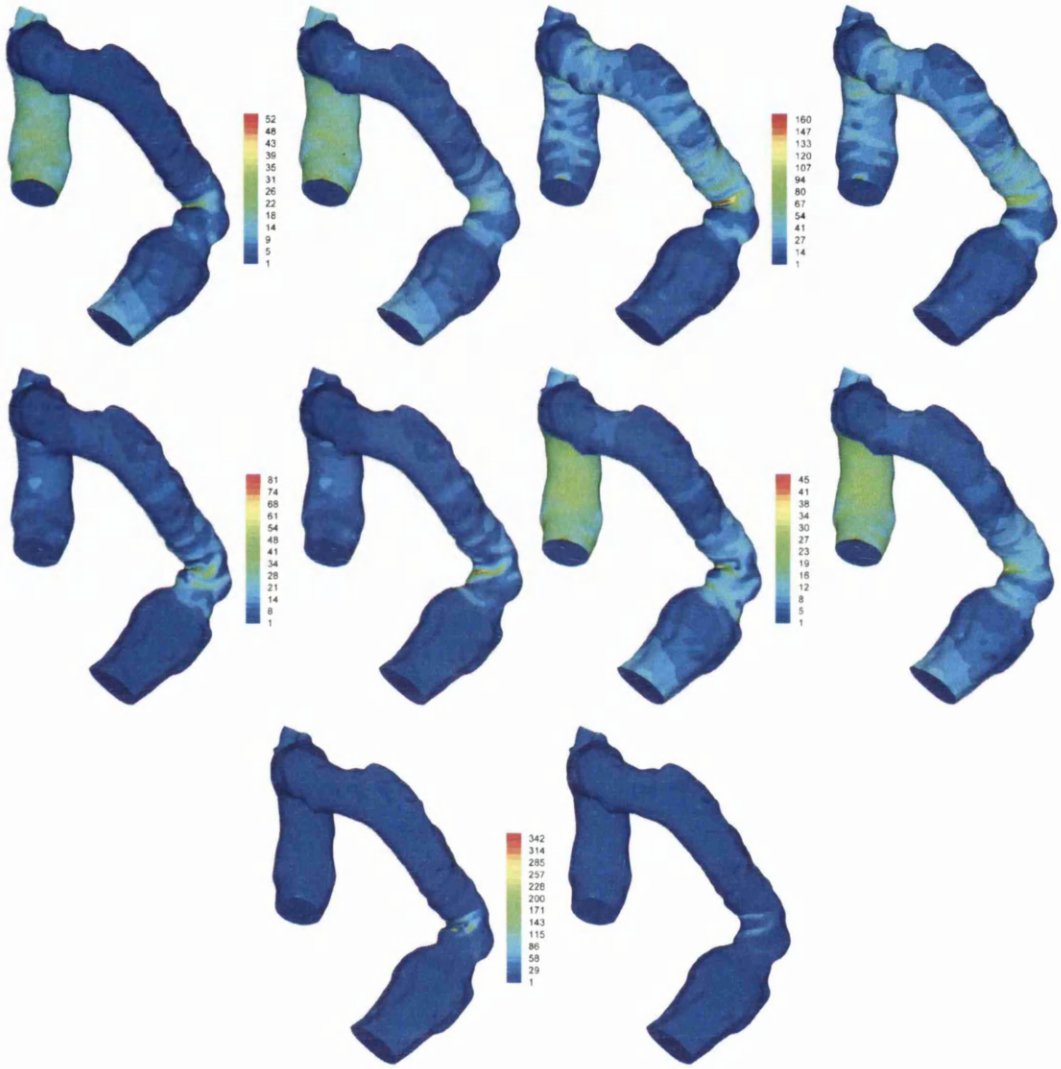

Figure 9.13: TAA Instantaneous wall shear stress [dyne/cm^2] distributions a) Mid Acceleration (wk) b) Mid Acceleration (nk) c) Peak (wk) d) Peak (nk) e) Mid Deceleration (wk) f) Mid deceleration (nk) g) Full reverse (wk) h) Full reverse (nk) i) Peak WSS (wk) j) Peak WSS (nk). [wk - with kink, nk - no kink]

9.6 Derived Haemodynamic Wall Parameters

While instantaneous WSS values provide individual snapshots, time-averaged WSS is employed to provide information over the full cardiac cycle. The time-averaged WSS distribution can be found in Figure 9.14. As expected it can be seen that the location of maximum τ_a occurs proximal to the kink. The maximum value of time-averaged WSS for the with kink case was 29.3 dyne/cm^2 and 20.3 dyne/cm^2 in the no kink case. Differences between the with kink case and no kink case are only visible in the neck region. Elevated values of time-averaged WSS occur along the arterial wall opposite the fold location in the with kink case, which extend partially upstream of the neck. Within the ascending aorta and aortic arch, the no kink case values are approximately 3-5% less. This difference is marginally higher within the descending aorta but upstream of the neck where the difference is 4-7%. The values of time-averaged WSS upon entering the aneurysm are higher and this is maintained within the aneurysm itself. Indeed, two regions exhibit a 20% higher time-averaged WSS value in the with kink case. While low WSS is believed to induce aneurysm growth. Once formed, the aneurysm is prone to rupture under higher WSS values thus the influence of the folded neck is paramount within the aneurysm.

Oscillating shear stress may also influence aneurysm growth. Figure 9.15 shows the oscillating shear index (OSI). It is clearly evident from Figure 9.15 that OSI is not high at the folding but it is very high further downstream in both cases. However, the extent in each case is different. In the folded neck case, the location of high OSI is found on the posterior wall and in the no kink case along a band within the aneurysm. Indeed, the artificially smoothed neck appears to induce a greater growth potential within the aneurysm than the folded neck. From the figure, it is also possible to note that the descending aorta upstream of the neck exhibits higher values in both cases. While the OSI distribution contains a number of high value regions, it is worth noting that the uneven nature of the arterial vessel wall (due both to underlying geometry and calcification) will have a localised influence on this, and as such a rigid wall assumption will exacerbate these influences which may be regarded as false positives.

Examining the time-averaged WSS and OSI distributions in combination, it is possible to determine that high values of oscillating shear stress (based on the OSI) correspond to low values of time-averaged WSS and vice versa. As mentioned previously, it is believed that high time-averaged WSS values contribute to aneurysm rupture while low time-averaged WSS and high OSI contribute to it's growth [124]. From this, it is possible to investigate the influence of the kink. From the results, a smaller region of

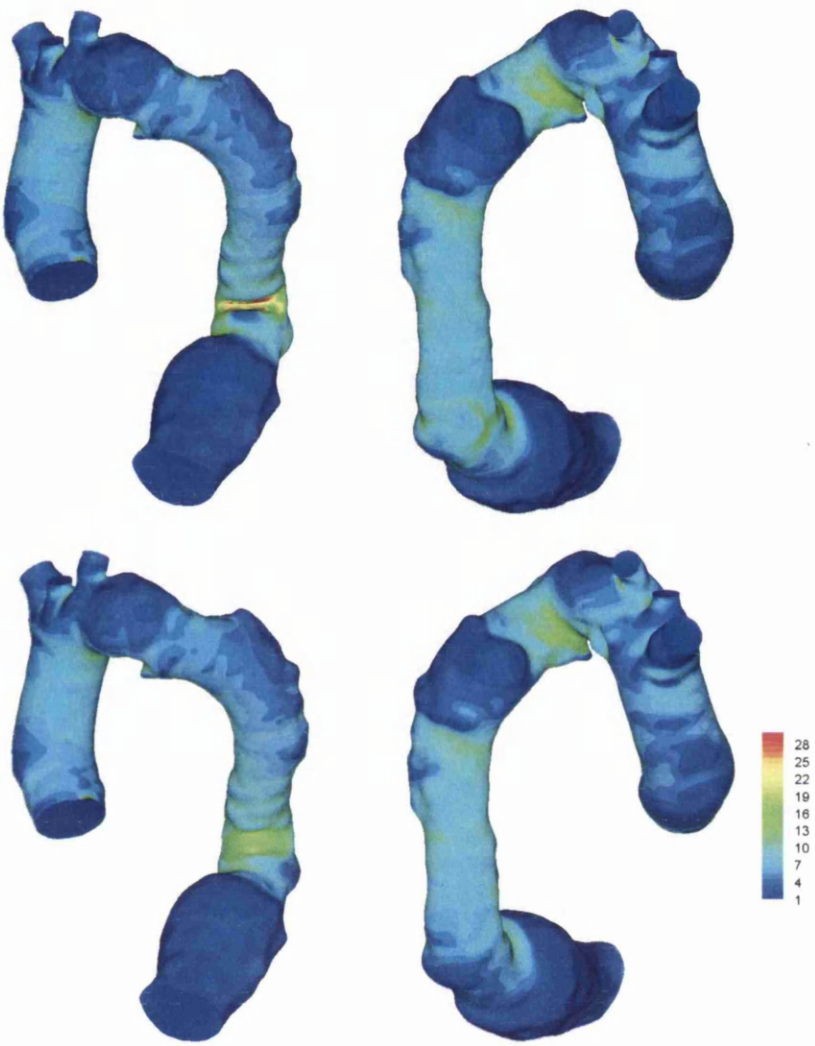

Figure 9.14: Time-averaged WSS (dyne/cm^2). (a) anterior with kink (b) posterior with kink (c) anterior without kink (d)posterior without kink.

the aneurysm experiences high OSI in the with kink case compared to the no kink case. However, the values for the time-averaged WSS are significantly higher in the with kink case, indicating an increased likelihood of rupture. From the artificially smoothed neck results it is clear that while the removal of the fold may reduce overall WSS values at the neck, this may exacerbate the aneurysm growth and future rupture at lower WSS values. Based upon these results, it is clear that the influence the neck geometry has on the flow and hence time-averaged WSS distribution. This demonstrates the need for the inclusion of wall shear stress analysis to be included in any intervention procedure. In order to function as a clinical tool within an intervention procedure, a classification

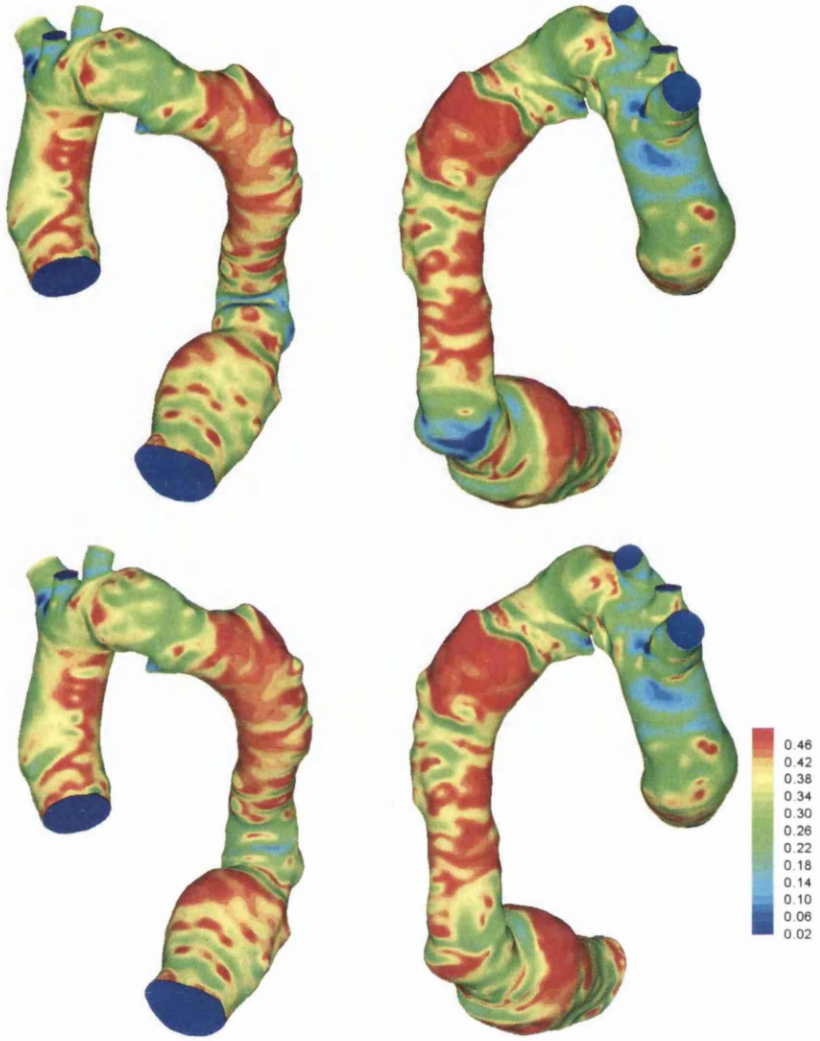

Figure 9.15: Oscillating Shear Index. (a) anterior with kink (b) posterior with kink (c) anterior without kink (d)posterior with kink.

system based on localised geometrical features may be required to refine the parameters for surgery.

9.7 Summary

A computational study of flow through an aorta with a patient-specific thoracic aneurysm has been presented in this chapter. Velocity distributions in the neck region were examined in both cases with and without a kink. The folded neck increased

disturbance within the flow at the neck region in all time instances. The wall shear stress (WSS) and oscillating shear index (OSI) presented clearly shows that the WSS was smaller on the aneurysm wall than the location of the folded neck. The location of peak WSS was located near the folding, just ahead of the aneurysm entrance. However, low and oscillating shear stresses were predicted downstream of the folded neck in both the with kink and no kink case. The results obtained clearly demonstrate the influence of a folded neck on the WSS distribution and magnitudes within the domain. Magnitude variations between the folded neck and no neck case ranged from 150% for the time-averaged WSS to 250% for the maximum instantaneous WSS values. The results thus far are certainly useful but the predictions can be improved by dynamically imposing wall displacement.

Chapter 10

Conclusions and Future Research

The aims of this thesis were threefold. The first was the development of a suitable method for producing answers to problems that required timely solutions. This was implemented through the development of the locally conservative Galerkin spatial discretisation within the characteristic based split scheme and application to three dimensional problems. The solver was further enhanced through the addition of the Spalart-Allmaras one equation turbulence model. The use of an artificially compressible form of the CBS scheme and the SA model allowed for straightforward parallelisation of the method using the Message Passing Interface within FORTRAN. Linear or greater than linear speedup was achieved even on patient-specific hybrid structured and unstructured meshes through a design of minimal inter-processor communication. METIS has been employed for domain decomposition of a serial mesh. From the parallel testing it was clear that the significance of inter-processor communication was negligible even when up to 85% of the local nodes were shared in a three dimensional case.

The second aim of the thesis was the investigation of modelling flow within patient-specific problems in order to assess the requirements needed to accurately assess the wall shear stress and associated wall parameters. This was undertaken through a number of sensitivity studies of both mesh and temporal discretisation. From the results, it was concluded that a purely unstructured mesh is unsuitable for the determination of resolved wall shear stress and other derived parameters. Ten or more boundary layers should be employed to reduce the relative error in the maximum WSS and time-averaged WSS below 2.5%. In cases of stenosis the shear stress is higher and for assessment of potential vascular remodelling, platelet deposition, rupture etc, determination of these values are essential. The choice of real time stepping within the artificially compressible

CBS scheme was also investigated in order to determine its suitability in modelling pulsatile blood flow. This analysis concluded that the choice of backward difference formula (BDF) did not alter the wall shear stress solution, although computational speed was significantly increased as the order of the BDF increased.

With the solver tested and the discretisation sensitivity determined, the final aim of this thesis was the analysis of patient-specific geometries and accurate determination of wall shear stress. One short patient-specific carotid and four long carotid domains were analysed in detail to assess the influence of underlying geometry on flow patterns (and hence WSS). Time-averaged WSS values near the flow divider were high in all cases. In the two long carotids without a stenosis near the bifurcation, the peak time-averaged values were 143 and 250 dyne/cm^2. In the two long carotids with a stenosis near the bifurcation, the peak time-averaged WSS at the apex increased dramatically to 467 and 805 dyne/cm^2. Both of these values (along with significant localised regions within each mesh) exceeded the threshold of 315 dyne/cm^2 for enhancing platelet thrombus formation [47]. In the two cases with no stenosis near the bifurcation, a region of potential atherosclerotic plaque formation was predicted. This was in good agreement with [21] for three out of four cases. More importantly, the fourth case displayed a local narrowing. Away from the flow divider, the downstream regions in all four carotids experienced complex and oscillating flow, as highlighted by the oscillating shear index and wall shear stress angle deviation wall parameters. In contrast, the common carotid artery experienced relatively uniform flow, with low spatial oscillation.

The influence of the flow division and flow rate were also analysed on one diseased carotid to assess the near stenosis implications. Four alternative flow cases were examined. The flow division and flow rate have a very modest impact on the derived wall shear stress parameter distributions. This is due to the overriding influence of the artery geometry. From the analysis, it is clear that for accurate assessment of the wall shear stresses the model must be validated using clinical data. Ultrasound measurements of proximal velocities at the stenosis would be one method of achieving this, without extra effort on behalf of the radiologist.

Finally, a thoracic aortic aneurysm was investigated to assess the influence of a folded neck on the resultant wall shear stress using the developed solver. The folded neck induced major local variation when compared to an artificially smoothed neck geometry. The folded neck case experienced significantly higher velocities proximal to the neck, as well as more highly disturbed flow. The presence of the folded neck induced changes of up to 150% within the time-averaged wall shear stress and 250% within the maximum instantaneous wall shear stress values. From these detailed studies, it is clear that the

patient-specific geometry has an important role within the distribution of wall shear stress.

One of the potential future avenues of research includes the large scale assessment of many patient-specific geometries. The work in this thesis has determined that while differences exist between patient-specific geometries there are also localised similarities which result in similar predicted wall shear stress values and distributions. A large scale study would allow the collection of sufficient data to potentially construct a databank of reference geometries. This would remove the need for large scale computational resources within the clinical setting and provide a rapid diagnostic tool. To improve the model, a number of approaches can be considered. Currently, the model utilises a fully explicit scheme which is easily parallelisable and will scale very well to large numbers of processors. The use of a semi-implicit scheme would reduce the number of overall iterations within each computational run, although parallel implementation (and linear scaling) is more complex. To improve the accuracy of the predicted results, vessel wall displacement information could be included from Magnetic Resonance Imaging. This would avoid the use of direct fluid-structure interaction models which would introduce extra complexity and assumptions within the model. While the flow division between the carotid arteries in this thesis is assumed, more ultrasound data (on the ICA downstream from the bifurcation) would allow for more accurate flow representation. This data would allow for an increased accuracy in applying a flow division, by allowing a transient flow division.

Appendix A

Matrix form of the CBS scheme

A.1 Introduction

This chapter outlines the full matrix expansion of the fully explicit scheme along with the matrix form of the Spalart-Allmaras one equation model.

A.2 Characteristic Based Split Scheme

A.2.1 Step 1

$$\begin{aligned} \mathbf{M}_1 &= \int_\Omega \mathbf{N}^{\mathbf{T}}\mathbf{N}d\Omega \\ &= \frac{6V}{5!}\begin{bmatrix} 2 & 1 & 1 & 1 \\ 1 & 2 & 1 & 1 \\ 1 & 1 & 2 & 1 \\ 1 & 1 & 1 & 2 \end{bmatrix} \approx \frac{6V}{5!}\begin{bmatrix} 5 & 0 & 0 & 0 \\ 0 & 5 & 0 & 0 \\ 0 & 0 & 5 & 0 \\ 0 & 0 & 0 & 5 \end{bmatrix} = \frac{V}{4}\begin{bmatrix} 1 & 0 & 0 & 0 \\ 0 & 1 & 0 & 0 \\ 0 & 0 & 1 & 0 \\ 0 & 0 & 0 & 1 \end{bmatrix} \end{aligned} \tag{A.1}$$

where V denotes the element volume. Integration of the shape functions $\mathbf{N}$ is undertaken using the relationships

$$\int_{\Omega} N^a N^b N^c d\Omega = \frac{a!b!c!6V}{(a+b+c+3)!} \qquad \int_{\Gamma} N^a N^b N^c d\Gamma = \frac{a!b!c!2A}{(a+b+c+2)!} \tag{A.2}$$

in 3D, where A denotes the face area. In 2D these relationships are defined as

$$\int_{\Omega} N^a N^b N^c d\Omega = \frac{a!b!c!2A}{(a+b+c+2)!} \qquad \int_{\Gamma} N^a N^b N^c d\Gamma = \frac{a!b!c!L}{(a+b+c+1)!} \tag{A.3}$$

where A represents the area of the element and L the length of the edge. The consistent mass matrix can be lumped in order to produce a matrix free algorithm, and the lumped form is employed within this work. The convective term $\mathbf{C}_1 \{\mathbf{u}_j \mathbf{U}_i\}^n$ is given as

$$\mathbf{C}_1 \{\mathbf{u}_j \mathbf{U}_i\}^n = \int_{\Omega} \frac{\partial \mathbf{N}^{\mathbf{T}}}{\partial \mathbf{x}_j} \mathbf{N} \{\mathbf{u}_j \mathbf{U}_i\}^n d\Omega = \frac{6V}{4!} \begin{bmatrix} \frac{\partial N_1}{\partial x_j} \\ \frac{\partial N_2}{\partial x_j} \\ \frac{\partial N_3}{\partial x_j} \\ \frac{\partial N_4}{\partial x_j} \end{bmatrix} \sum_{r=1}^{4} \{u_j U_i\}_r \qquad j = 1,2,3 \tag{A.4}$$

Within Equation A.4 two summations occur. One is defined by the Einstein notation j and is based on the coordinate components, the second r is based on a local nodal value summation over the four elemental nodes. The diffusive or viscous term $\mathbf{K}_1$ is defined as

$$\mathbf{K}_1 = \frac{1}{Re} \int_{\Omega} \frac{\partial \mathbf{N}^{\mathbf{T}}}{\partial \mathbf{x}_j} \boldsymbol{\tau}_{ij}^n d\Omega = \frac{V}{Re} \begin{bmatrix} \frac{\partial N_1}{\partial x_j} \\ \frac{\partial N_2}{\partial x_j} \\ \frac{\partial N_3}{\partial x_j} \\ \frac{\partial N_4}{\partial x_j} \end{bmatrix} \tau_{ij} \qquad j = 1,2,3 \tag{A.5}$$

and τ_{ij} is determined using

$$\tau_{ij} = \left(\frac{\partial \mathbf{N}}{\partial \mathbf{x}_j}\{\mathbf{u}_i\}^n + \frac{\partial \mathbf{N}}{\partial \mathbf{x}_i}\{\mathbf{u}_j\}^n - \frac{2}{3}\delta_{ij}\frac{\partial \mathbf{N}}{\partial \mathbf{x}_k}\{\mathbf{u}_k\}^n\right) \tag{A.6}$$

$$= \sum_{r=1}^{4}\left\{\frac{\partial N}{\partial x_j}u_i^n\right\}_r + \sum_{r=1}^{4}\left\{\frac{\partial N}{\partial x_i}u_j^n\right\}_r - \frac{2}{3}\delta_{ij}\sum_{r=1}^{4}\left\{\frac{\partial N}{\partial x_k}u_k^n\right\}_r \qquad j,k = 1,2,3$$

Since τ_{ij} is constant over the element the element contributions are averaged to determine a nodal approximation. Thus $\mathbf{f}_2$ is given as

$$\{\mathbf{f}_2\} = \frac{1}{Re}\int_\Gamma \mathbf{N}^{\mathbf{T}} n_j \mathbf{N}\{\hat{\tau}_{ij}\}^n \, d\Gamma \tag{A.7}$$

$$= \frac{1}{Re} n_j \frac{A}{12}\begin{bmatrix}2 & 1 & 1\\ 1 & 2 & 1\\ 1 & 1 & 2\end{bmatrix}\begin{Bmatrix}\hat{\tau}_{ij}^1\\ \hat{\tau}_{ij}^2\\ \hat{\tau}_{ij}^3\end{Bmatrix}^n \approx \frac{1}{Re} n_j \frac{A}{3}\begin{bmatrix}1 & 0 & 0\\ 0 & 1 & 0\\ 0 & 0 & 1\end{bmatrix}\begin{Bmatrix}\hat{\tau}_{ij}^1\\ \hat{\tau}_{ij}^2\\ \hat{\tau}_{ij}^3\end{Bmatrix}^n \tag{A.8}$$

where n_j is the j component of the face normal, $\hat{\tau}_{ij}^1$,$\hat{\tau}_{ij}^2$ and $\hat{\tau}_{ij}^2$ denote nodal values for the 3 local face nodes respectively and are defined by

$$\hat{\tau}_{ij}^a = \frac{1}{Ne}\sum_{e=1}^{Ne}\{\tau_{ij}\}_e \tag{A.9}$$

where a is a global node, $\{.\}_e$ the element value and Ne the number of elements connected to the node. Since nodal values for the convective face term are already available $\mathbf{f}_1$ can be determined by

$$\{\mathbf{f}_1\} = \int_\Gamma \mathbf{N}^{\mathbf{T}} n_j \mathbf{N}\{\mathbf{u}_j\mathbf{U}_i\}^n \, d\Gamma \tag{A.10}$$

$$= n_j \frac{A}{12}\begin{bmatrix}2 & 1 & 1\\ 1 & 2 & 1\\ 1 & 1 & 2\end{bmatrix}\begin{Bmatrix}\widehat{u_jU_i}^1\\ \widehat{u_jU_i}^2\\ \widehat{u_jU_i}^3\end{Bmatrix}^n \approx n_j \frac{A}{3}\begin{bmatrix}1 & 0 & 0\\ 0 & 1 & 0\\ 0 & 0 & 1\end{bmatrix}\begin{Bmatrix}\widehat{u_jU_i}^1\\ \widehat{u_jU_i}^2\\ \widehat{u_jU_i}^3\end{Bmatrix}^n$$

where $\widehat{u_jU_i}^a = u_jU_i{}^a$. The characteristic stabilisation terms are expressed as

$$\mathbf{K}_1^{\mathbf{CG}}\{\mathbf{u}_j\mathbf{U}_i\}^n = \frac{\Delta t}{2}\int_\Omega \frac{\partial \mathbf{N}^{\mathbf{T}}}{\partial \mathbf{x}_k}\hat{u}_k\frac{\partial \mathbf{N}}{\partial \mathbf{x}_j}\{\mathbf{u}_j\mathbf{U}_i\}^n \tag{A.11}$$

$$= \frac{\Delta t}{2}\hat{u}_k V\begin{bmatrix}\frac{\partial N_1}{\partial x_k}\\ \frac{\partial N_2}{\partial x_k}\\ \frac{\partial N_3}{\partial x_k}\\ \frac{\partial N_4}{\partial x_k}\end{bmatrix}\sum_{r=1}^{4}\left\{\frac{\partial N}{\partial x_j}(u_jU_i)^n\right\}_r \qquad j,k=1,2,3$$

where $\hat{u}_k$ is the value of u_k determined at the centroid of the element. The face term due to the characteristic-Galerkin stabilisation is determined using

$$\{\mathbf{f}_3\} = \frac{\Delta t}{2}\int_\Gamma \mathbf{N}^{\mathbf{T}}n_k\hat{u}_k\mathbf{N}\left\{\frac{\partial \widehat{\mathbf{u}_j\mathbf{U}_i}}{\partial \mathbf{x}_j}\right\}^n d\Gamma \tag{A.12}$$

$$= n_k\frac{\Delta t}{2}\hat{u}_k\frac{A}{12}\begin{bmatrix}2&1&1\\1&2&1\\1&1&2\end{bmatrix}\begin{Bmatrix}\widehat{f}_i^{\,1}\\ \widehat{f}_i^{\,2}\\ \widehat{f}_i^{\,3}\end{Bmatrix}^n \approx n_k\frac{\Delta t}{2}\hat{u}_k\frac{A}{3}\begin{bmatrix}1&0&0\\0&1&0\\0&0&1\end{bmatrix}\begin{Bmatrix}\widehat{f}_i^{\,1}\\ \widehat{f}_i^{\,2}\\ \widehat{f}_i^{\,3}\end{Bmatrix}^n \qquad k=1,2,3$$

where $\hat{u}_k$ is the value of u_k determined at the centroid of the face, f_i^a represents the nodal numerical flux value at node a due to the face stabilisation term, defined by

$$f_i^a = \frac{1}{Ne}\sum_{e=1}^{Ne}\left(\sum_{r=1}^{4}\left\{\frac{\partial N}{\partial x_j}(u_jU_i)^n\right\}_r\right) \qquad j=1,2,3 \tag{A.13}$$

A.2.2 Step 2

The mass matrix $\mathbf{M}_2$ is lumped as before giving

$$\mathbf{M}_2 = \int_\Omega \mathbf{N}^{\mathbf{T}}\mathbf{N}d\Omega \approx \frac{V}{4}\begin{bmatrix}1&0&0&0\\0&1&0&0\\0&0&1&0\\0&0&0&1\end{bmatrix} \tag{A.14}$$

The convection term in Step 2 is denoted by

$$\begin{aligned}
\mathbf{C}_2\{\mathbf{U}_i+\Delta\mathbf{U}_i^*\}^n &= \int_\Omega \frac{\partial \mathbf{N}^\mathbf{T}}{\partial \mathbf{x}_i}\mathbf{N}\{\mathbf{U}_i^n+\Delta\mathbf{U}_i^*\}\,d\Omega \qquad (A.15)\\
&= \frac{V}{4}\begin{bmatrix}\frac{\partial N_1}{\partial x_i}\\ \frac{\partial N_2}{\partial x_i}\\ \frac{\partial N_3}{\partial x_i}\\ \frac{\partial N_4}{\partial x_i}\end{bmatrix}\sum_{r=1}^{4}\{U_i^n+\Delta U_i^*\}_r\\
&= \frac{V}{4}\begin{bmatrix}\frac{\partial N_1}{\partial x_i}\\ \frac{\partial N_2}{\partial x_i}\\ \frac{\partial N_3}{\partial x_i}\\ \frac{\partial N_4}{\partial x_i}\end{bmatrix}\sum_{r=1}^{4}\{U_i^*\}_r \qquad i=1,2,3
\end{aligned}$$

The expression for the convection face term $\mathbf{f_4}$ is

$$\begin{aligned}
\{\mathbf{f}_4\} &= \int_\Gamma \mathbf{N}^\mathbf{T}\mathbf{N}n_i\{\mathbf{U}_i^n+\Delta\mathbf{U}_i^*\}\,d\Gamma \qquad (A.16)\\
&= n_i\frac{A}{12}\begin{bmatrix}2&1&1\\1&2&1\\1&1&2\end{bmatrix}\begin{Bmatrix}\widehat{U_i^*}^1\\ \widehat{U_i^*}^2\\ \widehat{U_i^*}^3\end{Bmatrix}\approx n_i\frac{A}{3}\begin{bmatrix}1&0&0\\0&1&0\\0&0&1\end{bmatrix}\begin{Bmatrix}\widehat{U_i^*}^1\\ \widehat{U_i^*}^2\\ \widehat{U_i^*}^3\end{Bmatrix} \qquad i=1,2,3
\end{aligned}$$

where the numerical value at node a is $\widehat{U_i^*}^a = U_i^{*a}$. The pressure term is given as

$$\begin{aligned}
\mathbf{K}_2\{\mathbf{p}\} &= \Delta t\int_\Omega \frac{\partial \mathbf{N}^\mathbf{T}}{\partial \mathbf{x}_i}\frac{\partial \mathbf{N}}{\partial \mathbf{x}_i}\{\mathbf{p}\}^n\,d\Omega\\
&= \Delta t V\begin{bmatrix}\frac{\partial N_1}{\partial x_i}\\ \frac{\partial N_2}{\partial x_i}\\ \frac{\partial N_3}{\partial x_i}\\ \frac{\partial N_4}{\partial x_i}\end{bmatrix}\sum_{r=1}^{4}\left\{\frac{\partial N}{\partial x_i}p^n\right\}_r \qquad i=1,2,3 \qquad (A.17)
\end{aligned}$$

and the pressure face term is defined as

$$\{\mathbf{f}_5\} = \int_\Gamma \mathbf{N}^\mathbf{T}\mathbf{N}n_i \left\{\widehat{\frac{\partial \mathbf{p}}{\partial \mathbf{x}_i}}\right\}^n d\Gamma$$

$$= n_i \frac{A}{12}\begin{bmatrix}2 & 1 & 1\\ 1 & 2 & 1\\ 1 & 1 & 2\end{bmatrix}\begin{Bmatrix}\widehat{g_i}^1\\ \widehat{g_i}^2\\ \widehat{g_i}^3\end{Bmatrix}^n \approx n_i \frac{A}{3}\begin{bmatrix}1 & 0 & 0\\ 0 & 1 & 0\\ 0 & 0 & 1\end{bmatrix}\begin{Bmatrix}\widehat{g_i}^1\\ \widehat{g_i}^2\\ \widehat{g_i}^3\end{Bmatrix}^n \quad i = 1,2,3 \text{(A.18)}$$

where since the flux is constant over the element, the numerical nodal value is defined based upon the elemental contributions as

$$g_i^a = \frac{1}{Ne}\sum_{e=1}^{Ne}\left(\sum_{r=1}^{4}\left\{\frac{\partial N}{\partial x_i}p^n\right\}_r\right)_e \quad i = 1,2,3 \tag{A.19}$$

A.2.3 Step 3

The mass matrix is expressed as before

$$\mathbf{M}_3 = \int_\Omega \mathbf{N}^\mathbf{T}\mathbf{N}d\Omega \approx \frac{V}{4}\begin{bmatrix}1 & 0 & 0 & 0\\ 0 & 1 & 0 & 0\\ 0 & 0 & 1 & 0\\ 0 & 0 & 0 & 1\end{bmatrix} \tag{A.20}$$

The pressure correction term is calculated using

$$\mathbf{C}_3\{\mathbf{p}\}^n = \int_\Omega \frac{\partial \mathbf{N}^\mathbf{T}}{\partial \mathbf{x}_i}\{\mathbf{p}\}^n d\Omega \tag{A.21}$$

$$= \frac{V}{4}\begin{bmatrix}\frac{\partial N_1}{\partial x_i}\\ \frac{\partial N_2}{\partial x_i}\\ \frac{\partial N_3}{\partial x_i}\\ \frac{\partial N_4}{\partial x_i}\end{bmatrix}\sum_{r=1}^{4}\{p^n\}_r \tag{A.22}$$

The pressure correction face term $\mathbf{f}_6$ can be determined from

$$\begin{aligned}\{\mathbf{f}_6\} &= \int_\Gamma \mathbf{N}^\mathbf{T}\mathbf{N} n_i \{\mathbf{p}\}^n \, d\Gamma \\ &= n_i \frac{A}{12}\begin{bmatrix}2 & 1 & 1\\ 1 & 2 & 1\\ 1 & 1 & 2\end{bmatrix}\begin{Bmatrix}\widehat{p}^1\\ \widehat{p}^2\\ \widehat{p}^3\end{Bmatrix} \approx n_i \frac{A}{3}\begin{bmatrix}1 & 0 & 0\\ 0 & 1 & 0\\ 0 & 0 & 1\end{bmatrix}\begin{Bmatrix}\widehat{p}^1\\ \widehat{p}^2\\ \widehat{p}^3\end{Bmatrix}\end{aligned} \tag{A.23}$$

Finally the pressure stability terms are calculated using

$$\begin{aligned}\mathbf{K}_3 \{\mathbf{p}\}^n &= \frac{\Delta t}{2}\int_\Omega \frac{\partial \mathbf{N}^\mathbf{T}}{\partial \mathbf{x}_k}\hat{u}_k \frac{\partial \mathbf{N}}{\partial \mathbf{x}_i}\{p\}^n \, d\Omega \\ &= \frac{\Delta t}{2} V \hat{u}_k \begin{bmatrix}\frac{\partial N_1}{\partial x_k}\\ \frac{\partial N_2}{\partial x_k}\\ \frac{\partial N_3}{\partial x_k}\\ \frac{\partial N_4}{\partial x_k}\end{bmatrix} \sum_{r=1}^{4}\left\{\frac{\partial N}{\partial x_i}p^n\right\}_r \qquad k = 1,2,3\end{aligned} \tag{A.24}$$

where $\hat{u}_k$ is the value at the centroid of the element. The pressure stability face term is defined as

$$\{\mathbf{f}_7\} = \frac{\Delta t}{2}\int_\Gamma \mathbf{N}^\mathbf{T}\mathbf{N} n_k \left\{\frac{\partial \mathbf{p}^n}{\partial \mathbf{x}_i}\right\} d\Gamma \tag{A.25}$$

$$= \frac{\Delta t}{2} n_k \frac{A}{12}\begin{bmatrix}2 & 1 & 1\\ 1 & 2 & 1\\ 1 & 1 & 2\end{bmatrix}\begin{Bmatrix}\widehat{h}_i^{\,1}\\ \widehat{h}_i^{\,2}\\ \widehat{h}_i^{\,3}\end{Bmatrix}^n \approx \frac{\Delta t}{2} n_k \frac{A}{3}\begin{bmatrix}1 & 0 & 0\\ 0 & 1 & 0\\ 0 & 0 & 1\end{bmatrix}\begin{Bmatrix}\widehat{h}_i^{\,1}\\ \widehat{h}_i^{\,2}\\ \widehat{h}_i^{\,3}\end{Bmatrix}^n \qquad k = 1,2,3$$

where $\hat{u}_k$ is the face centroidal value of u_k. Since the flux is constant over the element, the numerical nodal value is defined based upon the elemental contributions as

$$h_i^a = \frac{1}{Ne}\sum_{e=1}^{Ne}\left(\sum_{r=1}^{4}\left\{\frac{\partial N}{\partial x_k}p^n\right\}_r\right)_e \qquad k = 1,2,3 \tag{A.26}$$

A.3 Spalart Allmaras Model

In order to maintain the matrix free solution procedure the mass matrix $\mathbf{M}^{SA}$ is lumped as before giving

$$\mathbf{M}^{SA} = \int_{\Omega} \mathbf{N}^{\mathbf{T}}\mathbf{N} d\Omega = \approx \frac{V}{4} \begin{bmatrix} 1 & 0 & 0 & 0 \\ 0 & 1 & 0 & 0 \\ 0 & 0 & 1 & 0 \\ 0 & 0 & 0 & 1 \end{bmatrix} \tag{A.27}$$

The convection components of the transport equation are expressed as

$$\begin{aligned} \mathbf{C}^{SA} &= \int_{\Omega} \frac{\partial \mathbf{N}^{\mathbf{T}}}{\partial \mathbf{x}_i} \{\hat{\boldsymbol{\nu}}\mathbf{u}_i\} \, d\Omega \\ &= \frac{V}{4} \begin{bmatrix} \frac{\partial N_1}{\partial x_i} \\ \frac{\partial N_2}{\partial x_i} \\ \frac{\partial N_3}{\partial x_i} \\ \frac{\partial N_4}{\partial x_i} \end{bmatrix} \sum_{r=1}^{4} \{\hat{\nu} u_i\}_r \qquad i = 1,2,3 \end{aligned} \tag{A.28}$$

$$\begin{aligned} \mathbf{f}_1^{SA} &= \int_{\Gamma} n_i \mathbf{N}^{\mathbf{T}}\mathbf{N} \{\hat{\boldsymbol{\nu}}\mathbf{u}_i\}^n \, d\Gamma \\ &= n_i \frac{A}{12} \begin{bmatrix} 2 & 1 & 1 \\ 1 & 2 & 1 \\ 1 & 1 & 2 \end{bmatrix} \begin{Bmatrix} \widehat{\hat{\nu}u_i}^1 \\ \widehat{\hat{\nu}u_i}^2 \\ \widehat{\hat{\nu}u_i}^3 \end{Bmatrix}^n \approx n_i \frac{A}{3} \begin{bmatrix} 1 & 0 & 0 \\ 0 & 1 & 0 \\ 0 & 0 & 1 \end{bmatrix} \begin{Bmatrix} \widehat{\hat{\nu}u_i}^1 \\ \widehat{\hat{\nu}u_i}^2 \\ \widehat{\hat{\nu}u_i}^3 \end{Bmatrix}^n \qquad i = 1,2,3 \end{aligned} \tag{A.29}$$

The convection stabilisation term can be calculated using

$$\begin{aligned} \mathbf{K}_1^{SA} &= \frac{\Delta t}{2} \int_{\Omega} \frac{\partial \mathbf{N}^{\mathbf{T}}}{\partial \mathbf{x}_k} \hat{u}_k \frac{\partial \mathbf{N}}{\partial \mathbf{x}_i} \{\hat{\boldsymbol{\nu}}\mathbf{u}_i\} \, d\Omega \\ &= \frac{\Delta t}{2} V \hat{u}_k \begin{bmatrix} \frac{\partial N_1}{\partial x_k} \\ \frac{\partial N_2}{\partial x_k} \\ \frac{\partial N_3}{\partial x_k} \\ \frac{\partial N_4}{\partial x_k} \end{bmatrix} \sum_{r=1}^{4} \left\{ \frac{\partial N}{\partial x_i} \hat{\nu} u_i \right\}_r \qquad i = 1,2,3 \end{aligned} \tag{A.30}$$

The diffusion components are defined as

$$\begin{aligned}
\mathbf{K}_2^{SA} &= \frac{1}{Re\sigma_{\hat{\nu}}}\int_\Omega \frac{\partial \mathbf{N}^\mathbf{T}}{\partial \mathbf{x}_i}(1+\hat{\nu})\frac{\partial \mathbf{N}}{\partial \mathbf{x}_i}\{\hat{\boldsymbol{\nu}}\}\,d\Omega \\
&= \frac{1}{Re\sigma_{\hat{\nu}}}V(1+\bar{\hat{\nu}})\begin{bmatrix}\frac{\partial N_1}{\partial x_i}\\ \frac{\partial N_2}{\partial x_i}\\ \frac{\partial N_3}{\partial x_i}\\ \frac{\partial N_4}{\partial x_i}\end{bmatrix}\sum_{r=1}^{4}\left\{\frac{\partial N}{\partial x_i}\hat{\nu}\right\}_r \qquad i=1,2,3 \qquad \text{(A.31)}
\end{aligned}$$

$$\begin{aligned}
\mathbf{f}_2^{SA} &= \frac{1}{Re\sigma_{\hat{\nu}}}\int_\Gamma n_i\mathbf{N}^\mathbf{T}\mathbf{N}(1+\hat{\nu})\left\{\frac{\widehat{\partial\hat{\nu}}}{\partial \mathbf{x}_i}\right\}^n d\Gamma \qquad \text{(A.32)}\\
&= \frac{1}{Re\sigma_{\hat{\nu}}}(1+\bar{\hat{\nu}})n_i\frac{A}{12}\begin{bmatrix}2&1&1\\1&2&1\\1&1&2\end{bmatrix}\begin{Bmatrix}\widehat{a_i}^1\\ \widehat{a_i}^2\\ \widehat{a_i}^3\end{Bmatrix}^n\\
&\approx \frac{1}{Re\sigma_{\hat{\nu}}}(1+\bar{\hat{\nu}})n_i\frac{A}{3}\begin{bmatrix}1&0&0\\0&1&0\\0&0&1\end{bmatrix}\begin{Bmatrix}\widehat{a_i}^1\\ \widehat{a_i}^2\\ \widehat{a_i}^3\end{Bmatrix}^n \qquad i=1,2,3
\end{aligned}$$

where $\bar{\hat{\nu}}$ represents the element arithmetic mean of $\hat{\nu}$ and a_i is the nodal average of the elemental contributions which is expressed as

$$a_i = \frac{1}{Ne}\sum_{e=1}^{Ne}\left(\sum_{r=1}^{4}\left\{\frac{\partial N}{\partial x_i}\hat{\nu}^n\right\}_r\right)_e \qquad \text{(A.33)}$$

The remaining diffusion component and its stabilisation is given by

$$\begin{aligned}
\mathbf{K}_3^{SA} &= \frac{c_{b2}}{Re\sigma_{\hat{\nu}}}\int_\Omega \mathbf{N}^\mathbf{T}\left(\frac{\partial \mathbf{N}}{\partial \mathbf{x}_i}\{\hat{\boldsymbol{\nu}}\}\right)^2 d\Omega - \frac{\Delta t c_{b2}}{2Re\sigma_{\hat{\nu}}}\int_\Omega \frac{\partial \mathbf{N}^\mathbf{T}}{\partial \mathbf{x}_k}\hat{u}_k\left(\frac{\partial \mathbf{N}}{\partial \mathbf{x}_i}\{\hat{\boldsymbol{\nu}}\}\right)^2 d\Omega \qquad \text{(A.34)}\\
&= \frac{c_{b2}}{Re\sigma_{\hat{\nu}}}\frac{V}{4}\begin{bmatrix}1\\1\\1\\1\end{bmatrix}\sum_{r=1}^{4}\left\{\left(\frac{\partial N}{\partial x_i}\hat{\nu}\right)^2\right\}_r + \frac{\Delta t}{2}\frac{c_{b2}}{Re\sigma_{\hat{\nu}}}V\hat{u}_k\begin{bmatrix}\frac{\partial N_1}{\partial x_k}\\ \frac{\partial N_2}{\partial x_k}\\ \frac{\partial N_3}{\partial x_k}\\ \frac{\partial N_4}{\partial x_k}\end{bmatrix}\sum_{r=1}^{4}\left\{\left(\frac{\partial N}{\partial x_i}\hat{\nu}\right)^2\right\}_r \qquad i=1,2,3
\end{aligned}$$

The source terms are expressed as

$$\begin{aligned}\mathbf{K}_4^{SA} &= c_{b1}\hat{S}\int_\Omega \mathbf{N}^{\mathbf{T}}\mathbf{N}d\Omega \\ &= c_{b2}\hat{S}\frac{V}{20}\begin{bmatrix}2&1&1&1\\1&2&1&1\\1&1&2&1\\1&1&1&2\end{bmatrix}\end{aligned} \tag{A.35}$$

and

$$\begin{aligned}\mathbf{K}_5^{SA} &= \frac{c_{w1}f_w}{Re}\int_\Omega \mathbf{N}^{\mathbf{T}}\mathbf{N}d\Omega \\ &= \frac{c_{w1}f_w}{Re}\frac{V}{20}\begin{bmatrix}2&1&1&1\\1&2&1&1\\1&1&2&1\\1&1&1&2\end{bmatrix}\end{aligned} \tag{A.36}$$

The source stabilisation terms are given by

$$\begin{aligned}\mathbf{K}_6^{SA} &= \frac{\Delta t}{2}c_{b1}\int_\Omega \frac{\partial \mathbf{N}^{\mathbf{T}}}{\partial \mathbf{x}_k}\hat{u}_k\hat{S}\mathbf{N}\left\{\hat{\nu}\right\}d\Omega \\ &= \frac{\Delta t}{2}c_{b1}\hat{S}\hat{u}_k\frac{V}{4}\begin{bmatrix}\frac{\partial N_1}{\partial x_k}\\ \frac{\partial N_2}{\partial x_k}\\ \frac{\partial N_3}{\partial x_k}\\ \frac{\partial N_4}{\partial x_k}\end{bmatrix}\sum_{r=1}^{4}\left\{\hat{\nu}\right\}_r \qquad k=1,2,3\end{aligned} \tag{A.37}$$

and

$$\mathbf{K}_7^{SA} = \frac{\Delta t}{2}\frac{c_{w1}f_w}{Re}\int_\Omega \frac{\partial \mathbf{N}^{\mathbf{T}}}{\partial \mathbf{x}_k}\hat{u}_k \mathbf{N}\left\{\frac{\hat{\boldsymbol{\nu}}}{\mathbf{y}}\right\} d\Omega \tag{A.38}$$

$$= \frac{\Delta t}{2}\frac{c_{w1}f_w}{Re}\hat{u}_k\frac{V}{4}\begin{bmatrix}\frac{\partial N_1}{\partial x_k}\\ \frac{\partial N_2}{\partial x_k}\\ \frac{\partial N_3}{\partial x_k}\\ \frac{\partial N_4}{\partial x_k}\end{bmatrix}\sum_{r=1}^{4}\left\{(\hat{\nu}/y)^2\right\}_r \qquad k=1,2,3$$

Appendix B

The Message Passing Interface (MPI) toolset

B.1 Introduction

The Message Passing Interface (MPI) library was employed in this work in order to parallelise a number of programs. The general implementation procedure is outlined in this appendix, along with the specific MPI subroutines employed within these programs. The MPI library was utilised within both the main CBS code itself and the post-processing program in order to fully parallelise the execution pipeline. It was also used within the domain decomposition stage in the preparation of the necessary sub-domain files prior to execution of the CBS code.

B.2 General Implementation

Like any computing language there are certain required steps that must be undertaken to implement MPI subroutines within a computational program. In order to implement MPI subroutines within FORTRAN it is necessary that the line "include mpif.h" be placed within the preamble of any FORTRAN subroutine that itself calls an MPI routine. The second requirement is that the first MPI subroutine called is MPI_INIT. This subroutine initialises the MPI library for use within the FORTRAN program. Although not a requirement *per se*, the final MPI call should be MPI_FINALIZE. This terminates the MPI library usage within the FORTRAN program, although this does

not terminate the program itself or indeed specify whether the initialised slave nodes are deactivated. Thus, it is recommended that only minimal commands occur prior and subsequent to MPI_INIT and MPI_FINALIZE respectively.

B.3 MPI Subroutines

Although there are several hundred MPI routines within the current MPI-2.2 standard only a limited number have been employed within the computational programs used by this work. The thirteen subroutines used are outlined in detail within this section. The MPI library, as previously mentioned, can be employed within the C, C++ and FORTRAN languages. The FORTRAN implementation varies slightly from the two other implementations with an additional component, namely an error handler, returned by every MPI subroutine. This error handler *ierror* is shown within this section and its removal would outline a C or C++ implementation. For example, two MPI subroutines have already been mentioned in this appendix namely

CALL MPI_INIT(ierror)

CALL MPI_FINALIZE(ierror)

In C this would become

MPI_INIT()

MPI_FINALIZE().

Two other basic MPI subroutines are called subsequent to the initialisation of the parallel program. These are

CALL MPI_COMM_RANK(MPI_COMM_WORLD, myRank, ierror)

CALL MPI_COMM_SIZE(MPI_COMM_WORLD, numProcs, ierror)

with the program now in a parallelised mode, it is necessary for each processor to know what is its designated name (or rank) is and how many processors have also been initialised. These two commands fulfil this purpose with MPI_COMM_RANK determining the patch rank (*myRank*) and MPI_COMM_SIZE gathering the number of processors (*numProcs*). *myRank* will vary from 0 to *numProcs*-1. These two values are essential in establishing inter-processor communication such that the right

information reaches the required processor. The remaining argument in both commands is MPI_COMM_WORLD. This argument is the communicator, and is basically a name for a collection of processors that can communicate with each other.

The two following MPI routines are linked and can be instigated at any point within the FORTRAN program, although it is traditional that they occur close to MPI_INIT.

CALL MPI_TYPE_CONTIGIOUS(3,MPI_REAL8,Vec3,ierror)

CALL MPI_TYPE_COMMIT(Vec3,ierror)

these MPI calls simplify the communication in later MPI calls through the creation of additional data types. Standard data types such as MPI_REAL8, MPI_INTEGER4, MPI_DOUBLE_PRECISION are predefined. These are based on their FORTRAN counterparts REAL(KIND=8), INTEGER(KIND=4) and DOUBLE PRECISION. Derived data types build on these data types easing inter-processor communication. In the example command outlined above, the derived data type combines 3 MPI_REAL8 values into what is regarded as 1 *Vec3*. This derived data is then initiated across all processors with MPI_TYPE_COMMIT.

With what can be regarded as the preliminary MPI calls outlined, the main MPI calls are now detailed. The first of which is

CALL MPI_BCAST(nreal,1,MPI_INTEGER4,0,MPI_COMM_WORLD,ierror)

this subroutine deals with one way communication from a source to a list of designated recipients. The information broadcast in this case is the variable *nreal* from the processor with rank (*myRank*) 0 to every processor within the collection MPI_COMM_WORLD. MPI_COMM_WORLD in this case is every initialised processor. Two further pieces of information are required, namely how big is variable *nreal* which in this case is 1 and what data type is *nreal*. In this case it is MPI_INTEGER4. An example of transferring an array of information in this manner would be

CALL MPI_BCAST(narray,10,Vec3,0,MPI_COMM_WORLD,ierror)

However, *narray* contains more than 10 pieces of information since *Vec3* as outlined above itself contains 3 MPI_REAL8 values. *Vec3* can be used since *narray* is arranged as a matrix (3,10), with for example u,v and w components of the velocity for 10 datapoints. A point also worth noting is that a process of rank 0 is also known as the master node.

In order to achieve full inter-processor communication, it is possible to utilise

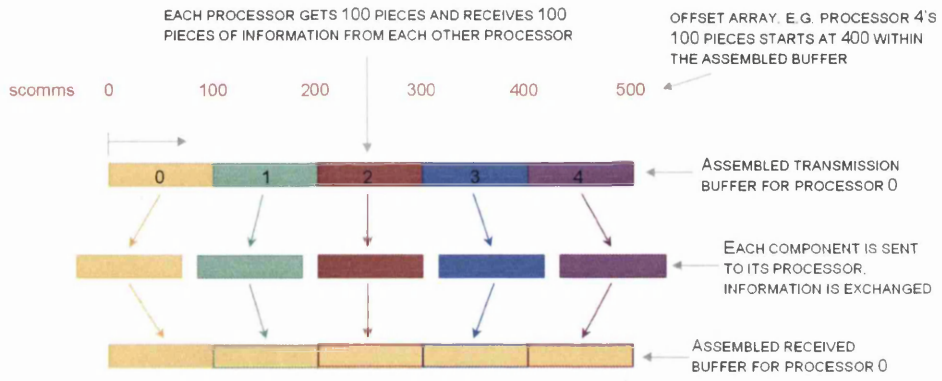

Figure B.1: Graphical representation of MPI_ALLTOALL

CALL MPI_ALLTOALL(rtmpm(1,1), 100, MPI_REAL8, rtmpm(1,2), 100, MPI_REAL8, MPI_COMM_WORLD, ierror)

and its variant

CALL MPI_ALLTOALLV(rtmpm2(1,1,1), ncomms, scomms, Vec3, rtmpm2(1,1,2), ncomms, scomms, Vec3, MPI_COMM_WORLD, ierror)

These MPI calls are utilised as the name suggests in all processors sharing information with all other processors. In the case of MPI_ALLTOALL, a fixed amount of information is exchanged between processors. Prior to using these commands it is typical that the information to be transferred is first placed into a temporary array, which is organised into a sending component and a receiving component. In the MPI_ALLTOALL example listed above, the temporary array is called *rtmpm*. With 100 communications being conducted between each processor in MPI_COMM_WORLD the array's size would typically be (100numProcs,2). The first argument in the call is the start location in the buffer for the transfer out, followed by the size of transfer (100 in this instance) and the type of information being transferred (MPI_REAL8). The second part of the call deals with the information to be received. The first argument of this part is the start location in the buffer for receiving data and then information as before on the amount of data to be received from each processor and what type. This can be visualised in Figure B.1.

The routine MPI_ALLTOALLV is a more complex version of MPI_ALLTOALL, and is the version employed within the CBS code. The call MPI_ALLTOALLV allows for asynchronous communication across processors. As before, the call can be visualised as two parts, the arguments needed for output specification and the arguments needed on the information being received. In the example given above, the information

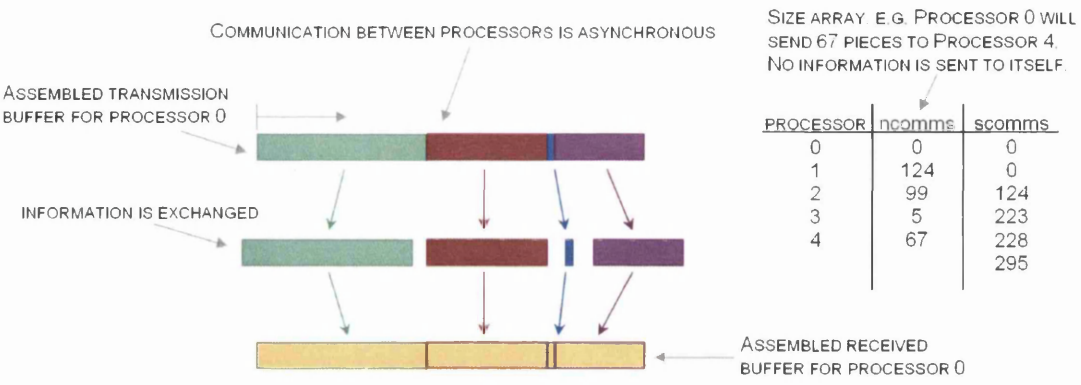

Figure B.2: Graphical representation of MPI_ALLTOALLV

is stored within the temporary array *rtmpm2* with the arrangement (3,*ntotcomm*,2) where *ntotcomm* is the total number of communications. With the communication transfer being asynchronous, two information arrays are required to specify how much information is transferred and to which processor. The first array (*ncomms*) consists of the number of transfers to each processor while the second array (*scomms*) details the offset needed within the buffer to transfer the correct information to the right processor. This is represented in Figure B.2.

The third type of communication employed after MPI_BCAST and MPI_ALLTOALLV is

CALL MPI_ALLGATHERV(LocalCoord, icomm, Vec3, GlobalCoord, ncomms, scomms, Vec3, MPI_COMM_WORLD, ierror)

This MPI subroutine is employed to gather information local to an individual processor together into a global array which is available to each individual processor. This method of communication is only employed within the turbulent CBS code in order to gather information on the wall nodes within the preprocessing stage. The first argument contains the information to be passed into the global array. The next two arguments specifies the amount of information to be transferred and the data type. The following four arguments concern the information received, the first contains the information itself, the second the amount received from each processor and the third the offset in the array needed to access the information received from that processor. The final component is the data type of the received information.

The final type of communication used within the programs is

CALL MPI_ALLREDUCE(ival, ival2, 1, MPI_INTEGER4, MPI_SUM, MPI_COMM_WORLD, ierror)

this command can be utilised in order to pass information into a buffer where an operation can be performed before transfer of the resultant to each processor. There are several options for the operator, from the example given above MPI_SUM, to MPI_MAX or MPI_MIN. The input value (*ival*) is given as the first argument and the second argument lists the return variable (*ival2*). The third and fourth arguments list the amount of information to be transferred and the data type respectively.

Two further MPI calls are made within the parallel programs, although these are not essential to the running of the program itself. These MPI calls provide information on the time duration of the program run. These do not need the *ierror* error handler.

starttime=MPI_WTIME()

accuracy=MPI_WTICK()

the first call returns a floating point number of seconds. This timed value gives an elapsed time since a past time point. This time point will not alter during the run time of the parallel program allowing for determination of elapsed time. MPI_WTICK returns the resolution of the MPI_WTIME call, its value represents the number of seconds between two successive processor clock ticks.

Bibliography

[1] U. Ghia, K. N. Ghia, and C. T. Shin. High-re solutions for incompressible flow using the Navier-Stokes equations and a multigrid method. *Journal of Computational Physics*, 48:387 – 411, 1982.

[2] J. P. Mynard and P. Nithiarasu. A 1D arterial blood flow model incorporating ventricular pressure, aortic valve and regional coronary flow using the locally conservative galerkin (LCG) method. *Communications in Numerical Methods in Engineering*, 24:367–417, 2008.

[3] R. Ross. Mechanisms of disease - atherosclerosis - an inflammatory disease. *New England Journal of Medicine*, 340(2):115–126, 1999.

[4] American Heart Association Working Group. Heart disease and stroke statistics - 2009 update. *Circulation*, 119:e21–e181, 2009.

[5] P. Libby. Inflammation in atherosclerosis. *Nature*, 420:868–874, 2002.

[6] P. Libby, P.M. Ridker, and A. Maseri. Inflammation and atherosclerosis. *Circulation*, 105:1135–1143, 2002.

[7] P.M. Ridker, C.H. Hennekens, J.E. Buring, and N.Rifai. C-reactive protein and other markers of inflammation in the prediction of cardiovascular disease in women. *New England Journal of Medicine*, 342:836–843, 2000.

[8] W. Droge. Free radicals in the physiological control of cell function. *Physiological reviews*, 82:47–95, 2002.

[9] P.M. Ridker, M. Cushman, M.J. Stampfer, R.P. Tracy, and C.H. Hennekens. Inflammation, aspirin, and the risk of cardiovascular disease in apparently healthy men. *New England Journal of Medicine*, 336:973–979, 1997.

[10] E. Euthman. Carotid Plaque. http://www.flickr.com/photos/euthman/121061911/sizes/l/in/set-72057594114099781/.

[11] Dr Heyman Luckraz. Personal communication 2010.

[12] Patient UK: Ruptured Aortic Aneurysm. Website:http://www.patient.co.uk/showdoc/40024966/.

[13] C.C.A. Macintyre F.G.R. Fowkes and C.V. Ruckley. Increasing incidence of aortic aneurysms in england and wales. *British Medical Journal*, 298:33–35, 1989.

[14] A.J. Lusis. Atherosclerosis. *Nature*, 407:233–241, 2000.

[15] D. Tang, C. Yang, S. Mondal, F. Liu, G. Canton, T. S. Hatsukami, and C. Yuan. A negative correlation between human carotid atherosclerotic plaque progression and plaque wall stress: In vivo MRI-based 2D/3D FSI models. *Journal of Biomechanics*, 41:727–736, 2008.

[16] J.M. Hill, G. Zalos, J.P.J. Halcox, W.H. Schenke, M.A. Waclawiw, A.A. Quyyumi, and Toren Finkel. Circulating endothelial progenitor cells, vascular function, and cardiovascular risk. *New England Journal of Medicine*, 348:593–600, 2003.

[17] M.F. Fillinger, S.P. Marra, M.L. Raghavan, and F.E. Kennedy. Prediction of rupture risk in abdominal aortic aneurysm during observation: Wall stress versus diameter. *Journal of Vascular Surgery*, 37:724–732, 2003.

[18] D. N. Ku, D. P. Giddens, C. K. Zarins, and S. Glagov. Pulsatile flow and atherosclerosis in the human carotid bifurcation - positive correlation between plaque location and low and oscillating shear-stress. *Atherosclerosis*, 5(3):293–302, 1985.

[19] F. P. Glor, Q. Long, A. D. Hughes, A. D. Augst, B. Ariff, S. A. McG. Thom, P. R. Verdonck, and X. Y. Xu. Reproducibility study of magnetic resonance image-based computational fluid dynamics prediction of carotid bifurcation flow. *Annals of Biomedical Engineering*, 31:142–151, 2003.

[20] P. Papathanasopoulou, S. Zhao, U. Köhler, M. B. Robertson, Q. Long, and P. Hoskins. MRI measurement of time-resolved wall shear stress vectors in a carotid bifurcation model, and comparison with CFD predictions. *Journal of Magnetic Resonance Imaging*, 17:153–162, 2003.

[21] M. R. Kaazempur-Mofrad, A. G. Isasi, H. F. Younis, R. C. Chan, D. P. Hinton, G. Sukhova, G. M. LaMuraglia, R. T. Lee, and R. D. Kamm. Characterization of the atherosclerotic carotid bifurcation using MRI finite element modeling, and histology. *Annals of Biomedical Engineering*, 32:932–946, 2004.

[22] S. A. Urquiza, P. J. Blanco, M. J. Vénere, and R. A. Feijóo. Multidimensional modelling for the carotid artery blood flow. *Computational Methods in Applied Mechanics in Engineering*, 195:4002–4017, 2006.

[23] A. D. Jeays, P. V. Lawford, R. Gillott, P. Spencer, D. C. Barber, K. D. Bardhan, and D. R. Hose. Characterisation of the haemodynamics of the superior mesenteric artery. *Journal of Biomechanics*, 40:1916–1926, 2007.

[24] S. E. Lee, S-W. Lee, P. F. Fischer, H. S. Bassiouny, and F. Loth. Direct numerical simulation of transitional flow in a stenosed carotid bifurcation. *Journal of Biomechanics*, 41:2551–2561, 2008.

[25] K. T. Nguyen, C. D. Clark, T. J. Chancellor, and D. V. Papavassiliou. Carotid geometry effects on blood flow and on risk for vascular disease. *Journal of Biomechanics*, 41:11–19, 2008.

[26] J. Hwang, A. Saha, Y. C. Boo, G. P. Sorescu, J. S. McNally, S. M. Holland, S. Dikalov, D. P. Giddens, K. K. Griendling, D. G. Harrison, and H. Jo. Oscillatory shear stress stimulates endothelial production of from p47phox-dependent nad(p)h oxidases, leading to monocyte adhesion. *Journal of Biological Chemistry*, 278:47291–47298, 2003.

[27] J. Hwang, M. H. Ing, A. Salazar, B. Lassègue, K. Griendling, M. Navab, A. Sevanian, and T. K. Hsiai. Pulsatile versus oscillatory shear stress regulates nadph oxidase subunit expression. *Circulation Research*, 93:1225–1232, 2003.

[28] T. Nagel, N. Resnick, C. F. Dewey Jr, and M. A. Gimbrone Jr. Vascular endothelial cells respond to spatial gradients in fluid shear stress by enhanced activation of transcription factors. *Arterisoscelerosis, Thrombosis, and Vascular Biology*, 19:1825–1834, 1999.

[29] C. Cheng, D. Tempel, R van Haperen, A. van der Baan, F. Grosveld, M. Daemen, R. Krams, and R. de Crom. Atherosclerotic lesion size and vulnerability are determined by patterns of fluid shear stress. *Circulation*, 113:2744–2753, 2006.

[30] B. C. Berk, J-I Abe, W. Min, J. Surapisitchat, and C. Yan. Endothelial atheroprotective and anti-inflammatory mechanisms. *Annals of New York Acadamy of Sciences*, 947:93–111, 2001.

[31] B.C. Berk. Atheroprotective signaling mechanisms activated by steady laminar flow in endothelial cells. *Circulation*, 117:1082–1089, 2008.

[32] O. Traub and B.C. Berk. Laminar shear stress : Mechanisms by which endothelial cells transduce an atheroprotective force. *Arteriosclerosis Thrombosis and Vascular Biology*, 18:677–685, 1998.

[33] S. Vyalov, B. L. Langille, and A. I. Gotlieb. Decreased blood flow rate disrupts endothelial repair *in vivo*. *American Journal of Pathology*, 149:2107–2118, 1996.

[34] A.M. Malek, S.L. Alper, and S. Izumo. Hemodynamic shear stress and its role in atherosclerosis. *Journal of the American Medical Association*, 282:2035–2042, 1999.

[35] J. B. Sharefkin, S.L. Diamond, S.G. Eskin, L.V McIntire, and C.W. Dieffenbach. Fluid flow decrease preproendothelin mrna levels and suppresses endothelin-1 peptide release in cultured human endothelial cells. *Journal of Vascular Surgery*, 14:1–9, 1991.

[36] M. L. Bots, A. Hofman, Paulus T. V. M. De Jong, and D. E. Grobbee. Common carotid intima-media thickness as an indicator of atherosclerosis at other sites of the carotid artery the Rotterdam Study. *Annals of Epidemiology*, 6(2):147–153, 1996.

[37] S. J. Vermeersch, F. P. Glor, L. A. Crowe, B. Ariff, M. Bol, P. Segers, A. D. Hughes, X. Y. Xu, Thom SMcG, D. N. Firmin, and P. R. Verdonck. Relationship between carotid artery intima-media thickness and wall shear stress derived parameters. *Computer Methods in Biomechanics and Biomedical Engineering*, 8(4):279–280, 2005.

[38] E.M.Pedersen, S. Oyre, M. Agerbaek, I.B. Kristensen, S. Ringgaard, P. Boesiger, and W.P. Paaske. Distribution of early atherosclerotic lesions in the human abdominal aorta correlates with wall shear stresses measured *in vivo*. *Eur J Vasc Endovasc Surg*, 18:328–333, 1999.

[39] S-W. Lee, L Antiga, J. D. Spence, and D. A. Steinman. Geometry of the carotid bifurcation predicts its exposure to disturbed flow. *Stroke*, 39:2341–2347, 2008.

[40] S. Hyun, C. Kleinstreuer, P.W. Longest, and C.Chen. Particle-hemodynamics simulations and design options for surgical reconstruction of diseased carotid artery bifurcations. *Journal of Biomechanical Engineering*, 126:188–195, 2004.

[41] H. F. Younis, M. R. Kaazempur-Mofrad, R. C. Chan, A. G. Isasi, D. P. Hinton, A. H. Chau, L. A. Kim, and R. D. Kamm. Hemodynamics and wall mechanics in human carotid bifurcation and its consequences for atherogenesis - investigation of inter-individual variation. *Biomechanics and Modeling in Mechanobiology*, 3:17–32, 2004.

[42] S. Z. Zhao, X. Y. Xu, A. D. Hughes, S. A. Thom, A. V. Stanton, B. Ariff, and Q. Long. Blood flow and vessel mechanics in a physiologically realistic model of a human carotid arterial bifurcation. *Journal of Biomechanics*, 33:975–984, 2000.

[43] R. Torii, M. Oshima, T. Kobayashi, K. Takagi, and T. E. Tezduyar. Computer modeling of cardiovascular fluid-structure interactions with the deforming-spatial-domain/stabilised space-time formulation. *Computer Methods in Applied Mechanics and Engineering*, 195:1885–1895, 2006.

[44] R. Torii, M. Oshima, T. Kobayashi, K. Takagi, and T. E. Tezduyar. Fluid-structure interaction modeling of aneurysmal conditions with high and normal blood pressures. *Computational Mechanics*, 38:482–490, 2006.

[45] H. Gao, Q. Long, M. Graves, J. H. Gillard, and Z-Y Li. Carotid arterial plaque stress analysis using fluid-structure interactive simulation based on in-vivo magnetic resonance images of four patients. *Journal of Biomechanics*, 42:1416–1423, 2009.

[46] L. Grinberg, A. Yakhot, and G. E. Karniadakis. Analyzing transient turbulence in a stenosed carotid artery by proper orthogonal decomposition. *Annals of Biomedical Engineering*, 37:2200–2217, 2009.

[47] P.A. Holme, U. Orvim, M.J.A.G Hamers, N.O. Solum, F.R.Brosstad, R.M Barstad, and K.S. Sakariassen. Shear-induced platelet activation and platelet microparticle formation at blood flow conditions as in arteries with a severe stenosis. *Arteriosclerosis Thrombosis and Vascular Biology*, 17:646–653, 1997.

[48] K.S. Sakariassen, P.A. Holme, U. Orvim, R.M. Barstad, N.O.Solum, and F.R.Brosstad. Shear-induced platelet activation and platelet microparticle formation in native human blood. *Thrombosis Research*, 92:S33–S41, 1998.

[49] A. Mailhac, J.J.Badimon, J.T.Fallon, A. Fernandez-Ortiz, B. Meyer, J.H. Chesebro, V. Fuster, and L.Badimon. Effect of an eccentric severe stenosis on fibrin(ogen) deposition on severely damaged vessel wall in arterial thrombosis. relative contribution of fibrin(ogen) and platelets. *Circulation*, 90:988–996, 1994.

[50] H.C. Groen, F.J.H. Gijsen, A van der Lugt, M.S. Ferguson, T.S. Hatsukami, A.F.W. van der Steen, C. Yuan, and J.J. Wentzel. Plaque rupture in the carotid artery is localized at the high shear stress region: A case report. *Stroke*, 38:2379–2381, 2007.

[51] E.S.Crawford and J.S.Coselli. *Semin Thorac Cardiovasc Surg.*, 3:300–322, 1991.

[52] J.B. Gardner M.H.Meissner S.H. Nicholls and Johansen K.H. Rupture in small abdominal aortic aneurysms. *J. Vasc. Surg.*, 28:884–888, 1998.

[53] H.A. Ashton D.R. Allen R.A.P. Scott, P.V. Tisi. Abdominal aortic aneurysm rates: A 7-year follow-up of the entire abdominal aortic aneurysm population detected by screening. *J. Vasc. Surg.*, 28:124–128, 1998.

[54] M.A. Coady J.A. Rizzo and J.A. Elefteriades. Procedures for estimating growth rates in thoracic aortic aneurysms. *Clin Epidemiol.*, 51:747–754, 1998.

[55] D. Mori and T. Yamaguchi. Computational fluid dynamics modeling and analysis of the effect of 3-d distortion of the human aortic arch. *Computer Methods Biomechanics and Biomedical Engineering*, 5:249–260, 2002.

[56] R.H. Mohiaddin N.B. Wood S. Thom F.P.P. Tan, A. Borghi and X.Y. Xu. Analysis of flow patterns in a patient-specific thoracic aortic aneurysm model. *Comp. Struct.*, 87:680–690, 2009.

[57] A. Mizukami. A mixed finite element method for boundary flux computation. *Computer Methods in Applied Mechanics and Engineering*, 57:239–243, 1986.

[58] P. M. Gresho, R. L. Lee, R. L. Sani, M. K. Maslanik, and B. E. Eaton. The consistent Galerkin FEM for computing derived boundary quantities in thermal and/or fluids problems. *International Journal for Numerical Methods in Fluids*, 7:371–394, 1987.

[59] T. J. R. Hughes, L. P. Franca, I. Harari, M. Mallet, F. Shakib, and T. E. Spelce. Finite element method for high- speed flows:consistent calculation of boundary flux. *Paper No.AIAA-87-0556, AIAA 25th Aerospace Sciences Meeting, Reno, Nevada*, 1987.

[60] M. Oshima, T. J. R. Hughes, and K. Jansen. Consistent finite element calculation of boundary and internal fluxes. *International Journal of Computational Fluid Dynamics*, 9:227, 1998.

[61] T. J. R. Hughes, G. Engel, L. Mazzei, and M. G. Larson. The continuous Galerkin method is locally conservative. *Journal of Computational Physics*, 163:467–488, 2000.

[62] T. J. R. Hughes and G. N. Wells. Conservation properties for the Galerkin and stabilised forms of the advection-diffusion and incompressible Navier-Stokes equations. *Computer Methods in Applied Mechanics and Engineering*, 194:1141–1159, 2005.

[63] P. Nithiarasu. A simple locally conservative Galerkin (LCG) finite element method for transient conservation equations. *Numerical Heat Transfer, Part B Fundamentals*, 46:357–370, 2004.

[64] C. G. Thomas. *A locally Conservative Galerkin (LCG) Method for convection-diffusion and Navier-Stokes equations.* PhD Thesis, Civil and Computational Engineering Centre, School of Engineering, Swansea University, 2006.

[65] C. G. Thomas and P. Nithiarasu. An element-wise, locally conservative Galerkin (LCG) method for diffusion and convection-diffusion problems. *International Journal for Numerical Methods in Engineering*, 73(5):642–664, 2008.

[66] C. G. Thomas, P. Nithiarasu, and R. L. T. Bevan. The locally conservative Galerkin (LCG) method for solving incompressible Navier-Stokes equations. *International Journal For Numerical Methods in Fluids*, 57:1771–1792, 2008.

[67] O. C. Zienkiewicz, R. L. Taylor, S. J. Sherwin, and J. Peiro. On discontinuous galerkin methods. *International Journal for Numerical Methods in Engineering*, 58:1119–1148, 2003.

[68] O. C. Zienkiewicz and R. Codina. A general algorithm for compressible flow and incompressible flow - part I. the split characteristic-based scheme. *International Journal for Numerical Methods in Fluids*, 20:869–885, 1995.

[69] O. C. Zienkiewicz, K. Morgan, B. V. K. S. Sai, R. Codina, and M. Vazquez. A general algorithm for compressible flow - part II. tests on the explicit form. *International Journal for Numerical Methods in Fluids*, 20:887–913, 1995.

[70] O.C. Zienkiewicz, B.V.K. Satya Sai, K. Morgan, and R. Codina. Split, characteristic based semi-implicit algorithm for laminar/turbulent incompressible flows. *International Journal for Numerical Methods in Fluids*, 23(8):787–809, 1996.

[71] R. Codina, M. Vázquez, and O.C. Zienkiewicz. A general algorithm for compressible and incompressible flows. part III: The semi-implicit form. *International Journal for Numerical Methods in Fluids*, 27:13–32, 1998.

[72] O.C. Zienkiewicz, P. Nithiarasu, R. Codina, M. Vázquez, and P. Ortiz. The Characteristic-Based-Split procedure: An efficient and accurate algorithm for fluid problems. *International Journal for Numerical Methods in Fluids*, 31:359–392, 1999.

[73] P. Nithiarasu, R. Codina, and O.C. Zienkiewicz. The Characteristic Based Split (CBS) scheme. In P.Neittaanmäki, T. Rossi, S.Korotov, E.Oñate, J. Périaux, and K. Knörzer, editors, *ECCOMAS 2004*, Jyväskylä, 24-28 July 2004. European Congress on Computational Methods in Applied Sciences and Engineering.

[74] R. Codina and O.C. Zienkiewicz. CBS versus GLS stabilization of the incompressible Navier-Stokes equations and the role of the time step as stabilization parameter. *Communications in Numerical Methods in Engineering*, 18:99–112, 2002.

[75] R. Codina, H. Coppola-Owen, P. Nithiarasu, and C.-B. Liu. Numerical comparison of CBS and SGS as stabilization techniques for the incompressible Navier-Stokes equations. *International Journal for Numerical Methods in Engineering*, 66:1672–1689, 2006.

[76] Ramon Codina. A stabilised Finite Element Method for generalised stationary incompressible flows. *Computer Methods in Applied Mechanics and Engineering*, 190:2681–2706, 2001.

[77] P. Nithiarasu. An efficient artificial compressibility (AC) scheme based on the charcteristic based split (CBS) method for incompressible flows. *International Journal for Numerical Methods in Engineering*, 56:1815–1845, 2003.

[78] P. Nithiarasu, J. S. Mathur, N. P. Weatherill, and K. Morgan. Three dimensional incompressible flow calculations using the characteristic based split (CBS) scheme. *International Journal for Numerical Methods in Fluids*, 44:1207–1229, 2004.

[79] P. Nithiarasu and O. C. Zienkiewicz. Analysis of an explicit and matrix free fractional step method for incompressible flows. *Computer Methods in Applied Mechanics and Engineering*, 195:5537 – 5551, 2006.

[80] P. Nithiarasu. A matrix free fractional step method for static and dynamic incompressible solid mechanics. *Int. J. Comp. Meth. Eng. Sci and Mech.*, 7:369–380, 2006.

[81] P. Nithiarasu, R. Codina, and O. C. Zienkiewicz. The characteristic based split scheme - a unified approach to fluid dynamics. *International Journal for Numerical Methods in Engineering*, 66:1514–1546, 2006.

[82] P.R. Spalart and S.R. Allmaras. A one-equation turbulence model for aerodynamic flows. paper 92-0439, AIAA, January 1992.

[83] O. C. Zienkiewicz, R. L. Taylor, and P. Nithiarasu. *The finite element method for fluid Dynamics*. Elsevier Butterworth Heinemann, London, 2005.

[84] P. Nithiarasu, C-B. liu, and N. Massarotti. Laminar and turbulent flow through a model human upper airway. *Communications in Numerical Methods in Engineering*, 23:1057–1069, 2007.

[85] M. Breuer, N. Jovicic, and K. Mazaev. Comparison of DES, RANS and LES for the separated flow around a flat plate at high incidence. *International Journal for Numerical Methods in Fluids*, 41:357–388, 2003.

[86] R.L.T.Bevan, R. Van Loon, and P. Nithiarasu. The locally conservative Galerkin (LCG) method - a discontinuous methodology applied to a continuous framework. *Advances in Applied Mathematics and Mechanics*, 1:319–340, 2009.

[87] R.L.T. Bevan, P. Nithiarasu, R. Van Loon, I. Sazonov, H. Luckraz, and A. Garnham. Application of a locally conservative Galerkin (LCG) method for modelling blood flow through a patient-specific carotid bifurcation. *International Journal for Numerical Methods in Fluids*, DOI: 10.1002/fld.2313.

[88] A.J. Chorin. Numerical solution of Navier-Stokes equations. *Mathematics of Computation*, 22:745–762, 1968.

[89] A.J. Chorin. On the convergence of discrete approximation to the Navier-Stokes equations. *Mathematics of Computation*, 23:341–353, 1969.

[90] G. Karner, K. Perktold, M. Hofer, and D. Liepsch. Flow characteristics in an anatomically realistic compliant carotid artery bifurcation model. *Computer Methods in Biomechanics and Biomedical Engineering*, 2(3):171–185, 1998.

[91] A.D. Augst, B.Ariff, S.A.G. McG. Thom, X.Y.Xu, and A.D.Hughes. Analysis of complex flow and the relationship between blood pressure, wall shear stress and intima-media thickness in the human carotid artery. *Am J Physiol Heart Circ Physiol*, 293:1031–1037, 2007.

[92] T.E.Tezduyar, S. Sathe, T. Cragin, B. Nanna, B.S. Conklin, J. Pausewang, and M. Schwaab. Modelling of fluid-structure interactions with the space-time finite elements: Arterial fluid mechanics. *International Journal for the Numerical Methods in Fluids*, 54:901–922, 2007.

[93] B. Liu, X-Y Liu, and Z-R Ding. The effects of physiological flow waveform on wall shear stress in carotid bifurcation model. *Journal of Hydrodynamics*, 21:669–674, 2009.

[94] N. Stergiopulos, B.E. Westerhof, and N. Westerhof. Total arterial inertance as the fourth element of the windkessel model. *Am J Physiol Heart Circ Physiol*, 276:81–88, 1999.

[95] P. Segers, E.R. Rietzschel, M.L. De Buyzere, N. Stergiopulos, N. Westerhof, I.M. Van Bortel, T. Gillebert, and P.R. Verdonck. Three- and four-element windkessel models: assessment of their fitting performance in a large cohort of healthy middle-aged individuals. *Proc IMechE*, 222:417–426, 2008.

[96] N. Westerhof and J.W. Lankhaar. The arterial windkessel. *Medical and biological engineering and computing*, 47:131–141, 2009.

[97] D. Bessems. *On the propagation of pressure and flow waves through the patient-specific arterial system.* PhD thesis, Eindhoven University of Technology, 2007.

[98] N. Stergiopulos, D.F. Young, and T.R. Rogge. Computer-simulation of arterial flow with applications to arterial and aortic stenoses. *Journal of Biomechanics*, 25:1477–1488, 1992.

[99] X. He and D.N. Ku. Pulsatile flow in the human left coronary artery bifurcation: Average conditions. *Journal of Biomechanical Engineering*, 118:74–82, 1996.

[100] Y. Tardy, N. Resnick, T. Nagel, M. A. Gimbrone Jr, and C. F. Dewey Jr. Shear stress gradients remodel endothelial monolayers in vitro via a cell proliferation-migration-loss cycle. *Arteriosclerosis, Thrombosis, and Vascular Biology*, 17:3102–3106, 1997.

[101] S. Oyre, E. M. Pedersen, S. Ringgaard, P. Boesiger, and W. P. Paaske. In vivo wall shear stress measured by magnetic resonance velocity mapping in the normal human abdominal aorta. *European Journal of Vascular and Endovascular Surgery*, 13:263–271, 1997.

[102] M. Lei, C. Kleinstreuer, and J.P. Archie Jr. Geometric design improvements for femoral graft-artery junctions mitigating restenosis. *Journal of Biomechanics*, 29:1605–1614, 1996.

[103] C. Kleinstreuer. *Biofluid Dynamics Principles and Selected Applications.* Taylor & Francis, 2006.

[104] J. R. Buchanan, C. Kleinstreuer, S. Hyun, and G. A. Truskey. Hemodynamics simulation and identification of susceptible sites of atherosclerotic lesion formation in a model abdominal aorta. *Journal of Biomechanics*, 36:1185–1196, 2003.

[105] Karypis Labs. Overview of the METIS software. http://glaros.dtc.umn.edu/gkhome/views/metis.

[106] Barcelona Supercomputing Center. Overview of CEPBA Tools. http://www.bsc.es/paraver.

[107] A. G. Malan, R. W. Lewis, and P. Nithiarasu. An improved unsteady, unstructured, artificial compressibility, finite volume scheme for viscous incompressible flows: Part ii. application. *International Journal for Numerical Methods in Engineering*, 54:715–729, 2002.

[108] P. A. B. deSampaio, P. R. M. Lyra, K. Morgan, and N. P. Weatherill. Petrov galerkin solutions of the incompressible navier-stokes equation in primitive variables with adaptive remeshing. *Computer Methods in Applied Mechanics and Engineering*, 106:143–178, 1992.

[109] R. C. Panton. *Incompressible Flow.* Wiley, New York, 1984.

[110] H. Schlichting. *Boundary Layer Theory (6^{th}) Edition.* McGraw-HillPublications, 1968.

[111] D. Wang, O. Hassan, K. Morgan, and N.Weatherill. Eqsm: An effective high quality surface grid generation method based on remeshing. *Computer Methods in Applied Mechanics and Engineering*, 195:5621–5633, 2006.

[112] D. Wang, O .Hassan, K. Morgan, and N. Weatherill. Enhanced remeshing from stl foles with applications to surface grid generation. *Communications in Numeriacal Methods in Engineering*, 23:227–239, 2007.

[113] G. Taubing. A signal approach to fair surface design. In *Proceeding of SIGGRAPH*, pages 351–358, August 1995.

[114] I. Sazonov, D. Wang, O. Hassan, K. Morgan, and N. Weatherill. A stitching method for the generation of unstructured meshes for use with co-volume solution techniques. *Computer Methods in Applied Mechanics and Engineering Corresponding*, 195:13–16, 1826–1845, 2006.

[115] N.P. Weatherill and O.Hassan. Effcient three–dimensional delaunay triangulation with automatic point creation and imposed boundary constraints. *International Journal for Numerical Methods in Engineering*, 37:2005–2040, 1994.

[116] O. Hassan, K. Morgan, K.J. Probert, and J. Peraire. Unstructured tetrahedral mesh generation for three-dimensional viscous flows. *International Journal for Numerical Methods in Engineering*, 39:549–567, 1996.

[117] J.S. Milner, J.A. Moore, B.K. Rutt, and D.A. Steinman. Hemodynamics of human carotid artery bifurcations: Computational studies with models reconstructed from magnetic resonance imaging of normal subjects. *Journal of vascular surgery*, 28:143–156, 1998.

[118] R. Balossino, G. Pennati, F. Migliavacca, L. Formaggia, A. Veneziani, M. Tuveri, and G. Dubini. Computational models to predict stenosis growth in carotid arteries - which is the role of boundary conditions. *Computer Methods in Biomechanics and Biomedical Engineering*, 12:113–123, 2009.

[119] I. Marshall, P. Papathanasopoulou, and K. Wartolowska. Carotid flow rates and flow division at the bifurcation in healthy volunteers. *Physiological Measurement*, 25:691–697, 2004.

[120] D.W. Holdsworth, C.J.D. Norley, R. Frayne, D.A.Steinman, and B.K.Rutt. Characterization of common carotid artery blood-flow waveforms in normal human subjects. *Physiological Measurement*, 20:219–240, 1999.

[121] I. Heliopoulos, M. Papaoiakim, G. Tsivgoulis, T. Chatzintounas, K. Vadikolias, N. Papanas, and C. Piperidou. Common carotid intima media thickness as a marker of clinical severity in patients with symptomatic extracranial carotid artery stenosis. *Clinical Neurology and Neurosurgery*, 111:246–250, 2009.

[122] K.A.Barbee, P.F.Davies, and R.Lal. Shear stress-induced reorganization of the surface topography of living endothelial cells imaged by atomic force microscopy. *Circulation Research*, 74:163–171, 1994.

[123] O. Smedby. Do plaques grow upstream or downstream? an angiographic study in the femoral artery. *Arteriosclerosis Thrombosis and Vascular Biology*, 17:912–918, 1997.

[124] M.M. Dua and R.L. Dalman. Hemodynamic influences on abdominal aortic aneurysm disease: Application of biomechaniocs to aneurysm pathophysiology. *Vascular Pharmacology*, 53:11–21, 2010.

Author's Publications

- C.G. Thomas, P.Nithiarasu and R. L. T. Bevan *The Locally Conservative Galerkin (LCG) Method for Solving Incompressible Navier-Stokes Equations*, International Journal for Numerical Methods in Fluids, **57**, 1771–1792, 2008.

- R. L. T. Bevan, P. Nithiarasu and R. Van Loon *The Locally Conservative Galerkin (LCG) Method for Solving Incompressible Navier-Stokes Equations*, Proceedings of the 16th UK Conference on Computational Mechanics (ACME). Newcastle-upon-Tyne, 1-2 April 2008

- R. L. T. Bevan, P. Nithiarasu and R. Van Loon *Patient-Specific Computational Modelling of a Carotid Bifurcation Using the Locally Conservative Galerkin (LCG) Method*, Proceedings of the first International Conference on Mathematical and Computational Biomedical Engineering, P.Nithiarasu and R.Lohner (Eds.). Swansea, June 29 - July 1, 2009

- R. L. T. Bevan, R. Van Loon and P. Nithiarasu *The locally conservative Galerkin (LCG) method - a discontinuous methodology applied to a continuous framework*, Advances in Applied Mathematics and Mechanics, **1**, 319–340, 2009.

- R. L. T. Bevan, P. Nithiarasu and R. Van Loon *Patient-Specific Computational Modelling of a Carotid Bifurcation Using the Locally Conservative Galerkin (LCG) Method*, Proceedings of the first International Conference on Mathematical and Computational Biomedical Engineering, P.Nithiarasu and R.Lohner (Eds.). Swansea, June 29 - July 1, 2009

- R.L.T. Bevan, P. Nithiarasu, R. Van Loon, I. Sazonov, H. Luckraz and A. Garnham *Application of a locally conservative Galerkin (LCG) method for modelling blood flow through a patient-specific carotid bifurcation*, International Journal for Numerical Methods in Fluids, DOI: 10.1002/fld.2313.

- P. Nithiarasu, R. L. T. Bevan, R. Van Loon, I. Sazonov and H. Luckraz *Analysis of wall shear stress parameters for patient-specific carotid bifurcations*, Proceedings of the fourth International Symposium on modelling of physiological flows. Sardinia, 2-5 June, 2010

- R. L. T. Bevan, P. Nithiarasu and R. Van Loon *An investigation of the locally conservative Galerkin (LCG) method and its application to a patient-specific carotid bifurcation*, HPC-Europa2 Transnational Access Meeting. Helsinki, 15-17 June, 2010

- R.L.T. Bevan, P. Nithiarasu, R. Van Loon, I. Sazonov, H. Luckraz and A. Garnham *Patient-specific blood flow simulation through an aneurysmal thoracic aorta with a folded proximal neck.*, International Journal for Numerical Methods in Biomedical Engineering, submitted.

- I. Sazonov, S.Y. Yeo, R.L.T. Bevan, X. Xie, R. van Loon and P. Nithiarasu *A modelling pipeline for flow through patient-specific stenotic carotid bifurcations*, International Journal for Numerical Methods in Biomedical Engineering, to be submitted Oct 2010.

- R.L.T. Bevan, C-B Liu, P. Nithiarasu, R. Van Loon and I. Sazonov *Three dimensional RANS calculations on unstructured meshes using an explicit CBS scheme*, International Journal for Numerical Methods in Fluids, in preparation.